FORMATION AND CHARACTERISATION OF INDIUM SELENIDE THIN FILMS BY ELEMENTAL EVAPORATION

A Thesis

Submitted for the Degree of

Doctor of Philosophy

in the Faculty of Science

By

BOBEN THOMAS

DEPARTMENT OF PHYSICS

COCHIN UNIVERSITY OF SCIENCE AND TECHNOLOGY

COCHIN-682 022 (INDIA)

DECEMBER 1989

CERTIFICATE

I hereby certify that the entire work embodied in this thesis has been carried out by the candidate under my gudiance in the Department of Physics, Cochin University of Science and Technology and in Indian Institute of Science, Bangalore (as guest worker) and that it has not been submitted for the award of any degree or diploma.

Prof. M.G.Krishna Pillai,
Deptartment of Physics,
(Supervisor Teacher)

Cochin- 682 022
December 13,1989.

DECLARATION

I hereby declare that the work presented in this thesis is based on the original work done by me under the guidance of Dr. M.G.K. Pillai, Professor (Rtd.), Department of Physics, Cochin University of Science & Technology, and has not been included in any other thesis submitted previously for the award of any degree.

Cochin- 682 022
December 13, 1989

Boben Thomas

CONTENTS

ACKNOWLEDGEMENTS

PREFACE

Chapter 1 INTRODUCTION .. 1

1.I: III-VI Compounds .. 2

1.I.A Layered Compounds .. 2

SECTION A

1.A Review of the Past Work .. 6

1.A.I.A Crystal Structure .. 6

1.A.I.B Electronic and Related Properties .. 12

1.A.I.C Optical and Allied Properties .. 19

1.A.I.D Transport Properties .. 23

1.A.I.E Photoconductivity .. 31

1.A.I.F InSe thin films .. 34

1.A.II Past work on In_2Se_3 including thin films .. 36

SECTION B

1.B.I Phase diagram of In-Se System .. 38

1.B.II Crystal Structure of InSe : A Sketch .. 40

1.B.III Crystal Structure of In_2Se_3 :A Sketch .. 44

References .. 47

Chapter 2 THEORITICAL ASPECTS .. 57

2.I Introduction .. 58

2.II.a Considerations in the formulation of a model for electron states .. 58

2.II.b Fivaz model for electron states .. 62

2.II.c Physical Consequences of the model .. 68

2.III Carrier movement in semiconducting layered compounds 72

2.III.A Temperature dependence of energy gap .. 76

2.III.B Scattering mode in the layered semiconductors .. 77

2.III.B Exponential dependence of electrical conductivity .. 78

References .. 79

Chapter 3 INSTRUMENTATION and MEASUREMENT TECHNIQUES 82

3.A INSTRUMENTATION .. 83

3.A.I Deposition System Fabrication .. 83

3.A.II Evaporation rate control Instrumentation .. 94

3.A.III Fabrication of metal cell for electrical and photoconductivity measurements .. 104

3.A.IV Resistivity .. 106

3.A.V Hall effect .. 109

3.A.VI Film Thickness measurement .. 112

3.B MEASUREMENT TECHNIQUES .. 118

3.B.I Deposition monitoring and process control .. 118

3.B.II X-Ray Diffraction .. 124

3.B.III Transmission Electron Microscopy (TEM) .. 125

3.B.IV ESCA OR XPS .. 127

3.B.V Chemical methods for Composition analysis .. 131

3.B.VI Determination of Optical constant,n .. 136

References .. 142

CHAPTER 4 SINGLE-PHASE STOICHIOMETRIC THIN FILMS OF InSe - PREPARATION AND CHARACTERISATION .. 145

4.I. Introduction .. 146

4.II. Experimental Details: Elemental evaporation .. 147

4.II.A Film Formation. .. 150

4.II.B Characterisation of the film .. 155

4.II.C Electrical measurements .. 163

4.II.D Optical Analysis .. 165

4.II.E Photoconductivity Measurements .. 166

4.II.F Photovoltaic effect in Indium selenide schottky barriers .. 170

4.III. Results and discussions. .. 171

4.III.A. Structure, and morphology. .. 171

4.III.B Compositional studies .. 182

4.III.C Electrical characteristion .. 197

4.III.D Optical measurements .. 198

4.III.E Photoconductivity measurements .. 203

4.III.F Photovoltaic effect in Indium selenide schottky barriers .. 213

4.IV Conclusions .. 230

References .. 231

Chapter 5 PREPARATION AND CHARACTERISATION OF α -In_2Se_3 THIN FILMS .. 235

5.I. Introduction .. 236

5.II. Experimental Details .. 237

5.II.B Characterisation procedures .. 239

5.III. Results and Discussions .. 239

5.III.A. Structure and morphology .. 239

5.III.B Compositional Studies .. 248

5.III.C. Electrical Measurements .. 256

5.III.D Optical Analysis .. 261

5.III.E Photoconductivity Measurements .. 270

5.IV Conclusions .. 276

References .. 277

CHAPTER 6 CONCLUSIONS AND FURTHER SCOPE .. 281

ACKNOWLEDGEMENTS

I take this moment to express my deep sense of gratitude to my supervisor, Professor M.G.K. Pillai for his valuable guidance, constant advice and patience during the course of this work. In fact, I was greatly benefited by allowing to work in an intrinsic outlook, right through my tenure as a research student.

It is, indeed, my great pleasure to thank Prof. T.R.N. Kutty for the generous help, understanding and endorsement I received from him. The completion of this thesis in the present form was made possible only because of the guidance and the facilities extended by him during my stay in the Indian Institute of Science, Bangalore as a guest worker and really the outcome of his inspiring and fervent concurrence.

I am greatly indebted to Prof. Vikram Kumar, Department of Physics, Prof. R.M. Vasu, Instrumention Centre of the Institute for useful suggestions and immense help I received during the course of this investigation.

I am thankful to Prof. Babu Joseph, Head of the Department of Physics, CUSAT, who evinced keen interest in the progress and development of my work.

I am thankful to my lab-mates in the Institute, Mr.Vivekanandan and Mr.Ravi for their support and co-operation all throughout the work. I also wish to express my humble praise and appreciation to Mr.Raghu and Miss. Audathai for their inexorable and impenitent helpfulness in completing this work. For this I would like to

express my pereninial thankfulness to them.

It is my pleasure to thank my friends Joy, Rajumon, Vijayamohanan, Sreedhar, Pradeep for their abundant help at various stages of this work. I am grateful to Mr. Sam Philip for extending his technical excellence and co-operation all throughout this work. I am also thankful to my friend Shalu Thomas for the discussions I made about the electronic fabrication part and the incomparable help I received during the last part of this work.

Further, I thank my innumerable friends in the Institute for their companionship and support which has made my stay in the Institute a memorable one. I am also grateful to my friends in CUSAT especially in the department of Applied Chemistry, Physics, and Law for their backing from time to time during the period. I shall always cherish their association.

The generous co-operation of the office, technical and library staff of the Department of Physics and staff of University Science Instrumention Centre, CUSAT is also acknowledged.

I thank deeply the authorities of the Indian Institute of Science, Bangalore for providing the short-term working facilities, which helped a lot in successful completion of this work.

Finally, the financial assistance received from the Department of Science and Technology is also gratefully acknowledged.

PREFACE

The semiconductor device field has undergone a true revolution due to the emergence and development of compound semiconductors in the 1950's. Semiconductor physics and technology before that period was featured by a strong emphasis on the semiconducting elements germanium and silicon. The technology of germanium had been puzzled out early before and this element became the prime substance for investigating different aspects related to semiconduction. Within no time silicon came on the scene and virtually substituted the position of germanium. In contrast,the study of compound semiconductors was neglected for a long time.

It was really the development of binary compound semiconductors that made the path clear for the first real light emitting diodes and laser sources. Soon after it was realised that suitable solid solutions of these compounds could be able to play a key role in many fields of physics,electronics and chemistry, employed in numerous practical applications. The direct energy gap of many of these binary compounds,in contrast to the indirect energy gap of germanium and silicon,and their high carrier mobilities pointed to potential for high-efficiency light emitting,light detecting and high-speed switching devices. Furthermore in view of their complete solid solubilities,these compounds could be an ideal basis for the preparation of semiconductor materials with the desired energy gap over a continuous broad spectrum of energies. Immediately,because of the

above mentioned reasons,their promise for use in unique electronic devices was recognised.

In the late 1950's and early 1960's a wide range of ternary semiconductor alloys were prepared and the dependence of the band structure on alloy composition was established. However,with the exception of a few such as GaP_xAs_{1-x} and GaAlAs which were used to make light-emitting diodes and microwave devices respectively,the ternary alloys were not widely applied to make devices.

The main obstacle in the application of ternary alloys was the nearly linear relationship between the lattice constant and bandgap. This imposed a severe constraint upon the choice of material since it was extremely difficult to grow high quality layers of poorly lattice matched semiconductors. In recent years although many of the ternary systems are under serious research activity for the use in various devices such as infra-red detectors,solar cells and semiconductor lasers,only a few have emerged as notable. It was the advent of low-loss optical fibre in the 1970s that created a genuine need to develop materials for optical applications over a wide range of wavelengths. GaAlAs heterojunction lasers and detectors,for example constitute a new generation of optoelectronic devices based on ternary semiconductor alloys. GaAlAs, apart from these finds application in high-frequency microwave devices and integrated circuits. Another material that gained importance during the last fifteen years is HgCdTe owing to its infra-red properties.

In recent years,the close relationship between the lattice constant and bandgap in ternary alloys was overcome by incorporating a fourth component,thus forming quaternary alloys. As a result,for example,the GaInAsP alloys could be produced lattice-matched to either GaAs or InP substrate. These alloys span the energy range 1.42-1.91 and 0.75-1.35 eV,respectively. The ability of these materials to form the desired energy gap E_g,which determines the spectral position of the edge luminescence band,and the photosensitivity band forms the basis for the technology of optoelectronic devices operating in a wide spectral range.

In the last decade, radically different requirements from the conventional ones, for new range of applications stimulated the research in varies group of materials. This was evident from the hundreds of publications, which reported the comprehensive investigations of different compounds in all possible combinations from among the groups in the periodic table.

The tremendous progress in understanding the basic material science of different new range of compounds has been stimulated by its scope and widened to the largest degree by the recent progresses in the optoelectronic field. The need to provide materials for applications in the long-wavelength range (eg.infrared detectors) has led to the development of binary compounds of III-VI (eg. GaSe and InSe) and II-VI (eg. CdS and HgCdTe) compounds. Although these alloys are not as well known as their III-V counterparts, a great deal of effort has been put into charecterising their properties. These III-VI compounds from

an academic as well as applied point of view, represent a qualitatively different class of alloys since most of these are characterised by a layered structure. Interestingly most of the aspects that are brought about by the layered compounds are new as well as overlooked in the ordinary (layered) binary compounds.

In the present investigations a systematic attempt has been made to grow and characterise stoichiometric thin films of the In- Se system of compounds, namely InSe and In_2Se_3.

CHAPTER 1

INTRODUCTION

Abstract:

This introductory chapter gives a comprehensive review of work so far carried out in the layered, indium monoselenide (InSe) and di-indium triselenide (In_2Se_3) materials. This includes a summary of structural, electronic, electrical, optical and optoelectronic properties of these materials. This chapter apart from presenting the problems, ~~existing~~ in the understanding of ~~analysing~~ the structural and physical properties of these materials, presents also the necessity of preparing them in the form of thin films, without any admixture of phases, by highlighting the distinguishing properties of single crystals.

1.I: III-VI Compounds

The title III-VI compounds designates, a group of compounds formed from elements of group III A and group VI A of the Periodic Table. Fig.1.1 shows the portion of interest from the Periodic Table. As follows, these are compounds of oxides, sulphides, selenides or tellurides of Boron, Aluminium, Gallium, Indium or Thallium. Evaluating on structural basis, these compounds can be easily categorised into two types: layered compounds and non-layered compounds.

1.I.A Layered Compounds

Layered compounds in the above mentioned group (i.e., the III-VI compounds) include the chalcogenides of gallium, indium and thallium. As the name conveys, the characteristic of these compounds is a layered structure, i.e., they are not just like the ordinary compounds in their structural configuration. Individual crystal planes are only loosely bound to each other by weak Van der Waals forces, although crystal structure resembles to ordinary compounds. Bulky crystals are easily cleavable in their layer planes. But their surfaces are highly inert towards external chemical contamination. Although structurally highly anisotropic, not all the physical properties are affected by this anisotropy. The ones more affected are those, more hinged on to the structure. So, by and large they exhibit a multitude of versatile and interesting properties. The electrical conductivities of these compounds, aloof from its dependence on

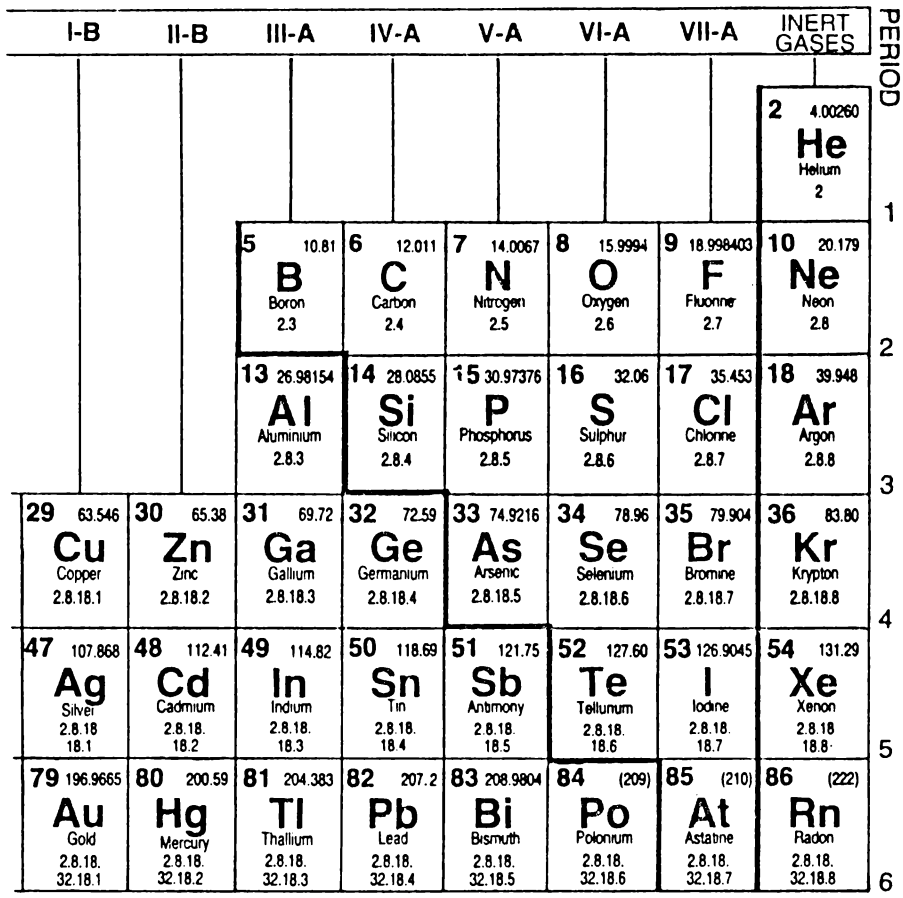

Fig.1.1 Portion of the Periodic table including the elements of groups IIIA and VIA.

preparation method, spans a wide range (10^2 to $10^{-14}ohm^{-1}cm^{-1}$). As to augment this, these compounds exist in a variety of stoichiometric combinations and exhibits a range of energy band gap (Table 1.1), which is highly advantageous from the technological point of view.

The application range of these compounds includes photovoltaic conversion using solar cells, solid state energy storage, photoreceptors for electrophotography, micro-molecular sensors, switching devices and infra-red detectors. They also have a distinctive advantage of high stability when exposed to high energy ionising radiations and so, can be used as high-energy detectors. Another promising property is their optical memory effect. Because of the high resolution obtainable, recently these compounds find application in optical recording also.

1.I.A.1 Indium - Selenium (In-Se) Compounds

Among the layered semiconductors, in view of the present requirements of solid state energy conversion and storage, the In-Se compounds are the most promising. This is mainly because of their prospective optoelectronic and intercalation properties. Recent developments on high-resolution optical recording identifies a wider role to these compound thin films, in future information storage activity.

Table 1.1

Forbidden energy gap of the III-VI layer compounds.

chalcogen / metal	S	Se	Te
Ga	GaS: 2.8 Ga_2S_3: 3.4	GaSe: 2.0 Ga_2Se_3: 1.9	GaTe: 1.66 Ga_2Te_3: 1.08
In	InS: 1.90 In_2S_3:1.98	InSe: 1.30 In_2Se_3: 1.39	InTe: 1.35* In_2Te_3: 1.14
Tl	**	TlSe: 0.73	**

** Not reliably established. * Based on preliminary reports.

SECTION A

1.A Review of the Past Work

In the last few years a lot of theoretical and experimental efforts were made to the investigations of the indium chalcogenides especially selenides. These comprise of their structural, chemical, electronic, electrical, optical and optoelectronic properties. Of these efforts, first we will try to look over the significant contributions in the structural aspect.

1.A.I.A Crystal Structure

1.A.I.A.1 Crystalline Structure: InSe

Recently, although some of the compositions in the In-Se system of compounds have unambiguously been established, still there remain some controversy over the existence of a few compounds in the system. The discrepancy in the reported data may be mainly due to the complexity of the structural features which results from polytypism. As a result, the composition of some of the compounds in this group is still uncertain and their crystal structure also has not been reliably established.

On the structure of InSe, the first information is from the communication of Schubert, Dorre and Gunzel[1] in 1954. They proclaimed the unit cell of InSe to be rhombohedral at room temperature with lattice parameters: a = 4.01 Å, c = 25.00 Å. This determination came exactly twenty years after the first synthesis of InSe by Klemm and Vogel[2].

In 1957, Sugaika[3] determined the InSe structure on a

Bridgmann-Stockbarger grown sample and found a hexagonal structure with a space group $P6_322$ having cell parameters: a = 19.2 $\pm$0.1 Å, c = 4.00 $\pm$ 0.02 Å. Comparing the cell parameters with other observations it is evident that the crystal axes in this report is a misexplicated one.

Semiletov[4] in 1958 proposed a different space group $P6_3/mmc$ for the hexagonal structure from the examination of InSe thin films by electron diffraction with lattice parameters: a = 4.04 Å, c = 16.93 Å, and Z = 4.

Relatively late in 1974, Celustka[5] modified the lattice constants to a better accuracy in the hexagonal structure with the same space group $P6_3/mmc$. They used the Oscillation and Weissenberg techniques and obtained the lattice constants: a = 4.005 $\pm$ 0.005 Å, c = 16.640 $\pm$ 0.004 Å.

In the same year Likforman and Guittard[6] published a detailed phase diagram (see page 39) of the In-Se system. They also investigated the InSe structure on a four-circle diffractometer and reported[7] R3m rhombohedral symmetry with unit cell parameters: a = 4.00 Å, c = 25.32 Å, and Z = 6.

Almost simultaneously with the above observation Nagpal and Ali,[8] also reported a structure with R3m unit cell and rhombohedral lattice parameters: a = 4.0046 $\pm$ 0.0005 Å, c = 24.960 $\pm$ 0.004 Å, and Z = 6. For this determination, they depended on the high-angle reflections of a Weissenberg photograph.

Table 1.2

Summary of structural determinations of Indium Selenide.

Structure	Space group	Lattice parameters(Å) and Z	Structure determination method	Crystal preparation method	Reference
Rhombohedral		a=4.02 c=25.05 Z=6			1
Hexagonal	$C6_322$	a=19.2 ±0.1 c=4.00 ±0.02	Oscillation diagram	Stoichiom. Bridgman	3
Hexagonal	$P6_3/mmc$	a=4.04 c=16.93	Electron diffraction	Thin films	4
Hexagonal	$P6_3/mmc$	a=4.005±0.005 c=16.640±0.004	Powder Oscillation Weissenberg	Zone melting	5
Rhombohedral	R3m	a=4.00 c=24.85 Z=6	Four-circle diffractometer	Reaction from elements	6 & 7
Rhombohedral	R3m	a=4.0046±0.0005 c=24.960±0.004	Powder Weissenberg	Cooling of melt	8
Rhombohedral	R3m	a=4.002±0.001 c=24.946±0.006 Z=6	Four-circle diffractometer	Transport reaction	9

Finally in 1980, a refinement of the rhombohedral structure given in Ref.7&8 was undertaken by Rigoult, Rimsky and Kuhn[9], on crystals produced by transport reactions and established that ε-InSe is having a R3m space group with unit cell parameters: a = 4.002 ± 0.001 Å, c = 24.946 ± 0.006 Å in hexagonal axes, and Z = 6. Table 1.2 gives a comprehensive account of all these developments of structural determinations.

1.A.I.A.2 Crystalline Structure: In_2Se_3

The earliest report on the structure of In_2Se_3 was given only in 1953, by Hahn[10] (high temperature phase with hexagonal lattice periods a = 4.00 Å, c = 19.24 Å) although the compound was synthesized[11] even long before in 1910. In fact, Hahn and Klinger[12] in a primary report in 1949, indicated that In_2Se_3 has a low symmetry structure. According to Hahn and Frank[13,14], the structure of In_2Se_3 is hexagonal with cell parameters: a = 3.99 Å, c = 19.0 Å, and Z = 2.

Subsequent works[3,15-17] by different groups showed that there exist at least three different crystal modifications of In_2Se_3: the graphite-like α-modification occur at room temperature, β-modification stable above 200°C and a ε-modification stable above 500-600°C.

In 1961, Semiletov[18,19] published a detailed account on the α and β-modifications of In_2Se_3 from an electron diffraction study of thin films. Semiletov described the room-temperature α-phase is essentially a hexagonal structure having lattice constants: a = 16.00 Å, c = 19.24 Å, Z = 32 and space group $P6_3$.

The setting up of this structure is on a two-layer hexagonal packing of Se atoms, with most of the In atoms in the tetrahedral positions of this packing, while 1/16 of the In atoms in the octahedral positions.

The high temperature phase of In_2Se_3 (β) is characterised, essentially by a wurtzite structure. The hexagonal lattice constants obtained are a = 7.11 Å, c = 19.30 Å having a space group $P6_5$. The basis of the structure is a two-layer hexagonal close packing of Se atoms, in which the In atoms occupy 1/3 of the tetrahedral spaces of this packing.

For this phase (i.e., β-In_2Se_3), Osamura, Murakami and Tomhe[20] gave a distinct structural model, in which they suggested a rhombohedral phase of $R\bar{3}m$ crystal symmetry with lattice spacing: a = 4.05 Å, c = 29.41 Å and Z = 3 in hexagonal axes. The indium atoms of this form are situated in octahedral spaces formed by selenium packing. But on comparison with the later reports, it is evident that some confusion prevails about the atomic parameters given in this structural assignment.

For the α-phase the space group they accredited is R3m having lattice parameters : a = 4.05 Å, c = 28.77 Å and Z = 3. The In atoms in this case occupy the tetrahedral spaces, formed by chalcogen packing.

In 1978, Likforman, Carre and Hillel[21] suggested a distorted wurtzite-like structure for the low-temperature form of In_2Se_3 of space group $P6_1$ with unit cell constants: a = 7.11 Å, c = 19.34 Å and Z = 6.

Popovic et al in 1979 described two room temperature modifications of α-In_2Se_3: hexagonal form and rhombohedral form. For these, the crystals were obtained by following two different growth techniques. In these, the hexagonal modification has cell constants alike to those reported by Hahn[10]. The cell periods are $a = 4.025 \pm 0.005$ Å, $c = 19.235 \pm 0.005$ Å, $Z = 2$ and having a space group $P6_3/mmc$. Concerned with the rhombohedral modification of α-In_2Se_3, the lattice constants reported are $a = 4.025 \pm 0.005$ Å, $c = 28.762 \pm 0.007$ Å, $Z = 3$ and the space group is found to be $R\bar{3}m$.

For the β-In_2Se_3 phase, at temperatures above 200°C, they suggested another rhombohedral modification of $R\bar{3}m$ space group having cell constants $a = 4.000 \pm 0.008$ Å, $c = 28.33 \pm 0.01$ Å in hexagonal axes, and $Z = 3$.

Finally in 1980, again Likforman et al[22] reported that several hexagonal and rhombohedral polytypes are possible for In_2Se_3 both for α- and β-phase. According to them α-phase is stable only above 550°C, but at lower temperature (<200°C) it is only in a metastable state, exhibiting several hexagonal and rhombohedral modifications having $a = 4.02$ Å and c parameters integral multiples of $c_1 = 9.56$ Å. They suggested that the α-phase is stable upto 200°C and transforms to β-phase for temperatures higher upto 350°C. This β-phase also exists in several polytypic forms. Again this transforms to γ-In_2Se_3; but is relatively slow and only between 400 and 550°C. But, the validity of these suggestions still remains to be established.

1.A.I.A.3 Crystalline Structure: In_4Se_3

Due to the uncertainity in the composition of an orthorhombic In-Se phase, lot of confusion was prevailing in the literature and was solved only in 1972 when the composition was finally confirmed as In_4Se_3. Even before that, Hogg et al[23] have presented the structures for these assuming it as In_4Se_3. Two years later i.e., in 1973 they presented[24] a comprehensive account of the structure, using a four-circle diffractometer and found that In_4Se_3 unit cell is orthorhombic with a = 15.297 $\pm$ 0.001 Å, b = 12.308 $\pm$ 0.001 Å, c = 4.081 $\pm$ 0.001 Å, Z = 4 and the space group can be ~~P_{nnm}~~ or $P_{nn}2$.

1.A.I.A.4 Crystalline Structure: In_6Se_7

For a long time the compound In_6Se_7 has been described under other compositions specifically In_4Se_5[1,25,26] and In_5Se_6[27-29]. But the investigations by Hogg[30] presented in 1971 revealed that the correct composition is In_6Se_7, and suggested that it is isomorphous with In_6S_7. The unit cell contains two formula units with a monoclinic structure having cell parameters a = 9.430 $\pm$ 0.005 Å, b = 4.063 $\pm$ 0.001 Å, c = 18.378 $\pm$ 0.004 Å, β= 109.34 $\pm$ 0.05° and the space group is $P2_1$. This structure can be illustrated of consisting of two separate sections of almost cubic close-packed arrays of Se atoms with In atoms in octahedral coordination.

1.A.I.B Electronic and Related Properties

1.A.I.B.1 Electronic energy levels

Electronic and associated properties of layered semiconductor InSe have been analysed by several investigators. Based on semi-empirical models several schematic band structures have been proposed. Early models were based on two-dimensional approximations but later three dimensional pictures also appeared. The proposed band structures however vary a great extent in its details.

Theoretical band structure calculations on InSe was reported for the first time by McCanny and Murray[31] in 1977 (Fig.1.2). This has been done using a semi-empirical tight-binding method[32] in a two-dimensional approximation. For this one-layer approximation they depended on the resemblance of reflectivity spectra of the different polytypes of an identical compound GaSe and concluded that the optical selection rules are dictated by the symmetry of the single layer. On the basis of the obtained atomic energy levels they were successful in correlating it with the reflectivity data of Andriyashik et al[33].

Another 2-dimensional band structure of InSe that appeared almost simultaneously is from Balzarotti et al[34] who applied a tight-binding (TB) method and explained their XPS experimental observations on the basis of that. For this calculation the empirical values namely lattice parameters and intralayer interatomic distances were taken from the values of Likformann et al[7]. They found that the admixture of In and Se atomic orbitals corresponding to different bands is quite similar to the same found in GaSe. They also marked the similarity of their

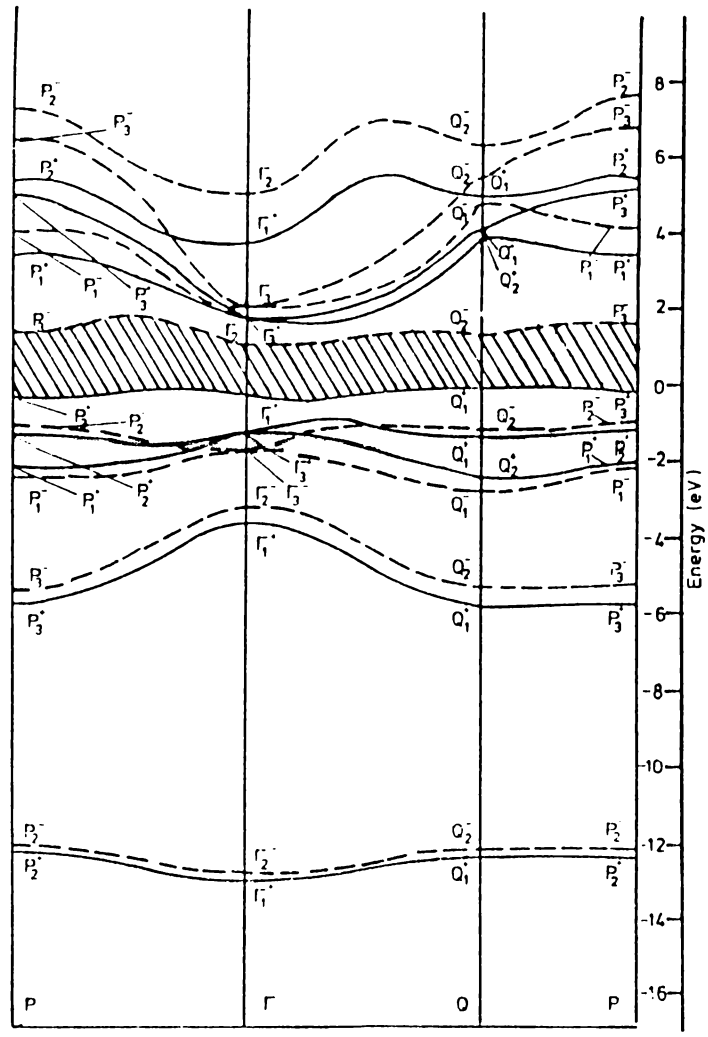

Fig.1.2 Band structure of InSe (after McCanny and Murray).

results with the experimental data of Larsen et al[35] from the polar-angle dependence of photoemission spectra.

But most of these models failed in explaining many of the properties found in this compound semiconductor. However, from later theoretical and experimental observations, it was concluded that, this is mostly due to the exceedingly high approximations applied in these calculations.

A little later in 1978, a three-dimensional pseudopotential and tight-binding calculations were reported by Depeursigne et al[36]. They also used the crystallographic data of Likformann et al[7]. The calculations showed that InSe is more ionic than GaS and GaSe[37], thus explained the smaller dispersion of the energy bands in InSe. The band structures obtained from both the calculations, although are in good agreement with most of the experimental data from XPS[34] and UPS[37] measurements, they differ markedly from the separation and the band dispersion found experimentally by Larsen et al[35]. Again their observation of InSe as an indirect band gap material is not consistent with the later experimental observations. On the other hand, these calculations showed the importance of the interlayer interaction in the calculation of energy levels from the natural coincidence of many of the experimental values.

Almost concurrently with the above calculation, Bourdon et al[38] presented an independent three-dimensional pseudopotential energy band diagram (Fig.1.3). For this computation, a rhombohedral structure of InSe was considered and

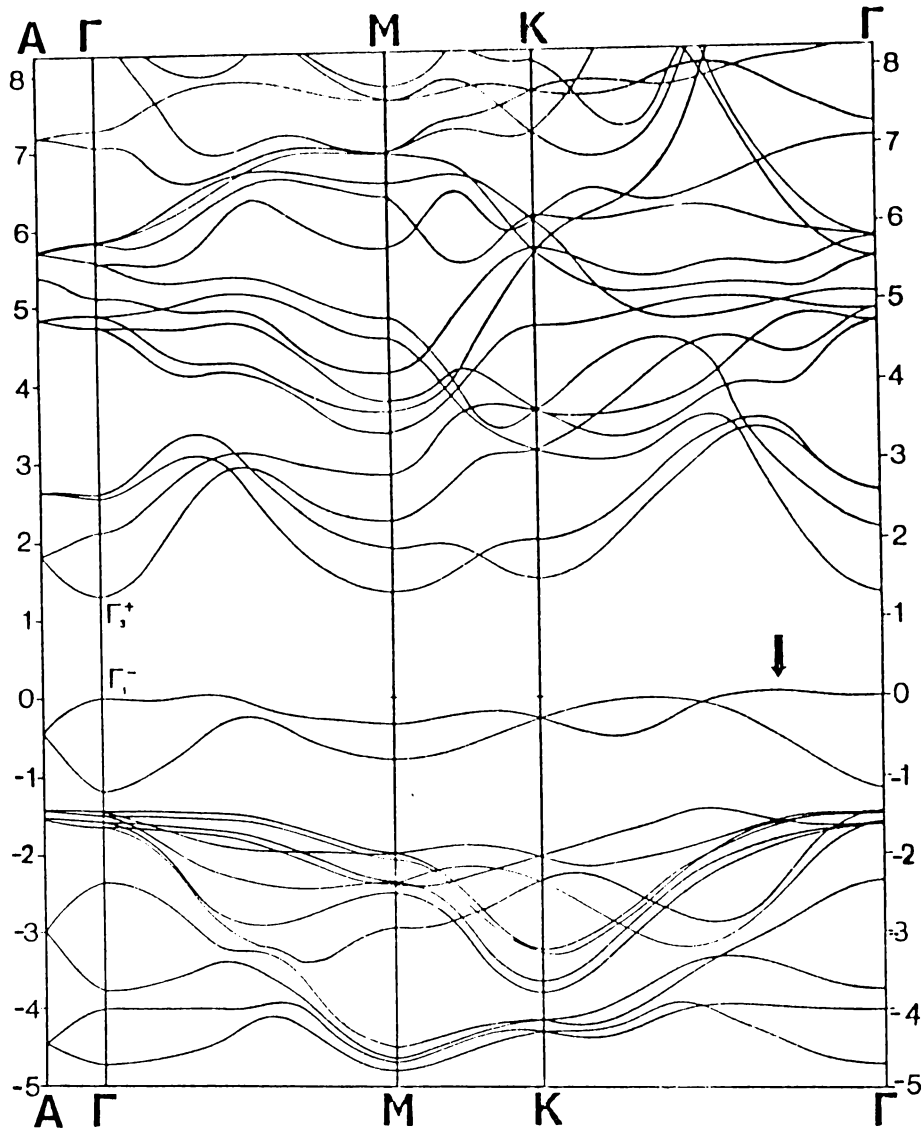

Fig.1.3 Band structure of InSe, calculated by Bourdon et al. Energies in eV _ Origin at ~~Γ extremum~~ of the valence band. Direct gap at Γ ($\Gamma_1^- \rightarrow \Gamma_3^+$).

the non-local pseudopotential was derived from Lin and Kleinman[39]. Electronic screening potentials were added following Friedel's sum rule[40].

According to the diagram the upper valence states and lower conduction states are coming from bonding and antibonding Indium states and the absolute maximum of the valence band is 20 meV higher than at the Γ extremum. The result is that InSe is expected to show only a weakly indirect behaviour in the band to band transitions. In general the above band scheme agree well with most of the UPS, XPS, UV reflectivity and high pressure measurements.

Succeedingly several modifications to the band schemes have been suggested with limited diversifications, but none of these truly account for the observed experimental results in full.

1.A.I.B.2 X-ray Photoelectron Spectra

A deeper understanding of the electronic properties of a material is provided through a combined analysis of XPS and UPS (X-ray and ultra-violet photoemission) and optical results, coupled with band structure calculations. Several investigators have reported valence-band-density-of-states spectra by the UPS[35,37] and XPS[34,41-43]. The density-of-states (DOS) histogram is helpful in determining the chemical states, and also the energy values of the joint effect of the valence states in a compound.

Comparing the reported spectra, there is a substantial agreement in the general shape, but minor differences in the

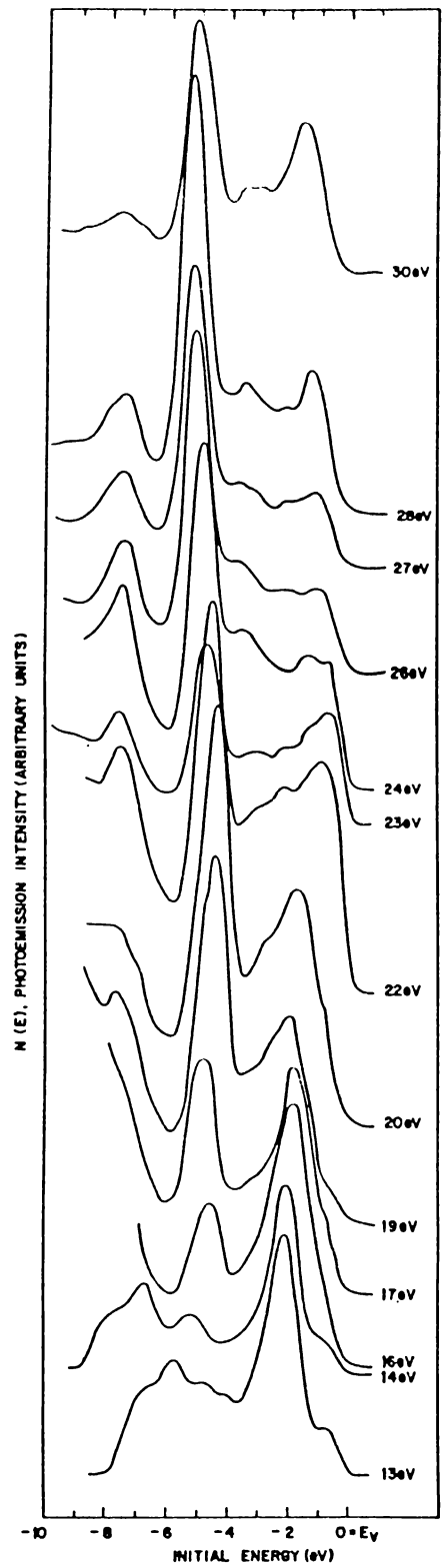

Fig.1.4 Photoelectron spectra of InSe single crystal for various photon energies ($\perp^r$ to cleavage plane)

energy values are often visible. This may be partially due to the matrix element effect upon the spectra.

However, most of the XPS and UPS work available in literature is related to the band structure features. McCanny and Murray[31] calculated two-dimensional (2D) TB bands for GaSe and InSe and compared their calculated DOS with experimental XPS and UPS. Benefited from this, they argued that the gross features of the valence band electronic structure can be adequately described by a two-dimensional model. Measurements by different authors[34,35,37,41,42] presents more or less similar results. Contrary to the above, Larsen et al[44] and others[43] favour more for a three-dimensional scheme, from UPS and XPS measurements.

Typical XPS energy distribution curves for indium selenide is shown in Fig.1.4. In the spectra the structure found between -0.5 and -1.5 eV is explained only in a three-dimensional band-scheme which is likely to be a consequence of a strong inter-layer interaction. In conformity with the other peak positions, XPS results strongly suggest a combined two-dimensional and three-dimensional band structure for InSe.

1.A.I.C Optical and Allied Properties

In indium selenides, optical properties for a broad wavelength range, excitonic absorption edge, reflectivity spectra, luminescence spectra and Raman spectra have widely been reported. Most of these measurements are confined to temperatures in the range 90-293 K and show strong similarities with GaSe.

Absorption spectrum of InSe shows a sharp increase (Fig.1.5)

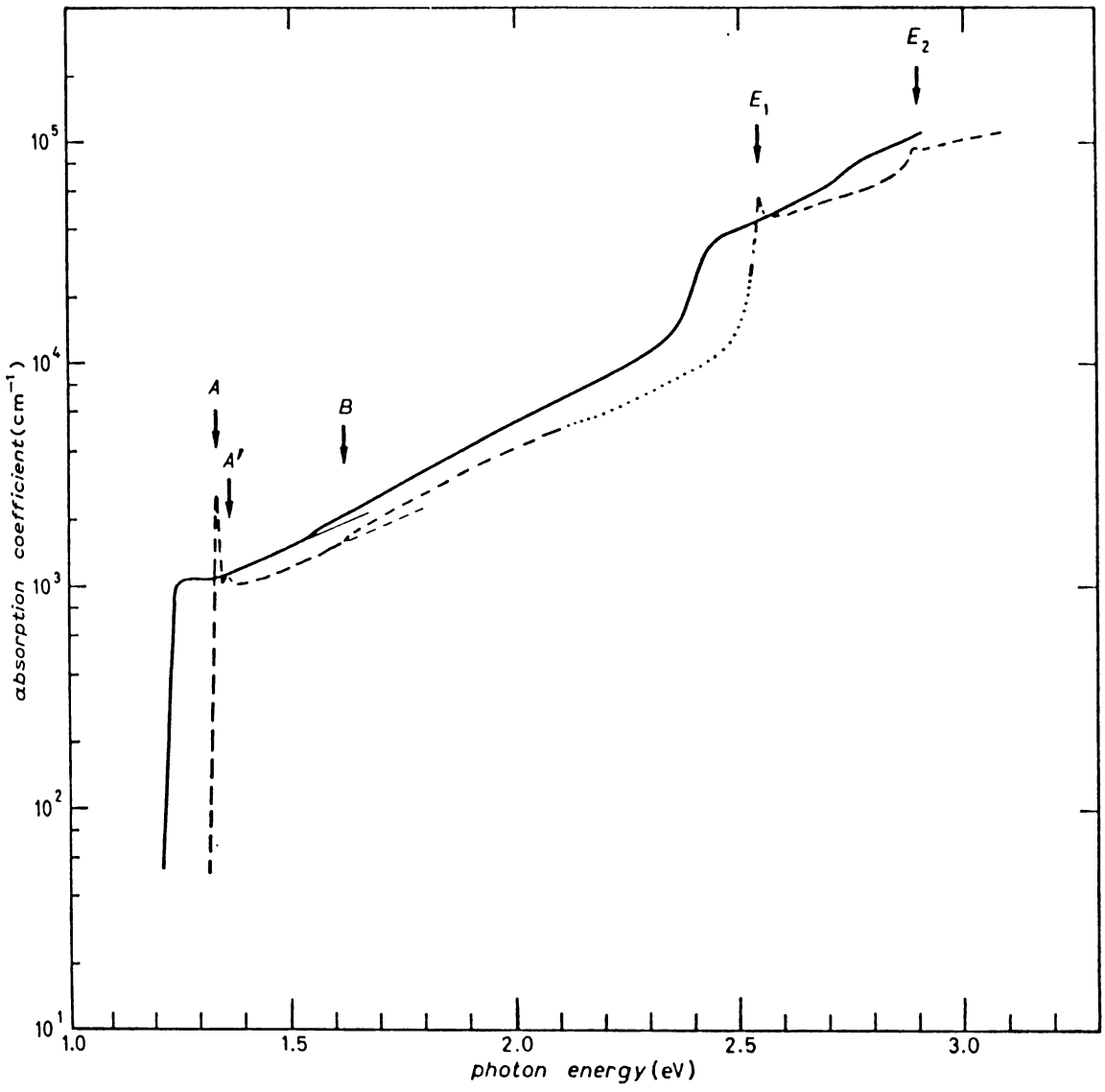

Fig.1.5 Spectrum of the absorption coefficient of InSe measured at room temperature (solid line) and at 10K (dashed line).

near the fundamental absorption edge at about 1.3 eV. The absorption above the fundamental gap rises slowly up to the second threshold at about 2.4 eV which corresponds to the direct forbidden edge[33]. It has been suggested[45] that InSe also possesses a subsidiary conduction band minimum located a little below the direct band minimum at the Γ-point.

An indirect absorption edge E_{id} with a temperature coefficient $dE_{id}/dt = -4.2 \times 10^{-4}$ eV/K was reported at 1.187 eV at 293K [33]. For this transition, it was found that a phonon of energy 21±5 meV has to be assisted.

The results of the reflectance measurements show marked difference from one author to the another[33,46-48]. Nevertheless the character of optical transitions as well as the peculiarities in the energy band structure are conveniently derived through a critical evaluation of the data.

The near-band-edge optical properties of InSe have also been of considerable interest. The absorption spectrum often shows a pronounced fine structure of the ground-state exciton (Fig.1.6). This fine structure of the exciton ground state in InSe is strongly sample dependent and attributed to the presence of stacking disorder[49].

A direct transition at 2.4 eV is characterised by an absorption structure whose exciton nature has been proved by low-temperature experiments[50] and is associated with an exciton transition bound to a M_o three-dimensional critical point[51]. The value of direct exciton binding energy in the fundamental

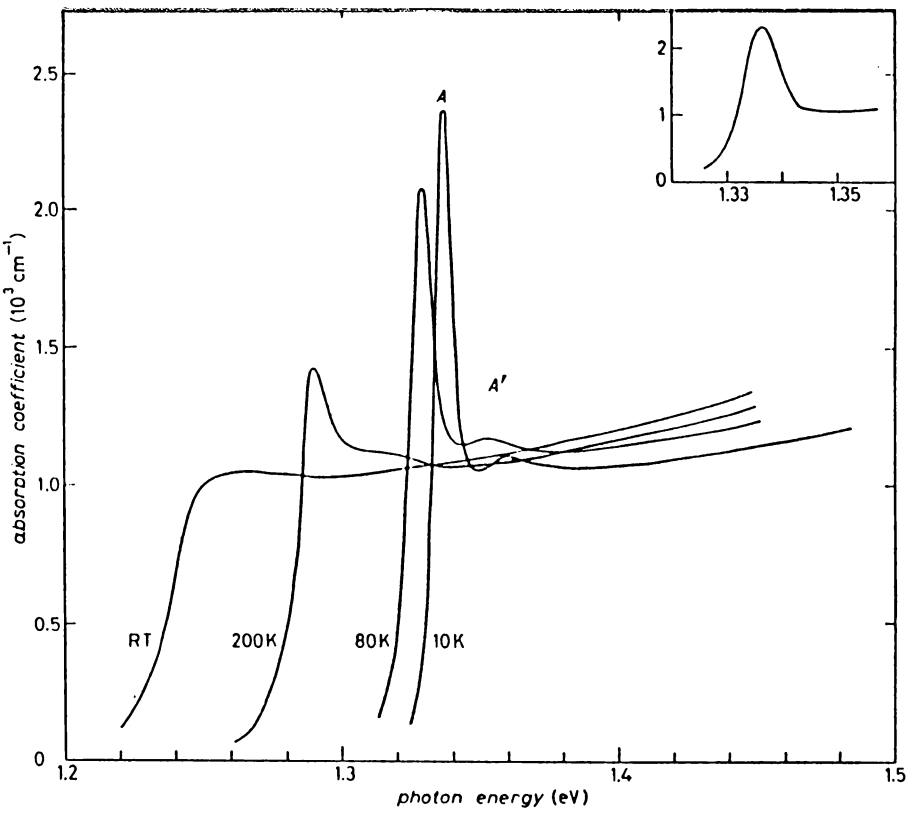

Fig.1.6 Plots of the absorption coefficient of InSe around the fundamental absorption edge at different temperatures showing the exciton peak

absorption region is calculated to be 14.5±0.5 meV, with a value of the effective mass m_e=0.10 m_o for electrons in the Γ minimum of the conduction band[52].

The temperature dependence of excitonic structure and band-gap in the range 1.6-300 K have also been reported[52]. Variation in the band-gap energy is accounted for a change in the electron-phonon interaction which causes an additional shift in the lattice positions and decreases the band gap when the temperature is raised.

1.A.I.D Transport Properties

1.A.I.D.1 Electrical Properties

Utilisation of a material as a semiconductor, to a great extent, depends upon its electrical transport properties. In order to obtain information about the scattering mechanisms of charge-carriers, depth of impurity centres, forbidden energy gap, carrier concentration, mobility, etc. and to draw an idea about the extent of domination of anisotropy on these properties, the investigations of the electrical properties have been increasingly pursued.

Measurements of conductivity and mobility in InSe have shown that electrical conduction in this material is highly anisotropic. At the same time, there are many discrepancies and contradictory results in connection with these measurements. But recent investigations suggest that this can be primarily due to the circumvention of structural causes, which is of importance in

this semiconductor.

One of the early reports on electrial conductivity is due to Damon and Redington[53] in which the room temperature conductivity was presented to be $5.3 \times 10^{-3} ohm^{-1} cm^{-1}$ and $8 \times 10^{-5} ohm^{-1} cm^{-1}$, parallel and perpendicular to the cleavage planes respectively. Electrical conductivity and Hall coefficient have been measured by Mori[54] from room temperature to 650 K. For this temperature range, the conductivity increases from 10^{-5} to 10^{-1} $ohm^{-1}cm^{-1}$ and Hall coefficient decreases from 10^{5} to 10^{3} cm^{3}/coulomb on increasing the temperature. But the report lacks the measurements in relation to the layer directions. However, the charge carrier density measured in the above samples is between 10^{13} and 10^{15} cm^{-3}, and interestingly, samples having a less carrier density had a larger mobility.

Another report on the measurements of temperature dependence of electrical conductivity and Hall coefficient in InSe single crystals in directions perpendicular and parallel to the c-axis, is from Atakishiev and Akhundov[55]. In the low temperature range, for directions perpendicular to the c-axis, the dependence of the mobility on temperature is in accordance with the three by two power of temperature, while at higher temperature this is inversely proportional to the square of temperature. So it is suggested that at low temperature range scattering of charge carriers may be due to ionised centres and at high-temperature range it may be primarily due to non-polar optical phonons. But the measurements parallel to the c-axis has shown that in all temperature ranges it is governed by the same rule, i.e.,

mobility grows exponentially with temperature. This exponential dependence shows that some hopping mechanism is responsible for the electron motion. Recent observations on temperature dependence of drift mobility measurements using time of flight technique[56] also support this view point.

An analysis of experimental data from resistivity, Hall-effect and SCLC (space-charge-limited-current) measurements in the low temperature range (100-300 K) has been reported by De Blasi et al[57]. The investigations showed that the Hall-mobility variations can be well accounted for by Schmid's three-dimensional model (see Chapter II) with the optical-phonon scattering.

Annealing studies[58] on undoped InSe single crystals have shown that for the shallow donor levels, the ionisation energy is independent of temperature, which again supports the three dimensional density of states concept.

Structural variations that result from the different polytypes of this material (InSe) are important when electrical transport properties are considered. This is because of the altered layer-layer interaction resulting from the different stacking sequence. There can also be contribution from the action of large number of stacking faults which adsorb charge carriers and inhibit motion perpendicular to the layers. As a result the conduction perpendicular to the layer planes exhibits an activated mobility with a mobility ratio $\mu_{\perp c}/\ \mu_{\parallel c}$ ~ 100 even at room temperature. In contrast, as presented earlier in the

optical properties, resonant Raman and exciton absorption measurements indicate that both the conduction and valence bands exhibit very little anisotropy with the effective mass showing some evidence of an anomalous anisotropy with $m_{||} < m_{\perp}$, which is in good agreement with Bourdon's calculation. Thus both two- and three-dimensional band structures provide a good description of the density of states.

The origin of the two-dimensional behaviour, i.e., anisotropy of the effective mass of conduction electrons, at low temperatures is less clear. But at low fields, it is suggested that this is due to extrinsic scattering mechanisms, such as interlayer potential barriers arising from structural defects. Moreover, any impurities present during the growth of the crystals will always get accumulated at defect planes. The overall effect is that the ionised impurities or defects form a charge sheet at the defect planes which cause a hindrance to the motion parallel to the c-axis. This situation when arises in an energy-level diagram is shown schematically in Fig.1.7.

Results of investigations of electrical properties of Lithium[59-62], tellurium[63] and anthracene[64] intercalated InSe crystals, have already been reported. Lithium has the advantage that it easily get introduced between the layers without disturbing the crystal lattice. By this process the dielectric constant has been found to increase substantially and thus shows the feasibility of thin film solid state batteries[64-66]. The intercalated compounds may also find variety of applications

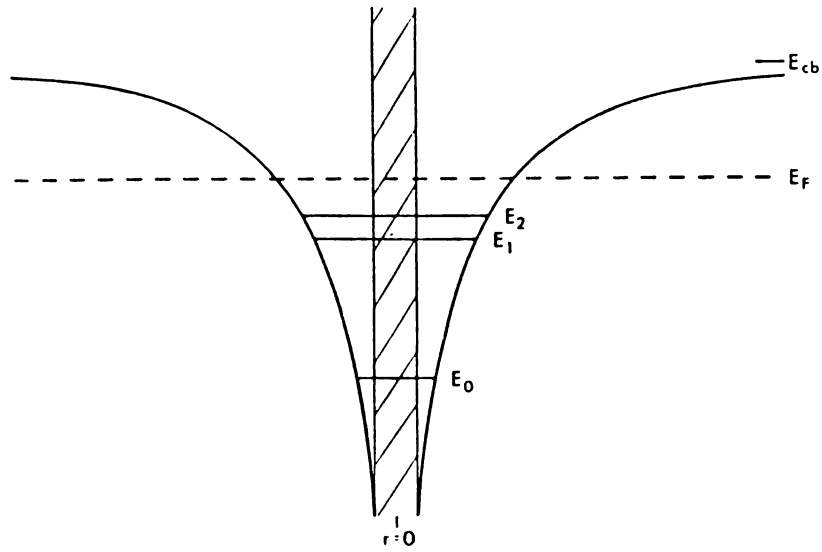

Fig.1.7 A schematic view of the potential wells which give rise to the two-dimensional accumulation layers. Ionised impurities are considered to accumulate at the plane r=0 which represents a stacking fault.

because of their remarkable photoconductive behaviour and photomemory effects[67].

1.A.I.D.2 Carrier Mobility related measurements

Variation of thermoelectric power has been studied in undoped[53,68,69] and doped[70] InSe single crystals. For the Bridgman grown tin-doped crystals the measurement results are available over a wide temperature range[70] (50 to 550 K). This shows that the thermopower is almost constant over the entire temperature range, except a small lowering of the curve at very low temperature, with an onset at around 75 K. Interestingly, at high temperature, it has been observed that there is a decrease of thermopower with increasing electron concentration. The high temperature results can be well accounted for by the same scattering mechanism used earlier to elaborate the temperature dependence of the electron mobility, namely Fivaz and Schmid model (see Chapter 2). The low temperature behaviour can be explained through a model proposed by Portal et al[71]. According to this model, electrons are trapped in planar defects and in that condition they act as a degenerate two-dimensional gas. As the temperature is lowered electrons are increasingly trapped in these defects and in consequence thermopower decreases.

The effect of impurity concentration on thermoelectric power has also been studied and found to be negligible.

1.A.I.D.3 Forbidden energy States

Without the addition of impurities, as-grown indium selenide crystals are n-type[45,72,73]. This n-type conductivity has been

shown to be due to shallow native donor[74], which originates because of selenium vacancy or of interstitial indium atom[75]. It is generally assumed that the problem of impurity levels in layered semiconductor InSe is more complex than in the normal three-dimensionally bonded crystals[57,76-83]. Impurities from group I(Au,Cu), II(Zn,Cd), IV(Pb) and V(P,As) are known to create acceptor levels in InSe. It has been observed that this p-type InSe reverts to n-type when annealed to more than 400°C [84-86].

Unusually it has been observed in this layered semiconductor (InSe) that, the impurities from the same column of the Periodic Table, act both as acceptor and donor. For example, from the group IV, Pb is an acceptor[87] but Sn is a donor[75,88,89]. The origin of this behavior is still less clear. However, it seems reasonable to attribute this to the similar atomic size and the same d-electron shells[38] of In and Sn. The d-electrons are to a certain extent responsible for the metal-metal bond in these compounds, and prevent the rotation of metal atoms and stabilise the Se-In pattern in the eclipsed configuration. When Sn is substituted, all the desired requisites exist for Sn to be in the InSe lattice[75].

At the same time, the explanation of Pb as an acceptor can be like this. When Pb atoms enter into the lattice it may be substituting two In atoms to merge into the layered configuration to form a CdI_2 like arrangement[90], which consequently gives an electron deficit and p-type conduction.

Isoelectronic impurities such as Ga, S or O do not change

the type of conduction in InSe[73]. Furthermore, the isoelectronically doped samples do not exhibit the presence of deep levels also. This implies that the deep levels may be associated with Se vacancies which get neutralised when taking up with impurities like S or O. This is further advocated by the point that electron mobility is much higher in isoelectronically doped samples than in undoped.

Among the donor impurities, Tin is the most suitable in InSe[75] as it permits to reduce the resistivity of the material without strongly affecting the electron mobility[91]. The shallow and deep donor of Sn is with ionisation energies of 44 and 120 meV respectively[75]. A shallow donor level at 22 meV is also reported[89] for this Sn doping. Moreover, except for tin, the relation between dopant concentration and the resultant carrier concentration is not clearly evident.

Another fairly studied dopant in InSe is Zn. Ikari et al[74] have studied the photoluminescence spectrum of Zn-doped InSe and explained the results through a model of donor-acceptor pairs. Shigetomi et al[92] by means of Hall and photo-Hall effect, have found an ionisation energy of 310 meV for the Zn level in InSe.

Various methods have been applied to study the energy levels in the forbidden energy gap. These include DLTS[75,87], TSC[93] and Field effect measurements[94]. By examining these results, it can be seen that the impurity levels cited for the same dopant in different reports do not agree with each other.

1.A.I.E Photoconductivity

Layered semiconductor indium selenide has been much less studied for its photoconductive properties. In conformity with the available literature[67,95-97], a fairly high photosensitivity is observable for the undoped InSe, at the lower energy side of the visible spectrum.

Increase in photosensitivity has been reported when doped with isoelectronic impurities i.e., from Group IV of the Periodic Table. The effect of doping with bismuth, lead and germanium has been reported by Bakumenko et al[96]. Doping InSe with sulphur[98] is reported to have a marked effect on photoconductivity, by changing the photoresponse spectrum and enhancing the photocurrent.

In undoped, Bridgman grown crystals, the photoconductivity spectrum shows features corresponding to excitons[67,96,99] near the absorption edge. This is indicative of the active participation of excitons in the photoconduction process. Highly interesting observations like anomalous photoconductivity[100], negative photoconductivity[101,102], photo-memory effect[103] etc., have also been observed in this semiconductor.

It is assumed that, the existence of the negative photoconductivity in InSe, is associated with the ambipolar injection of carriers into the bulk of the crystal and its features are explained by the transfer of the recombination flux from the slow r centers to the fast s centers under the influence of impurity-absorbed illumination[103,104]. The negative residual

photoconductivity can be destroyed by illuminating with light of wavelengths $\lambda < 1.3$ μm, and by the application of voltage pulses of amplitude corresponding to the quenching of the residual photoconductivity and heating at 350 K followed by cooling in darkness. This observation also clearly justifies the explanation given earlier for the negative photoconductivity detected in this material.

Korsunskii[105] developed a detailed model to account for the anomalous photoconductivity detected in InSe. According to this, there are special U centers which can capture nonequilibrium carriers and have their energy levels in the forbidden band. The nonequilibrium density of the minority carriers which may reach the U centers is low and hence the probability of penetration of a free carrier to a U center is also low, compared with the probability of the release of a carrier from a U center by a photon.

On the other hand, a different model suggested by Ryvkin[106-108] is based on a realistic three-dimensional structure and it accounts clearly for the effect of anomalous photoconductivity. In compliance with this, there may exist structural defects, dislocations and even impurities in the layered crystal which can create potential barriers between layers, which are responsible for the development of anomalous photoconductance.

Photovoltaic properties have also been described in a few investigations[109-115]. These include the formation of schottky

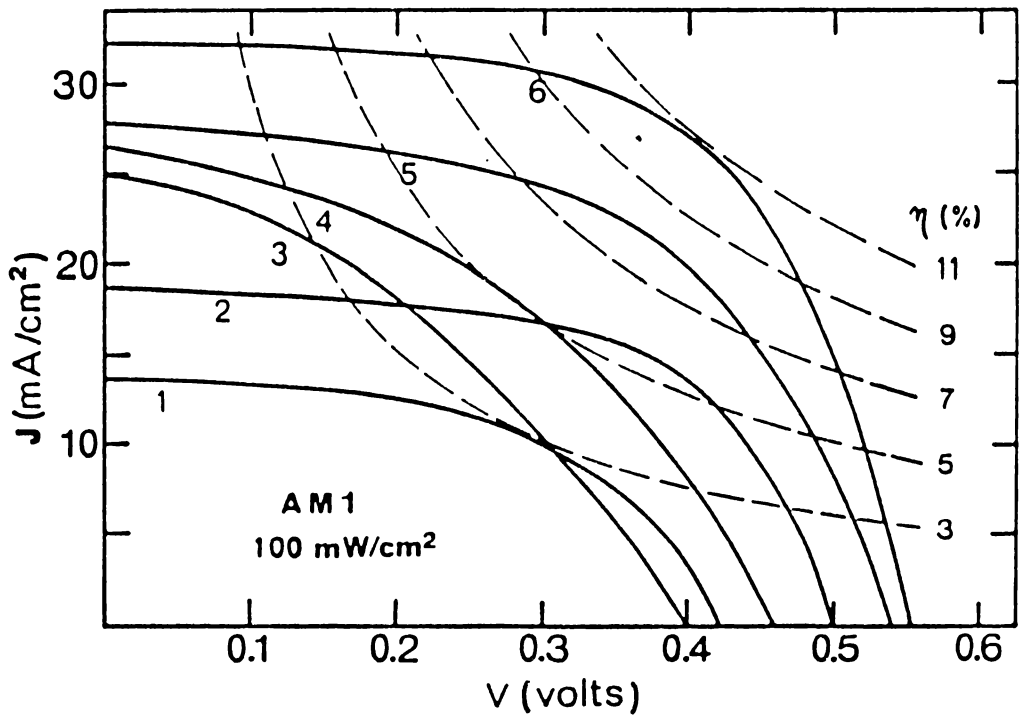

Fig.1.8 J-V characteristics under simulated AM1 conditions at room temperature; curves 1 to 5 :different unannealed cells. curve 6: cell annealed at 150°C.

junctions of Bi/p-InSe[67,109], Pt/n-InSe[67], Au/n-InSe[110-113], Al/n-InSe[114], Cu/n-InSe[114], SnO_2/InSe[114] and indium tin oxide (ITO)/p-InSe[67,115,116]. Of these the largest carrier collection has been obtained in ITO/p-InSe solar cells[67].

The factor that limits the efficiency of the above described photovoltaic cells is mainly the high resistivity of p-InSe or the compensated character of the as-grown InSe[117]. However, recently by improving the electrical parameters and by incorporating a back-surface-field (BSF) [118-120], the efficiency of these cells (Fig.1.8) have been improved to as high as 8-10%[121].

1.A.I.F InSe thin films

Eventhough, as a whole there ~~are~~ is a considerable number of papers concerned with the different aspects of the layered semiconductor indium selenide in the form of single crystals, the understanding about the preparation and the properties of InSe thin films is meagre, especially about the crystalline films. In fact, modern technology trend in the fabrication of devices, increasingly favours the utilisation of semiconductors in the form of thin films. In order to fulfil this, a broad awareness of the material behaviour in thin film form is inevitable. Since the last decade a considerable effort has been devoted in this direction.

Amorphous thin films of InSe have been prepared by vacuum evaporation[97,122-129], flash evaporation[130-133] and sputtering[134]. In these, most of the reports deal with electrical

or optical properties or both. But inappropriately the results of the investigation of the same composition itself varies from author to author. This indicates that the InSe thin film is highly sensitive to the conditions of preparation and the micro-structure.

One of the early reports of InSe thin film is due to Bode and Levinstein[97], who have undertaken some preliminary studies on the photoconductive aspects. Persin et al[122] in 1970 reported some electrical and optical properties of vacuum evaporated films. Subsequently in 1972 Persin et al[130], reported the preparation of the films by flash evaporation. At the same period Sharma et al[123] and Fitzgerald[135] published the crystallisation of α-InSe films prepared by single-source evaporation, and co-evaporation respectively. In 1980, Naidu et al[131] reported different electrical properties of flash evaporated InSe films. The photovoltaic aspect was studied succeedingly by Ando et al and found that it is a promising semiconductor. In the following years, Hashimoto et al[132], Krishna Sastry et al[133], and Chaudhuri et al[125] reported the effect of heat treatment of films prepared by flash evaporation or vacuum evaporation.

Segura et al[67] in 1983 gave a detailed account of the various aspects of photoconductivity and photovoltaic effect in indium selenide. The steady state photoconductivity and optical absorption has been described by DiGiulio et al[126,127] They also have published results on studies of ac-conductivity[128]. Recently Biswas et al[129], presented the effects of heat treatment on the optical and structural properties of InSe thin films.

But, only two communications are reported on the attempt for the formation of InSe films on hot substrates. They are from Guesdon et al[136] and Yudasaka et al[137] in 1987. Of these two papers, the former deals with the preparation of the films by vacuum evaporation and the later by double-source evaporation.

1.A.II Past work on In_2Se_3 including thin films

Reviewing the literature, several reports can be found on various aspects of In_2Se_3 thin films. These reports include a communication from Goryunova et al[138] which confirmed In_2Se_3 as a semiconductor. Miyazawa and Sugaike[15] presented the phase transitions of In_2Se_3 from the observations of single crystals of In_2Se_3 grown by means of double furnace technique. They found a transition of phase at around 200°C.

An initial account of electrical, thermo-electric and optical parameters have been reported by Brice et al[139]. In 1959, Newman[140] reported a detailed account of the phase transitions of In_2Se_3. In this, it is reported that In_2Se_3 has at least three phase modifications. Of which, α-modification is stable below 200°C, β-modification exists above 200°C and a second phase change happens around 600-700°C. Of the different phases of In_2Se_3, Suematsu et al[141] reported in 1966, that both α- and β-modifications are semiconducting. They measured the temperature dependence of electrical conductivity, Hall coefficient and thermo-electric power in a direction perpendicular to the c-axis. Also, doping with Ag, Mg, Cd, Bi, Sb ~~and~~ or I does not change the type of conduction (ie.,n-type) of In_2Se_3. A detailed description of

the optical absorption by single crystals of α- and β-In_2Se_3 have been outlined by Mushinskii et al[142]. They obtained the minimum energy required for the α-In_2Se_3 indirect and β-In_2Se_3 direct transitions as 1.0 eV and 1.16 eV respectively at 300 K.

In a technical note, Celustka and Popovic[5] in 1974 reported the temperature dependence of electrical conductivity of In_2Se_3 prepared by the zone-melting process. Subsequently the optical[5,143-145] and electrical[145,146] properties have been studied by different authors. In 1986, Balkanski et al[147] published a method to differentiate the α- and γ-varieties of In_2Se_3 by means of photoluminescence (PL) bands. The pure α-In_2Se_3 exhibits two PL bands at liquid helium temperature: one at 1.326 eV and the other at 1.523 eV. In contrast the mixed α- and γ-In_2Se_3 shows only one broad band at 1.319 eV.

A theoretical study of electronic properties by Guizzetti and Meloni[148] shows that the direct interband transitions are associated with the observed strongest peak of the reflectivity spectra, and the pseudodirect ones with the weaker structures. In the same report the energy band structure of In_2Se_3 by the empirical virtual-crystal pseudopotential method has also been presented. The annealing and doping effects on In_2Se_3 have also been recently reported by Fotsing et al[149].

The first report of the In_2Se_3 thin films formed by flash evaporation is from Persin et al[150] in 1972. Currently the interest in this compound thin film has widened to a larger degree and the electrical and optical properties have been

reported many a times. Julien et al[151] have grown In_2Se_3 thin films with good stoichiometry on hot substrates and obtained α- and β-phases. The optical studies showed that the band gap energies were 1.43 eV and 1.55 eV for the α- and β-phases respectively.

Herrero and Ortega[152] have attempted to grow β-In_2Se_3 thin films by electrochemical method and investigated its photo-conductive properties. Quite recently Yudasaka and Nakanishi[153] grew epitaxial films of In_2Se_3 on mica substrates and analysed the electrical properties. They found that the formed films are of n-type with conductivity nearly equal to 10^{-6} $ohm^{-1}cm^{-1}$.

The only article about the preparation of In_2Se_3 thin films by double-source evaporation is from Yudasaka et al[137] and they obtained films of γ-In_2Se_3 phase on glass substrates kept at higher temperatures. They accounted for the mechanism of film formation on hot substrates as the take in of the selenium atoms by the indium atoms accommodated on the substrate surface. A preliminary investigation on the spectral dependence of photocurrent shows that the strong absorption starts at around 1.9 eV and shifts slightly depending upon the film formation temperature.

SECTION B

1.B.I Phase diagram of In-Se System

An understanding of the phase equilibrium diagram of a compound is beneficial for the growth of a stoichiometric

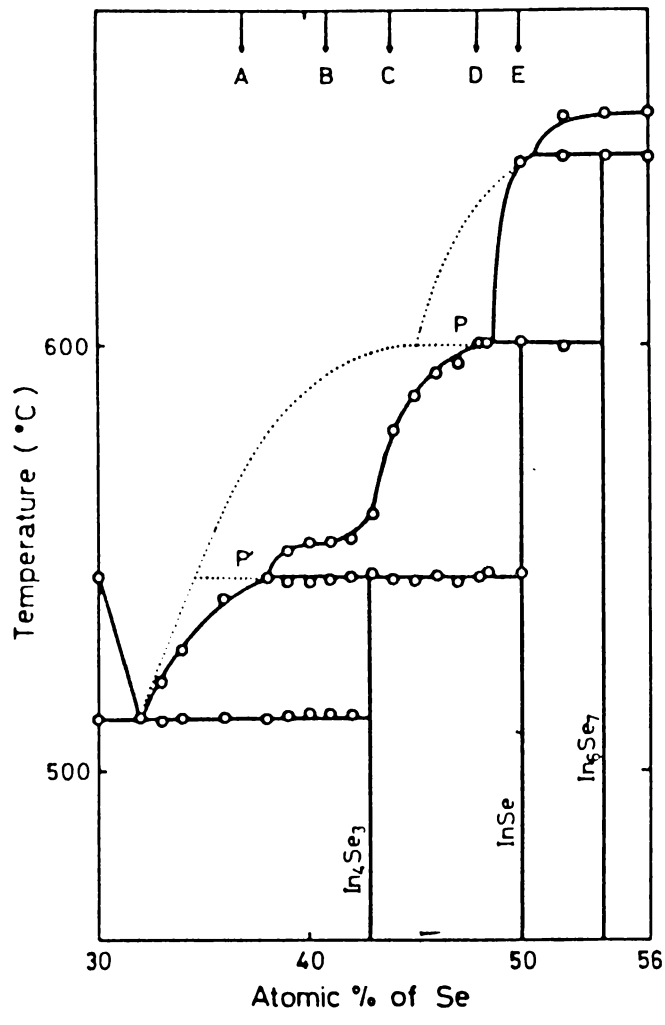

Fig.1.9 Equilibrium phase diagram of In-Se system. Values denoted by dashed lines are determined by Likforman et al [6].

crystalline material. In this the equilibrium is defined as the minimum energy for given values of the variables. A clear-cut interpretation of the constitution of a system is based on the presence of the different phases as a function of temperature.

Several investigations have been done by different groups to establish the equilibrium phase diagram of this system. The first investigation of this system was done by Slavnova et al[154] and established an acceptable melting point for InSe. Likforman and Guittard[6] published a detailed phase diagram in 1974. Detailed investigations on melting point by Celustka[5] and phase transitions by Imai et al[155,156] confirmed the scheme given by Likforman and Guittard. Fig.1.9 gives the phase diagram of the In-Se system. The result of the narrowness of the temperature ranges in the phase diagram for each of the phase is that, different phases often co-exist unless careful preparation conditions are observed.

1.B.II Crystal Structure of InSe : A Sketch

Indium selenide crystallise in layered structures. The crystal structure of a solid is decided by forces acting between its constituents. The bestowal of each force rely upon their valence electron configuration and atomic size. These forces can be of ionic, covalent, metallic or Van der Waals type. But in a layered structure the neutral sandwiches of the component layer atoms have necessarily to be held together by Van der Waals forces.

Like other group III monochalcogenides, indium monoselenide

(InSe) also grows in a layered crystal structure. Each "bidimensional" layer of InSe is structurally identical and is composed of single planes of selenium atoms on either side of a double plane of indium atoms[82]. The coordination number of the indium and selenium atoms are four and three respectively. Fig.1.10 illustrates the coordination of the indium and selenium atoms in a single layer. The ordering regularity of the atoms within the layers is in the sequence anion-indium-indium-anion. Within a layer the crystal bonding is thought to be primarily covalent. But Wieting and Verble[157] from the evidence of infrared measurements have proposed some ionic or Coulomb contribution to this.

Analysis of the arrangement of atoms of InSe shown in Fig.1.10 suggests that the chemical bonds within the layers are between In^{-1} and Se^{+1}, where by In^{-1} obtains a tetrahedral sp^3 coordination and Se^{+1}, a trigonal pyramidal p^3 coordination with a saturated s^2 subshell. The bonds between the layers are essentially of the Van der Waals type with the possibility of a very small ionic contribution as mentioned earlier. In γ-structural modification the layer separation of 3.8140 Å is quite large and the shortest Se-Se distance within a layer is 5.2808 Å, whereas the In-In and In-Se bond lengths within one layer are 2.7696 Å and 2.6335 Å respectively.

In InSe, the existence of three crystallographically distinct polytypes have been confirmed. The β- and ε-structures have two-layer hexagonal stacking (2H-β, 2H-ε) sequences, whereas the γ- structure has a three-layer rhombohedral stacking

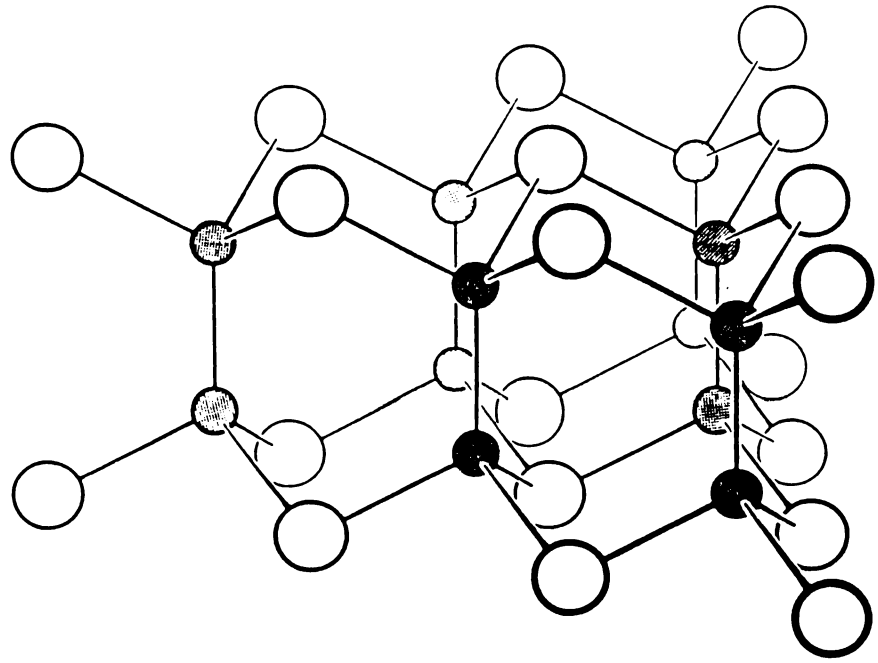

Fig.1.10 Perspective view of the indium and selenium atoms in a single layer of InSe. The large open circles represent the anions $\overset{(Se)}{\wedge}$, the small shaded circles indicate the cations $\overset{(In)}{\wedge}$.

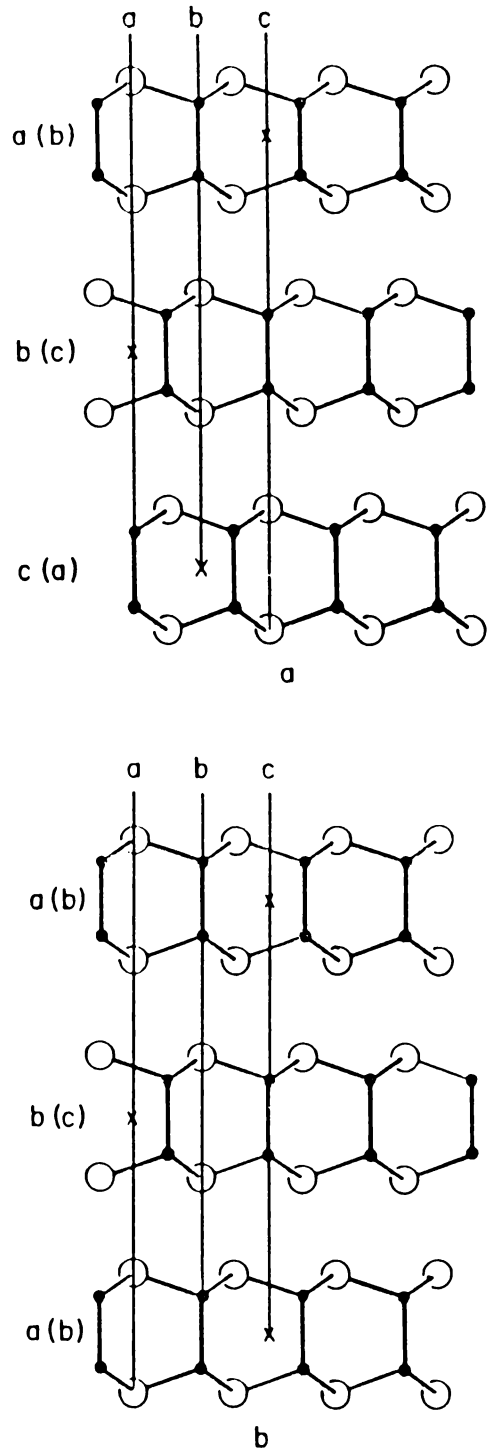

Fig.1.11 Schematic view of different stacking modification of InSe: (a) rhombohedral InSe (b) hexagonal InSe .

(3R-δ) sequence. The difference between the various suggested structures arises from the different stacking of the four-fold layers. This is illustrated in Fig.1.11 in which the structure of hexagonal and rhombohedral modifications of InSe are reproduced. To individualise the stacking sequence in the different structures the symbols a(b), b(c), c(a), ... are introduced in the figure in which the positions of the anions are a,b,c and those of the cations are (a), (b), (c).

1.B.III Crystal Structure of In_2Se_3 :A Sketch

The layered compound In_2Se_3 exhibits several crystalline phases. The basic structure (Fig.1.12) is made up of five-fold stacking of alternate indium-selenium atoms to form a tightly bound layer of -Se-In-Se-In-Se- which are separated from each other by Van der Waals weak interaction.

The α-In_2Se_3 structure as a whole is layered and contains complex hexagonal arrangement as viewed along c-axis with space group $P6_3/mmc$. The unit cell constants at room temperature are a=4.025 Å and c=19.235 Å. The alternating selenium and indium layers along the c axis have a repeat unit of Se-In-Se-In-Se and two such units form the unit cell with a hexagonal packing of the form BbCcBCcBbC..., here B and C denote selenium, whilst b and c denote indium. The bonding inside the layers is strongly covalent, while the interlayer interaction (Se-Se) is of the Van der Waals type.

The β-In_2Se_3 crystallise in rhombohedral lattice with a=4.000 Å, c=28.33 Å in hexagonal axes having 3 fold stacking of

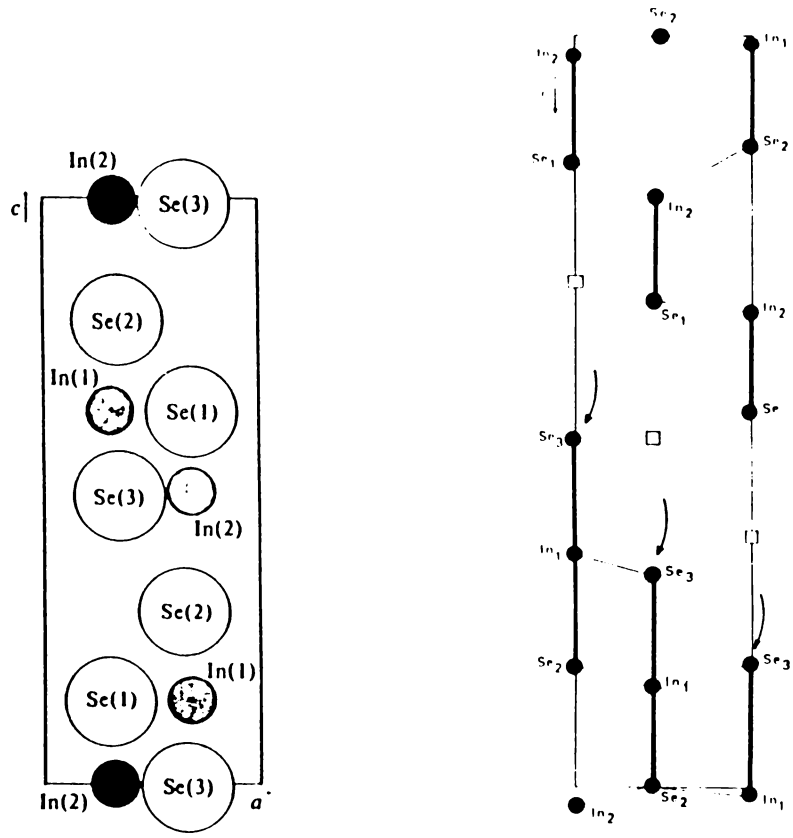

Fig.1.12 (a) Projection of xz plane of atoms of In_2Se_3 crystal.
(b) Schematic view of α modification of In_2Se_3.

atoms for a unit cell. Consistent with the present understanding the following sequence may be proposed for the phase transitions:

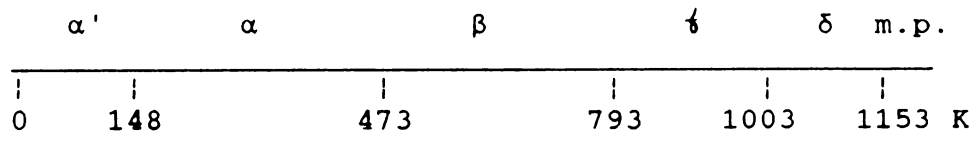

in which α is the room temperature phase.

The ɬ- phase which is stable above 793 K is also a hexagonal structure with space group $P6_1$ having unit cell parameters a=7.11 Å, c=19.34 Å having 6 layers and 30 atoms. It can be considered as a distorted wurtzite-like structure in which the indium atoms are either tetrahedrally or pentagonally coordinated. In this phase, selenium and indium layers are alternate and no adjacent Se-Se layers are found in the α-phase.

References:

1. K.Schubert,E.Dorre and E.Gunzel,Naturwissen., **41**,448 (1954).
2. W.Klemm and H.U.Vogel, Z.Anorg.Chem.,**219**,45(1934).
3. S.Sugaike,Mineralog.J.(Sapporo),**2**,63 (1957).
4. S.A.Semiletov,Kristallografija,**3**,288(1958).
5. B.Celustka and S.Popovic,J.Phys.Chem.Solids,**35**,287(1974).
6. A.Likforman and M.Guittard,Compt.Rend.(Paris),**C279**,33(1974).
7. A.Likforman,D.Carre,J.Etienne and B.Bachet,Acta Cryst.,**B31**, 1252(1975).
8. K.C.Nagpal and S.Z.Ali,Ind.J.Pure Appl.Phys.,**13**,258(1975).
9. J.Rigoult,A.Rimsky and A.Kuhn, Acta Cryst.,**B36**,916(1980).
10. H.Hahn,Angew.Chem.,**65**,538(1953).
11. A.Thiel and H.Koelsch,Z.anorg.Chem.,**66**,288(1910).
12. H.Hahn and W.Klinger,Z.anorg.Chem.,**260**,97(1949).
13. H.Hahn and G.Frank,Naturwissen.,**44**,533(1957).
14. H.Hahn and G.Frank,Z.anorg.allg.Chem.,**278**,333(1958).
15. H.Miazawa and S.Sugaika,J.Phys.Soc.Japan,**12**,312(1957).
16. P.C.Newman and W.Redhill,Z.anorg.allg.Chem.,**299**,158(1959).
17. S.A.Semiletov,Sov.Phys-Crystallo.,**5**,673(1961).
18. S.A.Semiletov,Sov.Phys-Crystallo.,**6**,158(1961).
19. S.A.Semiletov,Sov.Phys-Solid State,**3**,544(1961).
20. K.Osamura,Y.Murakami and Y.Tomhe, J.Phys.Soc.Japan, **21**,1848 (1966).
21. A.Likforman,D.Carre and R.Hillel,Acta Cryst.,**B 34**,1(1978).
22. A.likforman,P-H.Fourcroy,M.Guittard,J.Flahaut,R.Poirier and N.Szydlo,J.Solid State Chem.,**33**,91(1980).

23. J.H.C.Hogg,H.H.Sutherland and D.J.Williams,Chem.Commun.,**23**, 1568(1971).

24. J.H.C.Hogg,H.H.Sutherland and D.J.Williams,Acta Cryst.,**B29**, 1590(1973).

25. A.Thiel and H.Luckmann,Z.Anorgan.Allgem.Chem.,**172**,353(1928).

26. M.Hansen,Constitution of Binary Alloys,McGraw-Hill(1958).

27. T.N.Guliev and Z.S.Medvedeva,Russ.J.Inorg.Chem.,10,829(1965).

28. Z.S.Medvedeva and T.N.Guliev,Izv.Akad.Nauk SSSR Neorg.Mater., 1,845(1965).

29. A.A.Eliseev,T.N.Guliev and I.A.Korotkova,Izv.Akad.Nauk SSSR Neorg.Moscow,1966.

30. J.H.C.Hogg,Acta Cryst.,**B27**,1630(1971).

31. J.V.McCanny and R.B.Murray,J.Phys.C: Solid State Phys.,**10**, 1211(1977).

32. R.A.Bromley and R.B.Murray,J.Phys.C: Solid State Phys., 5,759 (1972).

33. M.V.Andriyashik, M.Yu.Sakhnovskii, V.B.Timiofeev and A.S.Yakimova, Phys.Stat.Solidi,**28**,277(1968).

34. A.Balzarotti, R.Girlanda, V.Grasso, E.Doni, F.Antonangeli, M.Piacentini and A.Baldereschi, Solid State Commun.,**24**,327 (1977).

35. P.K.Larsen,S.Chiang and N.V.Smith, Phys.Rev.,**B15**,3200(1977).

36. Y.Depeursinge, E.Doni, R.Girlanda, A.Baldereschi and K.Maschke, Solid State Commun.,**27**,1449(1978).

37. G.Margaritondo, J.E.Rowe and S.B.Christman, Phys.Rev.,**B15**, 3844(1977).

38. A.Bourdon, A.Chevy and J.N.Besson, Physics of Semiconductors 1978: Inst.Phys.Conf.Ser.No.43,p.1371.

39. P.J.Lin and L.Kleinman, Phys.Rev.,**142**,78(1966).

40. J.Friedel, in Pseudopotential theory of metals,Harrison(Ed.), Benjamin Inc.,1966.

41. R.H.Williams, J.V.McCanny, R.B.Murray, L.Ley and P.C.Kemeny, J.Phys.C: Solid State Phys.,**10**,1223(1977).

42. A.Balzarotti, R.Girlanda, V.Grasso, E.Doni, F.Antonangeli and M.Pianoentini, Cand.J.Phys.,**56**,700(1978).

43. N.V.Smith, P.K.Larsen and S.Chiang, Phys.Rev.,**B16**,2699(1977).

44. P.K.Larsen, M.Schluter and N.V.Smith, Solid State Commun.,**21**, 775(1977).

45. T.Ikari and Y.Koga,J.Phys.Soc.Japan,**47**,1017(1979).

46. V.V.Sobolev and V.I.Donetskich, Phys.Stat.Solidi,(b)**45**,K15 (1971).

47. K.Kumazaki and K.Imai, Phys.Stat.Solidi,(b)**149**, K183 (1988).

48. V.Grasso and P.Perillo, Solid State Commun.,**21**,323 (1977).

49. J.J.Forney, K.Maschke and E.Mooser, Il Nuovo Cimento,**38B**,418 (1977).

50. M.Piacentini, E.Doni, R.Girlanda, V.Grasso and A.Balzarotti, Il Nuovo Cimento,**54B**,269(1979).

51. A.M.Mezzasalma, G.Mondio and F.Neri, Solid State Commun.,**34**, 635(1980).

52. J.Camassel, P.Merle and H.Mathieu and A.Chevy, Phy.Rev.,**B12**, 4718(1978).

53. R.W.Damon and R.W.Redington, Phys.Rev., **96**,1498(1954).

54. S.Mori, J.Phys.Soc.Japan, **18**,308(1963).

55. S.M.Atakishiev and G.A.Akhundov, Phys.Stat.Solidi,(a) **32**,K33 (1969).

56. S.Shigetomi, T.Ikari, Y.Koga and S.Shigetomi, Phys.Stat. Solidi,(a) **88**,K71(1985).

57. C.De Blasi, G.Micocci, A.Rizzo and A.Tepore, Phys.Rev.,**B27**, 2429(1983).

58. S.Shigetomi, T.Ikari, Y.Koga and S.Shigetomi, Phys.Stat. Solidi(a), **86**,K69(1984).

59. C.Julien and E.Hatzikraniotis, Mat.Lett., 5,134(1987).

60. C.Julien, E.Hatzikraniotis, K.M.Paraskevopoulos, A.Chevy and M.Balkanski, Solid State Ionics, **18&19**,859(1986).

61. G.D.Guseinov, S.N.Mustafaeva and E.G.Abdullaev, Phys.Stat. Solidi(a), **88**,K205(1985).

62. I.Samara, M.Tsahiri and C.Julien, in Chemical Physics of Intercalation, Eds. P.A.Legrand and S.Flandrois, NATO-ASI Ser. (Plenum, New York,1987).

63. Z.D.Kovalyuk, P.I.Savitskii and K.D.Tovstyuk, Izv.Akad.Nauk SSSR, Ser. neorg. Mater., **18**,209(1982).

64. Z.D.Kovalyuk and I.V.Mintyanskii, Ukr.fiz.Zh., **27**,616(1982).

65. M.S.Whittingham, J.Solid State Chem., **29**,303(1979).

66. A.J.Jacobson, Solid State Ionics, 5,65(1981).

67. A.Segura, J.P.Guesdon, J.M.Besson and A.Chevy, J.Appl.Phys., **54**,876(1983).

68. M.Mavlonova, Izv.Akad.Nauk SSSR, Ser.Neorg.Mater., **17**,867 (1981).

69. Y.Tieche and A.Zareva, Phys.Stat.Solidi, **14**,K139(1966).

70. A.Casanovas, A.Cantarero, A.Segura and A.Chevy, Phys.Stat. Solidi(a),**92**,K155(1985).

71. J.C.Portal, J.Phys.Soc.Japan,**49**,Suppl.A,879(1980).

72. A.Chevy, A.Kuhn, M.S.Martin, J.Cry.Growth, 38,118(1977).

73. A.Chevy, These d' Etat, Universite de Paris VI (1982).

74. T.Ikari, S.Shigetomi, Y.Koga, and S.Shigetomi, Phys.Stat. Solidi(b),103, K81(1981).

75. A.Segura, K.Wunstel and A.Chevy, Appl.Phys., **A31**,139(1983).

76. C.De Blasi, G.Micocci, S.Mongelli, A.Tepore and F.Zuanni, Mat.Chem.Phys., **9**,55(1983).

77. R.Cingolani, L.Vasanelli and A.Rizzo, Nuovo Cimento, **6D**,383 (1985).

78. P.Soukiassian, J.Cazaux and J.Perrin, Phys.Stat.Solidi, (b) **66**,151(1974).

79. E.Kress-Rogers, G.F.Hopper, R.J.Nicholas, W.Hayes, J.C.Portal and A.Chevy, J.Phys.C:Solid State Phys., **16**,4285 (1983).

80. S.Shigetomi, T.Ikari, Y.Koga and S.Shigetomi, Phys.Stat. Solidi,(a)**108**,K53(1988).

81. A.Chevy, J.Appl.Phys., **56**,978(1984).

82. R.M.A.Lieth, in Preparation and Crystal Growth of Materials with Layered Structures (Reidel,Dordrecht,1977).

83. D.V.Korbutyak,L.A.Demchina,V.G.Litovchenco, and Z.D.Kovalyuk Sov.Phys.Semicond., **17**,508(1983).

84. A.Segura, J.P.Guesdon, J.M.Besson and A.Chevy, Rev.Phys. Appl., **14**,253(1979).

85. S.Shigetomi, T.Ikari, Y.Koga and S.Shigetomi, Jap.J.Appl. Phys., 21,L254(1982).

86. S.Shigetomi, T.Ikari, Y.Koga and S.Shigetomi, Jap.J.Appl. Phys., **27**,1271(1988).

87. A.Segura, M.C.Martinez-Tomas, B.Mari and A.Casanovas, Appl. Phys., **A44**,249(1987).

88. B.Mari, A.Segura and A.Chevy, Phys.Stat.Solidi,(b) **130**,793 (1985).

89. B.Mari and A.Segura, Appl.Phys., **A46**,125 (1988).

90. T.J.Wieting and J.L.Verble, in Electrons and Phonons in Layered Crystal structures, (ed.) T.J.Wieting and M.Schluter D.Reidal Pub.Comp., Dordrecht, Holland (1979).

91. P.Houdy, These de Troisieme Cycle, Universite de Paris VI (1982).

92. S.Shigetomi, T.Ikari, Y.Koga and S.Shigetomi, Jap.J.Appl. Phys., **20**,L343(1981).

93. G.Micocci, A.Rizzo and A.Tepore, J.Appl.Phys., **54**,1924(1983)

94. H.Fritzche, Electronic and Structural properties of Amorp. Semiconductors, eds.P.G.LeComber and J.Mort(Academic Press, New York,1973).

95. N.B.Brandt, Z.D.Kovalyuk and V.A.Kul'bachinskii, Sov.Phys. Semicond., **22**,1046(1988).

96. V.L.Bakumenko, Z.D.Kovalyuk, L.N.Kurbatov and V.F.Chishko, Sov.Phys.Semicond., **12**,1307(1978).

97. D.E.Bode and H.Levinstein, J.Opc.Soc.Amc., **43**,1209(1953).

98. B.T.Kolomiets and S.M.Ryvkin, Zh.Tekh.Fiz., **17**,987(1947).

99. J.C.Merle, R.Bartiromo, E.Borsella, M.Piacentini and A.Savoia, Solid State Commun., **28**,251(1978).

100. A.Sh.Abdinov and A.G.Kyazym-zade, Sov.Phys.Semicond., **9**,1290 (1976).

101. A.Sh.Abdinov and A.G.Kyazym-zade, Sov.Phys.Semicond., **10**,47 (1976).

102. A.Sh.Abdinov and A.G.Kyazym-zade, Sov.Phys.Semicond., 9,1537 (1976).

103. G.A.Akhundov, M.G.Aliev, A.Sh.Abdinov and A.G.Kyazym-zade, in Memory Effects and Photoconductivity in Inhomogeneous Semiconductors, Kiev(1974).

104. A.Rose, Concepts in Photoconductivity and Allied Problems, Interscience, New York (1963).

105. M.I.Korsunskii, Anomalous Photoconductivity Nauka, Moscow (1972).

106. S.M.Ryvkin, JETP Lett., 18,221(1973).

107. S.M.Ryvkin, Fiz.Tekh.Poluprov., 8,373(1974).

108. S.M.Ryvkin, Fiz.Tekh.Poluprov., 9,406(1975).

109. A.Segura, J.M.Besson, A.Chevy and M.S.Martin, Il Nuovo Cimento, 38B,345(1977).

110. C.Cleman, X.I.Saldana, P.Munz and E.Bucher, Phys.Stat.Solidi (a) 49,437(1978).

111. M.DiGiulio, G.Micocci, A.Rizzo and A.Tepore, J.Appl.Phys., 54,5839(1983).

112. M.DiGiulio, G.Micocci and A.Tepore, Solid State Electron., 27,1015(1984).

113. Y.Hasegawa and Y.Abe, Phys.Stat.Solidi(a), 70,615(1982).

114. T.T.Nang, T.Matsushita, M.Okuda and A.Suzuki, Jap.J.Appl. Phys., 16,253(1977).

115. T.Matsushita, T.T.Nang, M.Okuda, A.Suzuki and S.Yokota, Jap.J.Appl.Phys., 15,901(1976).

116. T.Matsushita, A.Suzuki, M.Okuda, H.Naitoh and T.Nakau, Jap.J.Appl.Phys., 22,762(1983).

117. A.Segura, J.L.Valdes, F.Pomer, A.Cantarero and A.Chevy, in Proc.5th E.C.Photovolt.Sol.Energy Conf., Kavouri,1983 (Reidel,Dordrecht,1984)p.927.

118. A.Sugura, J.L.Valdes, A.Cantarero, F.Pomer, J.P.Martinez, B.Mari and A.Chevy, in Proc. 6th Euro.Communities Photovolt. Sol.Energy Conf., Londres,1985 (Reidel,Dordrecht,1985),p.774

119. A.Sugura, J.L.Valdes, A.Cantarero, F.Pomer, J.P.Martinez, B.Mari and A.Chevy, in Proc.of MELECON, Madrid, 1985 (Elsevier, New York 1985),p.51.

120. A.Sugura, J.P.Martinez, J.L.Valdes and A.Chevy, in Proc. 7th Euro.Communities Photovolt. Sol. Energy Conf., Sevilla, 1986 (Reidel,Dordrecht,1987)p.475.

121. J.Martinez-Pastor, A.Segura, J.L.Valdes and A.Chevy, J.Appl. Phys., 62,1477(1987).

122. M.Persin, B.Celustka, B.Markovic and A.Persin, Thin Solid Films, 5,123(1970).

123. S.K.Sharma, V.G.Bhide, S.C.Jain and S.S.Agarwal, Thin Solid Films, 11,201(1972).

124. K.Ando and A.Katsui, Thin Solid Films, 76,141(1981).

125. S.Chaudhuri, S.K.Biswas and A.Choudhury,Solid State Commun., 53,273(1985).

126. M.DiGiulio, G.Micocci, R.Rella, P.Siciliano and A.Tepore, Thin Solid Films, 148,273(1987).

127. M.DiGiulio, D.Manno, R.Rella, P.Siciliano and A.Tepore, Solar Energy Materials, 15, 209(1987).

128. M.DiGiulio, R.Rella and A.Tepore, Phys.Stat.Solidi,(a) 100, K35(1987).

129. S.K.Biswas, S.Chaudhuri and A.Choudhury, Phys.Stst.Solidi, (a) **105**,467(1988).

130. M.Persin, A.Persin and B.Celustka, Thin Solid Films, **12**,117 (1972).

131. B.S.Naidu, A.K.Sharma, D.V.K.Sastry, Y.Syamalamba and P.Jayarama Reddy, J.Non-Cryst.Solids, **42**,637(1980).

132. H.Hashimoto, H.Nishimura and H.Suzuki, Jap.J.Appl.Phys., **20**, 1163(1981).

133. D.V.Krishna Sastry and P.Jayarama Reddy, Thin Solid Films, **105**,139(1983).

134. A.J.McEvoy, A.Parkes, K.Solt and R.Bichsel,Thin Solid Films, **69**,L5(1980).

135. A.G.Fitzgerald, Thin Solid Films, **13**, S5(1972).

136. J.P.Guesdon, C.Julien, M.Balkanski and A.Chevy, Phys.Stat. Solidi(a),**101**,495(1987).

137. M.Yudasaka, T.Matsuoka and K.Nakanishi, Thin Solid Films, **146**,65(1987).

138. N.A.Goryunova, V.S.Grigor'eva, B.M.Konovalenko and S.M.Ryvkin, Zh.tekh.Fiz.(Moscow), **25**,1675(1955).

139. J.C.Brice, P.C.Newman and H.C.Wright, Brit.J.Appl.Phys., **9**, 110(1958).

140. P.C.Newman, Z.Anorg.Allg.Chem., **299**, 158(1959).

141. H.Suematsu and T.Okada, J.Phys.Soc.Japan, **21**,1849(1966).

142. V.P.Mushinskii, V.I.Kobolev and I.Ya.Andronik, Fiz.Tekh. Poluprov., **5**,1251(1971).

143. K.Kambas and J.Spyridelis, Mat.Res.Bull., **13**,653 (1978).

144. K.Kambas, C.Julien, M.Jouanne, A.Likforman and M.Guittard, Phys.Stat.Solidi,(b) **124**, K105(1984).

145. K.Kambas and C.Julien, Mat.Res.Bull., 17,1573(1982).

146. C.Julien, M.Eddrief, M.Balkanski, E.Hatzikraniotis and K.Kambas, Phys.Stat.Solidi(a), 88,687(1985).

147. M.Balkanski, C.Julien, A.Chevy and K.Kambas, Solid State Commun., 59,423(1986).

148. G.Guizzetti and F.Meloni, Il Nuovo Cimento,1D,503(1982).

149. J.Fotsing, C.Julien, M.Balkanski and K.Kambas, Mat.Sci. and Eng., B1,139(1988).

150. M.Persin, A.Persin, B.Celustka and B.Etlinger, Thin Solid Films, 11,153(1972).

151. C.Julien, M.Eddrief, K.Kambas and M.Balkanski, Thin Solid Films, 137,27(1986).

152. J.Herrero and J.Ortega, Solar Energy Mat., 16,477(1987).

153. M.Yudasaka and K.Nakanishi, Thin Solid Films, 156,145(1988).

154. G.K.Slavnova, N.P.Luznaya and E.S.Medvedeva, Zh. Neorgan. Khim., 8,153(1963).

155. K.Imai, M.Sato and Y.Abe, J.Electrochem.Soc., 121,1674(1974)

156. K.Imai, K.Suzuki, T.Haga, Y.Hasegawa and Y.Abe, J.Cry.Growth 54,501(1981).

157. T.J.Wieting and J.L.Verble, Phys.Rev., B5,1473(1972).

THEORITICAL ASPECTS

Abstract:

This chapter deals with the theory suitable for the layered materials, in order to account for the optical scattering found in these materials InSe and In_2Se_3. A strong temperature dependence of charge carriers is the characteristic feature of optical scattering. This has been verified from optical and photoconductivity measurements. This chapter also explains the conductivity equation, appropriate to the layered structures, for the modified situation.

2.I Introduction:

In general, the usual solid state theory is applied to crystalline solids in which the atoms are formed in a cluster of nearly spherical symmetry. In agreement with this, the resulting approximate wave functions are also spherically symmetrical. Due to any unsymmetry in structure, when the wavefunctions deviate from spherical symmetry, a separate formulation of theory is unavoidable[1]. Such a restructuring of the theory is applicable to layered materials, as the charge distribution is asymmetrical due to the weaker forces that arise between layers. Within each layer the atoms are bound predominently by covalent forces[2,3]. As a result, these solids may also be expected to show properties significantly different from the regular solids[4,6].

2.II.a Considerations in the formulation of a model for electron states:

In order to construct a simple model emphasising this anisotropic effect, the crystal is represented by a one-dimensional potential in the same manner as in the Kronig-Penney model[7] (Fig.2.1). In such a model potential, the width of the potential wells in each cell of the layers depend on the local energy levels, which in succession change with the relative positions of the atoms in the unit cell. Hence, the particle energy states are modified by the atomic motions normal to the layers. Consequently, a short range interaction specific to the structure results and an optical scattering takes place by the

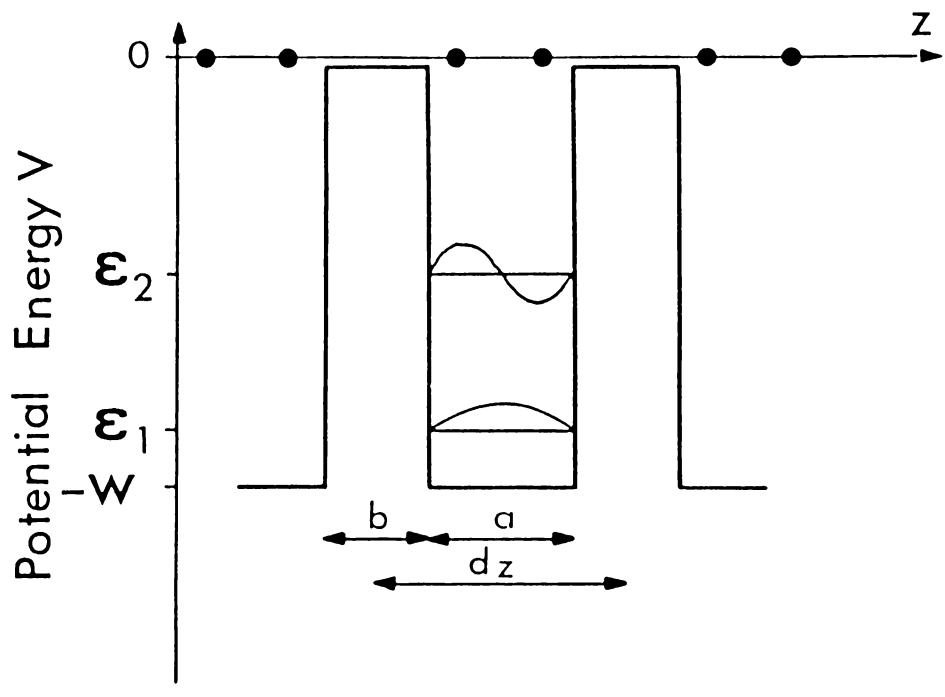

Fig.2.1 Square potential well model of layer structure.

phonons polarised normal to the layers[8].

The forces involved in the short-range electron-lattice interaction are simply the outward pressure forces which are associated with the storage of energy needed to localise the particle within the layers. As these forces pressurise to expand the layer lattice, they are balanced by elastic forces. The result is that, the particles are as if surrounded by a deformation of the layers, which resemble more like a local swelling[1] (Fig.2.2).

In formulating a model for layered semiconductors the following points from the experimental observations have to be considered.

1. In layered structures measurements have conclusively demonstrated that charge carriers interact predominantly with optical phonons. This turns out that the measured mobilities exhibit a strong temperature dependence, characteristic of optical scattering[6,9]. In some typical layered compounds, the large difference of population of acoustical and optical phonons, even at low temperatures, indicates the retention of the two-dimensional character[10].

2. In crystals, a large anisotropy in the conductivity[11] in different crystallographic planes can be thought of as a reflection of high mass anisotropy.

4. In contrast the excitonic behaviour shows that the masses are not strongly anisotropic[12-16]. Hence the electron

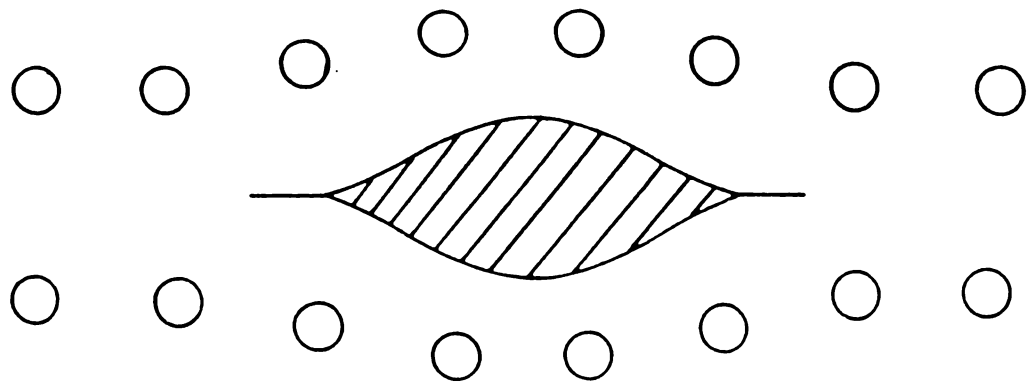

Fig.2.2 Perturbation to the carriers by the relative atomic motions normal to the layers.

states must be considered as extended in all directions even though the potential is highly anisotropic around an atom. Measurements of transport properties[17] also confirm the existence of such extended states[18,19] although weakly coupled to the lattice.

2.II.b **Fivaz model of electron states:**

In layered structures, spherically symmetrical wave functions are inappropriate due to an asymmetric nature of charge distribution. They consist of thin layers stacked upon each other, the atoms within each layer being bound by covalent forces, while the cohesion between layers arise from much weaker forces of the Van der Waals type. As a result, within each layer but outside the atomic cores the potential is low and varies slowly. Between the layers, the contributions of the different atoms add up to fairly high and wide potential barriers. So the carriers can be considered to travel in a series of parallel potential wells within which exist the local levels whose energies depend on the local width of the wells. As a result of this anisotropy, any model for electron states should contain a non- equivalence of directions.

A simple model is obtained by considering a hypothetical crystal consisting of a stack of N_z identical layers per unit length along the z-axis each layer being formed by a single row of N_x unit cells per unit area. The Brillouin zone of this hypothetical crystal is a cylinder of vertical axis with a horizontal cross-section of a certain shape. Introducing vectors in the direct or reciprocal spaces[20]

$$\mathbf{a} = \mathbf{a}_x + \mathbf{a}_z \qquad \ldots (2.1a)$$

$$= i a_x + j a_y + k a_z \qquad \ldots (2.1b)$$

where i,j,k are the unit vectors along the three perpendicular axis.

The radius vector r is then

$$\mathbf{r} = \mathbf{x} + \mathbf{z} = ix + jy + kz \qquad \ldots (2.2)$$

In a zero-order model, the cellular effective potential V(r-n) is almost separable into two independent parts, the first one Z(z) depending only on z and the other one, v(x) depending only on the horizontal variables :

$$V(\mathbf{r}) = Z(z) + v(\mathbf{x}) \qquad \ldots (2.3)$$

The corresponding Hamiltonian has eigenstates of the Bloch type which are products of the two separate components in the two different projections (ie.,horizontal and vertical) with quasi-momentum p.

$$|\mathbf{p}\rangle = |p_x\rangle . |p_z\rangle . \qquad \ldots (2.4)$$

Changing to Wannier cellular basis[21,22] since the physical significance of separation is more apparent,

$$|\mathbf{n}\rangle \simeq |n_x\rangle . |n_z\rangle . \qquad \ldots (2.5)$$

and these products are useful as trial functions in the following variational scheme.

Variational Scheme: Consider an ideal crystal containing one pair of atoms per unit cell. A realistic approximation to this crystal potential (Fig.2.3) can be made by a superposition of two components of largely different amplitude[23].

Considering the characteristic stacking of layers, the first component of the potential represents the layers where the covalent bonding is strong and the second symbolises the layers where the Van der Waals bonding is much weaker. In this, to describe the periodicity of the exact potential in the layer lattice, the strongly varying components, z, can then be added to a second one in x and y of much smaller amplitude[24].

Partitioning of Potential: The Cartesian co-ordinates are not separable near the ion cores where the potential has a spherical symmetry. Since these regions are small, we can use zeroth-order approximations for the separated states. In such a scheme the crystal potential is formally partitioned into two components[25], one Z depending only on z and a smaller residue v(r) not necessarily completely separable and which depends on all three coordinates :

$$V(\mathbf{r}) = Z(z) + v(\mathbf{r}) \qquad \ldots (2.6)$$

In a self-consistent way this partitioning can be defined by using variational principle which states that the energy is stationary with respect to variations of the components of the trial wavefunctions. This is a problem involving several variables[26] subject to subsidiary conditions, and its solution leads to the "Euler equations" which must be satisfied for the

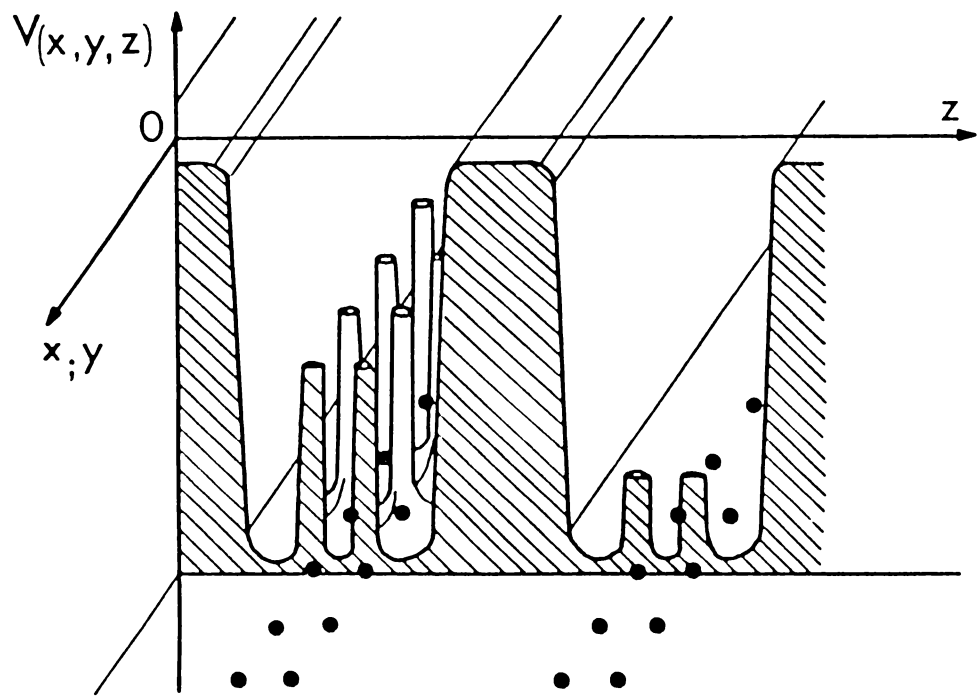

Fig.2.3 Schematic representation of the effective potential in a layered crystal.

considered function to be stationary.

Applying the inverted Wannier transformation to eqn.(2.5), one obtains the separated components of the Bloch functions

$$|p(r) = |p_x(x)\rangle . |p_z(z),$$

$$|p(x) = (N_x)^{-1/2} \sum_{n_x} \exp(ip_x n_x/\hbar \; | \; n_x(x)\rangle,$$

$$|p_z(z)\rangle = (N_z)^{-1/2} \sum_{n_z} \exp(ip_z n_z/\hbar \; | \; n_z(z)\rangle. \qquad \ldots (2.7)$$

In terms of these components and because of the hermiticity of the Hamiltonian[27] the Euler equations then reduce to a pair of Schrodinger-like equations:

$$[-\hbar^2 \nabla_x^2/2m + \sum_{n_x} v(x-n_x) - \varepsilon_x(p_x)] \times |p_x\rangle = 0, \qquad \ldots (2.8a)$$

$$[-\hbar^2 \nabla_z^2/2m + \sum_{n_z} Z(z-n_z) - \varepsilon_z(p_z)] \times |p_z\rangle = 0, \qquad \ldots (2.8b)$$

where

$$v(x) = \langle p_z | \sum_{n_z} v(\mathbf{r}-\mathbf{n}_z) | p_z \rangle \qquad \ldots (2.9)$$

defines an effective two-dimensional potential. The energy will then be extremum only if the partitioning of the potential satisfies the condition

$$\int |p_x(x)|^2 [V(r)-Z(z)] \, dx = 0 \qquad \ldots (2.10)$$

where the origin of v(r) has been chosen for convenience such that

$$\langle p|v(r)|p\rangle = 0$$

and the total energy will be

$$\varepsilon(p) = \varepsilon_x(p_x) + \varepsilon_z(p_z) \qquad \ldots (2.11)$$

So the components are completely separable and eqn.(2.9) specifies how the partitioning of the real potential is to be made: with u(x), the periodic part of the two-dimensional Bloch wave function, the condition given by eqn.(2.9) is fulfilled if the one-dimensional component of the potential is computed as

$$Z(z) = \int_{\text{cell}} u^*(x)\, V(r)\, u(x)\, dx \qquad \ldots (2.12)$$

Computation of this is done by an iterative procedure since u(x) is not known. Taking u(x) = constant, as a first guess of this function, we can obtain a zero-order approximation for Z(z) as

$$Z^{(o)}(z) = \int_{\text{cell}} V(r)\, dx \qquad \ldots (2.13)$$

Computing successively

$$v(r) = V(r) - Z^{(o)}(z) \qquad \ldots (2.14)$$

$$v(x) = \langle p_z | v(r) | p_z \rangle , \qquad \ldots (2.15)$$

$$Z^{(1)}(z) = \int |u(x)|^2\, V(r)\, dx \qquad \ldots (2.16)$$

After introducing this solutions in eqn.(2.10), a better approximation of Z(z) is then computed with which the process is repeated.

Thus variational principle is used to solve the three-dimensional eigenvalue problem by successively approximating the pair of equations (2.8a & b) in one and two dimensions.

In precise, the discussed first-order model by variational approach leads to the following important results.

Firstly, the horizontal components $|P_x\rangle$ of orthogonal three-dimensional states $|P\rangle$ are not necessarily mutually orthogonal when they pertain to different energy bands. This lack of orthogonality certainly modifies the selection rules for inter-band transitions and this in turn affects the optical absorption[28,29].

Secondly, as a consequence of the averaging given in eqn.(2.9), an effective horizontal potential is generated and this varies with a much smaller amplitude than the vertical component. As a result, the Wannier basis is eminently suited to generate matrix elements exhibiting the strong angular dependence of the local physical parameters which one expects in layered structures.

2.II.c Physical Consequences of the Model:

In order to make comparison with experiment, the above theoretical model is now applied to discuss some physical properties. Because of the localisation of the components of the Wannier functions, the matrix elements of the separated Hamiltonians on the Wannier basis (in the absence of degeneracies) will satisfy inequalities of the form

$$| \langle n| H_x |n\rangle | \ll | \langle n| H_z |n\rangle |, \qquad \ldots (2.17)$$

$$| \langle n+d_x| H_x |n\rangle | \gg | \langle n+d_z| H_z |n\rangle |, \qquad \ldots (2.18)$$

It follows that, the mean energy of each of the allowed bands can be obtained from the diagonal elements of the Hamiltonian. In structures with monoatomic layers such as graphite, we can see that the horizontal contributions are smaller than the vertical ones, the fundamental energy gap of a semiconductor occurs between two bands with common index or position. The electrons and holes in these bands have wavefunctions with the same z-component, but different, orthogonal x-components, and therefore behave as in the completely separable model.

If each of the layer in the layered structure contains more than one monoatomic sheet then degeneracies (or near-degeneracies) can be expected and results in the formation of a series of bands with nearly equal vertical contributions to their mean energy, which favour for the partially separable model.

Now, consider the broadening of the local levels into a particular band by the non-diagonal elements of H. Accordingly, for a propagation parallel to the layers, we express the energy spectrum in the low-lying conduction band by means of an effective-mass approximation. But for the propagation across the layers is more appropriately described by a tight-binding term. Therefore the energy of a particle moving at the bottom of a band can be expressed as

$$\varepsilon(\mathbf{p}) = (p_x^2+p_y^2)/2m_x-2I_z\cos(p_z d_z/h) \qquad \ldots (2.19)$$

where I_z is a small overlap energy and m_x an effective resistance to acceleration of the particle parallel to the layers.

The behaviour of particles in layered structure can be better understood by, getting the density of states from eqn. (2.19) by standard procedures:

$$D(\varepsilon) = \begin{cases} D_2 \cdot \cos^{-1}(1 - \varepsilon/2I_z)/\pi , & \text{for } \varepsilon < 4I_z, \\ (m_x N_z / 2\pi\hbar^2 = D_2 , & \text{for } \varepsilon > 4I_z, \end{cases} \quad \ldots (2.20)$$

where, ε is the excitation energy measured from the band edge.

Thus, when the energy, $\varepsilon << 4I_z$, the density of states approaches the familiar square root dependence D_3 corresponding to three-dimensional geometry. In other words in pure states, low energy particles are seen to retain three degrees of freedom and the density of states behaves as in ordinary solids. But when $\varepsilon \geq 4I_z$, it takes the constant value D_2 characteristic of two-dimensional geometry. Figure 2.4 shows the density of states at the bottom of a conduction band of a layered semiconductor.

Particles in thermal equilibrium may be a mixture of the two kinds of states and thus have quite unusual dynamical properties. Actually, the specific problem raised by layered structures is that as $4I_z$ is typically neither negligible nor comparable to the total band width, the vertical contribution to the energy can be neither ignored nor approximated by a simple quadratic term in p_z^2. This complication forbids a general treatment of dynamical problems and the principal verification of the above described theory comes from observation of lattice scattering in semiconductors.

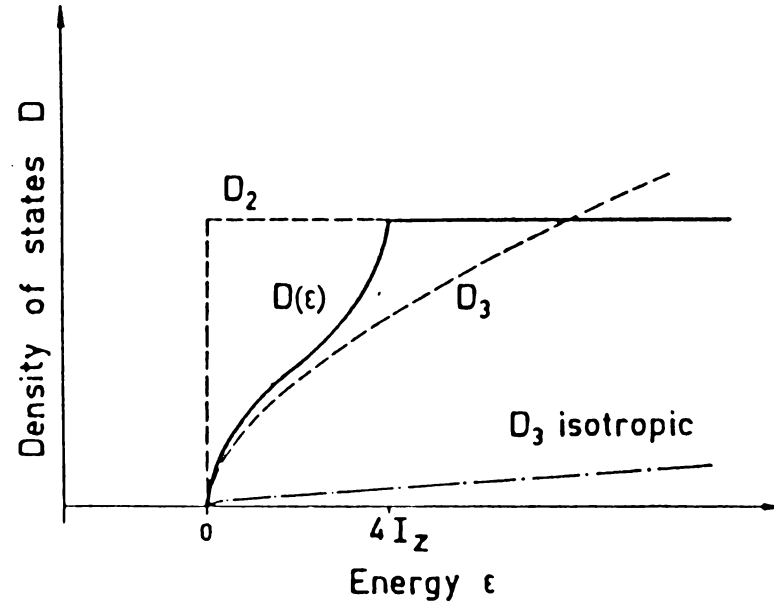

Fig.2.4 Density of states at the bottom of a conduction band in a layered structure.

2.III.Carrier movement in semiconducting layered compounds:

2.III.A Electron-lattice interaction:

Consider the interaction of an electron with the lattice in a layered crystal with t atoms per unit cell. The Hamiltonian describing the interaction between the electrons and phonons can be expressed as[1,8]

$$H = H_{el} + H_{lat} + H_{int} \qquad \ldots (2.21)$$

where H_{el} is the Hamiltonian of the carrier in the perfect lattice, H_{lat} is the Hamiltonian of the isolated lattice and H_{int} is the interaction Hamiltonian.

In order to evaluate the interaction matrix elements we obtain the deformation potential. Writing H_{int} in a linearised form[6,20]:

$$H_{int} = \sum_{n'i'ni} \eta_{n'i'} \frac{\partial V_{ni}(r - \eta_{n'i'})}{\partial \eta_{n'i'}} = - \sum_{n'i'ni} \eta_{n'i'} \frac{\partial V_{ni}(r - \eta_{n'i'})}{\partial r} \qquad \ldots (2.22)$$

where η_{ni} is the displacement of atom i in the cell n and V_{ni} the potential associated with this atom and moving with it. The gradient operator $\frac{\partial V}{\partial \eta}$ has diagonal matrix elements appropriate to the particular potential of layered structures in the Wannier basis and its components satisfy inequalities of the form

$$| \langle n | \frac{\partial V_{ni}}{\partial x} | n \rangle | \ll | \langle n | \frac{\partial V_{ni}}{\partial z} | n \rangle | \qquad \ldots (2.23)$$

Only phonons with small wave vectors can scatter the particles of

a weakly degenerate gas. Therefore one need to evaluate the scattering matrix only in the limit k=0. In this limit acoustic phonons represent bodily motions of cell with respect to one another ($\eta_{ni} = \eta_{ni'}$), while optical phonons correspond to internal distortions of undisplaced cells ($\eta_{ni} = \eta_{n'i}$). Further, applying the identity

$$\sum_k \eta_k \frac{\partial V_i}{\partial \eta_k} = \sum_{k<l} (\eta_k - \eta_l) \frac{\partial V_i}{\partial(\eta_k - \eta_l)} \qquad \ldots (2.24)$$

with $V_i = \langle n| V_{ni} |n\rangle$ and neglecting small three-center terms with $i \neq k \neq l$ we obtain after rearrangements:

$$\sum_i \sum_{n'i'} \eta_{n'i'} \frac{\partial V_{ni}}{\partial \eta_{n'i'}} = \sum_i \sum_{n' \neq n} (\eta_{ni} - \eta_{n'i}) \sum_{i'} \frac{\partial V_{ni}}{\partial(\eta_{ni} - \eta_{n'i'})} \qquad \ldots (2.25a)$$

to describe the acoustic modes, and

$$\sum_i \sum_{n'i'} \eta_{n'i'} \frac{\partial V_{ni}}{\partial \eta_{n'i'}} = \sum_i \sum_{i' \neq i} (\eta_{ni} - \eta_{ni'}) \sum_{n'} \frac{\partial V_{ni}}{\partial(\eta_{ni} - \eta_{n'i'})} \qquad \ldots (2.25b)$$

to describe the optical modes.

The above equations can be evaluated in the continuous approximation which describes the atomic motion in terms of local swelling of the lattice. In layered structures only the horizontal swellings appreciably modify the potential, the effect of the vertical ones being minor because of the weak Van der Waals forces between the layers. This gives rise to strongly direction-dependent gradients $\frac{\partial V}{\partial \eta}$ and thereby leads to a coupling

of the carriers to the optical modes. For optical modes (ω,q) the atomic displacements can be used as a measure of the deformation. Constructing a continuous deformation function[1]

$$\delta r_q(r) = e(\hbar/2M N\omega)^{1/2} \exp[iq.r] (a_q + a^{\dagger}_{-q}) \quad \ldots (2.26)$$

where N is the number of cellular oscillators in the vibrating crystal with a phonon frequency ω, $a^{\dagger}_q$ and a_q are creation and annihilation operators for a phonon in the state **q** and **e** is a unit polarisation vector given by

$$e_\alpha = M^{1/2} e_\alpha m_\alpha^{-1/2}, \qquad \alpha = 1, \ldots, t \quad \ldots (2.27)$$

and M is given by

$$M^{-1} = \sum_\alpha m_\alpha^{-1} |e_\alpha|^2 \quad \ldots (2.28)$$

In first order, we express the perturbing potential as a linear function of the deformation

$$V_q(r) = D.\ \delta r_q(r) \quad \ldots (2.29)$$

where D consists of t subvectors and is defined as the resultant gradient of the perturbing potential at the atomic sites with respect to the displacement of the atom about its normal position. The value of the deformation potential can be established by considering the limiting case where **k** = **q** =0. The matrix elements[30] are then like those appearing in the Jahn-Teller problem [31,32] in which the perturbation Hamiltonian are linear in the displacements of the atoms from the equilibrium position and can be computed by the perturbation treatment.

Lowest-order perturbation treatment: Let us consider that the strength of the electron-lattice interaction is measured by a

'coupling constant' g which is defined as[1]

$$g^2 = \frac{\varepsilon^2 \, m^{*3/2}}{2 \sqrt{2} \, \pi \, M \, N \, \hbar \, (\hbar\omega)^{3/2}} \qquad \ldots (2.30)$$

If energy and wave vector are measured in units of $\hbar\omega$ and $(2m^* / h)^{1/2}$ respectively, then defintion of coupling constant helps to write the Hamiltonian in the reduced form[8]

$$H = \sum_k k^2 c_k^\dagger c_k + \sum_q a_q^\dagger a_q + \sum_{k,q} \sqrt{4\pi} \, g (a_q + a_{-q}^\dagger) \, c_{k+q}^\dagger \, c_k \qquad \ldots (2.31)$$

where $c_k^\dagger$ and c_k are creation and annihilation operators for an electron in state **k** and $a_q^\dagger$ and a_q are creation and annihilation operators for a phonon in state **q**. Equation (2.31) is similar to the Frohlich Hamiltonian for polar interaction[33] and is suitable for a perturbation treatment. For short-range scattering by optical phonons the coupling constant is independent from the action terms **k** and **q**.

At absolute zero when no phonons are present the unperturbed states are

$$| \Psi^{(0)} \rangle = | \mathbf{k} \rangle \, | \, 0 \rangle \qquad \ldots (2.32)$$

The first order correction changes $| \Psi^{(0)} \rangle$ to

$$| \Psi^{(1)} \rangle = | \Psi^{(0)} \rangle + \sum_q \frac{| \mathbf{k} + \mathbf{q} \rangle \, | \, 1_{-q} \rangle \langle 1_{-q} | \langle \mathbf{k}+\mathbf{q} | H_1 | \mathbf{k} \rangle \, | \, 0 \rangle}{k^2 - (\mathbf{k}+\mathbf{q})^2 - 1} \qquad \ldots (2.33)$$

Computing the correction to the energy eigenvalues $\varepsilon_{kn}^{(0)} = k^2 + \sum_q n_q$ of the states $|\mathbf{k} \rangle \, |n_{\pm q} \rangle$. As the diagonal matrix elements of the interaction are zero, the lowest-order correction is

$$\varepsilon_{kn}^{(2)} = 4\pi g^2 \{ \sum_{q} [(n+1)/ \varepsilon(\mathbf{k}) - \varepsilon(\mathbf{k}+\mathbf{q}) - 1] + \sum_{q} [n/ \varepsilon(\mathbf{k}) - \varepsilon(\mathbf{k}+\mathbf{q}) + 1] \}$$

... (2.34)

It is seen that virtual transitions to electron states of large wave vector contribute to the self-energy $\varepsilon_{kn}^{(2)}$. To obtain the band shape for a given Brillouin-zone radius Q and a given mass at $\mathbf{k}= 0$, we have to compute the value of

$$\varepsilon_{on}^{(2)} = - \frac{4\pi g^2}{(2\pi)^3} \left[(n+1) \int_0^Q \frac{4\pi q^2 \, dq}{\varepsilon(q) + 1} + n \int_0^Q \frac{4\pi q^2 \, dq}{\varepsilon(q) - 1} \right] \quad ..(2.35)$$

for two extreme energy spectra:

(i) for a nearly free electron band

$$\varepsilon_{on}^{(2)} = -(2/\pi) Q g^2 (2n+1) \quad ... (2.36)$$

(ii) for a tight binding band

$$\varepsilon_{on}^{(2)} = -(4 \ln 2/\pi) Q g^2 (2n+1) \quad ... (2.37)$$

The ratio of the self-energy for the tight binding band to the self-energy for the nearly free electron band is nearly 1.4 and the bandwidth ratio is 0.4.

2.III.A.1 Temperature dependence of energy gap:

From the above equations, we infer that, the self-energy is mainly determined by the properties of electron bands near the extremum. In other words, its value is given by the effective mass rather than by the bandwidth. In practical units eqn.(2.37) can be written as

$$\varepsilon_{on}^{(2)} = - (4 \text{ In } 2 / \pi) \, g^2 \, (2n+1) (\hbar\omega)^{1/2} (\hbar^2 Q^2/2m)^{1/2} \quad \ldots (2.38)$$

This self-energy correction gives a temperature dependence to the energy gap[34].

Rewritting this in terms of valence and conduction band effective masses

$$\Delta E_g = \frac{- 4 \text{ In } 2}{\pi} \left[\frac{g_v^2}{\sqrt{2m_v^*}} + \frac{g_c^2}{\sqrt{2m_c^*}} \right] 2 n \hbar Q \sqrt{h\omega} \quad \ldots (2.39)$$

where the subscripts v and c refers to the valence and conduction bands respectively and n is the number of phonons in one particular mode.

2.III.B Scattering mode in the layered semiconductors:

In common semiconductors, acoustical modes of lattice vibrations mainly determine the carrier scattering. In comparison, in layered materials the relevent measurements (infra-red reflectivity[35,36], Raman[37-42] and mobility[9,17,22,43,44] measurements) have conclusively demonstrated that charge carriers interact dominantly with optical vibrations. Detailed study revealed that the optical scattering taking place in this material is by a short range interaction specific to this structure[22]. As a result of assymmetry between the intra- and inter-layer bond strengths, the band electrons in layered materials are weakly coupled to the lattice. This gives rise to electron- optical phonon interaction and strong scattering of the charge carriers by optical phonons. A strong temperature dependence of charge carriers is characteristic of the optical scattering[34].

2.III.B.1 Exponential dependence of electrical conductivity on temperature:

By analogy with amorphous semiconductors, a description of transport properties in layered semiconductors can be given by introducing a mobility edge ΔE, below which all states are localised. Above the edge, all states are delocalised and may carry a current across the sample, energy being associated mostly with propagation along the layer plane. Let $D(\varepsilon) \alpha \sqrt{\varepsilon}$ be the density of states in the conduction band in the perfect crystal. According to the Kubo-Greenwood formula, the conductivity is[1]

$$\sigma = e \int_{o}^{\infty} D(\varepsilon)\, f(\varepsilon)\, (1- f(\varepsilon))\, \mu(\varepsilon)\, d\varepsilon \qquad \ldots (2.40)$$

At high enough temperatures, the localised states' contribution is comparably less to the conductivity. Then

$$\sigma = e \int_{\Delta E}^{\infty} D_{del}(\varepsilon)\, f(\varepsilon)\, \mu(\varepsilon)\, d\varepsilon, \quad \text{when } f(E) << 1 \ldots (2.41)$$

As the band mobility is given by

$$\mu = (1/n) \int_{o}^{\infty} D(\varepsilon)\, f(\varepsilon)\, \mu(\varepsilon)\, d\varepsilon \qquad \ldots (2.42)$$

and for the lowest approximation $D_{del} \simeq D(\varepsilon)$, the conductivity is

$$\sigma = e\, n\, \mu\, e^{(-\Delta E/kT)}$$

or,

$$\sigma = \sigma_o\, e^{(-\Delta E/kT)} \qquad \ldots (2.43)$$

where σ_o is an empirical constant.

Thus, it can be seen that the conductivity is an exponential function of temperature.

References:

1. R.C.Fivaz and Ph.E.Schmid in Optical and Electrical Properties, (Ed.) P.A.Lee, (Reidel Publishing Company, Dordrecht, Holland 1976).
2. A.Likforman, D.Carre, J.Etienne and B.Bachet, Acta Cryst., **B 31**, 1252 (1975).
3. H.Kamimura and K.Nakao, J.Phys.Soc.Japan, **24**, 1313 (1968).
4. V.Augelli, C.Manfredotti, R.Murri and L.Vasanelli, Phys.Rev., **B 17**, 3221 (1978).
5. C.De Blasi, G.Micocci, A.Rizzo and A.Tepore, Phys.Rev.,**B 27**, 2429 (1983).
6. R.Fivaz and E.Mooser, Phys.Rev.,**163**, 743 (1967).
7. R.de L.Kronig and W.G.Penney, Proc.Roy.Soc.,**A 130**, 499 (1931)
8. Ph.E.Schmid, Nuovo Cimento, **21 B**, 258 (1971).
9. A.Segura, F.Pomer, A.Cantarero, W.Krause and A.Chevy, Phys.Rev.,**B 29**, 5708 (1984).
10. R.J.Nicholas, E.Kress-Rogers, J.C.Portal, J.Galibert and A.Chevy, Surface Science, **113**, 339 (1982).
11. S.A.Hussein, A.T.Nagat, A.M.Hafez, Y.H.Gameel and A.A.Belal, Ind.J.Pure & Appl.Phys.,**25**, 278 (1987).
12. J.Camassel, P.Merle, H.Mathieu and A.Chevy, Phys.Rev.,**B 17**, 4718 (1978).
13. J.L.Brebner and E.Mooser, Phys.lett.,**24A**, 274 (1967).
14. G.Ottaviani, C.Canali, F.Nava, Ph.E.Schmid, E.Mooser, R.Minder and I.Zschokke, Solid State Commun.,**14**, 933 (1974).
15. G.I.Abutalybov and M.L.Belle, Sov.Phys.Semicond.,8,1559(1975)

16. A.M.Mezzasalma, G.Mondio and F.Neri, Solid State Commun., **34**, 635 (1980).

17. A.Segura, C.Martinez-Tomas, A.Casanovas, A.Cantarero, J.Martinez-Pastor and A.Chevy, Appl.Phys.**A 48**, 445 (1989).

18. Y.Depeursinge, E.Doni, R.Girlanda, A.Baldereschi and K.Maschke, Solid State Commun., **27**, 1449 (1978).

19. E.Doni, R.Girlanda, V.Grasso, A.Balzarotti and M.Piacentini, Nuovo Cimento, **51 B**, 154 (1979).

20. R.C.Fivaz, Nuovo Cimento, **63 B**, 10 (1969).

21. G.H.Wannier, Elements of Solid State Theory, Ch.VI. University Press, Cambridge (1959).

22. R.Fivaz and E.Mooser, Phys.Rev.,**136 A**, 833 (1964).

23. R.Fivaz, Helv.Phys.Acta,**39**, 247 (1966).

24. R.Fivaz, J.Phys.Chem.Solids,**28**, 839 (1967).

25. A.I.Grubanov and A.D.Cherychelov, Sov.Phys.Solid State,**2**, 1253 (1960).

26. R.Courant, Differential and Integral Calculus,II, Interscience, New York (1961).

27. L.D.Landau and E.M.Lifshitz, Quantum Mechanics, Pergamon Press, London (1959).

28. J.L.Brebner, J.Phys.Chem.Solids,**25**, 1427 (1964).

29. B.Mari, A.Segura and A.Chevy, Phys.Stat.Sol.(b)**130**,793 (1985)

30. H.Ehrenreich, J.Phys.Chem.Solids,**9**, 129 (1959).

31. J.Bardeen and W.Shockley,Phys.Rev.,**80**, 72 (1950).

32. H.A.Jahn and E.Teller, Proc.Roy.Soc.,**A 161**, 220 (1937).

33. H.Frohlich, Polarons and Excitons, Ch.I, (London, 1963).

34. H.Y.Fan, Phys.Rev.,**82**, 900 (1951).

35. G.Lucovsky, R.M.White, J.A.Benda and J.F.Revelli, Phys.Rev., **B 7**, 3859 (1973).

36. V.V.Sobolev and V.I.Donetskich, Phys.Stat.Sol.(b) **45**, K 15 (1971).

37. R.Zallen and M.L.Slade, Phys.Rev.,**B9**, 1627 (1974).

38. R.Zallen, Phys.Rev.,**B9**, 4485 (1974).

39. T.J.Wieting and J.L.Verble, Phys.Rev.,**B3**, 4286 (1971).

40. J.C.Irwin, R.M.Hoff, B.P.Clayman and R.A.Bromley, Solid State Commun.,**13**, 1531 (1973).

41. A.Mercier and J.P.Voitchovsky, Solid State Commun., **14**, 757 (1974).

42. K.Kumazaki and K.Imai, Phys.Stat.Sol.(b)**149**, K 183 (1988).

43. P.Houdy, These de Troisieme Cycle, Universite de Paris VII, 1982.

44. A.Segura, J.P.Guesdon, J.M.Besson and A.Chevy, J.Appl.Phys., **54**, 876 (1983).

INSTRUMENTATION and MEASUREMENT TECHNIQUES.

Abstract:

First part of this chapter gives the details of instrumentation done in connection with the formation and characterisation of the materials InSe and In_2Se_3. This include fabrication of vacuum system and necessary accessories, evaporation rate control instrument, fabrication of metal cell for electrical and photoconductivity measurements, fabrication of four-probe set-up and jig for Fizeau fringe thickness measurement. The second part discusses precisely the underlined principle and the procedure adopted in various measurements. This comprise of quartz monitor (for flux rate monitoring), X-ray diffraction, Transmission electron microscopy, X-ray photoelectron spectroscopy, chemical and spectrofluorimetric methods for compositional analysis, and the determination of optical constant, n from reflectance spectra.

3.A. INSTRUMENTATION.

3.A.I Deposition System Fabrication:

Thin film deposition, especially the physical deposition technique known as evaporation requires a good degree of vacuum to form the material in the required composition and purity. The process of deposition starts by creating vacuum in the deposition chamber, usually of the order of 10^{-6} Torr or less. The actual deposition is followed by this. In the deposition procedure the supporting devices needed include, material sources, masking arrangements, power supplies, thickness monitoring devices, deposition rate controllers etc. Hence, a typical system consist mainly of two parts; the vacuum pumping system and the deposition setup.

The process of deposition chamber evacuation begins usually at atmospheric pressure and then proceeds to high vacuum. For producing high vacuum a variety of combinations of pumps such as, oil-diffusion, turbo- molecular, getter-ion and and cryo-absorption[1] are available. The most common pumping arrangement among these for production of high vacuum consists of a positive displacement mechanical pump for initial evacuation followed by a vapor-stream pump, usually called diffusion pump[2]. Schematic of such a typical system consisting of the oil diffusion pump (D.P.) backed by a mechanical rotary vane pump is shown in fig.3.1.

Diffusion pumps essentially are vapour ejectors and cannot discharge directly into the atmosphere. A mechanical pump is

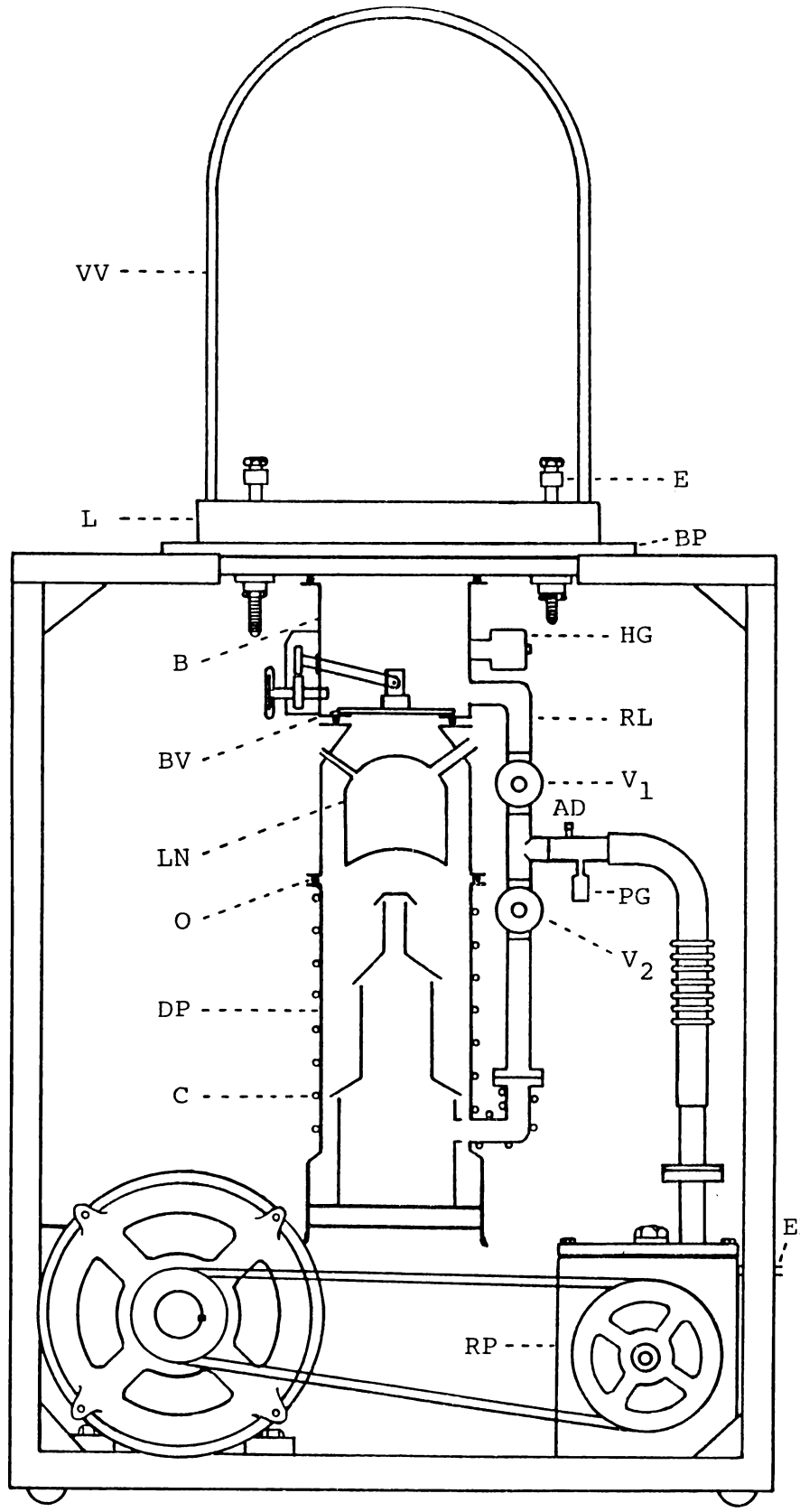

Fig.3.1 Schematic diagram of the fabricated high-vacuum system.

The components are,

AD -Air admittance valve; B -Baffle; BP -Base plate
BV -High vacuum isolation valve; C -Cooling tubes
DP -Diffusion pump; E -Electrical lead-ins
EX -Exhaust duct; HG -High-vacuum gauge; L -Gasket
LN -Liquid nitrogen trap; O -O-ring; PG -Forevacuum gauge
RP -Mechanical pump; RL -Roughing line; V1 -Roughing valve
V2 -Backing valve; VV -Vacuum vessel.

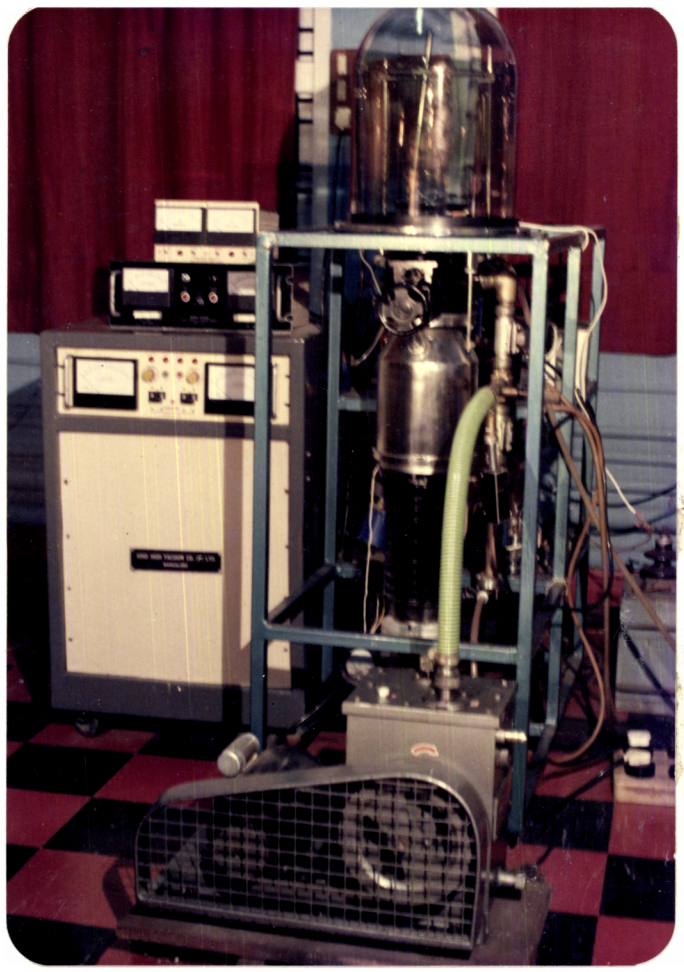

Fig.3.2 Photograph of the fabricated high vacuum evaporation system.

therefore required for the removal of the output discharge as well as for the initial evacuation. The second operation is commonly termed rough pumping or roughing[3-6]. This is to reduce the pressure in the diffusion system and to bring it to the correct operating range. When suitable operating pressure conditions are reached, the diffusion pump can take over. The mechanical pump is now used to maintain proper discharge pressure conditions for the diffusion pump at the foreline connection. This operation is called forepumping or backing[7]. By using diffusion pumping system, vacuum of the order of 10^{-6} Torr can be easily achieved. The photograph of such a set up utilising oil-diffusion pump, fabricated during the present investigation for the high vacuum metal evaporation is shown in fig.3.2.

3.A.I.a Co-evaporation set up

The photograph of the system used for the co-evaporation is shown in fig.3.3. For the deposition, it is provided with two sources, a substrate holder with heating facility and a thickness monitoring transducer, all that come inside a bell jar. The bell jar dome opens at gasket-sealed joint, L, and may be fully raised thus allowing complete assembly and positioning of the materials inside the chamber. Between the baffle and D.P. an LN_2 trap is provided. The evaporation sources for indium and selenium are molybdenum and alumina coated knudsen cell respectively (Fig.3.4). The rate monitor for selenium is a quartz crystal monitor (HHV model- CFM 1). Shutters and substrate heaters are also included since they frequently are important in growing good quality films at any desired thickness.

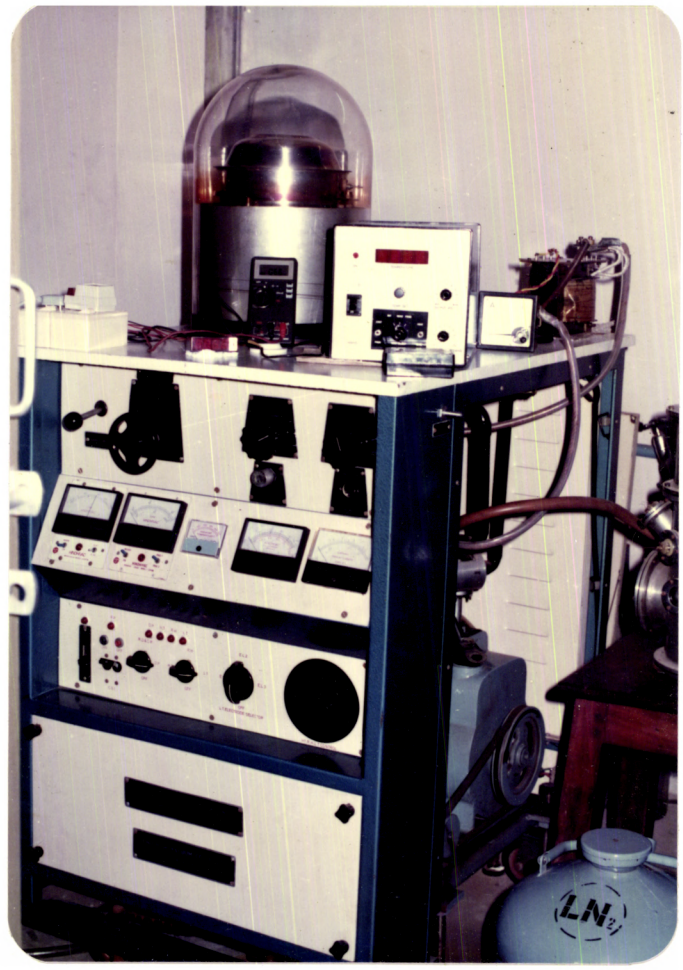

Fig.3.3 Photograph of the co-evaporation system.

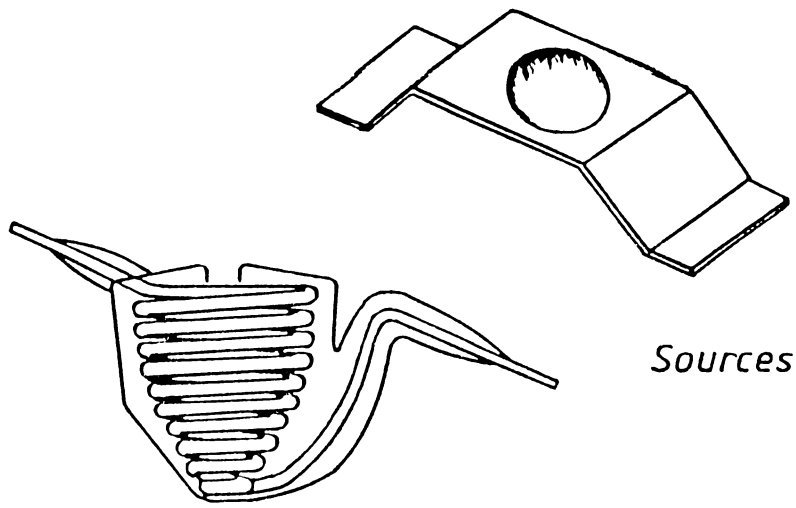

Fig.3.4 Evaporation Sources for indium and selenium.

3.A.I.a.1 Rotary Motion Feedthrough for shutters.

A simple reliable rotary feedthrough fabricated utilising O-ring seal, is shown in Fig.3.5. This particular design is very reliable since it is sealed at two positions using O-rings. These O-rings are separated by a stainless steel bush, through the centre of which the main shaft is moving. The main shaft is a finely polished S.S. rod. Since the O-rings are tightened from the end they make an effective seal between the feedthrough and the shaft. The sealing pressure is applied by tightening the nut. The O-rings are lubricated with silicone grease of low vapour pressure. These feed-throughs are found to be leak-free at 10^{-6} Torr pressure.

3.A.I.a.2 Electrical Feedthroughs

Vacuum evaporators generally require a multitude of electrical inputs and outputs for purposes such as heating evaporation sources and monitoring evaporation parameters. The availability of low outgassing epoxies can be made use of in the vacuum application by fabricating the necessary feedthroughs. Simple designs of a high current and a high voltage feedthroughs fabricated for the use are shown in fig.3.6 and fig.3.7 respectively. They are certainly inexpensive and give satisfactory results under the normal operating conditions. The insulation necessary for these feedthroughs are by using nylon or teflon depending on the application, and vacuum sealed by either curing Araldite or Torrseal on the joint.

In the case of high current feedthroughs if required water

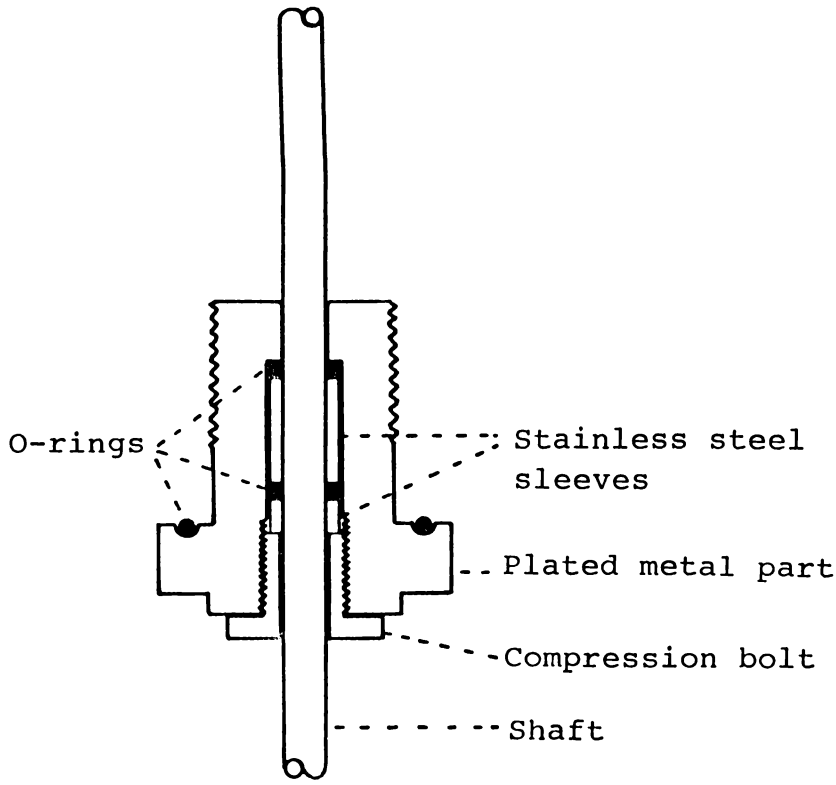

Fig.3.5 Schematic of the Rotary motion feedthrough.

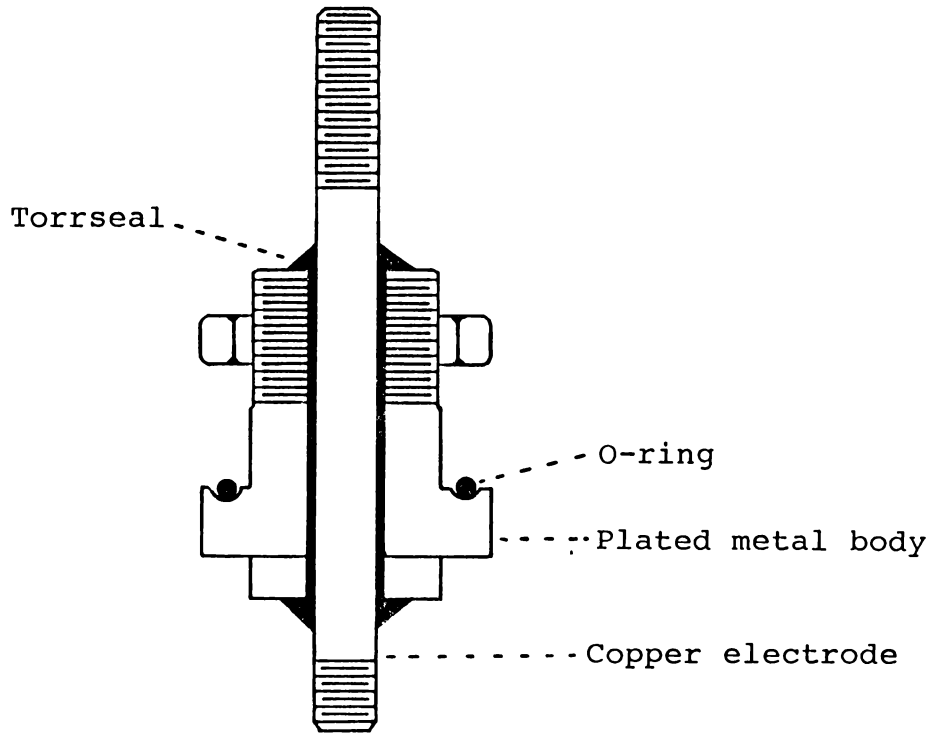

Fig.3.6 High-current, low-voltage lead-in.

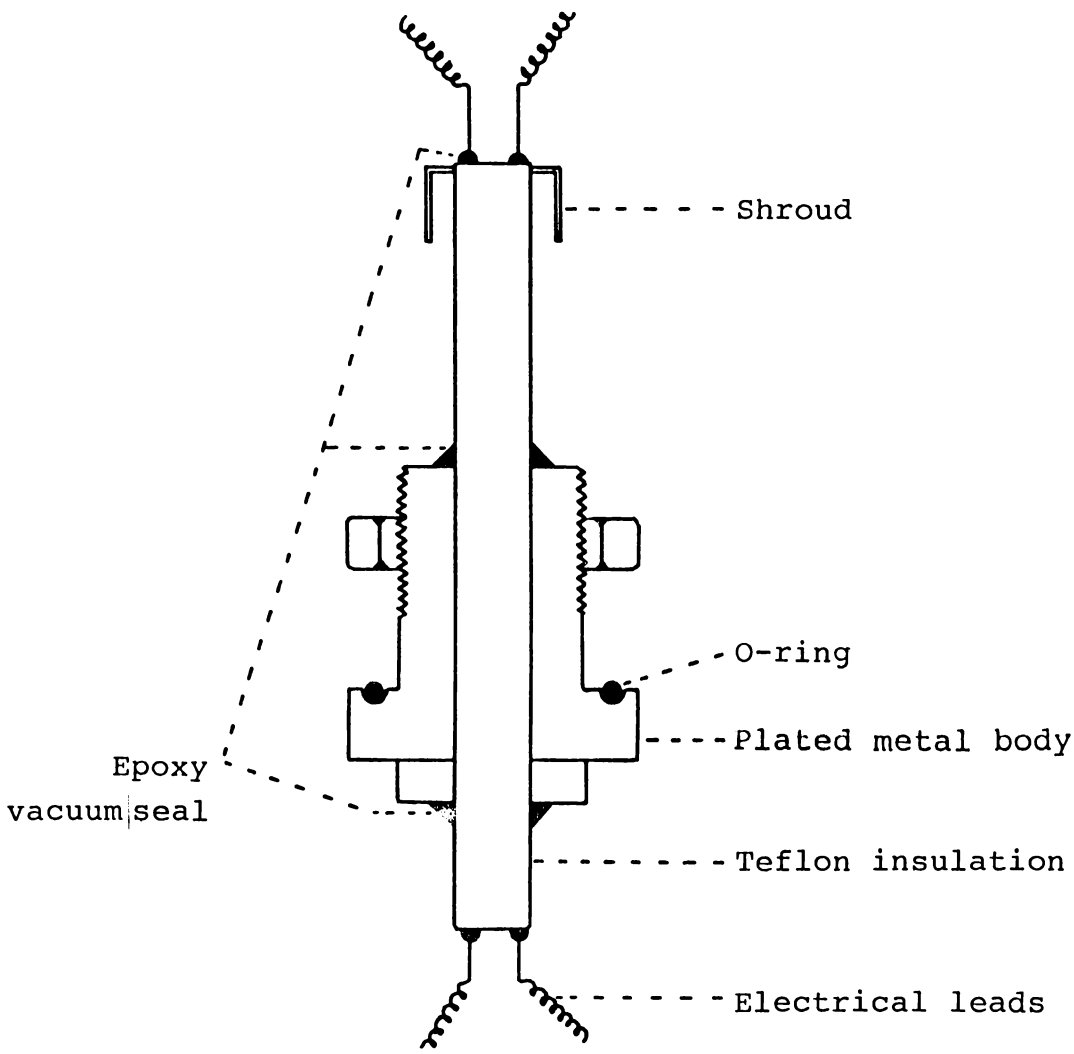

Fig.3.7 High-voltage lead-in.

cooling can also be provided. In the high voltage feedthroughs, leakage by electrical discharge is limited by providing long path-lengths and smoothly edged metallic terminals.

3.A.I.a.3 Substrate heater

The substrate temperature during growth has a strong influence on the properties and structure of the formed films. The most stricking factor is that, this strongly influences the formation of either an amorphous or a crystalline film. Also with increasing substrate temperature, the size of the crystallites increases and the number of lattice faults decreases.

When the substrates are heated during film deposition by mounting them against a flat metal heater plate the surface temperature may not be uniform. Although the objective is to obtain heat exchange by conduction, this is generally achieved in a very incomplete way. The reason is that the two surfaces, the heater plate and the substrate back, do not match perfectly but touch only in limited areas. As a result, the heat flow into the substrate is reduced, and the surface temperature is nonuniform. Using substrates of poor thermal conductivity such as glasses, gradients of 50 to 100^{o}C across the substrate thickness are frequently observed even at deposition temperatures around 400^{o}C.

Considering these, in the present investigations, a radial heating source is used to raise the temperature of the substrate. The thermal insulation needed to minimise temperature loss is achieved by covering it with ceramic wool inside a highly polished metallic envelope.

3.A.II. Evaporation rate control Instrumentation.

In the preparation of stoichiometric thin films by co-evaporation the main task is the precise control of the evaporation rate of the constituents. This can be surmounted by controlling accurately the source temperatures using an electronic control. Basically the system is a two-channel programmable proportional temperature controller. Each of the channel outputs can be programmed independently and, control the rate of heating of indium and selenium sources.

A block diagram of the fabricated controller circuit is shown in Fig 3.8. Basically this consists of two parts: one is the programmer part which takes care of the rate of increase of temperature and final set temperature, and the other is the proportional controller part, which actually controls and drives the SCR, to give the necessary power output to the heaters.

A detailed block diagram of one of the channels of the circuit (both channels are identical) is shown in fig. 3.9.

The basic principle underlying in the controller circuit is as follows. The sensor element senses the temperature of the target and compares it with the programmer output. For this, the programmer generates a signal depending upon the set rate and the final temperature. An error signal is produced[8] which is the difference of the programmer output and the measured temperature. This signal after amplification is fed to the proportional

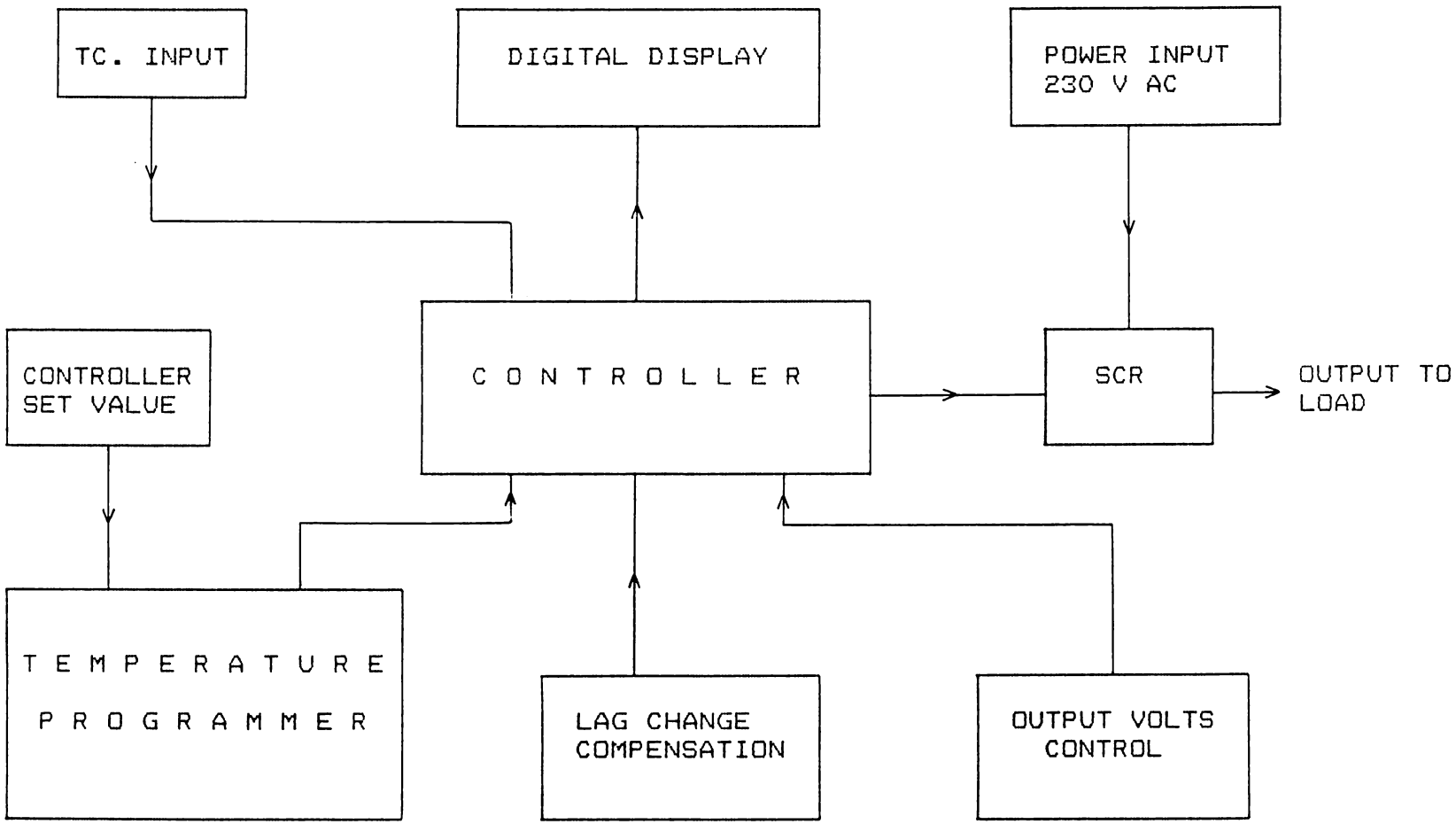

Fig.3.8 Block diagram of the fabricated temperature controller.

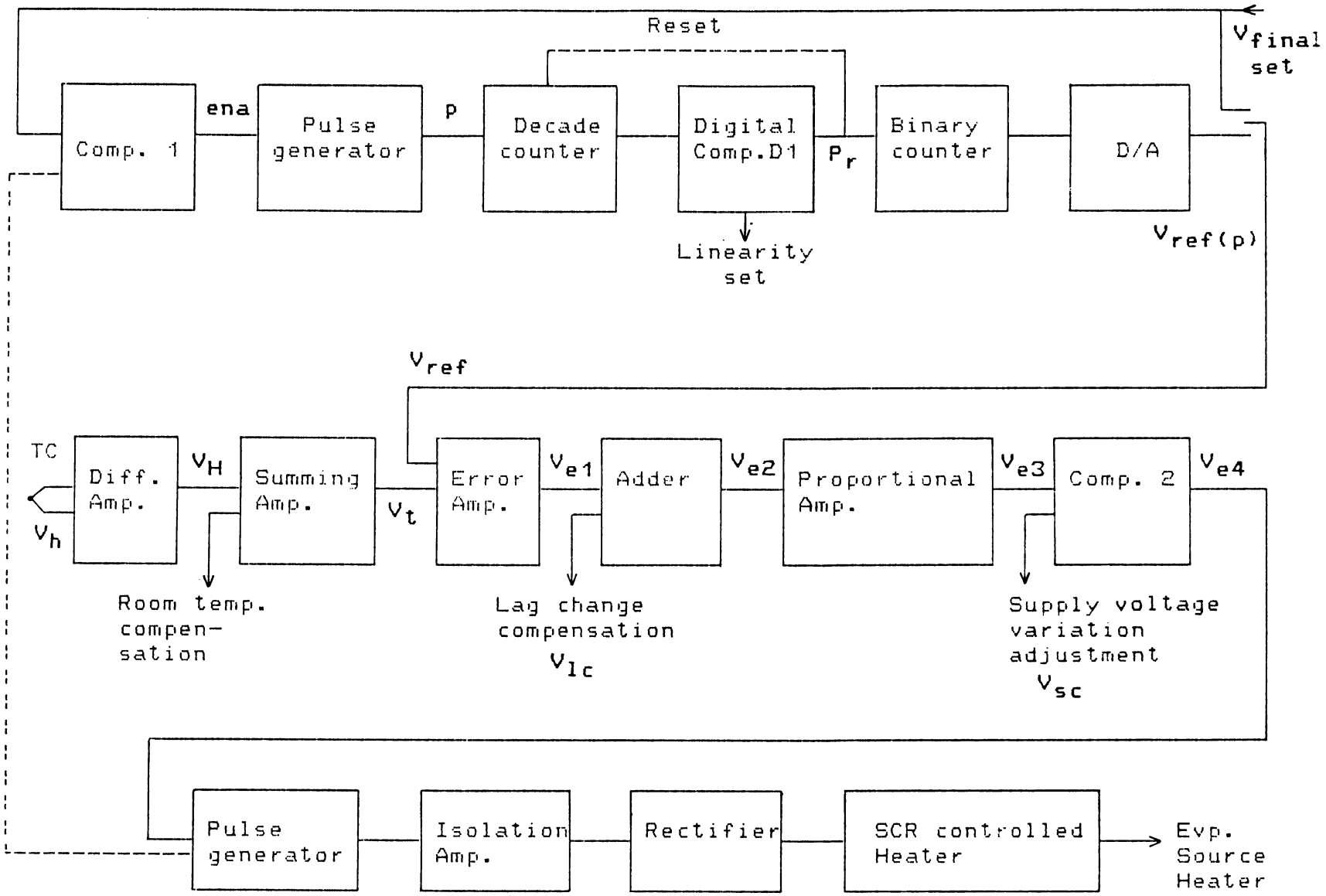

Fig.3.9 Detailed block diagram of the circuit part.

controller input. If this is a positive signal the controller output will change, to give the heater the necessary difference in power to reach the desired temperature[9-11].

The action of each of the parts is described in detail below.

3.A.II.a **Programmer part:**

The action of the programmer used here is based on the pulse counting technique, the output of which depend upon the set value in thumbwheel switches. In the initial part (Fig.3.10) the comparator 1 compares the set temperature with the actual temperature, the output of which is used to select the pulse generator. When the set temperature is higher than the measured temperature the pulse generator, generates pulses at constant rate. But when both the input values to the comparator 1 are the same the pulse generator is disabled. The pulse generator output,p is used as clock to the decade counter.

In the next stage digital comparator,D1 compares the output from the decade counter with linearity set. The linearity set value depends upon the thumbwheel setting which can be selected from 1 to 99. The digital comparator output pulse rate,p_r depends upon the incremental value set. That is, when pulse rate,p is at a constant rate, depending upon the value of the linearity set, the time taken by the decade counter to count upto the set value will vary. The digital comparator output,p_r is used as clock to the binary counter as well as to reset the decade counter. The binary counter output is fed to the D/A converter to convert the digital signal to analog signal and to drive the proportional

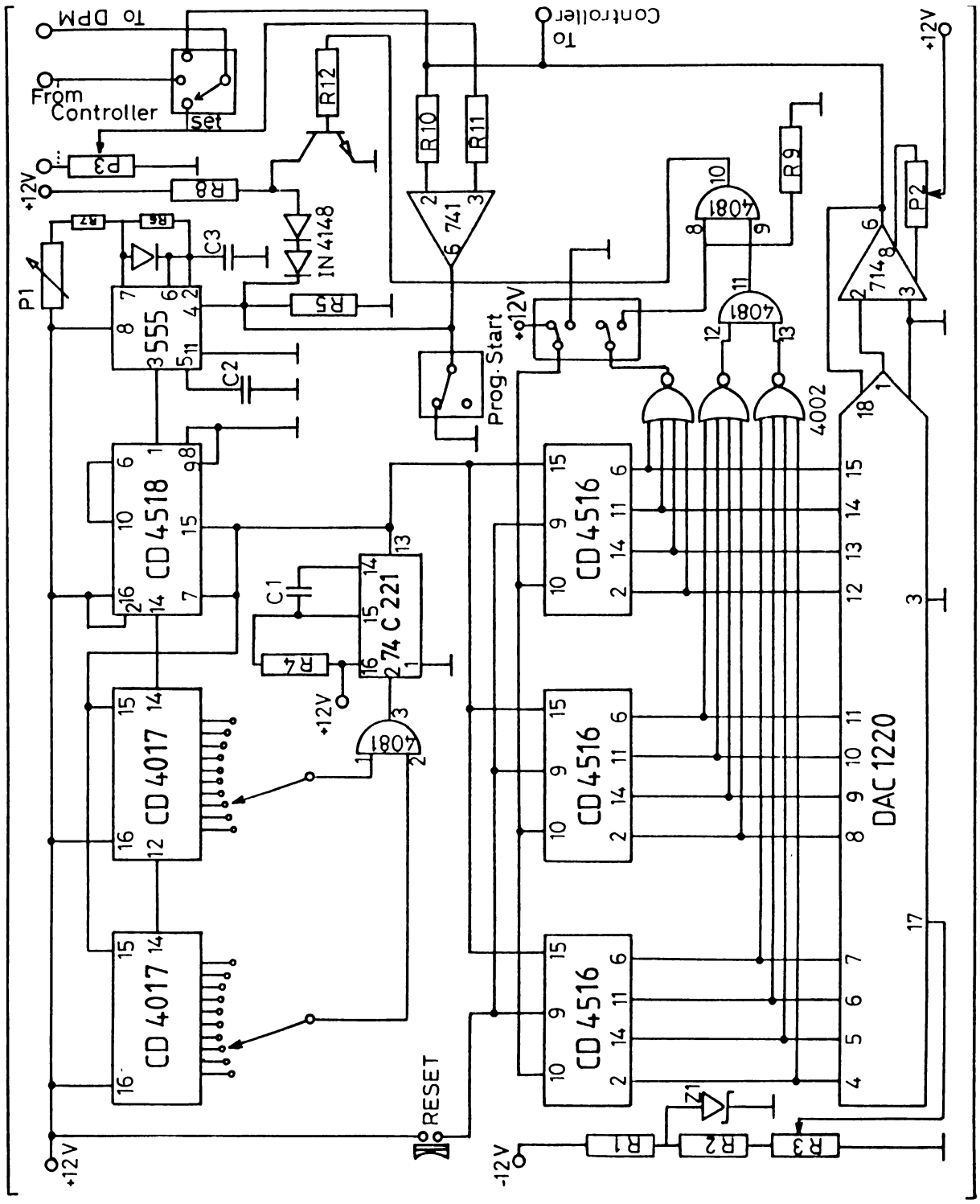

Fig.3.10 Circuit diagram of the programmer part.

controller when it is in the programmer mode. When the select switch is in the direct mode, the final set value bypasses the programmer output.

3.A.II.b Proportional controller part:

The proportional controller part (Fig.3.11) is intended to control the SCR to energise the source heater through a high current transformer. Signal to the controller is from thermocouple which is in contact with the sources. Differential amplifier amplifies the millivolt signal from the thermocouple. In the next stage summing amplifier corrects the room temperature change, with the help of a compensatory circuit, using an IC sensor LM 336 and thus generating V_{amb}. Error amplifier amplifies the difference in voltage from the summing amplifier output V_t and the programmer output $V_{rf(p)}$. In the next stage an adder is provided to adjust the thermal delay when the sensors are not in close contact with the sources. The output of the adder V_{e2} is amplified by a proportional amplifier before feeding it to the comparator 2. Using this comparator the supply voltage variations are compensated by sensing the power supply voltage to system. In the next stage pulse generator generates pulses based on the comparator 2 output V_{e4}. This is amplified and isolated by the isolation amplifier and rectified in the next stage. This rectified pulse is used to control the 'ON ' period of SCR to supply, power to the source heaters, via., a low voltage, high current transformer. The sources are usually well insulated from each other to achieve independent control as well as temperature stability.

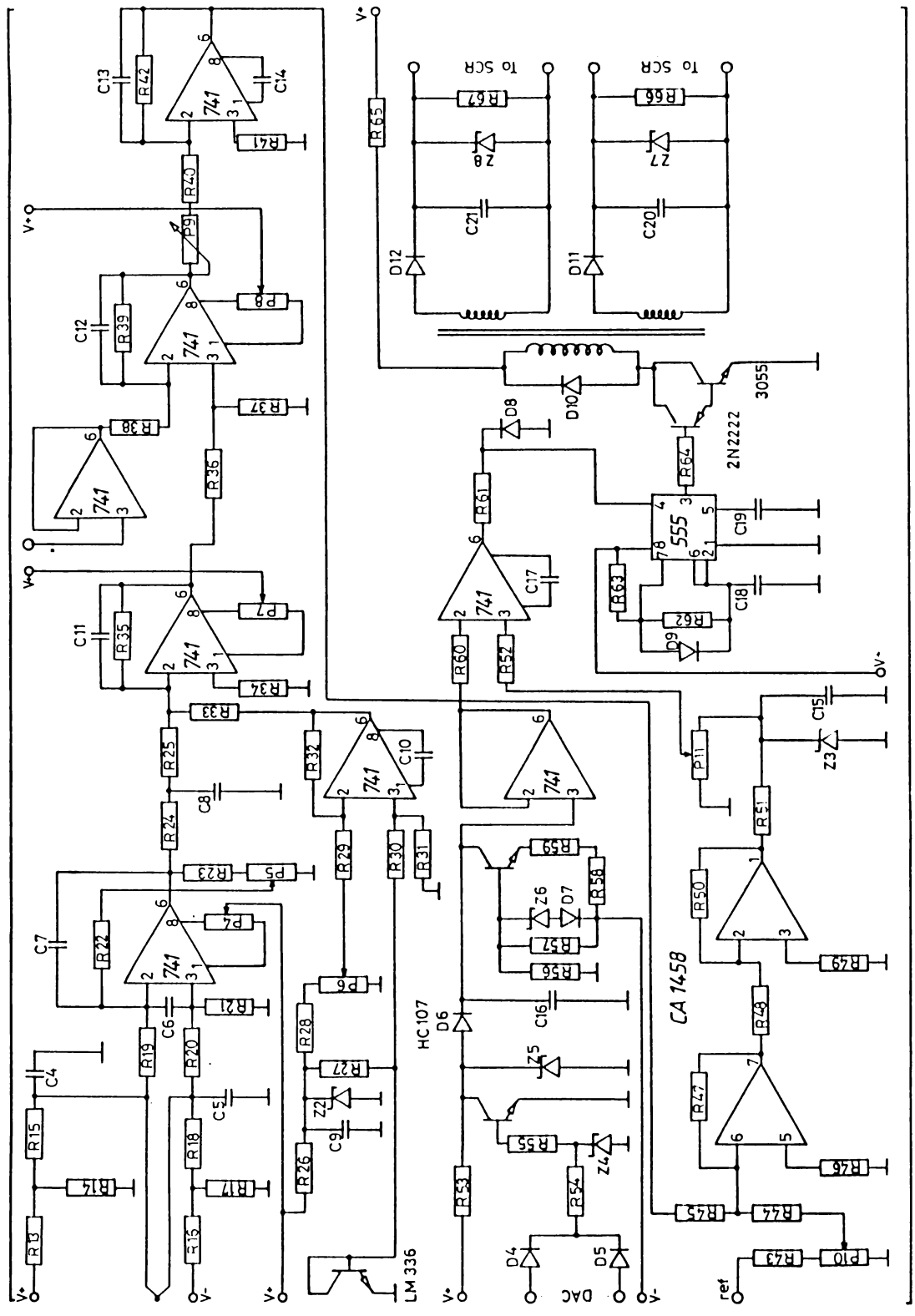

Fig.3.11 Circuit diagram of the proportional temperature controller part.

Performance:

The output of the controller was linear and the rate of evaporation obtained in different deposition cycles was found to be constant in compliance with the set rate.

3.A.II.c **Temperature indicator:**

Exceedingly popular and elegant method for measuring temperatures, is by evaluating the millivolt output from thermocouples using digital panel meters. For this the thermocouple can be of any type and specification. For estimating the millivolt output and displaying it, single, low cost CMOS IC's are largely available in market. Figure 3.13 shows a circuit for measuring temperature using a well-known IC 7107. In this CMOS LSI chip, most of the circuit for measuring and displaying the input millivolt information is included. Basically this is achieved by exploiting the advantages of dual-slope integration. A few external components needed for this include, the integrator and clock RCs, an accurate voltage reference and the display segments. This IC 7107 also includes an automatic zeroing cycle in its operation, and it even generates all the 7-segment multiplexed outputs to drive a 4-digit LED display directly.

3.A.II.c.1 **Dual slope integration:**

Dual-slope integration is used extensively in precision digital multimeters, as well as in conversion modules of 10-bit to 18-bit resolution. It offers good accuracy and high stability at a lower cost, combined with excellent rejection of power-line (and other) interference, for applications where speed is not

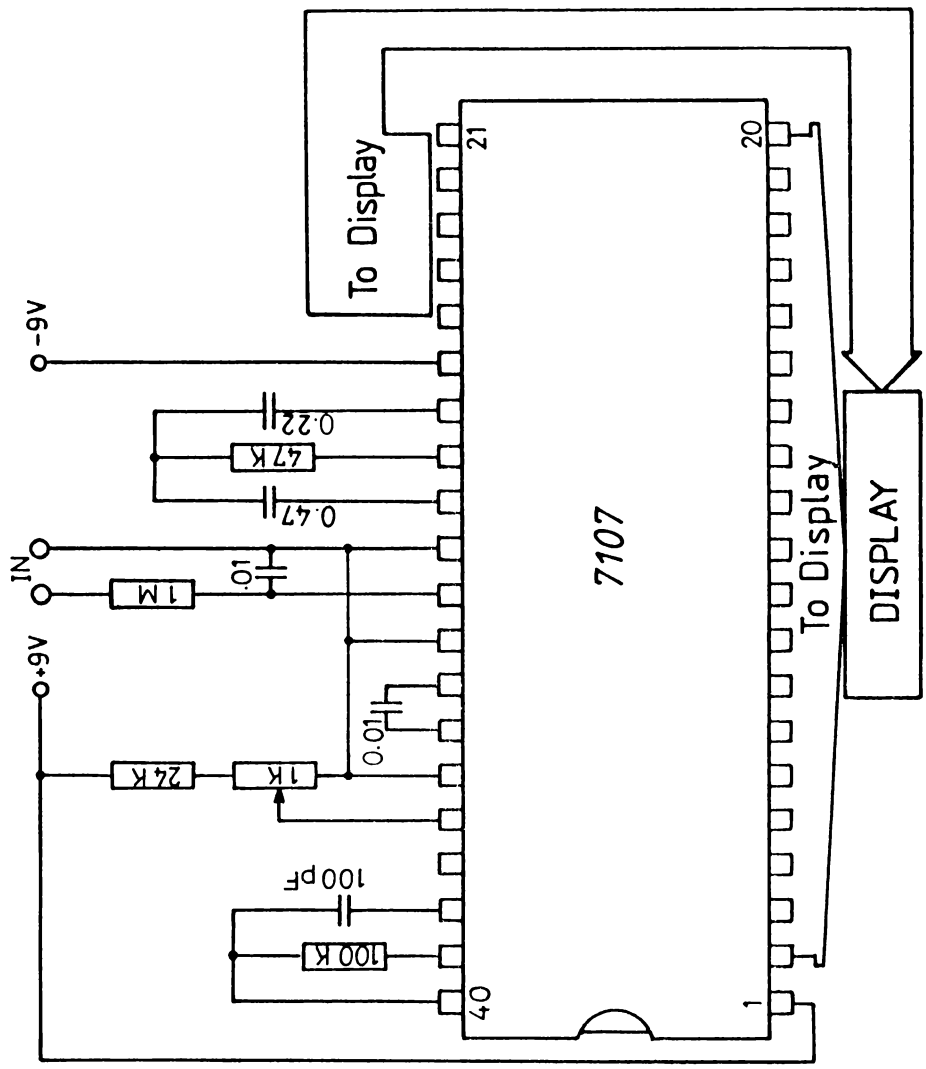

Fig.3.12 Circuit diagram of digital Panel meter.

important. With a module using this technique greater precision is achieved at a lowest cost. In this technique, it eliminates most of the capacitor and comparator problems inherent in single - slope integration. The mode of working of this can be explained as follows:

First, a current accurately proportional to the input level, charges a capacitor for a fixed time interval; then the capacitor is discharged by a constant current until the voltage reaches zero again. The time to discharge the capacitor is proportional to the input level and is used to enable a counter driven from a clock running at a fixed frequency. The final count is proportional to the input level and display it after suitable conversion.

The prime advantage of dual-slope integration is that it achieves very good accuracy without imposing extreme requirements on component stability. Specifically, the capacitor value does not have to be precisely stable, since the charge cycle and the discharge cycle both go at a rate inversely proportional to C. Similarly, drifts or scale errors in the comparator are cancelled out by beginning and ending of each conversion cycle at the same voltage. Each conversion cycle is followed by an "auto - zeroing" cycle in which the input is held at zero and thus eliminates the "zero - error" in the subsequent measurements.

In dual-slope converters only the discharge current has to be of high stability. Even the clock frequency does not have to be highly stable because the fixed integration time of the first

phase of the measurement is generated by sub-division from the same clock used to increment the counter. If the clock slows down by, say 10%, the initial ramp will go 10% higher than normal, requiring 10% longer ramp-down time. Since this is measured in clock pulses that are 10% slower than normal, the final output count will be the same.

3.A.III Fabrication of metal cell for electrical and photoconductivity measurements:

For making the resistivity and photoconductivity measurements, a high vacuum cell has been fabricated incorporating all the necessary facilities to carry out the measurements effectively. The photograph of the cell is shown in fig. 3.13.

The cell is made-up of mild steel material with a cylindrical stem having a number of side ports for fixing various attachments such as electrical connectors, vacuum gauges etc., and facilities such as cooling arrangements, sample loading and viewing ports etc. The cell is with flange fittings on top and bottom. All the ports are vacuum sealed either by neoprene or silicone 'O' rings. Low pressures of about 5×10^{-6} Torr can be reached inside the cell. For the measurement of vacuum, Pirani and Penning gauge heads are attached to two of the ports. The outer body of the cell is hard-chrome plated but the inner portion is chemically blackened. The main portion of the cell is having inner dimensions of 18 cm diameter and 30 cm height. The removable sample holder is fixed at the bottom end of a one-end

Fig.3.13 Photograph of the metal cell used for measurements.

closed metallic tube embedded to the top flange.

For electrical resistivity measurements the sample holder consists of a copper disc of diameter 4 cm with sliding arrangements for sample loading. Connections to the film are made by Teflon insulated, screw-tightened contacts with handy screw heads. The sample holder is also provided with a cartridge heater of 100 watt power to facilitate the sample heating. A platinum resistance thermometer measures the temperature variations of the sample. The electrical connections to the vacuum cell are made through multiple pin ceramic vacuum connectors.

For photoconductivity measurements the cell is provided with quartz windows for illuminating the sample. For these measurements, the electrical sample holder can be replaced with a sample holder having an opening of 2.5cm at the centre. Details of the measurements are given in chapter 4.

3.A.IV **Resistivity:**

Different methods employed for the measurement of resistivity of films are

1. Four - point probe method or four probe method.
2. Van der Pauw method

For obtaining the room temperature resistivity immediately after deposition the four - probe method has been more convenient. But for the subsequent measurements and also for the Hall measurements, the Van der Pauw technique has been made use of.

3.A.IV.a Four - point probe method:

This is the most handy and common method for measuring the resistivity of a semiconductor material. The simplest arrangement consists of four in - line equidistant point probes separated by a distance S (Fig.3.14). For measurement, when the probes are lowered onto a semiconductor material it make contacts with the surface of the material, to flow a small current I through the outer probes and to measure a voltage V across the two inner probes. When the thickness of the material is small compared to the probe spacing, the resistivity is given by[12,13]

$$\rho = 4.53 \; (V/I)\; t \quad \text{(ohm.cm)} \qquad (t \ll s) \qquad \ldots (3.1)$$

3.A.IV.b Van der Pauw method:

This is a very effective and popular method used for determining the electrical resistivity of low resistivity materials. Four ohmic contacts A, B, C and D are formed at the periphery of a film of thickness t, and are used to pass current and measure developed voltage (Fig. 3.15). Let $R_{AB,\,CD}$ is determined by the ratio of a current I_{AB} allowed to flow across the contacts A and B to a potential drop V_{CD} produced between the contacts C and D. Similarly $R_{BC,DA}$ is determined by flowing a current I_{BC} between the contacts B and C and measured the potential drop V_{DA} across the contacts D and A. Then Van der Pauw has shown that[14]

$$\exp\left[\frac{-\pi t}{\rho} R_{AB,CD}\right] + \exp\left[\frac{-\pi t}{\rho} R_{BC,DA}\right] = 1 \qquad \ldots (3.2)$$

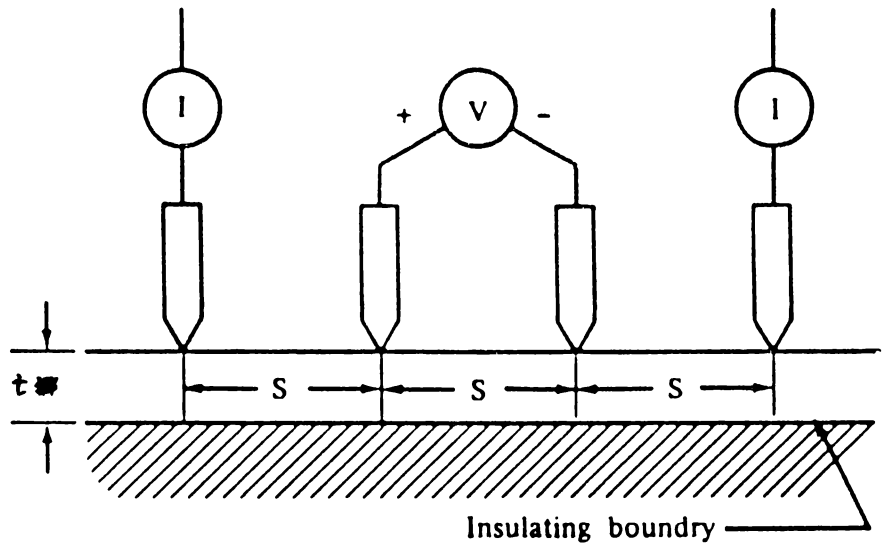

Fig.3.14 Measurement of resistivity: Collinear array Four-point probe.

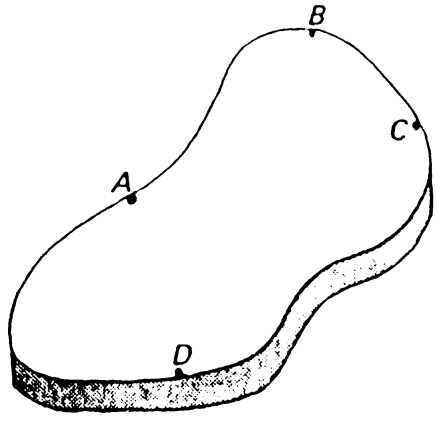

Fig.3.15 Measurement of resistivity: Van der Pauw's method.

When all the contacts are symmetrical this equation yields

$$\rho = (\pi t / \ln 2) (V_{CD} / I_{AB}) \quad \ldots (3.3)$$

3.A.V. **Hall effect:**

In working with a semiconductor, it is important to know whether the current is being carried by electrons or by holes and to have an estimate of the number of carriers involved in the process of current transport. These are usually determined by measuring Hall coefficient.

The physical basis for the Hall measurements lies in the fact that a magnetic field causes the current carriers to travel in curved paths[15]. The result is that the carriers pile up on the side of the sample to build up a Hall voltage. Since the direction of the charge displacement is always dependent on the type of the carrier, the sign of the Hall coefficient gives whether the current is being carried by holes or by electrons[16].

Consider a semiconductor bar, having its axis pointing in the X - direction (Fig.3.16). Let an electric field F_x, applied in the X - direction, cause a current density J_x to flow in that direction, and let a magnetic field B_z be applied perpendicular to its axis. Let the carriers have a charge q (q = - e for an electron, q = + e for a hole) and let n be the carrier concentration. Then if, v_x is the particle velocity in the x-direction[17].

$$J_x = nq\, v_x = nq\, \mu\, F_x \quad \ldots (3.4)$$

and the average magnetic force in the Y-direction on the moving

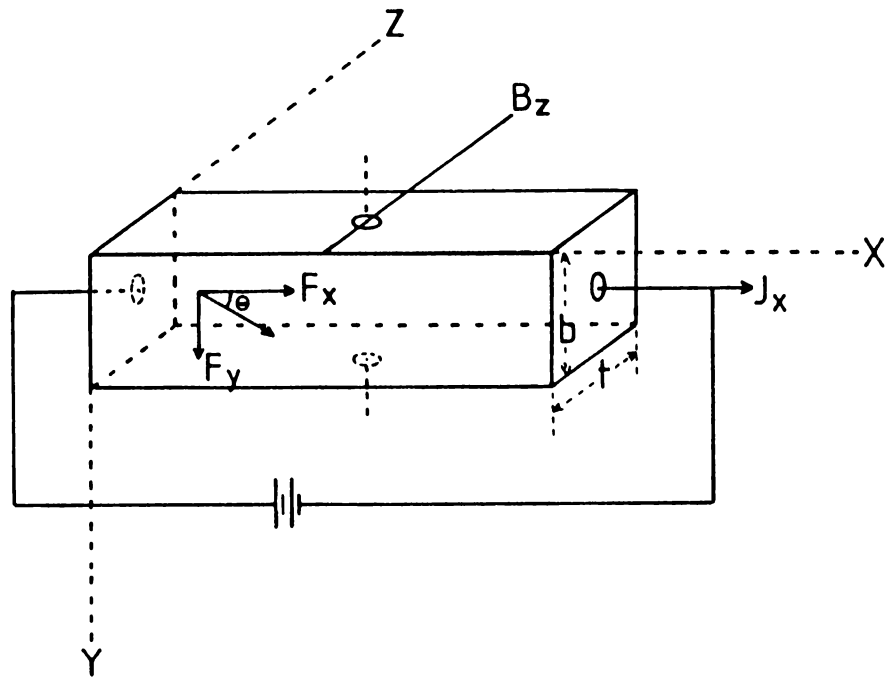

Fig.3.16 Hall effect in a semiconductor sample film. An electric field F_x is applied in the x-direction, giving rise to a current density J_x. A magnetic field B_z (or H) applied in the z-direction causing a Hall field F_y in the y-direction; Θ is the Hall angle.

charge q, is

$$- q\ v_x\ B_z \qquad \ldots (3.5)$$

Since no current can flow under equilibrium conditions as an electronic field F_y will be set up in the Y- direction, giving rise to an electric force

$$q\ F_y \qquad \ldots (3.6)$$

This exactly balance the magnetic force (3.5). Hence

$$q\ F_y = q\ v_x\ B_z \qquad \ldots (3.7a)$$

$$\text{ie.,} \quad F_y = v_x\ B_z \qquad \ldots (3.7b)$$

Substituting for $v_x = \frac{J_x}{qn}$,from (3.4) we have

$$F_y = \frac{J_x\ B_z}{qn} = R\ J_x\ B_z \qquad \ldots (3.8)$$

$$\text{where } R = \frac{1}{qn} \qquad \ldots (3.9)$$

is known as the Hall coefficient, and is obtained by measuring the developed transverse voltage across the sample. The quantity F_y in eqn.(3.7a) is the transverse voltage across the sample.

$$\text{So,} \quad F_y = \frac{-V}{b} \qquad \ldots (3.10)$$

$$\text{ie.,} \quad q\ \frac{V}{b} = \frac{1}{c}\ v_x\ H \qquad \ldots (3.11)$$

where b is the breadth of the sample and c is the velocity of light in c.g.s. units. When t is the thickness of the material,

the current density in the x direction is I/bt, so that

$$v_x = \frac{I}{nbt} \qquad \ldots (3.12)$$

where n (or p) is the electron (or hole) density. Therefore

$$q \frac{V}{b} = \frac{IH}{cnbt} \text{ , in c.g.s units} \qquad \ldots (3.13)$$

Converting to practical units and substituting the value of c, we have

$$V = 10^{-8} \frac{IH}{nqt} \qquad \ldots (3.14)$$

where $q = 1.60 \times 10^{-19}$ coulomb and V in volts.

The product of Hall coefficient and conductivity gives the mobility.

$$R \sigma = \mu \qquad \ldots (3.15)$$

where μ is called the " Hall mobility" μ_H.

3.A.VI. Film Thickness measurement

3.A.VI.a Multiple-beam Interferometry:

3.A.VI.a.1 Fizeau fringe of equal thickness:

In thin films, since the film thickness is usually in the range of a wavelength of visible light, various types of optical interference phenomena have been found to be fruitful for the accurate determination of film thickness. In the present investigations multiple - beam interferometric technique namely

Fizeau fringe of equal thickness (Tolansky technique) [18] has been employed for the measurement of film thickness. The most stricking advantages of this method are simplicity, reliability and handiness. The principle behind this method is that, when a reflecting surface is brought together into close proximity with a partially reflecting one, interference fringes are produced and the measurement of which can be made use of for the direct determination of the absolute film thickness with high accuracy.

3.A.VI.a.2 Theory:

The theory of the multiple-beam interference occurring in a transparent plane parallel plate of uniform thickness has been first given by Airy[19].

Tolansky[20] and co-workers employed this method for measuring thin film thickness and established the multiple beam interferometry.

Let AB and CD be two parallel reflecting surfaces confining a medium of refractive index μ (Fig.3.17a). When a beam of light is incident on it at an angle θ the optical path difference between two beams is $2\mu d \cos\theta$, where d is the thickness. The interference fringes occur as the beams interfere constructively. i.e., when the phase difference between successive beams is an integral multiple of 2π.

$$\delta = 2\pi / \lambda \cdot 2\mu d \cos\theta \qquad \ldots (3.16)$$

When the angle θ is very small, the phase difference resulting from the path difference between successive beams is

approximately $(2S/\lambda)\ 2\pi$. Here λ is the wavelength of the incident light and S is the distance between the plates AB and CD forming the fringes. The condition for constructive interference can be given as[18],

$$2S/\lambda . 2\pi + 2\delta = a_1 . 2\pi \qquad \ldots (3.17)$$

where a_1 is an integer and δ, is the phase change due to reflection. For high reflectivity films, δ is nearly equal to π. So the eqn. (3.17) modifies to

$$S = \frac{a_1 - 1}{2} . \lambda = a_2 . \frac{\lambda}{2} \qquad \ldots (3.18)$$

Thus, the intensity maxima in the interference corresponds to a distance

$$S = \frac{\lambda}{2}$$

In the presence of a step due to a film thickness on the substrate, the distance S causes to change by an amount equal to the film thickness t. Then the film thickness is given by

$$t = \frac{d}{\text{fringe spacing}} \times \frac{\lambda}{2} \qquad \ldots (3.19)$$

For Mercury - Green this equation can be rewritten as

$$t = 2730 \times \frac{\text{fringe shift}}{\text{fringe spacing}} \qquad \ldots (3.20)$$

Under the best conditions, the resolution of the method is ± 5 Å, in a direction normal to the substrate surface.

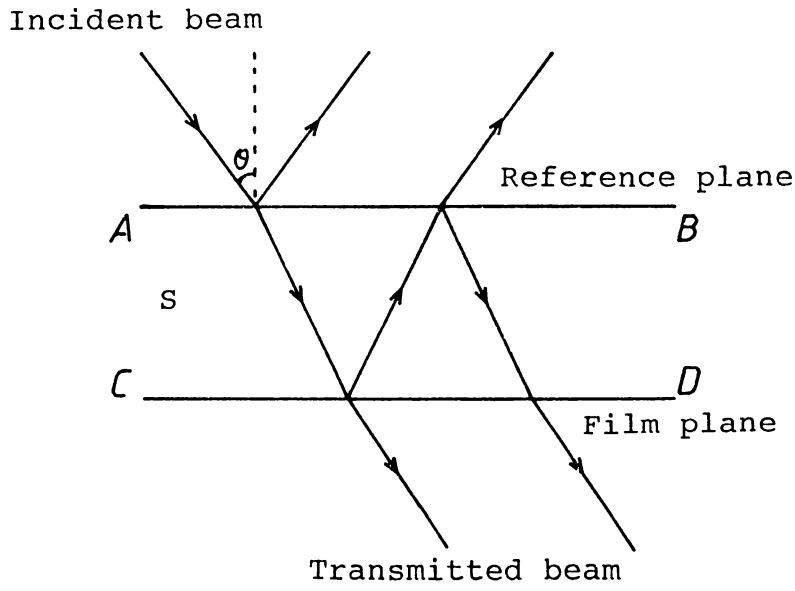

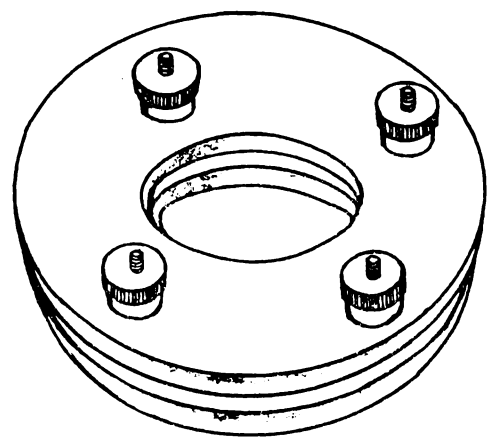

Fig.3.17(a) Schematic representation of multiple beam interferometry.

(b) Measurement jig for multiple beam interferometry.

3.A.VI.a.3 **Jig fabrication:**

Description of the fabricated jig (Fig.3.17b) is as follows. Two circular rings each of diameter 60 mm and thickness 6 mm have been machined from a hollow brass cylinder. Four equi-distant screws with handy screwheads form the distance adjustment arrangement and is useful to tune up the fringes. The screws are having spring sleeves to hold them apart. The measurement plate with the film is placed between the two rings with the semi-silvered plate above. From the top, the jig is a circular ring with a centre aperture of 30 mm diameter. When the fringes are formed, they are viewed through this aperture. The vernier microscope is positioned vertically above the jig facing the semi-silvered plate.

In order to prevent the jig from corrosion and for the smoothness of the surface, it has been chromium plated.

3.A.VI.b **Fizeau fringes of equal thickness: Measurement**

Experimental setup (Fig.3.18) and measurement of film thickness by Fizeau fringes of equal thickness can be described as follows:

Mercury vapour lamp with a green filter (λ = 5460 Å; bandwidth 15 Å) serves as a monochromatic source of light. The monochromatic output from the filter after collimation is made to incident on a glass plate, kept at an angle 45^{o} with the incoming rays, under a low power vernier microscope, so that a portion of the light is reflected vertically downwards to measurement jig.

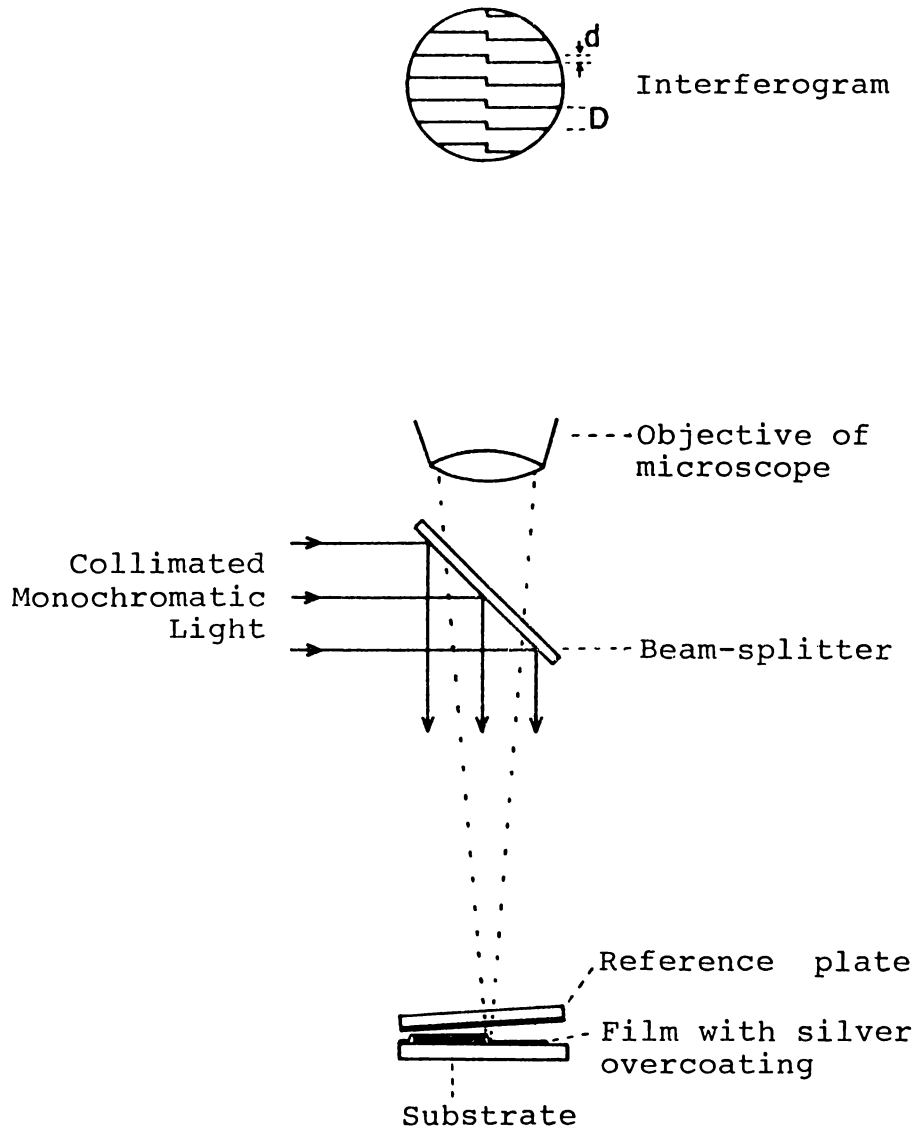

Fig.3.18 Schematic view of Interferometer arrangement for producing Fizeau fringes of equal thickness.

In the measurement jig, the film whose thickness is to be measured which forms a step with the substrate when overcoated with a reflecting silver film is placed with a semi-transparent plate, above it. An air-wedge is formed between the two surfaces and the distance can be altered to get well-defined fringes by adjusting the screws attached to the jig. Viewing on top through the vernier microscope, the displacement of the fringes at the film edge (formed between film and substrate at the silver over-coated position) is visible. Taking successive readings of each fringe on either side of the shifted position of the fringes, the fringe width as well as the displacement can be obtained. The thickness of the film is then given by

$$t = \frac{\text{fringe shift}}{\text{fringe spacing}} \times \frac{\lambda}{2} \qquad \ldots (3.21)$$

where λ is the wavelength of the monochromatic light used.

3.B. MEASUREMENT TECHNIQUES

3.B.I Deposition monitoring and process control

Several methods are available to monitor the mass of a deposited film in situ: an ionisation monitor method, a quartz fiber microbalance method, and a quartz crystal oscillator method. Making use of any of the methods, in addition to the thin film thickness, the deposition rate can also be obtained. Hence they find application in controlling the rate of deposition of the constituent elements or compounds in a multisource evaporation.

3.B.I.a Quartz crystal method

The possibility of using piezoelectric quartz resonators for mass sensing was put forwarded by Sauerbrey[21,22] in 1957. The principle behind this is that the frequency of a quartz crystal is dependent upon the vibrating mass. Thus when a small mass is uniformly deposited over the crystal surface, the shift in resonant frequency is linearly proportional to the mass. Since the frequency shift is independent of the physical properties of deposited material, the deposited mass can be determined by simple frequency measurements without the knowledge of its physical properties.

A quartz crystal oscillator is noted for its advantage of the simplicity of construction and the accuracy. Apart from this its advantages such as imperviousness to external vibrations and mechanical shocks makes it a good choice in thin film deposition processes as thickness and rate monitor.

3.B.I.b Theoretical background:

If a quartz crystal is excited to thickness-shear oscillations by an alternating electric field, the resonance frequency is inversely proportional to the thickness of the quartz plate t_q

$$f = \frac{v_{tr}}{2t_q} = \frac{N}{t_q} \qquad \ldots (3.22)$$

where v_{tr} is the velocity of the elastic transverse wave in the direction of the plate thickness t_q; N is the frequency constant,

for AT-cut crystals N = 1670 KHz/ mm [24].

From eqn.(3.22), change in the resonant frequency df caused by an infinitesimal change in crystal thickness dt_q should be related to

$$\frac{df}{f} = \frac{-dt_q}{t_q} \qquad \ldots (3.23)$$

Writing this eqn. in terms of crystal mass m and change of crystal mass dm, we have

$$\frac{df}{f} = \frac{-dm}{m} = \frac{-dm}{\varrho_q t_q A} \qquad \ldots (3.24)$$

where ϱ_q, is the density of quartz and A is the area of the plate. From eqn. (3.22) and (3.24)

$$\frac{df}{f} = \frac{-f}{N \varrho_q} \cdot \frac{dm}{A} \qquad \ldots (3.25)$$

$$\text{ie., } df = \frac{-f^2}{N_q} \cdot \frac{dm}{A} \qquad \ldots (3.26)$$

Equation (3.26) predicts that the frequency shift is linearly proportional to the deposited mass and not dependent on the physical properties of the film. Since in thickness-shear oscillations, an antinode is formed at the surface of the quartz plate, the material deposited will act upon the frequency only by its weight. This means that the elastic constants do not contribute to the frequency shift, provided that the film is sufficiently thin.

For films which are not thin compared with the thickness of

the quartz plate, the change of the elastic constants of the crystal due to the deposit must also be taken into consideration. According to this, the choice of a crystal with an initial frequency f_o, depends upon the accuracy or range of measurement desired, ie., ultimately on the " sensitivity for mass determination", C_{fo}. The factor

$$C_{fo} = f_o^2 / N \varrho_q \qquad \ldots (3.27)$$

indicates, the frequency shift for a unit-mass increase on the area of the crystal.

Consequently, the thinner the films to be measured, the higher the sensitivity desired, and the higher should be the f_o. If the thickness range to be determined is large, then the deviation from linearity should occur as late as possible, so crystals with low f_o should be chosen. A meaningful compromise between sensitivity and mass-loading capacity seems to hold crystals with an initial frequency f_o between 5 and 6 MHz.

Though, the AT cut quartz crystals have the smallest realisable temperature coefficient of frequency of $\pm$ 5 x 10^{-6} over the interval from -5 to + 55^{o}C for 35^o 20' angle of cut[25], it is yet needful to safeguard the crystal against temperature variations to get high frequency stability. Therefore the crystal housing is usually a water cooled metallic enclosure to shield the heat radiation, with a narrow opening to accommodate the depositing mass[26].

For the use in vacuum deposition, the sensitivity of the

crystal oscillator is usually about 10^{-9} gm/cm^2.

3.B.I.c Working of quartz crystal monitor:

Block diagram explaining the working of a quartz crystal monitor is shown in fig.3.19. An AT cut 6.0 MHz quartz crystal is the monitor crystal. The electrodes on either side were formed by evaporating thin Aluminium films. Aluminium matches very well with quartz, both in density and acoustic impedance. When the material deposits on the crystal the frequency changes. Since a gadget needed to measure such a six-digit frequency precisely is expensive, it is converted to an easily measurable low frequency with the help of a 6.5 MHz reference oscillator. For this the monitor frequency and the reference oscillator frequency is mixed, and the difference in frequency (500 KHz before deposition; increasing to 650 KHz as coating proceeds) is extracted by tuned circuits. The amplified signal is mixed with the output from a variable frequency oscillator (500 to 650 KHz: tuned by zero-set potentiometer), to produce a zero reading at the start of each deposition cycle. The final frequency signal obtained is converted to a voltage which is displayed as thickness on a voltage to thickness calibrated panel. The measured frequency also compares with a set frequency, and it terminates the deposition by bringing the shutter above the source and putting off the sources when the set frequency and the measured frequency during deposition are equal.

To obtain the deposition rate the change of frequency Δf is differentiated with time signal and is displayed directly on rate-meter.

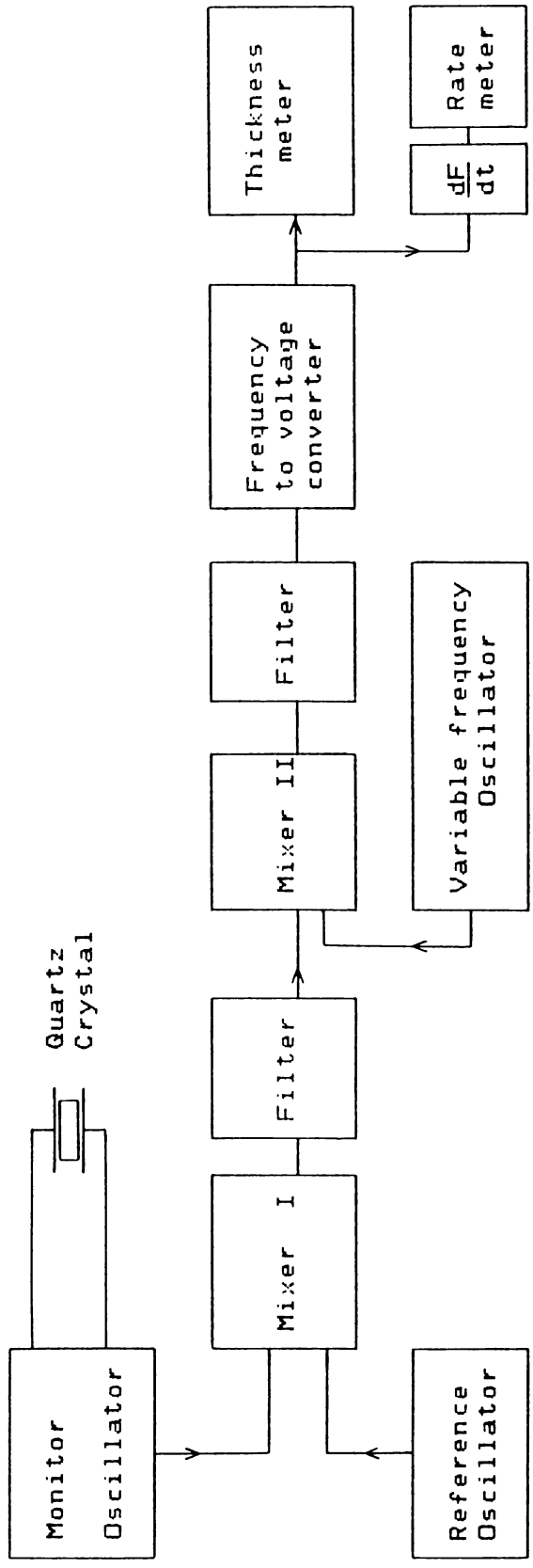

Fig.3.19 Block diagram of Quartz crystal thickness monitor.

Thus, if a quartz crystal wafer is placed so that the film material is deposited upon it at the same rate as upon the substrate, the frequency change of the crystal will be an accurate measure of the average thickness of the film. But one point to be noted is that it needs calibration for each material.

For repeated use, when the crystal is deposited by sufficiently thick material, it is removed by diping in 5% NaOH solution at about 40^{o}C. After rinsing well in distilled water, it is dried and then deposit Al electrodes on both sides. Thus the same crystal can be used for a number of times[27].

3.B.II X-Ray Diffraction

The X-ray diffraction (XRD) method in determining film structures have now become highly dependable with the availability of high-intensity X-ray generators, highly selective monochromators, and sensitive low-noise diffractometer equipment. By use of a goniometer and counter, lattice spacings and intensities can be determined with considerably higher accuracy, but greater film thickness are required than for electron diffraction. For obtaining good spectra, in the case of strongly texturized films 100-300 Å are sufficient but thicknesses of about 1000 Å are needed for the usual polycrystalline films.

For the present study the diffractometer used was a Philips 1070/76 equipment. In this X-ray beam is incident at an angle,θ on the film and the detector is at an angle 2θ. The spectra are recorded as intensity of reflections versus 2θ, by an attached

chart recorder. Accelerating voltage applied was 30 kV at a tube current of 20 mA for the Cu source. For the present characterisation of the films, X-ray beam used was a monochromatised Cu K_α radiation which is scanned onto the films, at an angle between 3° and 35°(ie., θ is varied from 3° to 35°).

3.B.III Transmission Electron Microscopy (TEM)

Transmission electron microscopy (TEM) is by far the most widely used instrumental technique for obtaining structural features of thin films. Because of its operational flexibility by use of numerous available special attachments and the high resolution obtainable (<10 Å) make them suitable to be used exclusively for the standard structure investigations on thin films. The magnification that can be achieved in the TEM is nearly about 2×10^5.

The present investigations made use of a Philips EM301 transmission electron microscope. For that the sample preparation is as follows. The films were first removed from the quartz substrates using 40% HCl and immediately diluting it with distilled water and then, the floating films were carefully removed onto the grid. The accelerating voltage was between 80 - 100 kV and the magnification was kept in between 2000x and 6000x. The film thicknesses used for this study was always less than 1000 Å.

3.B.III.a Electron Diffraction.

Electron diffraction provides the most direct structural

evidence and is ideally suited for the study of thin films[28]. The sample preparation methods are same as those described in the TEM studies. For electron diffraction a monochromatic electron beam is used exclusively. The diffracted beam from the lattice points forms the diffraction pattern in the back focal plane of the objective which is then magnified by the intermediate and then by a projector lens to form the final diffraction pattern on a fluorescent screen. With the help of apertures, it is possible to get a clear Selected Area Diffraction (SAD) of the specimen.

Electron diffraction pattern, in the case of amorphous films consists of a few broad rings. Polycrystalline films yield Debye- Scherrer patterns with numerous, more or less sharp concentric rings. Missing rings and ring intensities which vary in a symmetrical manner in the circumference indicate a texturised film in which the crystallites exhibit a preferred orientation in one or more crystallographic directions and random orientation in the others.

Laue diagrams, consists of individual spots generated by single- crystalline films, while multiple scattering from well-ordered single crystals give Kikuchi patterns. In these two patterns a spread of diffraction pattern intensity is clearly observable as the scattering function for electrons decreases to larger scattering angles (which is proportional to $1/\sin^4 \theta$). This decrease in intensity can be compensated by rotating sectors or photographic dodging.

3.B.IV ESCA OR XPS :

The pervasive use of X - ray photoelectron spectroscopy as an analytical tool[29] stems from its ability to detect chemical shifts of a fraction of an electron volt in core electron binding energies of upto 1500 eV. The reproducibility of binding energies measurements on a given instrument is usually within 0.1 eV, which is sufficient for most of the chemical shift measurements.

XPS, (Originated in the laboratories of K.Siegbahn[30], who gave the acronym 'ESCA'), has been established as an analytical technique in many different areas of materials science. Over the last few years high reliability and greater resolution have been achieved on this technique by improving the vacuum capabilities, analyser sensitivity, energy resolution, sample handling and data acquisition. For a broad materials science application, combined use of XPS and AES (Auger Electron Spectroscopy), on a given problem, usually provides most of the analytical information desired.

3.B.IV.a Basic principles of XPS :

XPS is a photoemission process using a monochromatic beam of soft X-rays. The specimen under ultra-high vacuum (UHV) conditions is irradiated with soft X-rays from either an Al K_α (1486.6 eV) or Mg K_α (1253.6 eV) source. These sources have a natural width at half-maximum of about 0.9 eV and 0.8 eV respectively. If the photon energy $h\nu$, exceeds the binding energy E_B of a core electron, it may be absorbed by the electron, which is then excited into an available state above the Fermi

energy. If the energy of the ejected core electron exceeds the work function of the sample, it may be emitted into the vacuum. The XPS experiment comprises of determining the kinetic energies of these photoelectrons. In an XPS instrument the basic requirements are briefly described as follows. They include

(1) the UHV chamber, with an efficient sample load-lock system,

(2) the twin anode Mg / Al source, and

(3) the hemispherical electron energy analyser, focusing lens system and electron detector.

For photons with energy $h\nu$, interacting with an electron with binding energy E_B, the ejected electron kinetic energy is given by[29]

$$E_k = h\nu - E_B - \Phi_{anlsr} \qquad \ldots (3.28)$$

where E_k is the photoemitted electron kinetic energy (relative to the Fermi level), and Φ_{anlsr} is the work function of the analyser. For a fixed photon energy, the measured kinetic energies give an absolute measure of the core level binding energies, E_B, which allow atomic identification.

No two elements have the same set of binding energies and analysis of multiple core levels can usually give unequivocal atomic identification[31]. Furthermore, the escaping photoelectron kinetic energy is also determined by the initial state, on the atom from which it originated. Changes in oxidation state of the atom concerned give rise to 'chemical shifts' in the kinetic energy and thus binding energy. Such chemical shifts can be used to identify the various oxidation states of surface atoms, and

these usually appear in the range 0.1 to 10 eV. Accordingly, XPS provides both compositional and chemical information.

3.B.IV.b Sample Preparation :

Samples with a few mm^2 of minimum area are located at the focus of the X-ray electrostatic lens system by means of vacuum load-lock arrangement. Routinely they are fixed in position with double-sided adhesive tape or attached by means of clamps. Irradiation usually causes charging (0 - 10 eV) of the samples. In the case of conducting samples this can be greatly reduced by providing proper earthing, with the aid of conducting silver pastes. For non-conducting specimens the obtained binding energies are to be corrected, with reference to Carbon (1s) level at 284.8 eV to get the correct binding energies.

3.B.IV.c **Quantitative Analysis.**

For constant incident X-ray flux, the photoelectron current is given by.

$$I = K N \sigma \lambda T \qquad \ldots (3.29)$$

where I,photocurrent for a given peak, K,a constant, N,density of atoms in analysed layer, σ ,photoelectron cross section, λ,escape depths or mean free path and T,spectrometer transmission function.

For the present analyser, since the transmission function T is proportional to the square root of the kinetic energy of the photoelectron, $\sqrt{KE}$, the relative atomic concentrations can be found out from[32,33]

$$\frac{N_A}{N_B} = \frac{I_A}{I_B} \cdot \frac{\sigma_B}{\sigma_A} \cdot \frac{\sqrt{KE_B}}{\sqrt{KE_A}} \cdot \frac{\lambda_B}{\lambda_A} \qquad \ldots (3.30)$$

where, I is the intensity of the photoelectron signal, σ is the theoretical cross section[34], KE is the kinetic energy of the electrons and λ is its mean free path[35]. For repeated routine determinations the last three terms can be substituted by finding out a sensitivity factor for the instrument, for a material under consideration.

The accuracy of XPS, for the usual quantitative determination is reasonable when appropriate reference standards are used. In absolute terms, the detection limit for any one element, relative to another depends on the relative cross sections but an estimate of 0.1 wt% for the average case can be made. But XPS is not suitable for trace elemental analysis as the sensitivity is limited, because of the analysis of a small detected volume from the emitted photoelectrons.

Estimation of photoelectron intensity I, from peak heights are usually not desirable, due to the possibility of variation in half-widths, especially for polycrystalline materials[36]. But satisfactory results can be obtained by a computer integration of peak areas, and comparing with a standard composition. When comparing XPS with AES, XPS has the advantage that the theoretical cross sections are available, although the overall accuracy of quantitative analysis from either technique is comparable.

3.B.V. Chemical methods for Composition analysis:

3.B.V.a Physical and Chemical methods: General Aspects.

Methods for compositional analysis can be broadly classified in two heads__ physical and chemical. Because of the distinct advantage of each over the other, both of these are widely used in compositional analysis. But whenever there is a need for an accurate analysis, chemical methods are found to be suitable and give excellent results. On the other hand physical methods are preferable, to provide a quick analysis for thin films and enjoys the distinct advantage as a non-destructive method.

The Physical methods for compositional analysis are usually matrix-dependent. In these a standard is always necessary either to compare or to correct the instrumental parameters. But often the nonavailability of suitable standard is a problem. In addition to that frequently difficulties are encountered by the matrix interference.

In this context, chemical methods possess unique advantage of high reliability in stoichiometric analysis. Apart from this, the requirement of standards for comparison or calibration can almost be avoided in most cases. In chemical methods it is possible that the interference effects resulting from matrix and coexisting elements can be suppressed and/or separated through suitable chemical treatment steps.

Classical wet chemical techniques based on gravimetry, titrimetry and electrochemistry are most commonly used for major

Table 3.1

Sensitivity of some important Analytical Techniques.

Technique	Applications	Sensitivity	Precision
Gravimetry	Major- and minor- phase concentration	1- 10 mg	0.1%
Titrimetry	Concentration, also	10^{-5} M in soln.	0.1%
	impurities	10^{-6} -10^{-7} M in soln.	0.2- 1.0%
Coulometry	Major-phase concen.	--	0.001- 0.005%
X-ray fluorescence	Consituents	20- 200 ppm	0.1- 0.5%
Spectrophotometry	Impurities	10- 100 ppm in soln.	1- 5%
Spectrofluorometry	Impurities	0.1- 10 ppm in soln.	0.5- 5%

element analyses and stoichiometry[37]. Of these the most precise determination of elemental analysis is based on the electrochemical method _ constant current coulometry. In this method a reliability of 0.001 - 0.01% can easily be achieved.

Among the instrumental methods for an accurate determination of stoichiometry the fluorescence methods are suitable and are characterised with a high detection sensitivity. In these methods an accuracy of ± 0.1% is obtainable when calibrated with suitable standards. Table 3.1 precisely illustrates the application and sensitivity of some of the above methods.

3.B.V.1 Compositional Analysis of Indium-Selenium Compounds

The method of analysis of indium-selenium compounds is based on estimating one of the component of the film, and by a prior knowledge of the total weight of the film, its composition is found out. Usually, as the estimation of selenium yields better results it is selected for the estimations in the current investigations. For this, first of all, the weight of the film has to be found out accurately. Then the film is dissolved in concentrated HNO_3 with a little amount of concentrated HCl. The dissolved film is then estimated for the amount of selenium and from this the amount of indium is found out.

Different methods tried for estimating selenium are given below:

3.B.V.1.a Titrimetric Methods :

The first method we tried is titrimetry, following the

procedure given by Vogel[38].

Classical wet chemical technique, titrimetry is based on the amount of a standard solution consumed in a reaction. Normally they are used for determination at a precision of ± 0.1%. and with refinements in analytical techniques can be further extended to ± 0.01%.

For the estimation, the film is dissolved in concentrated acid, to form selenious acid as described above. Since permanganate easily oxidises selenious acid, the amount of selenium can be found out by titration. The reproducibility of this method was found to be very weak. This made us to try other methods as given below.

3.B.V.1.b **Iodometric Methods**

1. By Hydrochloric Acid Reduction :

With a reasonable excess of KI solution, iodine is liberated according to

$$H_2SeO_3 + 4\ HCl + 4\ KI \rightarrow Se + 2\ I_2 + 4KCl + 3\ H_2O.$$

The liberated iodine is found out by titrating with standard thiosulphate solution, and the equivalence is Se ≡ 4I. This method has the clear advantage of requiring only one standard solution. But one drawback is that the precipitated red selenium formed in this reaction poses difficulties in determining the starch-iodide end point. Additionally, the precipitated selenium tends to occlude some iodine, but in the present case since low concentration of selenium is involved this difficulty was expected to be minimal.

But this procedure also, was found to be not reproducible always. So this estimation is tried in another fashion.

2. By Excess Thiosulphate Method :

Selenious acid is reduced by an excess of sodium thiosulphate solution[38]

$$H_2SeO_3 + 4\ Na_2S_2O_3 + 4\ HCl \longrightarrow Na_2SeS_4O_6 + Na_2S_4O_6 + 4\ NaCl + 3\ H_2O$$

The excess $Na_2S_2O_3$ is then back-titrated in the usual way with standard iodine solution.

$$2Na_2S_2O_3 + I_2 \longrightarrow Na_2S_4O_6 + 2\ NaI$$

Therefore 1 ml. 0.1 N $Na_2S_2O_3$ ≃ 1 ml. 0.1N iodine ≃ 0.001974 gm. selenium. This determination is done at room temperature in a solution containing 10-20% hydrochloric acid. The conventional starch - iodide end point is used.

This method also was tried, but failed to give good results as the HNO_3 used for dissolving the InSe film was found to interfere.

3.B.V.2 Spectrofluorimetric Method :

As indicated above fluorimetric method is one of the most sensitive among the methods for the estimation of Se. For this a reliable fluorimetric reagent for determining selenium is 2, 3 - diaminonaphathalene (DAN). The sensitivity of DAN in the determination of Se is in the nanogram range of 0.002 µg Se. This organic compound for the determination of selenium was introduced

by Parker and Harvey[39]. The reagent forms a bright red, extremely fluorescent 4, 5 - benzopiazselenole,

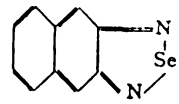

when reacted with selenium (in the form of selenous acid). The formed 4,5- benzopiazselenole can be extracted with cyclohexane or dekalin (mixture of Decahydronaphthalene with less than 0.01% tetralin) or with toluene. Depending upon the solvent, the piazselenole shows a slight shift in the position of the florescence maximum. The compound displays a brilliant lime-green fluorescence (i.e. 521 nm) when excited at 366 nm in either cyclohexane or dekalin. In toluene the fluorescence maximum occurs at 540 nm with an exciting wavelength 390 nm.

Detailed procedure for the estimation of Se using DAN is discussed in Chapter 4.

3.B.VI Determination of Optical constant, n.

Several methods for evaluating the optical parameters characterising thin films can be seen in literature. Among these methods, the most widely used method for obtaining optical constant, n is by measuring both transmission and reflection spectra. But these involves tedious calculations, entailing iterative procedures and thus often non-systematical. Recently Manifacier et al[40] gave a relatively simple method for calculating the optical constants of non-absorbing thin films on

non-absorbing substrates. In spite of its simplicity there are more practical disadvantages to this method. The most significant among them is that the average oscillatory transmittance normally slope down to zero with increasing film absorption, especially near the band-edge absorption region. So often this causes to impart the optical constants of a very narrow region. So, in order to obtain the optical constants a relatively simple method described by Ohlidal et al[41] is used in the present work.

In this method the spectral dependences of the reflectances of the film are used to determine the thickness and spectral dependence of the optical constant n. This is due to the fact that, in the process of multiple interference the amplitude of the reflected beams are contributed from both the reflection and transmission coefficients. Owing to this, reflection measurements can also provide information similar to transmission measurements. One advantage of using reflectance spectra is that, the oscillatory reflectance does not slope down to zero with increasing film absorption. Accordingly, the reflectance extrema can be better located and analysed. Further the reflection measurements can be made independent of the substrate surface and its flatness. The optical parameters of films on higher absorbing substrates can also be measured using reflectance spectra.

3.B.VI.a Theory

When a parallel beam of monochromatic light falls on the film (Fig.3.20) the reflectances R and R' can be expressed as[41]

$$R = \frac{r_1^2 + r_2^2U^2 + 2r_1r_2U \cos x_1}{1 + r_1^2r_2^2U^2 + 2r_1r_2U \cos x_1} \qquad \ldots (3.31)$$

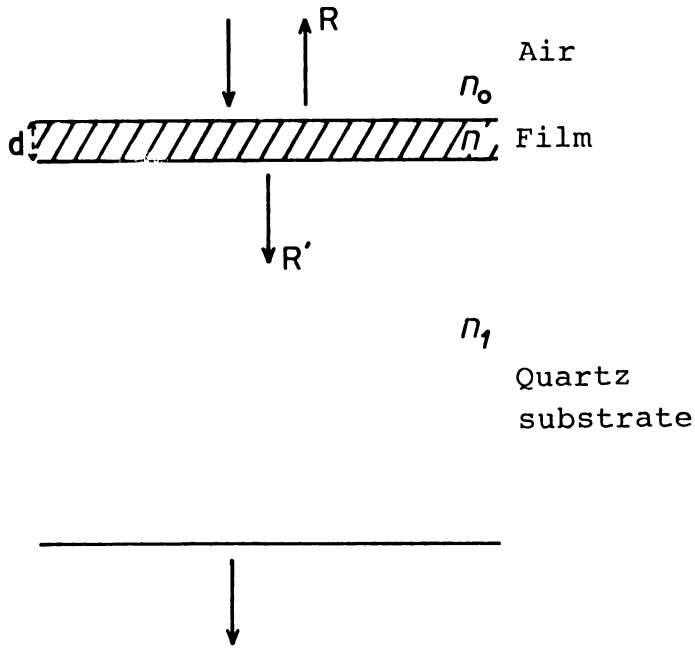

Fig.3.20 Schematic representation of the occurrence of reflectance by a thin film.

$$R' = \frac{r_2^2 + r_1^2U^2 + 2r_1r_2U \cos x_1}{1 + r_1^2r_2^2U^2 + 2r_1r_2U \cos x_1} \quad \ldots (3.32)$$

Hence, $$r_1^2 = \frac{(1-n)^2 + k^2}{(1+n)^2 + k^2} \quad \ldots (3.33a)$$

$$r_2^2 = \frac{(n-n_1)^2 + k^2}{(n+n_1)^2 + k^2} \quad \ldots (3.33b)$$

$$U = \exp\,[-(4\pi / \lambda)kd] \quad \ldots (3.34a),$$

and

$$x_1 = (4\pi / \lambda)nd \quad \ldots (3.34b)$$

where R is the ambient side reflectance, R', the substrate side reflectance, n, refractive index of the film, n_1,refractive index of the substrate, k, the absorption index of the film, d, the thickness of the film and λ the wavelength.

For weakly absorbing films

$$(1-n)^2 >> k^2 \quad \text{and} \quad (n-n_1)^2 >> k^2$$

So this follows that

$$r_1^2 = \frac{(1-n)^2}{(1+n)^2} \quad \ldots (3.35a)$$

$$r_2^2 = \frac{(n-n_1)^2}{(n+n_1)^2} \quad \ldots (3.35b)$$

If the film is sufficiently thick several interference extrema exist by reflection. Then envelopes of these extrema can be constructed. The envelopes of the maxima exist at wavelengths obeying the equation.

$$nd = (2m-1)\ (\lambda_{ex}/4) \qquad \ldots (3.36)$$

The values of the envelope of extrema R_{ex} and R'_{ex} for odd interference order are given by

$$R_{ex} = (r_1 - Ur_2)^2/(1 - r_1r_2U)^2 \qquad \ldots (3.37)$$

$$R'_{ex} = (r_2 - Ur_1)^2/(1 - r_1r_2U)^2 \qquad \ldots (3.38)$$

Solving equation (3.37) and (3.38) for n, we have

$$n = n_1 \left| \frac{n_1 - 1 \mp R_{ex}^{1/2} \pm R'^{1/2}_{ex} n_1}{n_1 - 1 \pm R'^{1/2}_{ex} \mp R_{ex}^{1/2} n_1} \right|^{1/2} \qquad \ldots (3.39)$$

Thus the value of n can be determined. The thickness can be determined from equation (3.36) by giving suitable value of $m = 1, 2, 3 \ldots$, or more easily by using the positions of the adjacent maxima of the maximum envelope

$$2n(\lambda_1)d = (2l - 1)\ \lambda_1/2 \qquad \ldots (3.40)$$

$$2n(\lambda_2)d = (2l + 1)\ \lambda_2/2 \qquad \ldots (3.41)$$

Hence

$$d = \frac{1}{2} \cdot \frac{\lambda_1 \lambda_2}{\lambda_1 n(\lambda_2) - \lambda_2 n(\lambda_1)} \qquad \ldots (3.42)$$

where $n(\lambda_1)$ and $n(\lambda_2)$ denote the refractive indices of the

film at the wavelengths λ_1 and λ_2 respectively. Usually for calculations the higher wavelength is always taken as λ_1.

Thus the value of refractive index,n and film thickness,d can be determined.

References:

1. A.Roth, 'Vacuum technology', North-Holland, Amsterdam (1976).
2. L.G.Carpenter, 'Vacuum Technology', Adam Hilger, London (1970).
3. R.Glang, R.A.Holmwood and J.A.Kurtz, High-Vacuum Technology in L.I.Maissel and R.Glang (Eds.), 'Handbook of thin film Technology', McGraw-Hill, New York (1983).
4. A.Guthrie, 'Vacuum Technology', John Wiley, New York (1963).
5. G.Lewin, 'Fundamentals of Vacuum Science & Technology', McGraw-Hill, New York (1965).
6. A.H.Turnbull, R.S.Barton and J.C.Riviere, 'An Introduction to Vacuum Technique', George Newnes, London (1962).
7. H.A.Steinherz, 'High Vacuum Engineering', Reinhold, New York (1963).
8. J.E.Warren, 'Control instruments mechanisms', W.Fouesham, England, (1967).
9. W.F.Coxon, 'Temperature measurement and control', Heywood, London (1960).
10. M.Kutz, 'Temperature control', Academic Press, New York (1968).
11. W.K.Roots, 'Fundamentals of temperature control', Academic Press, New York (1969).
12. L.B.Valdes, Proc.IRE, **42**, 420 (1954).
13. M.A.Logan, Bell System Tech.J., **40**, 885 (1961).
14. L.J.Van der Pauw, Philips Res.Repts., 13, 1 (1958).
15. E.H.Sondheimer, Phys.Rev., 80, 401 (1950).

16. E.H.Putley, 'The Hall Effect and Related Phenomena', Butterworths, London (1960).

17. W.Shockley, 'Electrons and Holes in Semiconductors', D.Van Nostrand, New Jersey (1950).

18. R.W.Berry, P.M.Hall and M.T.Harris, 'Thin film Technology', D.Van Nostrand, New Jersey (1968).

19. G.Airy, Math.Tracts, 381 (1831).

20. S.Tolansky, 'Multiple-Beam Interferometry of Surfaces and Films', Dover, New York (1970).

21. G.Z.Sauerbrey, Phys.Verhandl., 8, 113 (1957).

22. G.Z.Sauerbrey, Z.Physik, **155**, 206 (1959).

23. W.P.Mason, 'Piezoelectric Cryatals and Their Applications in Ultrasonics', Van Nostrand, New York (1956).

24. R.A.Heising, 'Quartz Crystals for Electrical Circuits', Van Nostrand, New York (1946).

25. F.P.Phelps, Proc.11th Annual Symposium on Frequency Control, Fort Monmouth, New Jersey (1957).

26. K.H.Behrndt, Vacuum Sympos.Trans.,1959,Pergamon Press, London (1960).

27. R.P.Riegert, 'Proc.4th Intern. Vacuum Congr., 1968', The Institute of Physics and the Physical Society, London.

28. S.Amelinckx, R.Gevers and J.Van Landuyt (Eds.), 'Diffraction and Imaging Techniques in Material Science' Vol.II, North-Holland, Amsterdam (1978).

29. D.Briggs and M.P.Seah (Eds.), 'Practical Surface Analysis by Auger and X-ray Photoelectron spectroscopy', John Wiley & Sons, Chichester (1983).

30. K.Siegbahn, C.N.Nord 'man, R.Nordberg, K.Hamrin, J.Hedman, G.Johansson, T.Bergmark, S.E.Karlsson, I.Lindgren and B.Lindberg, 'ESCA- Atomic, Molecular and Solid State Structure studied by means of Electron spectroscopy', Almqvist and Wiksells Boktrykkeri AB, Uppsala, Sweden, 1967.
31. J.C.Riviere, 'Surface analysis of High temperature materials: Chemistry and Topography', G.Kemeny (Ed.), Elsevier, 1984.
32. D.R.Penn, J.Elect.Spect.Rel.Phenom., 9, 29 (1976).
33. A.W.C.Lin, N.R.Armstrong and T.Kuwana, Anal.Chem., **49**, 1228 (1977).
34. J.H.Scofield, J.Elect.Spect.Rel.Phenom., 8, 129 (1976).
35. R.J.Thorn, J.Elect.Spect.Rel.Phenom., 31, 207 (1983).
36. C.N.Sayers and N.R.Armstrong, Surface Science, 77, 301 (1978)
37. R.A.Laudise, 'Analytical Chemistry: Key to Progress on National Problems', NBS Special Publication 351, 19 (1972), US Department of Commerce, National Bureau of Standards, Washington.
38. A.I.Vogel, 'A Text-book of Quantitative Inorganic analysis', 3rd Edn., Longmans Green, London (1962).
39. C.A.Parker and L.G.Harvey, Analyst, 87, 558 (1962).
40. J.C.Manifacier, J.Gasiot and J.P.Fillard, J.Phys. E, 9, 1002 (1976).
41. I.Ohlidal, K.Navratil and E.Schmidt, Appl.Phys., **A 29**, 157 (1982).

SINGLE-PHASE STOICHIOMETRIC THIN FILMS OF InSe - PREPARATION AND CHARACTERISATION.

Abstract:

Formation of crystalline, monophasic Indium selenide (InSe) thin solid films by elemental evaporation onto hot substrates is discussed in this chapter. The compound formation as well as the composition of the formed films are verified by XPS (X - ray photoelectron spectroscopy) analysis. The composition is further confirmed by spectrofluorimetric method. Dependence of film crystallinity and composition on substrate temperature are analysed. The prepared films are characterised for its structural, electrical, optical, and photoconductive properties. Schottky junctions with Au are also formed on these InSe thin films and analysed for its photoelectronic behaviour.

4.I. Introduction

Indium monoselenide (InSe) is a semiconducting layered compound. In recent years much interest has been shown in this compound since it exhibits good photoelectric properties[1-14] and can be used as an active media for the generation of visible and near-infrared radiation. In the form of heterodiode it is expected to provide photovoltaic devices with high quantum efficiencies in the near -IR wavelength region, which is promising for optical fibre communication systems.

4.I.A. Statement of Problem

Although research literature gives a large number of reports about the various structural as well as physical aspects of InSe single crystals, very little is reported about the properties of these in the form of thin solid films. The main difficulty encountered in the preparation of this compound thin film is the coexistence of other phases such as In_4Se_3, In_2Se_3 and In_6Se_7[7,15,16].

Probably due to the easiness of preparation flash evaporation is preferred in the formation of a compound thin film. In the case of InSe also, the situation is the same and most of the reported work have been carried out on films prepared by flash evaporation[17-22]. One of the main disadvantage in using this method lies in the fact that it imposes some constraint on substrate temperature due to the escape of the easily fugitive

selenium. In this context the elemental evaporation seems to be a potentially useful method for growing stoichiometric epitaxial thin films of this compound. However, in the case of InSe, only a few reports have appeared in this direction of elemental evaporation.

In this chapter, the method of elemental evaporation for the preparation of InSe thin films and their characterisation using different techniques are discussed. Photoconductivity of the films over a wide wavelength range was measured and the involved mechanism is discussed in detail. In addition, an analysis of the pertinent characteristics of the fabricated schottky junctions are also discussed.

4.II. Experimental Details: Elemental evaporation.

In experimental practice for the preparation of InSe films by elemental evaporation, the main difficulty encountered is in the control of the evaporation rate of source materials : indium and selenium. Moreover the narrowness of formation range of InSe in the phase-diagram of In-Se (please see Chapter 1.B) leads to different stoichiometric compounds in a single deposition. Again, any temperature above an optimum temperature for getting a good crystalline film, results in the escape of selenium from the stoichiometric InSe films.

For the formation of the films the source materials were separate charges of 99.999% pure indium and selenium from Koch-light, UK and John Baker Inc., Colorado, respectively. Indium was

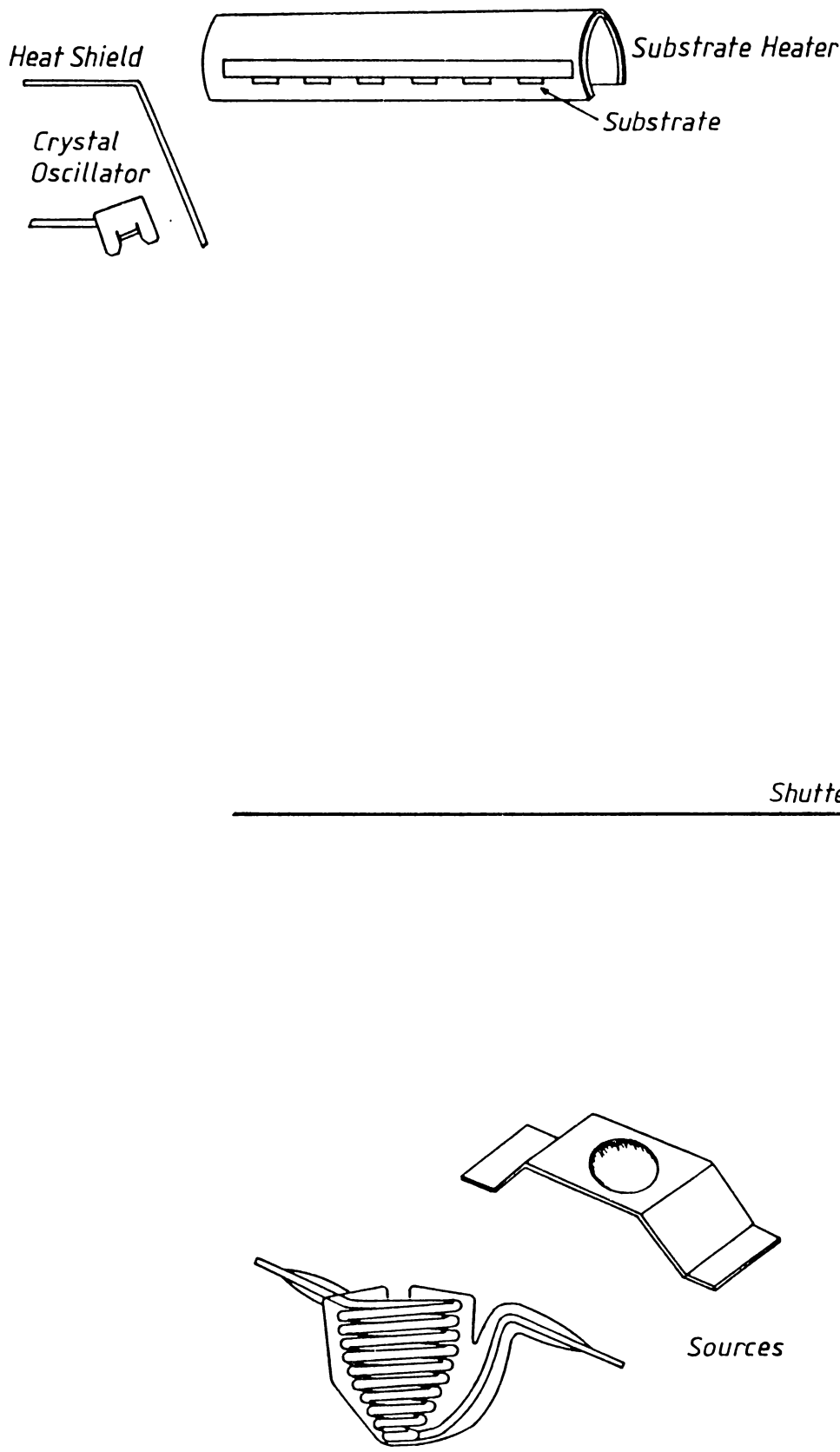

Fig.4.1 Schematic diagram of the co-evaporation source arrangement.

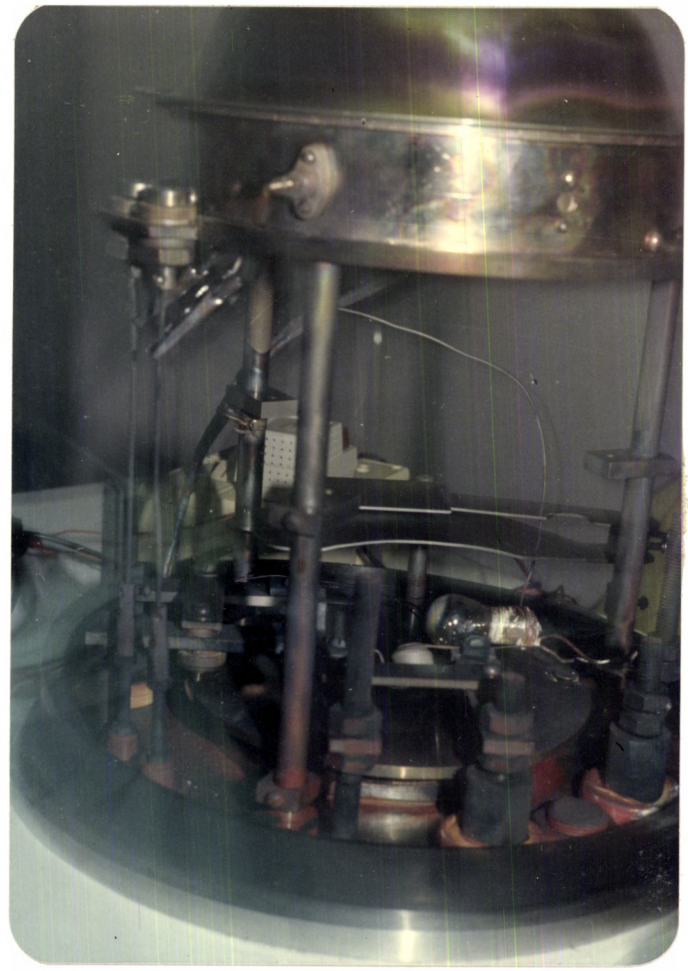

Fig.4.2 Photograph of the co-evaporation chamber.

evaporated from a molybdenum crucible and selenium from an alumina-coated tungsten Knudsen cell (Fig. 4.1). The Knudsen cell has a dimension of 1.8 x 1.8 x 1.7 cm^3, with an orifice diameter, and length of 6 mm. and 5 mm. respectively. The molybdenum crucible for indium evaporation has a hemispherically shaped dimple of 4.5 mm. radius. In the elemental evaporation, the prime importance in growing a stoichiometric film rests on controlling how precisely the supply rate of the individual components of the source materials. Since an easy-sublimating material like selenium is involved in the formation of the film, the control of evaporation needs additional attention. For this apart from selecting the suitable geometries for the sources (photograph of the arrangement is shown in fig.4.2), for the precise control of the source temperatures of selenium and indium during evaporation, we used a programmable controller fabricated for this purpose (please see Chapter 3). Cooled quartz crystal monitors are used to monitor the rate of deposition and thickness of the deposits, and the evaporation rate from the sources was relatively controlled in such a way as to achieve the desired stoichiometry and film thickness[23]. The thickness of the films obtained was counterchecked by Fizeau interference fringe technique.

4.II.A Film Formation.

4.II.A.1 Substrate cleaning

Substrate cleanliness is an important factor that influence on the initial growth of the film and the existance of pinholes. Consequently a perfectly cleaned substrate is of vital importance

for the development of high quality films.

The standard cleaning procedure adopted for this work involves a mechanical cleaning followed by a chemical treatment. Glass or fused quartz substrates were first washed with detergent and then rubbed with absorbent cotton containing a small amount of liquid soap. After rinsing in doubly distilled water it was chemically treated in chromic acid solution and then rinsed with deionised water. After this cleaning the substrates were put inside an ultrasonic bath containing isopropyl alcohol or trichloro ethylene and then flushed with distilled deionised water.

The samples were then kept inside a vapour degreasing chamber containing isopropyl alcohol or trichloro ethylene. The substrates remained inside the chamber until they were put inside the evaporator. Before positioning the substrates inside the vacuum evaporator they were dried by blowing with a jet of dry nitrogen. After loading the substrates inside the deposition chamber they were utimately cleaned in glow discharge, after evacuating the chamber to a pressure of 10^{-2} to 10^{-3} Torr.

4.II.A.2. Deposition of InSe film.

4.II.A.2.a Dependence of atomic fluxes on film formation.

At a fixed vacuum, the condensation of a vapour on a solid surface mainly depend on the incident atomic flux or fluxes and on substrate temperature. For a progressive condensation, the involed energies, are largely dependent on the kind of vapour and

on surface conditions. Moreover a continuous condensation of the vapour is possible only if the temperature of the substrate is below a critical temperature. Thus it has been found that a so-called 'stoichiometric interval' exists[24] for the reactive deposition of stoichiometric indium selenide in a narrow temperature range (Fig 4.3).

At first, flux rates from both selenium and indium sources were independently calibrated as a function of source temperature. For this purpose, selenium was evaporated from a Knudsen cell kept at the desired temperatures and the rates of deposition (time derivative of frequency shifts) were noted in the quartz crystal monitor. The rate of deposition was calibrated by measuring the thickness of the thin film deposited at a uniform rate for a fixed interval, on glass substrates kept side by side with the quartz oscillator in the deposition chamber. For obtaining the incident flux rate, the rate of deposition read directly at the quartz oscillator was multiplied with the ratio of density to molecular weight and converted it to the number of atoms[25]. With selenium source temperature in the range 410- 430, it was found to give a constant incident flux rate 2.5- 4.5x 10^{15} atoms cm^{-2} s^{-1}. The molecular complexity of Se in the vapour phase varies from Se_2, Se_3, Se_4, ... Thus, in order to avoid any confusion in the flux rate expressed, we prefered to use atoms cm^{-2} s^{-1}, instead of molecules cm^{-2} s^{-1} [26]. Our attempts to use source geometries other than Knudsen cell for Se failed to give a consistent Se flux rate with reproducibility. Using a Knudsen cell of the previously described dimensions and

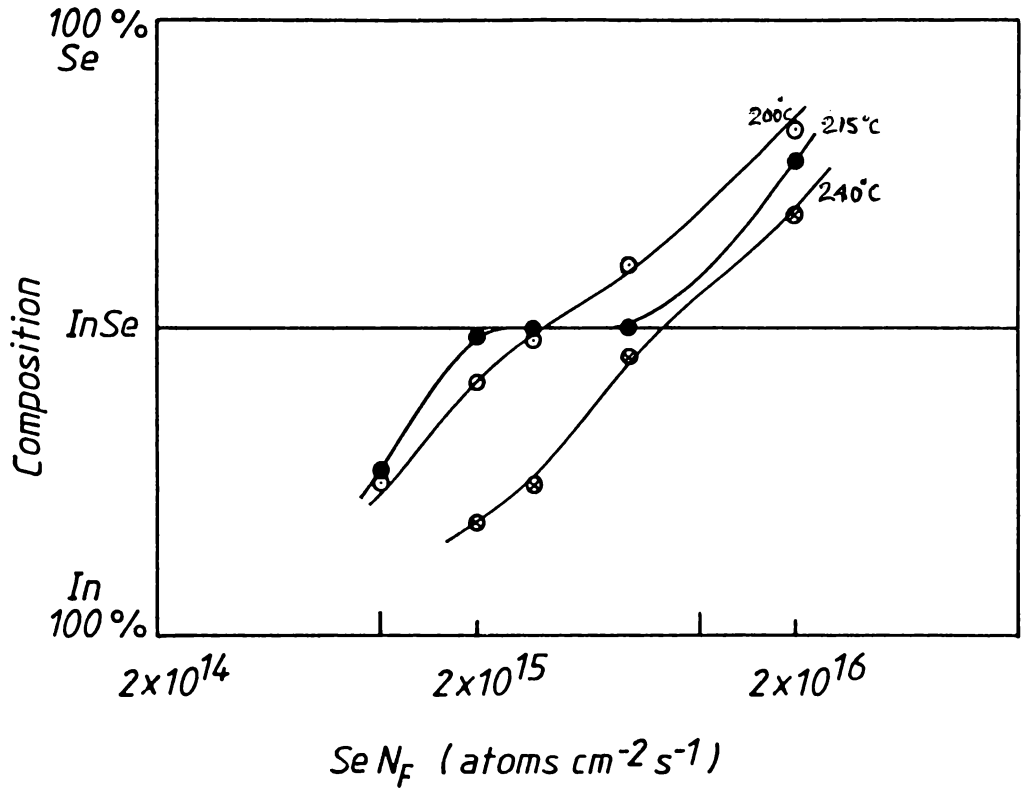

Fig.4.3 Dependence of atomic fluxes on film formation.

controlling the temperature accurately (within ±1 K),it was found to give an extremely reproducible flux rate which could be varied as a function of source temperature.

Following the above procedure, indium flux rate as a function of source temperature was also obtained. With the source temperature between 950- 1000 K, the indium flux rate was found to be between 1.5- 3.0×10^{15} atoms cm^{-2} s^{-1}.

4.II.A.2.b Deposition Procedure

To deposit a stoichiometric compound film, with a shutter located under the substrates (maintained at the desired temperature) the source temperatures of both Se and In were increased to get the fixed flux rates within the above specified source temperature ranges. When hot substrates were used, slightly higher values of Se flux rate were found beneficial due to the preferential re-evaporation of Se from the substrates.

The films were deposited on clean glass or quartz substrates kept at elevated temperatures. The substrate temperature during evaporation was varied between 400 to 528 K in the interval of approximately 20 K in different depositions. This was done in order to study the influence of substrate temperature on the film formation. The substrate temperature was measured using a flat-ended thermocouple placed on the substrate. The distance between the substrate and the evaporation source was normally about 15 cm. and thickness of the formed films was in the range of 500 to 8000 Å (unless otherwise stated) . Prior to all depositions the chamber was evacuated to an initial pressure

less than 1.5 x 10^{-6} Torr and after deposition the substrates were carefully cooled to achieve the desired stoichiometric single phase films. The substrate cooling rate was about 2K min^{-1} after the depositions.

4.II.A.2.c Comprehensive deposition procedure

After loading the substrates and source materials inside the vacuum chamber it was pumped down to a pressure of ~1.5 x 10^{-6} Torr utilising liquid nitrogen trap. After reaching the vacuum the substrates were heated to a temperature between 423 K and 528 K at a linear rate. The linear heating rate was specified in order to avoid any possible breakage to the substrate due to an over-stress caused at a fast non-linear heating cycle. After reaching the desired substrate temperature the deposition was started. Prior to that the sources were baked for a short time under shutter to remove any adsorbed gases present. The rate of increase of temperature of the sources can independently be set on the programmable control by thumb- wheel switches and the maximum temperature can also be set at any value by adjusting a variable potentiometer attached to the controller. This ensures the reproducibility in the rate of heating of the sources and the final maximum temperature. Further the rates of deposition were read on the quartz crystal monitors.

4.II.B Characterisation of the film.

4.II.B.1 Structural aspects

4.II.B.1.1 Calculation of X-ray powder patterns

For the calculation of the X-ray powder patterns a DEC-10

Table 4.1

Calculation of X-ray powder patterns for Gamma- InSe

```
A=  4.00200  C= 24.94600
WL= 1.54180

CALCULATION BETWEEN TL =  1.0 AND TH =  36.0 DEGREES THETA

DIFFRACTION GEOMETRY = DEBYE SCHERRER
SPACE GROUP     GIVEN ON SPCGRP -CARD R 3 M
HIGH LAUE SYMMETRY :  THERE IS NO SYMMETRY CENTRE AT THE ORIGIN

RHOMBOHEDRAL BRAVAIS LATTICE

CONDITIONS LIMITING POSSIBLE REFLECTIONS :- HKL WITH -H+K+L=3N ONLY

     NUMBER OF ATOMS IN UNIT CELL

    ELEMENT      NUMBER OCCUP=   NTOTAL
 IN  1      3.0*  1.000=   3.000
 IN  2     18.0*  1.000=  18.000
 SE  1     18.0*  1.000=  18.000
 SE  2     18.0*  1.000=  18.000

SCATTERING FACTOR COEFFICIENTS/
IN   19.1624  0.5476 18.5596  6.3776  4.2948 25.8499  2.0396 92.8029  4.9391
   NUMBER OF ELECTRONS=   49      (CALCULATED USING ABOVE COEFFICIENTS)
   DELFR= -0.126  DELFI=  5.045  (ANOMALOUS DISPERSION CORRECTION TERMS)

NUMBER OF ELECTRONS IN UNIT CELL   F(0,0,0)=    1029
SE   17.0006  2.4098  5.8196  0.2726  3.9731 15.2372  4.3543 43.8163  2.8409
   NUMBER OF ELECTRONS=   34      (CALCULATED USING ABOVE COEFFICIENTS)
   DELFR= -0.879  DELFI=  1.139  (ANOMALOUS DISPERSION CORRECTION TERMS)

NUMBER OF ELECTRONS IN UNIT CELL   F(0,0,0)=    2253

ATOM  POSITIONS:
ELEMENT   X/A       Y/B       Z/C     FMULT   OCCUP   BTEMP

IN  1  0.000000 0.000000 0.000000 0.1667  1.0000  0.000
IN  2  0.111000 0.111000 0.111100 1.0000  1.0000  0.000
SE  1  0.828300 0.828400 0.828600 1.0000  1.0000  0.000
SE  2  0.616700 0.616700 0.616900 1.0000  1.0000  0.000
```

- T A B U L A R L I S T OF INTENSITIES FOLLOWS -

H	K	L	THETA	2THETA	D	SIN2	H	K	L	INTENS	F+(HKL)	F-(HKL)	PHA+	PHA-	MULT	LPG
0	0	3	5.3	10.6	8.3153	8.6	0	0	3	932.3	649.0	582.0	153.8	-141.3	2	114.86
0	0	6	10.7	21.4	4.1577	34.4	0	0	6	1000.0	1325.3	1277.4	-81.3	90.1	2	27.64
1	0	1	13.0	26.0	3.4329	50.4	1	0	1	890.4	847.1	890.3	18.1	-6.3	6	18.40
0	1	2	13.3	26.7	3.3393	53.3	0	1	2	93.2	299.1	279.9	92.3	-66.8	6	17.34
1	0	4	14.7	29.5	3.0295	64.8	1	0	4	466.2	706.4	733.3	141.8	-130.8	6	14.03
0	1	5	15.7	31.4	2.8464	73.3	0	1	5	89.3	320.6	353.6	-169.8	-172.4	6	12.24
0	0	9	16.1	32.3	2.7718	77.4	0	0	9	2.6	80.5	119.8	151.3	127.6	2	11.54
1	0	7	18.1	36.2	2.4846	96.3	1	0	7	595.4	1014.2	1015.1	-64.3	75.3	6	9.03
0	1	8	19.4	38.8	2.3181	110.6	0	1	8	202.0	611.2	667.0	-55.1	69.4	6	7.70
0	0	12	21.8	43.5	2.0788	137.5	0	0	12	63.5	698.6	711.8	111.3	-97.1	2	5.97
1	0	10	22.4	44.8	2.0247	145.0	1	0	10	191.2	747.7	710.5	59.3	-45.2	6	5.61
1	1	0	22.7	45.3	2.0010	148.4	1	1	0	42.2	347.6	347.6	10.0	10.0	6	5.46
1	1	3	23.3	46.7	1.9455	157.0	1	1	3	98.8	556.8	542.5	122.9	-111.3	6	5.10
1	1	-3	23.3	46.7	1.9455	157.0	1	1	-3	98.8	542.5	556.8	-111.3	122.9	6	5.10
0	1	11	24.0	47.9	1.8977	165.0	0	1	11	241.1	879.6	890.5	69.5	-57.2	6	4.80
1	1	6	25.3	50.6	1.8030	182.8	1	1	6	5.9	161.0	133.0	-63.1	89.8	6	4.24
1	1	-6	25.3	50.6	1.8030	182.8	1	1	-6	5.9	133.0	161.0	89.8	-63.1	6	4.24
0	2	1	26.5	53.0	1.7288	198.9	0	2	1	10.8	206.3	213.4	36.1	-11.3	6	3.83
2	0	2	26.7	53.4	1.7164	201.7	2	0	2	57.0	490.3	482.5	74.9	-62.1	6	3.76
1	0	13	27.3	54.7	1.6788	210.9	1	0	13	41.6	451.1	401.7	-160.7	175.4	6	3.56
0	2	4	27.5	55.0	1.6697	213.2	0	2	4	24.8	335.4	328.7	165.7	-153.8	6	3.51
0	0	15	27.6	55.2	1.6631	214.9	0	0	15	25.2	527.2	633.4	-180.0	-171.1	2	3.48
2	0	5	28.1	56.2	1.6370	221.8	2	0	5	0.3	41.8	36.0	-110.8	170.7	6	3.35
1	1	9	28.4	56.7	1.6224	225.8	1	1	9	69.8	582.4	571.2	14.5	0.1	6	3.27
1	1	-9	28.4	56.7	1.6224	225.8	1	1	-9	69.8	571.2	582.4	0.1	14.5	6	3.27
0	1	14	29.1	58.2	1.5847	236.7	0	1	14	73.4	610.5	607.2	-146.2	159.9	6	3.09
0	2	7	29.6	59.3	1.5584	244.7	0	2	7	3.4	137.5	131.1	-39.2	71.1	6	2.96
2	0	8	30.6	61.2	1.5147	259.0	2	0	8	45.3	507.6	503.5	-19.1	33.1	6	2.76
1	1	12	32.3	64.7	1.4417	285.9	1	1	12	6.7	183.0	229.2	62.9	-45.6	6	2.45
1	1	-12	32.3	64.7	1.4417	285.9	1	1	-12	6.7	229.2	183.0	-45.6	62.9	6	2.45
0	2	10	32.8	65.6	1.4232	293.4	0	2	10	33.0	470.6	460.6	45.0	-30.2	6	2.37
1	0	16	32.8	65.7	1.4219	293.9	1	0	16	8.0	240.6	216.8	-40.6	73.1	6	2.37
0	0	18	33.8	67.6	1.3859	309.4	0	0	18	76.6	1271.1	1267.0	7.9	4.7	2	2.23
2	0	11	34.0	68.1	1.3769	313.5	2	0	11	5.0	172.2	202.8	42.3	-19.8	6	2.19
0	1	17	34.8	69.6	1.3513	325.5	0	1	17	73.0	756.2	717.4	-7.0	22.0	6	2.10

- G R A P H I C R E P R E S E N T A T I O N OF THE POWDER PATTERN OMITTED -

computer version of a program, (developed at the University of Geneve, Switzerland) has been made use of. This program was written for calculating the theoretical powder patterns from a strictest minimum of input information. This is accomplished by deriving all symmetry parameters such as general equivalent positions from the Hermann-Mauguin space-group symbols, by calculating automatically the multiplicities of special positions, and by calling the necessary constants, such as scattering factor tables, anomalous dispersion correction terms and X-ray wavelengths corresponding to different sources from the data files in the program. A typical calculation for rhombohedral τ-InSe is given in Table 4.1.

4.II.B.1.2 X-ray Diffraction(XRD)

To obtain the features related to the crystallinity of the grown films the X-ray diffraction (XRD) method was made use of. From the obtained spectra it is possible to determine the crystalline nature and to identify the phases that were present in the films. The X-ray diffraction equipment used was a Philips 1070/76 apparatus with monochromatized Cu K_α radiation. The X-ray tube was operated normally at 30kV and at a current of 20mA. The specimens used were having an area 2 cm^2, and the beam was scanned for 2θ in the range 5^o and 70^o.

4.II.B.1.3 Transmission Electron Microscopy(TEM) observations.

The present investigations made use of a Philips EM 301 transmission electron microscope. For that the sample preparation is as follows. The films were first removed from the

quartz substrates using 40% HCl and immediately diluting it with distilled water and then, the floated films were carefully removed onto the grid. The accelerating voltage was 80 kV and the magnification was kept in between 2000x and 6000x . The film thickness used for this purpose was always less than 1000 Å.

4.II.B.2 Compositional Aspects.

4.II.B.2.1 XPS studies

In order to confirm the compound formation we performed ESCA (XPS) measurements using a Vacuum Generators(VG) Escalab spectrometer with a 180° hemispherical electrostatic analyser. The ESCA spectra of the samples were recorded using Mg K_α radiation, over the characteristic kinetic energy range investigated. The residual vacuum in the analysis chamber was typically 10^{-8} Torr.

Samples with a minimum of 8mm x 8mm area were located at the focus of the X-ray electrostatic lens system by means of vacuum load-lock arrangement. They were fixed in position with double-sided adhesive tape or attached by means of clamps. Charging of the samples, when they were exposed to the radiations, was considerably reduced by giving proper earthing with the help of conducting silver pastes. Again the obtained core orbital binding energies were referred to the residual oil vapour contamination Carbon (1s) peak taken at 284.8 eV to get the exact binding energies. The reproducibility of the results was ±0.1 eV.

For quantitative analysis, data acquisition and peak area integration were performed by an attached computer. The spectra were corrected for background emission, and the charge broadening was accounted by comparing it with single crystal FWHM's. The composition of the films was calculated[27,28], making use of the theoretical photo-ionization cross-sections[29] and the mean-free path of electrons[30] for the observed kinetic energies.

4.II.B.2.2 Chemical Analysis.

For the chemical analysis the common method adopted to prepare a solution of the film is as follows. The film was at first weighed using an accurate microbalance. It was then dissolved in a known quantity of 10 M HCl (typically 5 ml) containing a minimum amount of 10 M HNO_3 (typically 3 ml) by heating gently to convert it to selenious acid. Excess of nitric acid was removed by repeated evaporation on a water-bath with dilute HCl under reflux. These solution containing selenium was then diluted to give the required stock solution. In all these, the reagents used were of analytical grade. But in the case of HNO_3 it was distilled before use.

4.II.B.2.2.1.By Hydrochloric acid reduction

Excess of 0.1 N KI was added by shaking well to the known amount of test solution till the liberation of iodine was stopped. Then the amount of the iodine formed was found out by titrating with standard thiosulphate solution (See also Chap.3). As the end-point was approached, a few drops of dilute starch

solution was added. The change from blue to colourless solution gave the indication of the end-point.

4.II.B.2.2.2.By Excess thiosulphate method.

0.1 N Sodium thiosulphate was added in excess to the known quantity of test solution. It was then back-titrated with standard iodine solution. Similar to the above case a few drops of dilute starch solution was added as the end-point is reached. The starch-iodide colour was the indication.

4.II.B.2.2.3.Fluorimetric method.

2,3 - Diaminonaphthalene (DAN) was obtained from Koch-Light Laboratories, UK. This was recrystallised as follows. Dissolved 1 gm. of DAN in 20 ml of ethanol in a 100 ml beaker. Boiled to dissolve and filtered the solution through a small Whatman No.1 filter-paper. The filtrate was then freezed slowly to a temperature between $-10^{o}C$ and $-20^{o}C$. The formed crystals were filtered off, washed with cyclohexane, and dried. Recrystallised DAN obtained in the form of white needles. Special attention was paid to do all these operations in diffuse day light. DAN crystals used throughout the work was formed by the recrystallisation process described above. The recrystallised DAN was checked for the blank fluorescence, and if found necessary recrystallisation was repeated. On keeping it days together in air, it was found that the DAN was getting air-oxidised, forming an yellow-brown material.

4.II.B.2.2.3.a Preparation of DAN solution.

A solution of 2,3 - diaminonaphthalene was prepared by

dissolving 500 mg. of recrystallised DAN in 500 ml of 0.1 N HCl. The solution was stirred well for dissolving completely.

4.II.B.2.2.3.b Preparation of standard selenium solution for reference:

A standard selenium solution was prepared by dissolving 50 mg. amount of elemental selenium (99.999% pure) in 5 ml. con.HCl with a minimum amount of 2 ml. con.HNO_3 by heating mildly. The HNO_3 was then evaporated off in the presence of $HClO_4$ on a water-bath, adding sufficient dilute HCl; both to reduce selenate to provide a final solution containing 0.1 N acid. The stock solution was diluted in various dilutions to find out the fluorescence at various concentrations and that enabled to draw the calibration graph. Apart from these, two solutions __ (0.1 µg and 0.01 µg of Se per ml. in 0.1 N $HClO_4$) __ were prepared from the stock solutions, for serving as a comparative standard in the usual determinations.

4.II.B.2.2.3.c Fluorimetric Procedure.

To the dissolved InSe film containing selenium, added 0.5 ml of 0.1 M EDTA (disodium salt of ethylene diamine tetra- acetic acid) solution and 0.5 ml. of 0.1 M sodium flouride solution. After stirring well, to the above solution, 5 ml of DAN solution (prepared as described earlier) was added to adjust the pH to 2.0. Again 5 ml of 0.1% (v/v) DAN solution was added to the above mixture and allowed to stand for 2 hours. It was then extracted with 10 ml of toluene by shaking for 1 minute, and transferred to a spectrofluorometer cuvette for measurement.

The fluorescence intensity of the sample was measured in a Hitachi- 650-60 spectrophotofluorometer at an exciting wavelength of 390 nm and a fluorescent wavelength of 540 nm by comparing with a reference standard. It was then collated with a linear calibration curve in the range 0 and 1 μgm. of selenium per 10 ml. of toluene to obtain the exact amount of selenium that embodied in the film.

4.II.C Electrical measurements.

4.II.C.1 Electrical conductivity

The electrical conductivity of the grown films was measured by a van der Pauw arrangement. For this, ohmic contacts were realised by evaporating circular spots of indium onto the films, through masks. The thickness of the films were in the range 1000 - 8000 Å. The measurements were made under 10^{-3} Torr using a GenRad 1658 RLC Digibridge. Whenever the magnitude of current was very low (less than 10^{-5} Amp.), a Keithley 600B electrometer was employed for the measurements.

The sample film was loaded in a metal chamber to isolate it from the ambience. The dependence of current transport with applied voltage, film thickness and temperature were analysed. Bias voltages were applied to the film from a d.c voltage source comprising of dry cells and a potential divider network. A precision multi- turn potentiometer allowed the voltage adjustments in millivolt accuracy. For obtaining the activation energy values, the conductivities were measured between 300 and 420 K. An Fe-Co thermocouple attached to the sample jig enabled

temperature measurements with the aid of a Keithley-193A, 6- 1/2 digit, digital multimeter. The temperature was controlled by a proportional controller attached to the heating source. In all cases the measurements were repeated in a batch of films, of different thicknesses.

4.II.C.2 Determination of Carrier type

The hot-point probe measurements is a common technique for quickly determining whether a semiconductor is n-type or p-type. The measurement is very simple as follows. The semiconductor surface is touched by two identical probes from a digital multimeter, of which one is heated priorly by a soldering iron while the other is kept at room temperature. Depending upon the type of carriers one of the probe will show a voltage of a relative positive polarity. Whenever the spacing between the probes are varied magnitude variations can also be seen in these observed currents.

4.II.C.3 Hall measurements.

Hall measurements were carried out at room temperature using the dc van der Pauw technique. The sample film was usually mounted on a copper jig which could be aligned at the axial centre of the pole pieces of a magnet. The connections to the film were made by providing copper pressure contacts onto the ohmic junctions formed at the four corners of a typically 10 x 10 mm^2 sample. The current through the sample was monitored by a precision current controller which gave a digital read-out and the Hall voltage developed across the sample was measured using a

digital multimeter having measurement ranges from 1 nV. A uniform magnetic field was applied, either from a EG & G 6 kG magnet or from a Janis research 7 Tesla superconducting magnet.

In the measurements, special care was always taken to record the readings only after the magnetic field had stabilised at the required settings. Both the magnetic field and the current through the sample were reversed for each set of readings to minimise the error voltages caused by various thermoelectric and galvanomagnetic effects. The magnitude of the applied current was generally chosen small enough so that the potential drop across the contacts were no longer large; at the sametime, the current was large enough to obtain a measurable Hall voltage, usually of the order of a few mV.

4.II.D Optical Analysis.

4.II.D.1 Optical transmission

The optical measurements were carried out at room temperature using a dual-beam Hitachi U3400 spectrophotometer in the wavelength range 0.6- 2.5 μm. Transmission spectra of InSe films of different thicknesses at room temperature is recorded in a number of films.

4.II.D.2 Optical absorption

Absorbance can be recorded directly by the spectrophotometer in its absorbance mode. This is the quantity defined by $\log_{10} (I_o/I)$, of which I_o is the intensity of the incident wavelength and I, the intensity of the transmitted

wavelength. So the absorption coefficient,α can be written as

$$\alpha = 1/d \log (I_o/I) \quad \ldots (4.1)$$

where d is the length of the absorbing path.

The absorption coefficient,α, of the films at different photon energies, $h\nu$, was calculated from absorbance data. The temperature dependence of bandgap is measured in the temperature range 300- 370K. The temperature coefficient of bandgap is also estimated from this data.

4.II.D.3 Determination of refractive index.

The method used was the oscillatory dependence of reflectance spectra (for theory see Chapter 3) on wavelength due to the interference. Reflection measurements were performed either in Hitachi model U 3400 or in Hitachi 330 double-beam spectrophotometer. Reflectance spectra of InSe films on quartz substrates, of different thicknesses were recorded in the wavelength range 600-2500 nm.

The refractive index was then calculated using the values of the points at the envelopes of the spectrum using the equation given in Chapter 3. The thicknesses of the films could also be found out from the positions of the consecutive maxima or minima of the spectra.

4.II.E Photoconductivity Measurements.

4.II.E.1 Measurement- Common Aspects.

The films were grown as described before (please see the

film formation part). The samples used were generally of 1 to 2 cm^2 area and thickness in the range of 2000 to 8000 Å. Unless otherwise specified the samples were of n-type with resistivity 10^2 to 10^4 ohm.cm. The photoconductivity measurements were made using the gap electrode geometry as shown in Fig.4.4. For this indium electrodes were evaporated followed by a short heat treatment in vacuum. In order to avoid electrode- effects in photocurrent the electrodes were then covered with an opaque and non-conducting lacquer.

The metal chamber described earlier was put to use to isolate the sample film from the ambience. A 500 W projector lamp and a xenon lamp (Oriel instruments) were used as the excitation sources, with a selected band conveniently filtered. The projector lamp and xenon lamp spans spectral ranges 420-2500 nm and 280-2500 nm respectively. For irradiance the bands were selected by a double grating Oriel monochromator. To circumvent the heating up of the monochromator and the sample film, a water filter was included in between the light source and the monochromator. The schematic of the photoconductivity measurement setup is shown in fig.4.5. The lamp intensities were calibrated using a Hewlett-Packard Silicon photodiode (HP 5082-4207) of known spectral response and quantum yield.

The measurements were started after evacuating the metal chamber with sample film inside to a pressure of 10^{-3} Torr. A DMM (Keithley- 193 A) was used to obtain the photocurrent values and a multimeter (ITL- 475) was employed to monitor the bias voltage values.

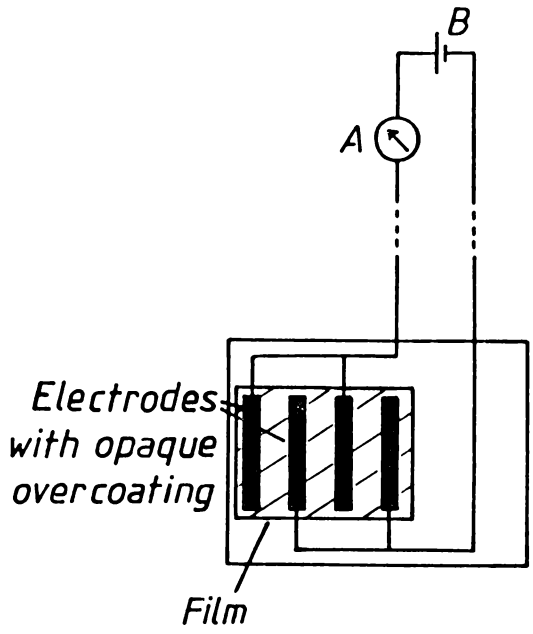

Fig.4.4 Photoconductivity measurement: Gap geometry of electrodes.

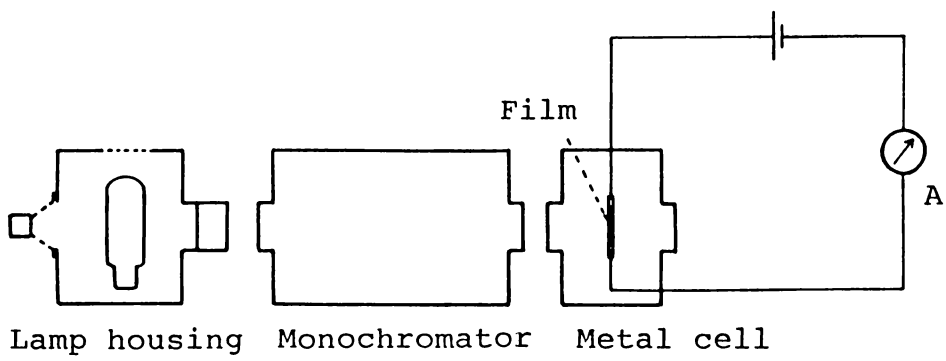

Fig.4.5 Schematic of the photoconductivity measurement set up.

4.II.E.2 Spectral response of photocurrent.

The distribution of photocurrent for different wavelengths (a band of 5nm) in the range 650 to 1200 nm, for a fixed incident photom flux, was measured using the setup as described above. For this ohmic contacts were realised by depositing indium onto the films in the geometry as described in the earlier part (photoconductivity measurements-common aspects). Then connections to the ohmic contacts were made by the pressure contacts attached in the sample jig. The measurements were performed at the ambient temperature and higher temperatures, and repeated for different bias voltages and thickness values.

4.II.E.3 Temperature dependence of photocurrent.

The variation of normalised photocurrent with temperature was analysed in similiar films described above, for different thickness values. The bias voltages were applied similiar to dark conductivity studies. As described in the dark conductivity studies an Fe-Co thermocouple in combination with a digital mutimeter having a resolution of 0.1 μV was employed for the temperature measurements. The temperature at different set points was controlled by a proportional controller.

4.II.E.4 Intensity dependence of photocurrent.

The dependence of photocurrent on the incident flux for different wavelengths was studied in the above films. The intensity was adjusted using neutral density filters. The measurements were carried out on In-InSe-In (gap geometry)

structures as above. The intensity of the light was converted to lux- ampere using the known quantum yield of the photo-diode.

4.II.F Photovoltaic effect in Indium selenide schottky barriers :

Schotty junctions were obtained by depositing Indium selenide film on an evaporated gold film (semi-transparent) of thickness 300-800 Å. The top opaque contacts were obtained by evaporating indium metal. Cells formed in this way were having an area between 0.2 and 1 cm^2.

4.II.F.1 Spectral response.

Keeping the incident photon flux constant, the dependence of photocurrent on wavelength in the range 650-1300 nm was studied using the procedure similar to that described in the photoconductivity measurements. The readings were taken without any bias voltage and always at room temperature.

4.II.F.2 I-V characteristics.

The I-V characteristics were obtained by the usual direct-current method. The cells were formed as described above and the setup used was the same as that outlined in the dark conductivity measurements. The measurements were taken for different thickness values.

4.II.F.3 C-V Measurements.

The capacitance-voltage characteristics of the junctions were studied using a GenRad 1658 RLC Digibridge at three fixed frequencies (500Hz,1KHz and 5KHz). The bias voltages were applied

from the dc voltage source as described in the dark electrical conductivity measurements. The bias voltages were monitored using a digital multimeter.

4.II.F.4 Diffusion length determination.

The sample schottky barrier cell was illuminated through the semitransparent contact, Au. The intensity of the incident monochromatic radiation was measured at various wavelengths that yielded a constant photocurrent. Absorption coefficients were found out by the method described in the determination of optical constants.

4.III. Results and discussions.

4.III.A. Structure, and morphology.

4.III.A.1 X-ray diffraction analysis

4.III.A.1.a Effect of deposition temperature

Typical X-ray diffraction patterns for the films grown at different temperatures (400K to 528K) are given in Fig.4.6(a)-(d). It is evident that the substrate temperature has a significant influence on the structure and composition of the formed films. When the substrate temperature is below 423 K, films are either amorphous or of fine-grained nature, whereas films grown above 423K are all polycrystalline. The formation of stoichiometric, monophasic film is observed as the substrate temperature is nearer to 488 K. But,these films show a tendency to dissociate on raising the substrate temperatures above 488K, as is evident from the diffraction pattern (Fig 4.6 (d)).

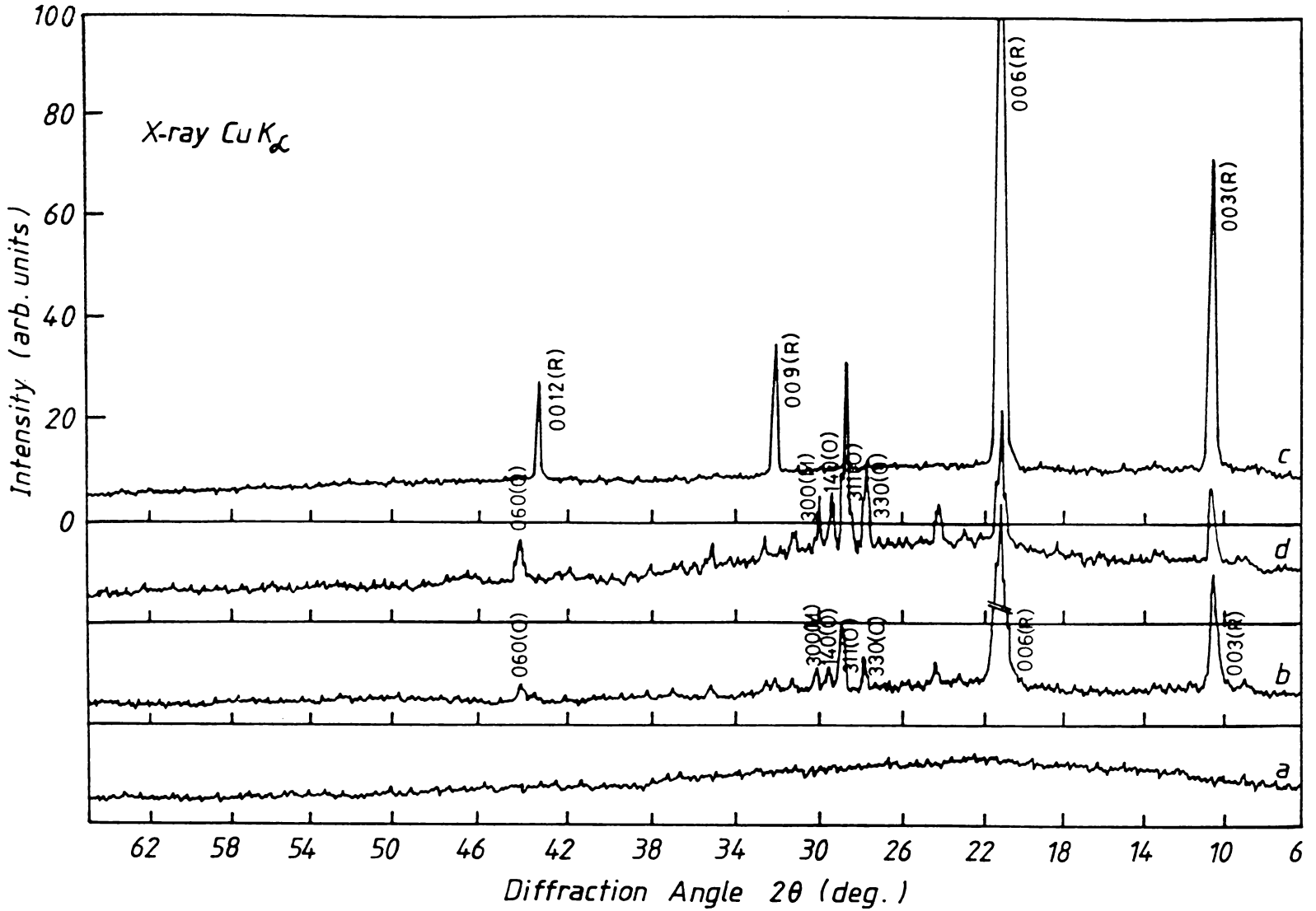

Fig.4.6 X-ray diffraction (Cu K_α radiation) patterns of films deposited at different substrate temperatures. (a) 400K ; (b) 468K ; (c) 488K ; (d) 523K.
(R - rhombohedral InSe ; O - orthorhombic In_4Se_3 and M - monoclinic In_6Se_7).

4.III.A.1.b Evidence of formation of monophase (rhombohedral) films.

X-ray diffraction patterns given in Fig 4.6(b)and 4.6(c) (grown at substrate temperatures 468K and 488K) indicate that the films consist chiefly of the rhombohedral phase of InSe[31] with a relatively negligible amount of other phases. The most intense diffraction peaks (Fig 4.6(c)) correspond to the (0 0 3n) type reflections and are consistently dominant in all the samples. This suggests a preferential orientation of crystallites with c-axis perpendicular to the substrate surface[16]. The additional peaks with very low intensity (<2%), present in the samples can be assigned to the orthorhombic phase of In_4Se_3[32]. When substrate temperatures >488K are employed for the formation of the films, as the flux ratio is constant, increasing substrate temperature enhances the preferential reevaporation of selenium and therefore the stoichiometry changes at higher substrate temperatures causing the appearance of In_4Se_3 in the films[26] (Fig.4.6(d)).

4.III.A.1.c Effect of heat treatment.

Annealing of films after deposition has a pronounced effect on the crystallinity and composition of the film as evident from Fig 4.7(a)-(d). It is to be mentioned here that the patterns given in Fig.4.7(b)-(d) correspond to the film shown in Fig.4.7(a). The films start to dissociate under prolonged annealing time. But, annealing for shorter intervals of time improves the crystallinity of the films (Fig 4.7(b)). The XRD

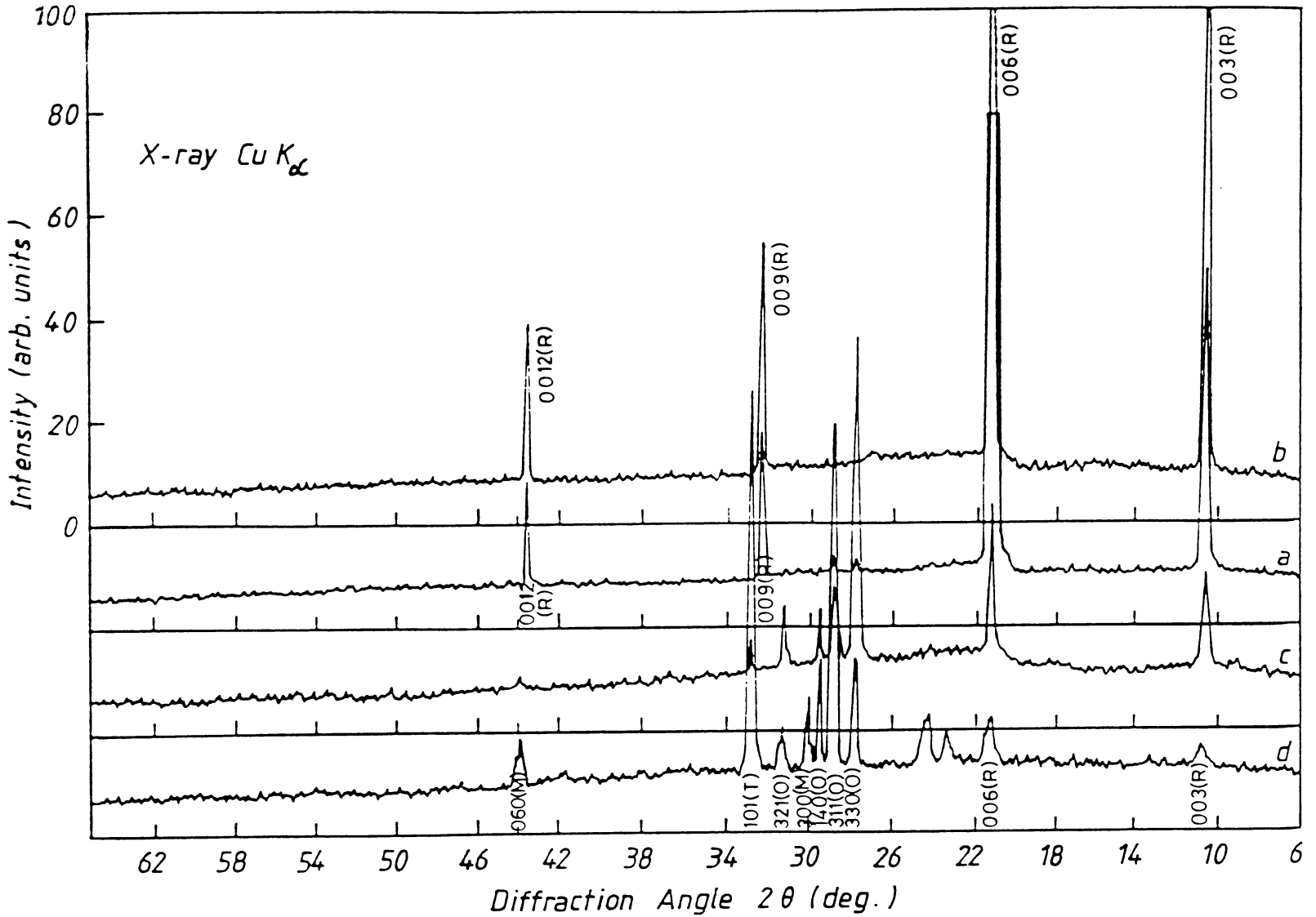

Fig.4.7 X-ray diffraction patterns of films subjected to post-depositional annealing at 533K for different durations. (a) as-deposited ; (b) 15min. ; (c) 40min. ; (d) 60 min. (R - rhombohedral InSe ; O - orthorhombic In_4Se_3 ; M - monoclinic In_6Se_7 and T - tetragonal In.)

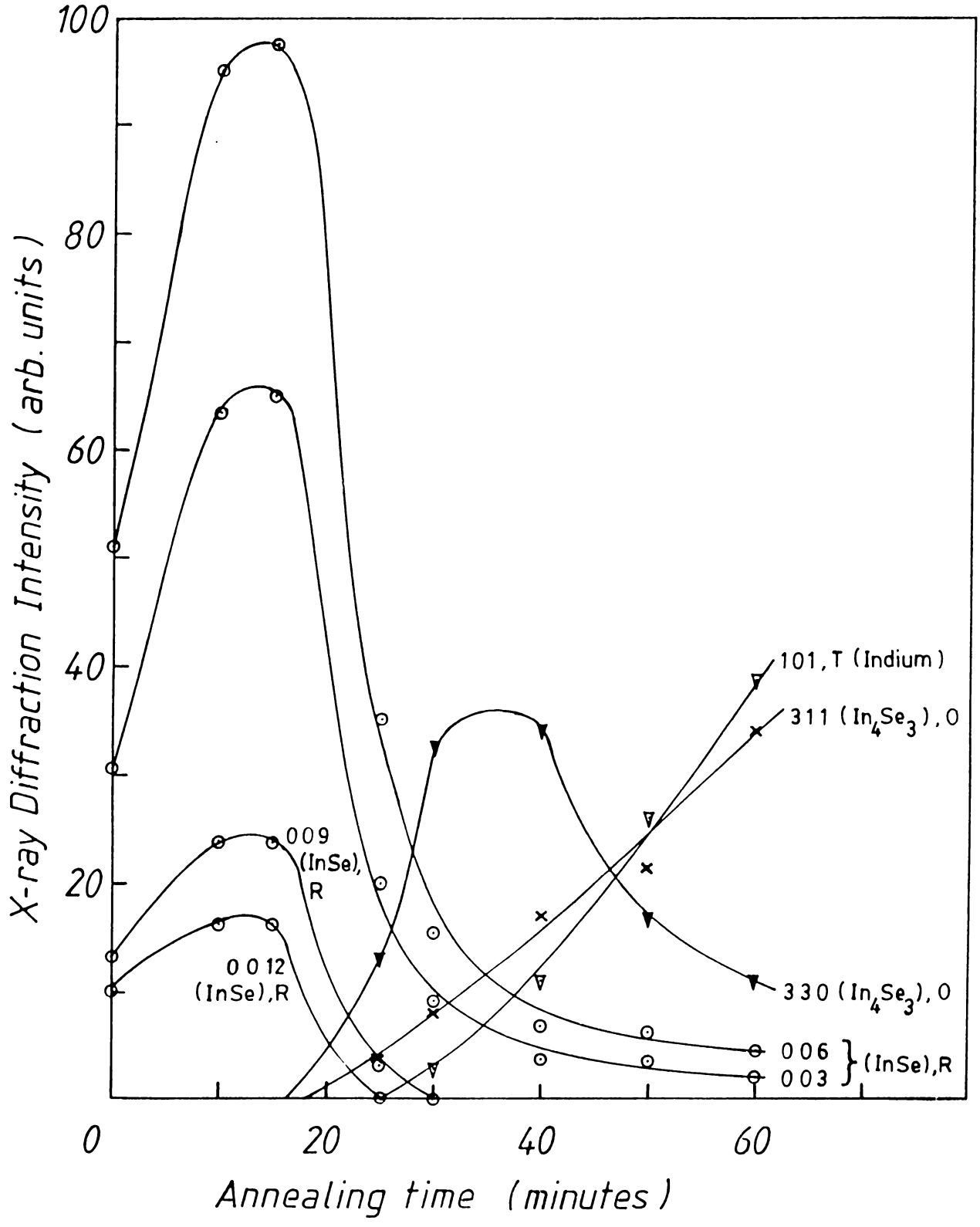

Fig.4.8 Variation in the relative intensity of different X-ray reflections as a function of annealing time.
(R - rhombohedral InSe ; O - orthorhombic In_4Se_3 and T - tetragonal In.)

lines become sharper and the characteristic lines of rhombohedral InSe become very prominent. It can also be seen that the grain size also increases in this case as indicated from the decreasing half-line-widths of X-ray reflections. Again, short annealings remove the minor phase and the films become completely single phased (rhombohedral) InSe.

Diffraction patterns shown in Fig 4.7(c) and 4.7(d) indicate the dissociation of the film due to the escape of selenium from the film. This is evident from the samples annealed for 60 minutes where the reflections from free indium also appear. The changes can be well accounted for, by studying Fig.4.8, where the intensities of different reflections vary as a function of annealing time. It can be seen that, after an optimum annealing time, the films gradually change to a mixed phase, with orthorhombic In_4Se_3 phase dominating.

These results indicate that for obtaining a monophase film, a short post-deposition annealing rather than keeping the substrate temperature high during deposition is perferable. However, further annealing beyond the optimum time affects adversely, and results in the formation of selenium deficient phases.

4.III.A.1.d. Broadening of peaks

A qualitative estimate of the mean size of the crystallites in polycrystalline films is usually obtained from the broadening of the peaks in the X-ray diffraction spectra by using the Scherrer formula[33,34]

$$C = k \lambda / \beta \cos \theta \qquad \ldots (4.2)$$

Table 4.2

Typical crystallite size with deposition substrate temperature.

Deposition substrate temperature K	Crystallite size		
	XRD peak at $2\theta = 29.5^{\circ}$	XRD peak at $2\theta = 21.4^{\circ}$	TEM
488	0.93 (0.97)	0.95 (1.0)	1.1 (1.2)
463	0.63	0.65	0.66
478	0.84	0.87	0.9

Values in brackets show the variation after post-depositional annealing.

where k is a constant usually between 0.9 and 1.0, β is the effective width of the main peak at half-maximum intensity (FWHM) corrected for instrumental broadening, θ is the diffraction angle at which the peak appears, λ is the wavelength of radiation used and C is the mean size of the crystallites. It is to be mentioned that this method is not effective if the mean size of the crystallites exceeds 1.0 μm. Table 4.2 shows the calculated values of C together with their deposition substrate temperatures. An increase in C with temperature similiar to that described in Section 4.III.A.1.c can be seen, but the values obtained are slightly lower than the grain size values determined from the TEM measurements. The broadening of the peaks[35] may also be due to non-uniformity in the interplanar spacing because of the stress in the crystallites.

4.III.A.2 TEM studies

Transmission electron micrographs of typical InSe films grown at different substrate temperatures are shown in figures 4.9 to 4.11. The corresponding Selected area diffractograms (SAD) are shown below. When the substrate temperature is lower the film morphology shows polycrystalline structure having fine crystallites. Micrograph of a film deposited at a substrate temperature of 488K, with a short post-depositional annealing is shown in Fig 4.10. The corresponding SAD pattern is shown below. It can be seen that the films are polycrystalline and are coarse grained with a mean crystalline size of around 1.2 μm. The SAD pattern shows that the individual crystallites are single crystals.

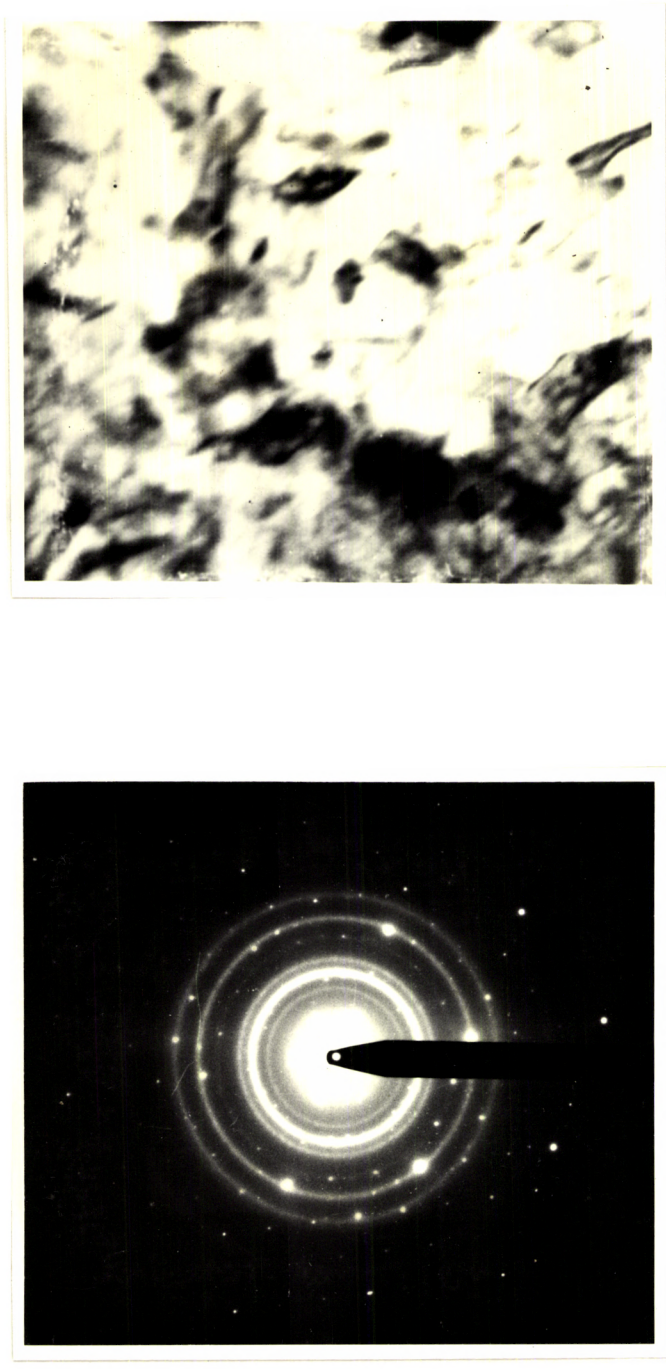

Fig.4.9 Electron micrograph of InSe film deposited at lower temperature (453 K) and the corresponding SAD pattern.

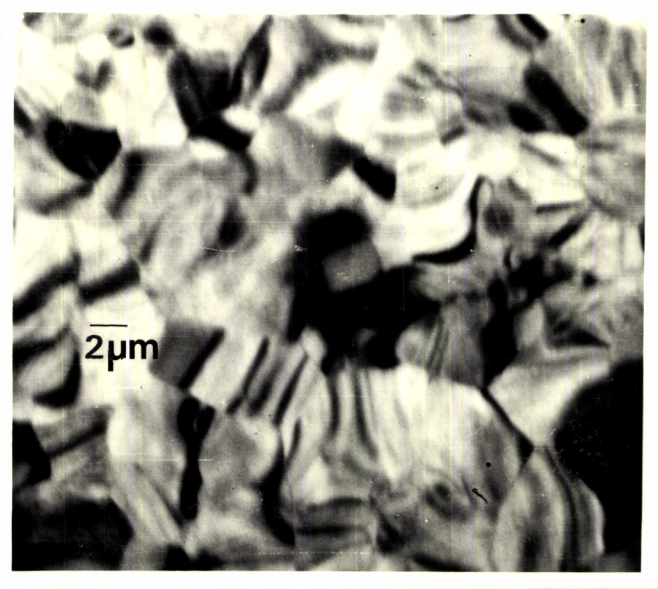

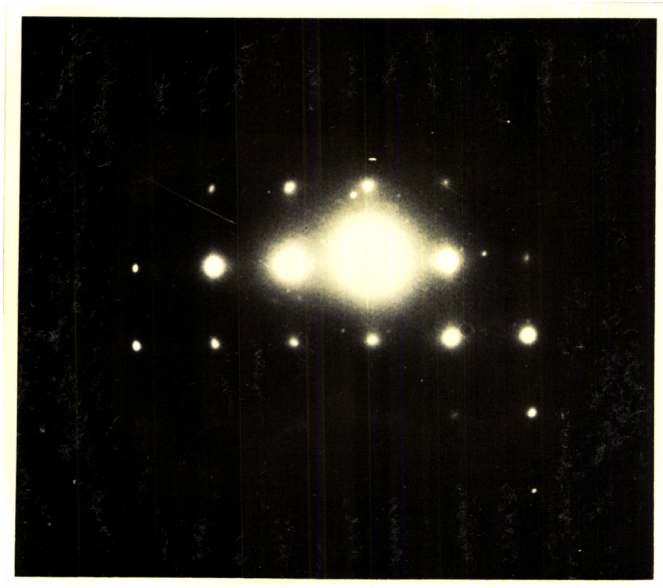

Fig.4.10 Electron micrograph showing the grains of InSe film and its SAD pattern. (Deposition substrate temperature 483 K with short -duration annealing).

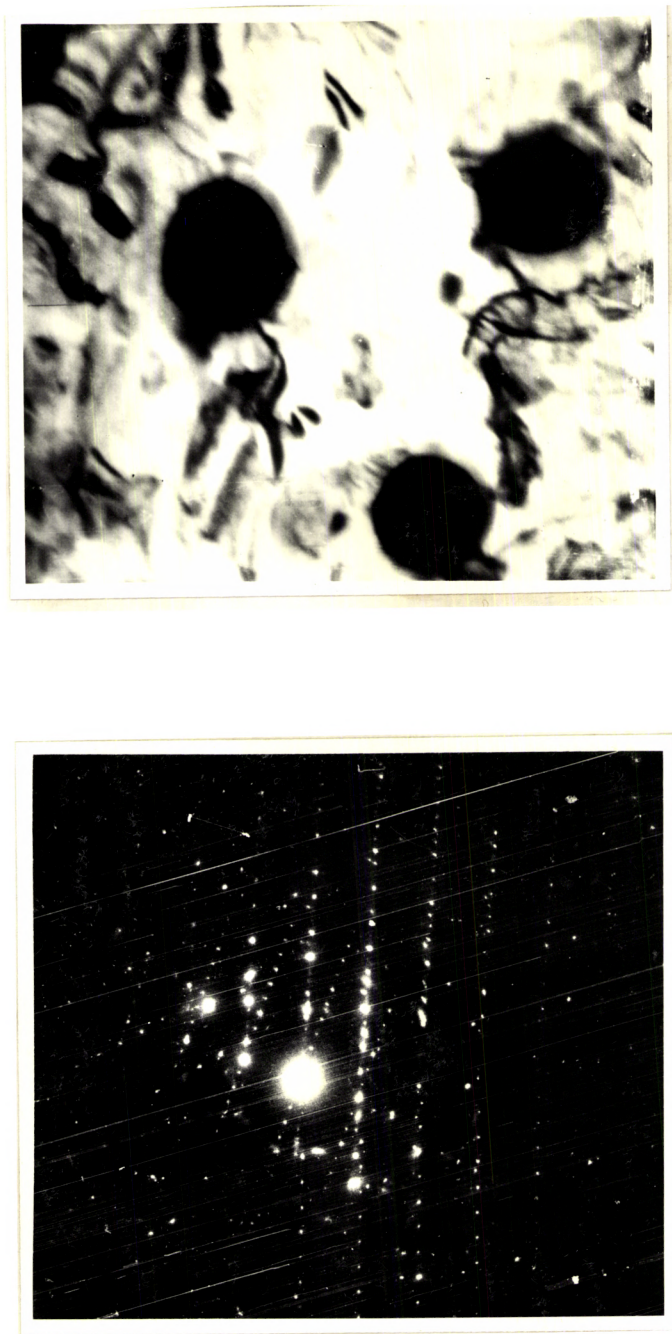

Fig.4.11 Electron micrograph of InSe film deposited at higher substrate temperature (523 K) and the corresponding SAD pattern.

4.III.B Compositional studies

4.III.B.1 XPS Studies

To obtain the composition of the film and also the valence state of the elements, an XPS analysis has been carried out. Fig.4.12 shows a portion of the XPS spectrum depicting the In $4d_{(5/2,3/2)}$ and Se $3d_{(5/2,3/2)}$ levels for the presently obtained InSe films. The binding energy of $4d_{(5/2,3/2)}$ in the case of elemental indium is 16.2 eV and for elemental selenium, the $3d_{(5/2,3/2)}$ appears at 56.7 eV. When compared, the present values are 17.4 eV and 53.4 eV respectively. The chemical shift in binding energy, $\Delta BE = (Se\ 3d_{(5/2,3/2)}) - (In\ 4d_{(5/2,3/2)})$ decreases from 40.5 eV in the individual elements to 36.0 eV in the present films. The present XPS data are well comparable with that of single crystal and sputtered films of InSe (Table 4.3). These data clearly indicate the formation of a compound of indium and selenium which is further supported by the variations in the indium $3d_{5/2}$ band as shown in the resolved spectra (Fig.4.13).

For elemental indium $3d_{5/2}$appears at 443.6 eV. The FWHM of the In $3d_{5/2}$ band varied between 1.9-2.1 eV for different samples studied and evidenced to be much sensitive to charge broadening than the Se $3d_{(5/2,3/2)}$peak, which registered the FWHM in the range of 1.95-2.05 eV. From the indium 3d and selenium 3d peaks, the composition of the films was calculated. For the compounds in the In-Se system, the $3d_{5/2}$ increases with Se/In ratio upto 0.75 and decreases at higher Se/In ratio (Fig.4.14). The presently observed binding energy of In $3d_{5/2}$= 444.5 eV therefore

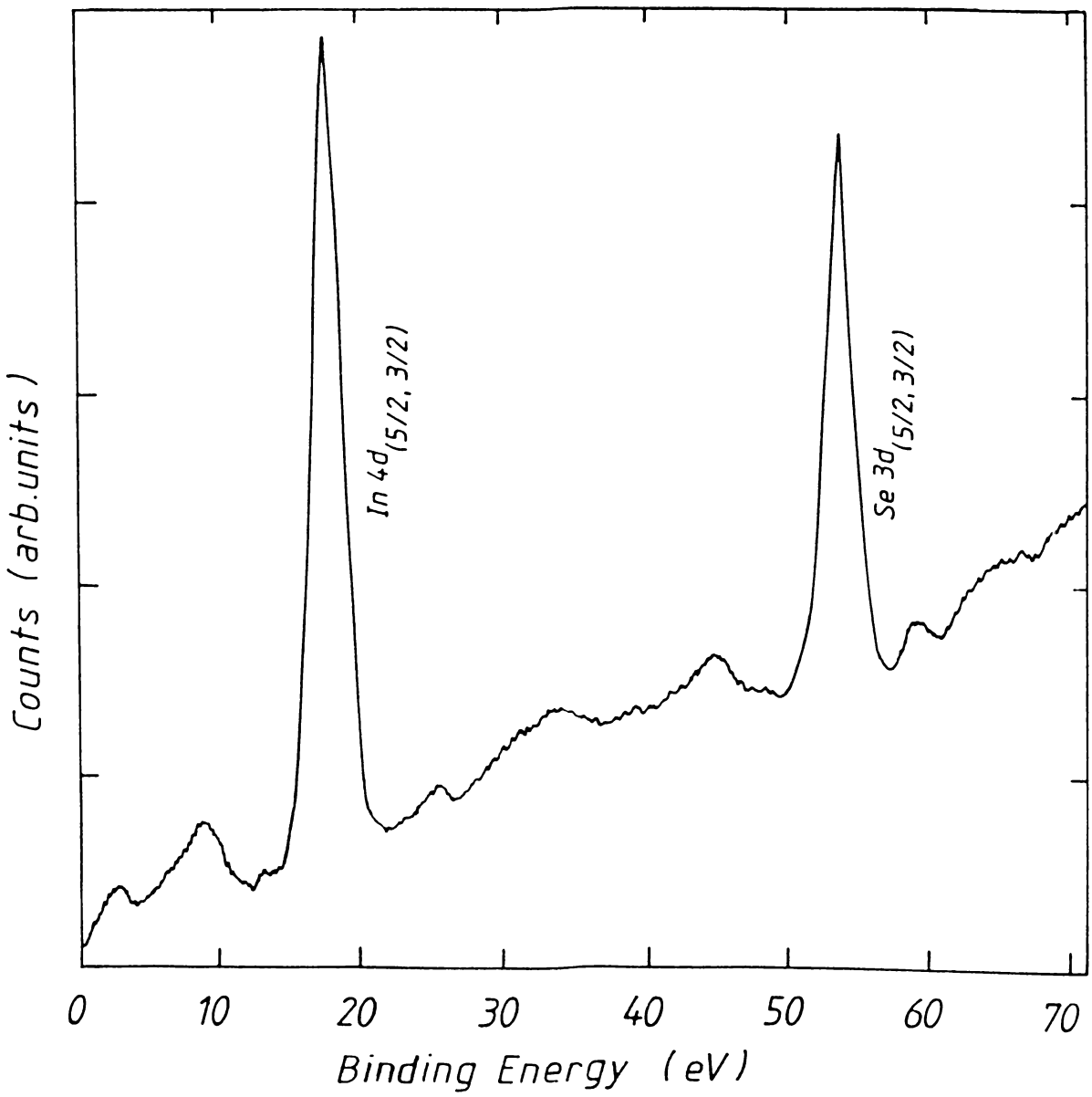

Fig.4.12 XPS spectrum showing the In $4d_{(5/2,3/2)}$ and Se $3d_{(5/2,3/2)}$ levels for InSe films.

Table 4.3

Comparison of the XPS binding energies

Sample	Se $3d_{5/2,3/2}$ (eV)	In $4d_{5/2,3/2}$ (eV)	Δ BE (eV)
InSe sputtered film [36]	53.5	17.4	36.1
In or Se element [36,37]	56.7	16.2	40.5
InSe (single crystal)	53.4	17.3	36.1
InSe (present work)	53.4	17.4	36.0

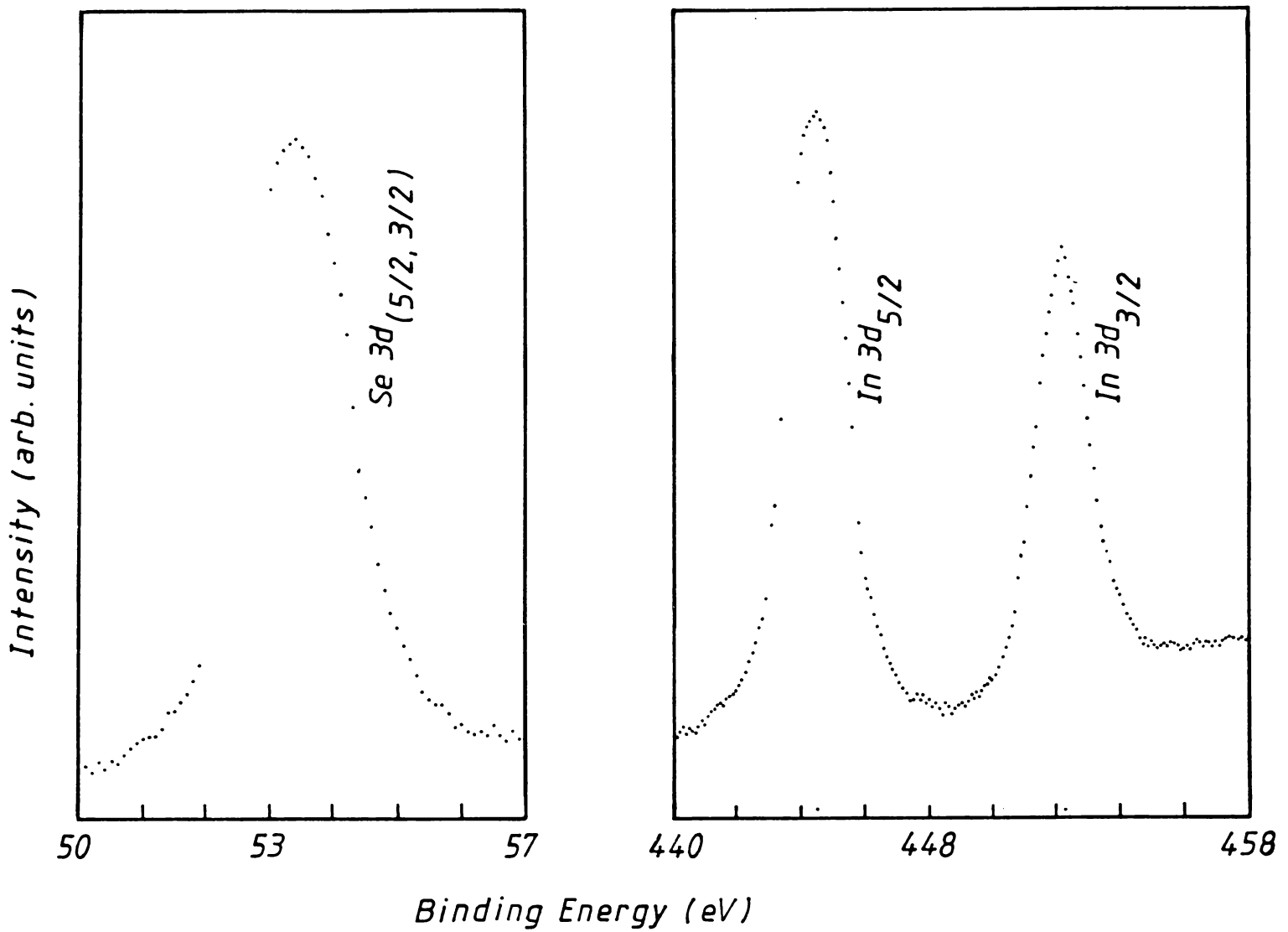

Fig.4.13 XPS spectra for In $3d_{5/2}$, In $3d_{3/2}$ and Se $3d_{(5/2,3/2)}$ in InSe thin films.

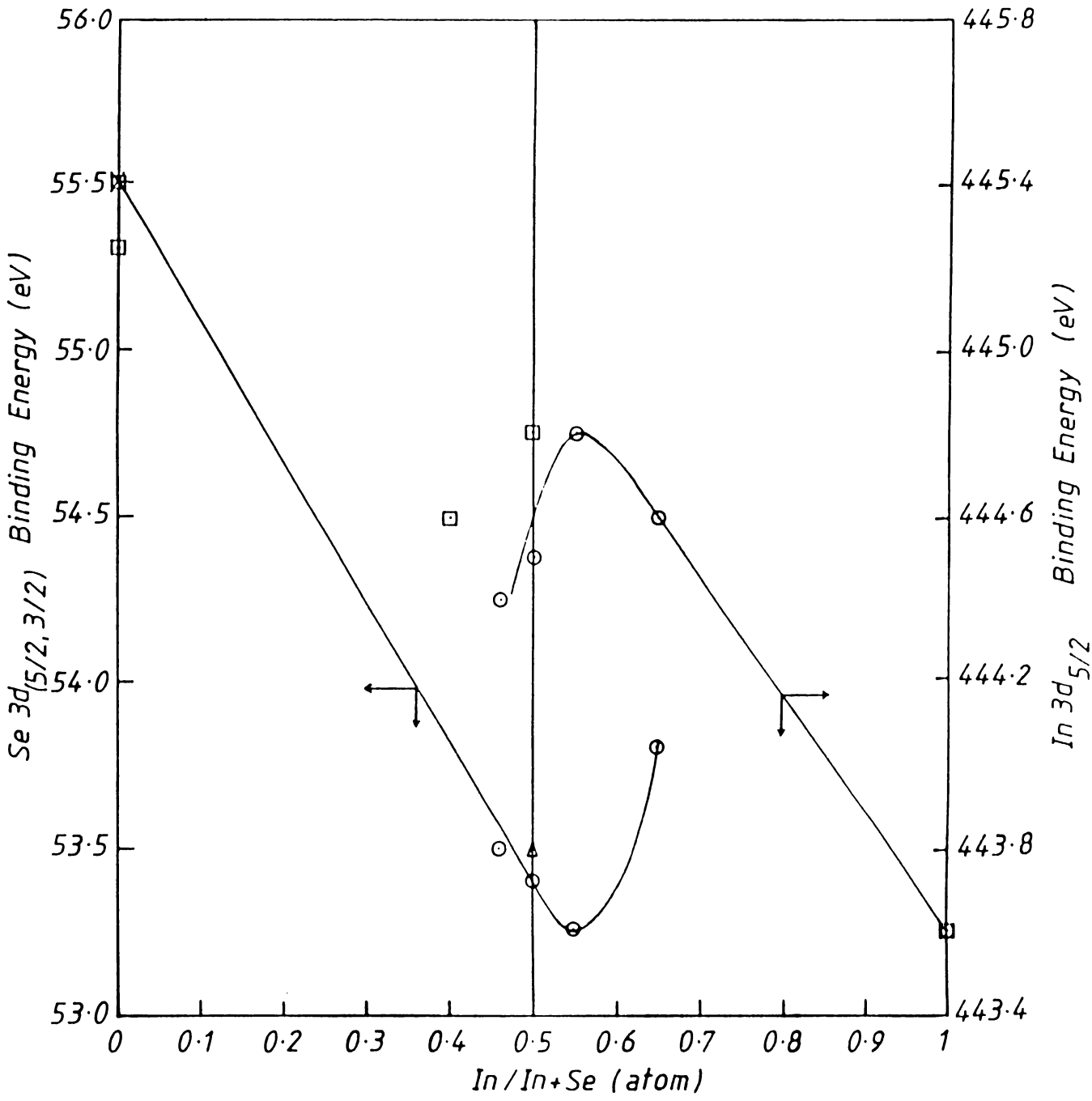

Fig.4.14 Variation in the indium $3d_{(5/2)}$ and selenium $3d_{(5/2,3/2)}$ bands as a function of In/In+Se ratios.
(⊙) present work ; (■) from [38] ; (X) from [39] ;
(△) from [36]

correspond to Se/In~1.0. Figure 4.14 also shows the variations in the Se $3d_{(5/2,3/2)}$ level with changing Se/In ratio and confirms the above composition of the present films.

4.III.B.2 Chemical Analysis.

The characteristic fluorescence spectra of the 4,5 - benzopiazselenol in toluene, is shown in Fig.4.15. Table 4.4 shows some typical results of the comparative selenium estimations of DAN with that of Iodometric for known amounts of Se. The agreement between the amount of Se taken and that estimated by DAN fluorimetry discloses that the loss of selenium is negligible and the realiability is high for this method, over the concerned range. The typical results of the determination of Se in the InSe samples are given in Table 4.5A. From the obtained values the stoichiometry of the samples can be easily calculated (Table 4.5B) as the total weight of the sample is known.

The principle involved in the estimations is as follows: Selenium in the form of selenous acid reacts with DAN in acid solution to produce a strongly fluorescent reddish coloured precipitate, 4, 5 - benzopiazselenol[40], but the rate of reaction decreases as the acidity is increased. So, an optimum concentration of 0.1 N HCl has been chosen for the present estimations. At this concentration, the rate of reaction is found to be nominal and the acidity is adequate to hold most metals in solution.

The fluorescent spectra of the piazselenol in toluene shows

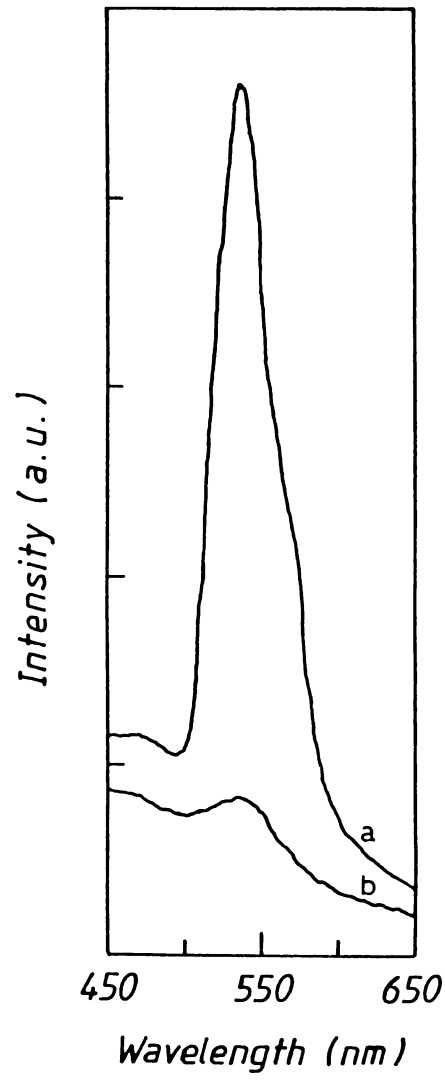

Fig.4.15 a: Typical fluorescence peak at 540 nm (excitation wavelength 390 nm) of DAN complex formed with selenium.

b: Blanck emission

Table 4.4

Selenium estimation: Standard solutions

Sample no.	Material	Amount (known) in 10^6ml. mg.	Estimated Se	
			Mean by Iodometry in 1000 ml. mg.	Mean by DAN fluorimetry in 1 ml. µg.
1	Se	18.97	0.014805	0.018943
2	Se	12.21	0.009870	0.012196
3	Se	62.45	0.054285	0.062441
4	Se	120.53	0.11844	0.12050
5	Se	84.33	0.079947	0.08429

Table 4.5A

Se Estimation: Typical InSe samples

Sample no.	Material	Total weight gm.	Dilution ml.	Estimation of Se DAN fluorimetry µg/ml.			
				1	2	3	Mean Se
68	InSe	0.00152	10^4	0.0633	0.0620	0.0608	0.06203
118	InSe	0.00125	10^4	0.0497	0.500	0.0513	0.05033
O-32	InSe	0.00271	10^4	0.1101	0.1097	0.1112	0.11033
190	InSe	0.00082	10^3	0.3411	0.3359	0.3364	0.33780
R-93	InSe	0.00197	10^4	0.0801	0.0801	0.0798	0.0800
362	InSe	0.00163	10^4	0.0664	0.0663	0.0664	0.06637

Table 4.5B

Se Estimation: InSe samples

Sample no.	Total weight W gm.	Se determined by DAN W_{Se} gm.	Indium $W_{In} = W - W_{Se}$ gm.	Molar ratio In:Se
68	0.00152	0.6203×10^{-3}	8.997×10^{-4}	100: 100.27
118	0.00125	0.5033×10^{-3}	7.467×10^{-4}	100: 98.03
O-32	0.00271	1.1033×10^{-3}	1.6067×10^{-3}	100: 99.86
190	0.00082	3.378×10^{-4}	4.822×10^{-4}	100: 101.87
R-93	0.00197	8.00×10^{-4}	1.170×10^{-3}	100: 99.43
362	0.00163	6.637×10^{-4}	9.663×10^{-4}	100: 99.87

maxima at 540 nm for the incident radiation of 390 nm or 480 nm. Since the 390/540 peaks were stronger than the 480/540 peaks and the corresponding blank readings were comparable in both cases, measurement were carried out at the 390/540 peaks.

The piazselenol extracted in toluene for the fluorescence studies shows a slight shift from the fluorescence maxima reported for that extracted using cyclohexane or dekalin. These are in accordance with the observations made by Parker and Harvey[40]. The EDTA solution and sodium fluoride solutions are used mainly because they enjoy the ability to mask some of the slightly interfering ions like zinc, aluminum or sodium and to a limited extent to copper.

In the estimations when the amount of Se in the testing solution is awfully small, it is found that a peak appears at 600 nm. This has been confirmed to be due to the excess 2,3-diaminonaphthalene that is being extracted by the toluene.

The factor that limits the sensitivity in the estimation is the blank fluorescence arising from traces of impurity in the DAN reagent. This can be minimised by repeated recrystallisation of the reagent in diffused daylight. The sensitivity of DAN in the determination of Se is in the nanogram range of 0.0005 µgm. The intensity of fluorescence at the 540 peak has been found to be proportional to a concentration of selenium upto at least 0.5 µgm (Fig.4.16), although the normal range for measurement is 0.01 to 0.35 µgm. of selenium per 10 ml toluene.

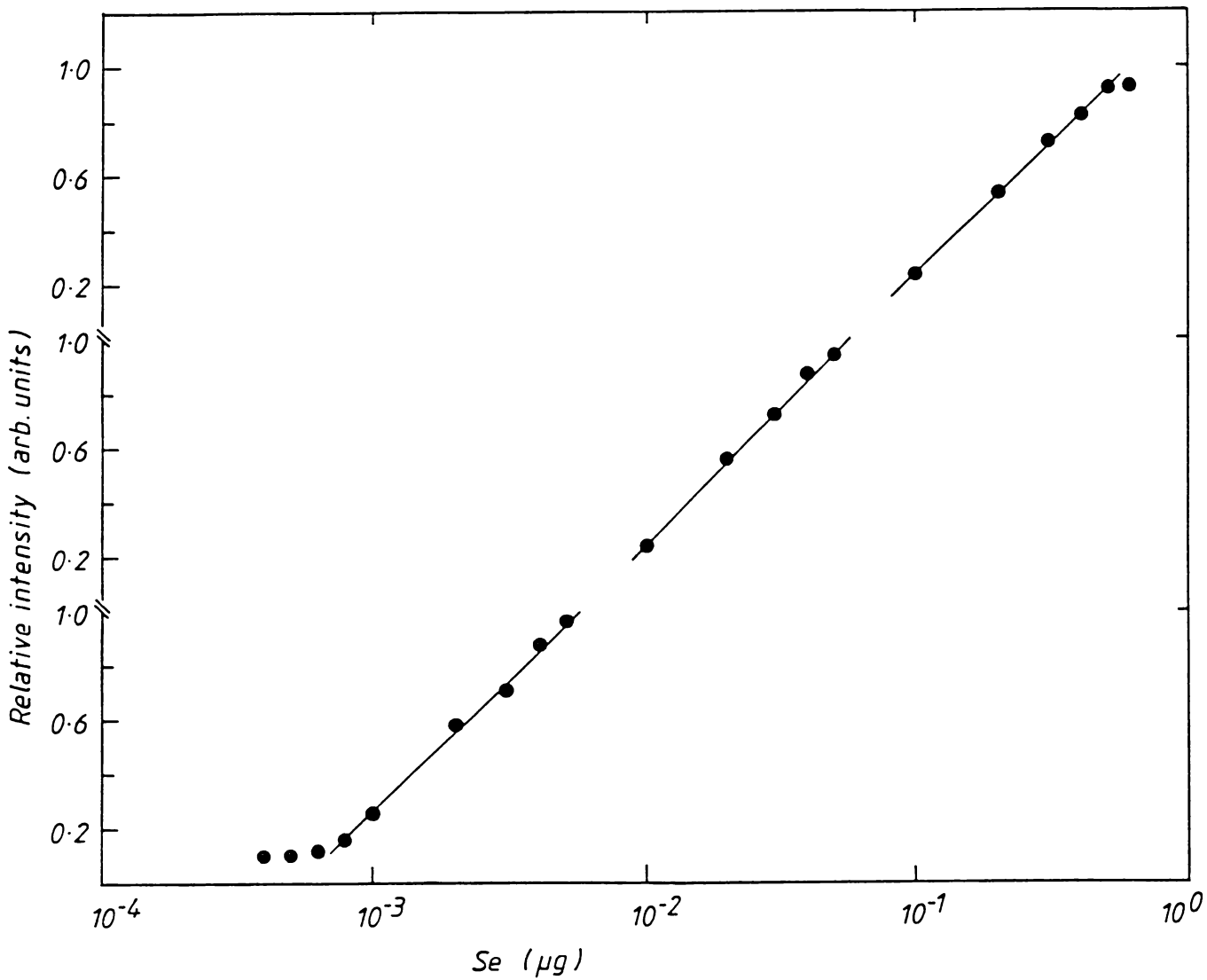

Fig.4.16 Plot of DAN- complex fluorescence emission vs. Amount of selenium content.

Table 4.6

Electrical properties of as-deposited InSe films

Thickness ~ 510 nm

Substrate temp. (K)	Conductivity ($ohm^{-1}cm^{-1}$)	Carrier type	Activation energy (eV)	Hall coefft. (cm^3C^{-1})	Carrier concent. (cm^{-3})
400	5.61×10^{-6}	n	0.15	--	--
488	8.12×10^{-2}	n	0.625	4.08	1.53×10^{18}
503	1.05×10^{-4}	n	0.89	--	--
528	9.17×10^{-6}	-	1.02	--	--

Table 4.7

Changes in electrical properties of InSe film deposited at 488K with further annealing.

Film thickness 510 nm ; Annealing temperature:533K

Annealing time	Conductivity ($ohm^{-1}cm^{-1}$)	Carrier type	Activation energy (eV)	Hall coefft. (cm^3C^{-1})	Carrier concent. (cm^{-3})
15 min.	$4.32x10^{-1}$	n	0.63	1.09	$5.75x10^{18}$
30 min.	$5.14x10^{-3}$	n	0.755	6.74	$9.27x10^{17}$
40 min.	$3.75x10^{-5}$	n	0.89	--	--
60 min.	$4.51x10^{-9}$	-	--	--	--

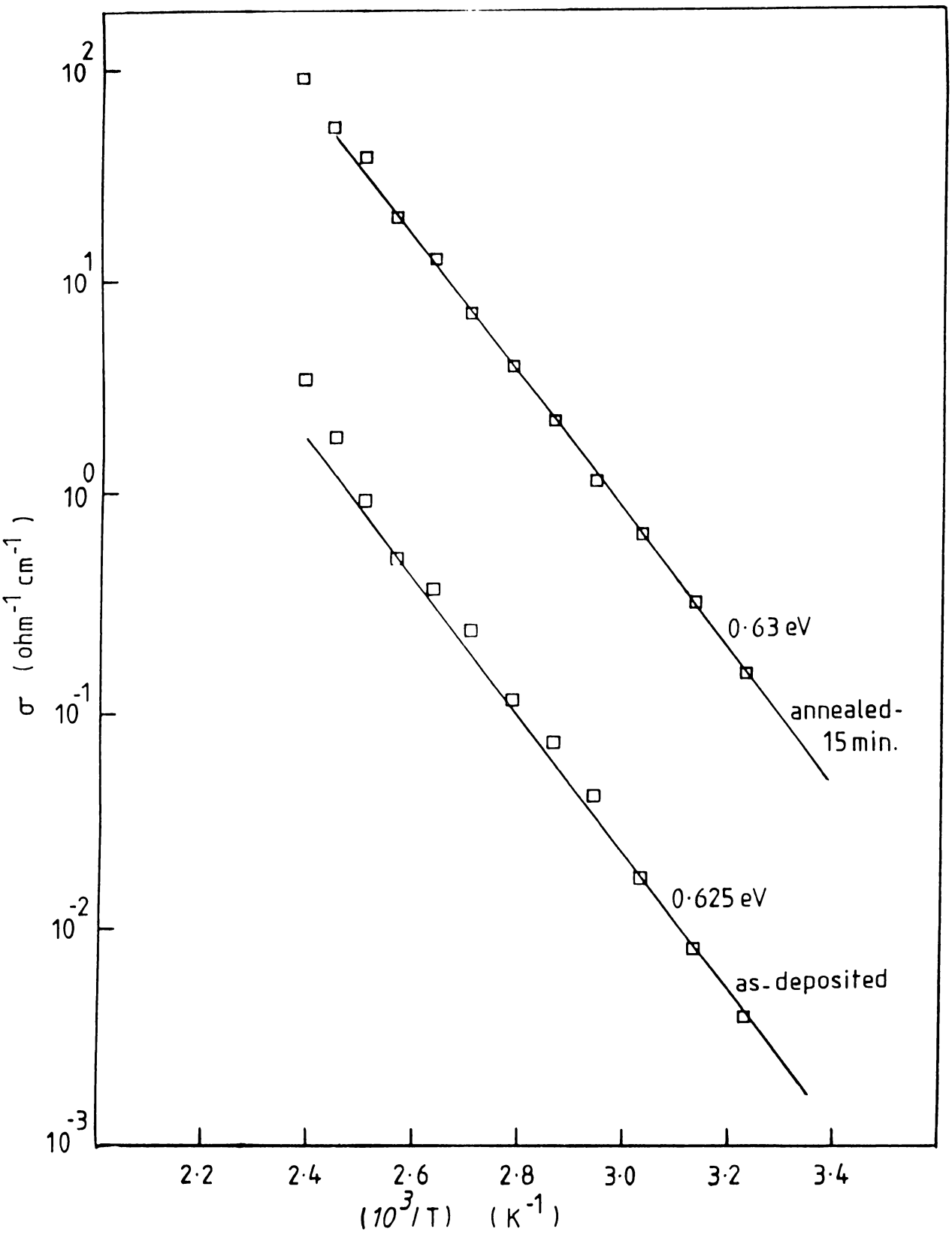

Fig.4.17 The temperature dependence of conductivity for the stoichiometric films in the temperature range 300K-420K.

4.III.C Electrical characterisation

4.III.C.1 Electrical conductivity

The surface conductivity , σ , measured at room temperature and the activation energy values along with Hall coefficient and carrier concentration are listed in Table 4.6. This shows a drop in conductivity as the substrate temperature for deposition is increased beyond 488 K and is consistent with the phase (or structural) changes happening to the film as observed in XRD spectrum. Again, the post-deposition annealing time also brings a similar change and is summarised in Table 4.7. Fig.4.17 gives the temperature variation of conductivity for the stoichiometric films. These results show the formation of a superior quality film at a lower annealing time. The effect has alreadly been mentioned in the XRD analysis. The highest conductivity obtained for the films is 4.0 $x10^{-1}$ ohm^{-1} cm^{-1} under the conditions T_s=488K and post-deposition annealing at 533 K for 10-15 minutes under ~$3x10^{-6}$ Torr pressure.

4.III.C.2 Determination of Carrier type

The results of the hot probe measurements are listed in Table 4.6 along with the conductivity values.

The hot probe heats the semiconductor immediately under it, with a consequent rise of number of higher energy carriers. These then move with higher thermal velocities and diffuse out of the hot region faster than the slower neighbours. The net effect is the hot region becoming slightly depleted of majority carriers. These energetic carriers will be predominantly holes in the case of a p-type material and electrons in an n-type material. Current will therefore flow through the multimeter and the direction of

current depends on the sign of the charge. Thus, on an n-type semiconductor, the hot probe is the more positive one, while on a p-type it is the more negative.

4.III.C.3 Hall effect measurements

For films with conductivity $>10^{-5}$ $ohm^{-1}.cm^{-1}$ the Hall coefficient and carrier concentration, N, have also been obtained (Table 4.6 and 4.7). These values of carrier concentration are higher than those reported for thin films. The values of mobility are lower when compared with single crystals, but accountable for the presence of grain boundaries present in polycrystalline films.

4.III.D Optical measurements

4.III.D.1 Optical absorption

The spectrophotometer recording of the typical transmission spectra for different thicknesses is shown in fig.4.18. For thicker films the decrease of transmission near fundamental energy gap is more sharper than thinner films. This is due to the fact that, for thinner films, 'structures' due to multiple reflections are occuring.

Absorption coefficient,α ,of the films at different photon energies, $h\nu$, has been calculated from absorbance data. Absorption coefficient calculated at 950 nm is about 4.8×10^4. The absorption coefficient shows a proportional variation in the region of concern and indicates a direct allowed optical transition. The optical energy gap is then found out (Fig.4.19) by plotting $[(\alpha - \alpha_o)h\nu]^2$ versus photon energy, in accordance with the expression[41,42],

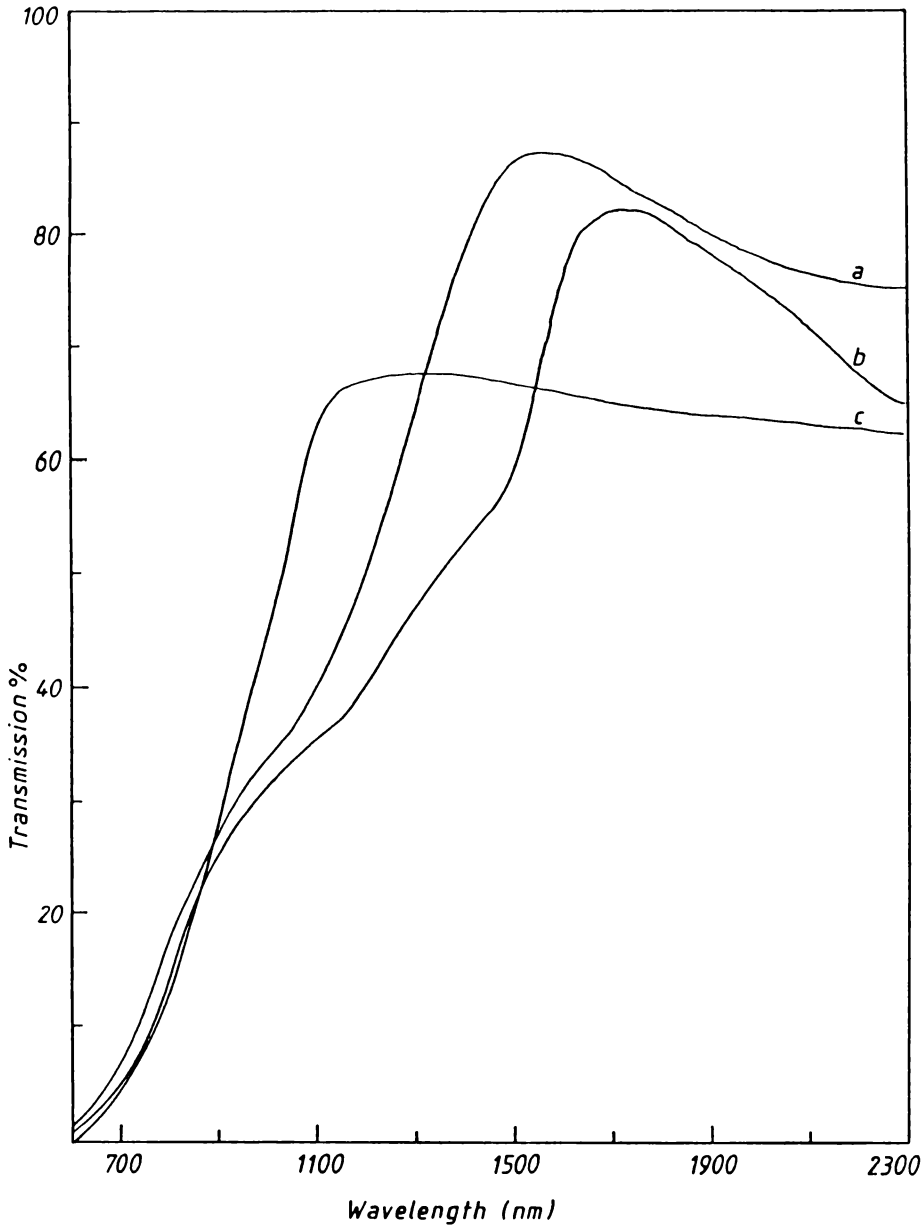

Fig.4.18 Typical transmission spectra of InSe films of different thicknesses.

a• 3100 Å; b• 5600 Å; c• 6700 Å.

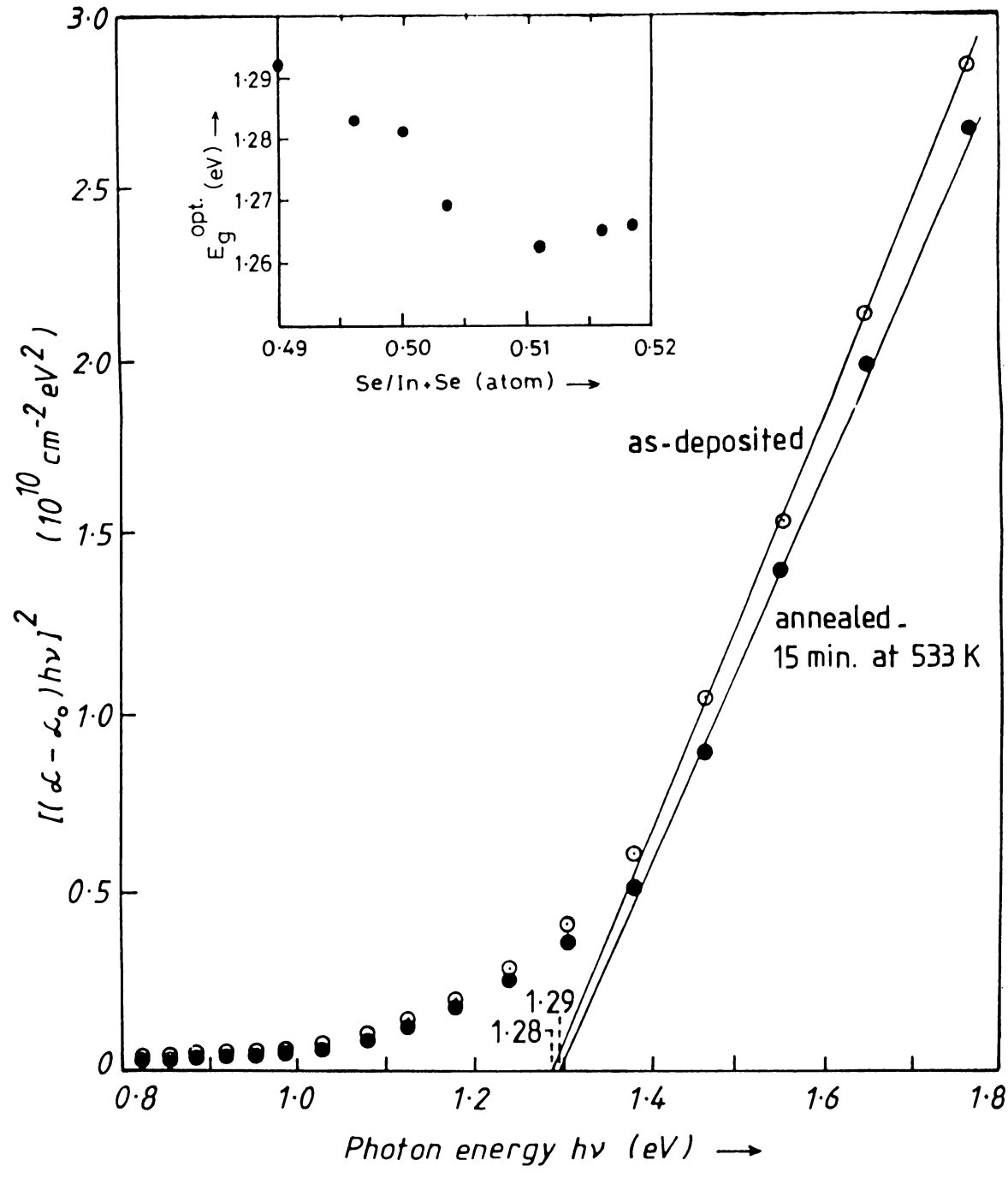

Fig.4.19 The plot of $[(\alpha - \alpha_o)h\nu]^2$ vs. photon energy for the stoichiometric InSe films, near the optical absorption edge for the as-deposited and annealed samples. Inset: Variation of $E_g^{opt.}$ for the films (unannealed) with slightly excess selenium content.

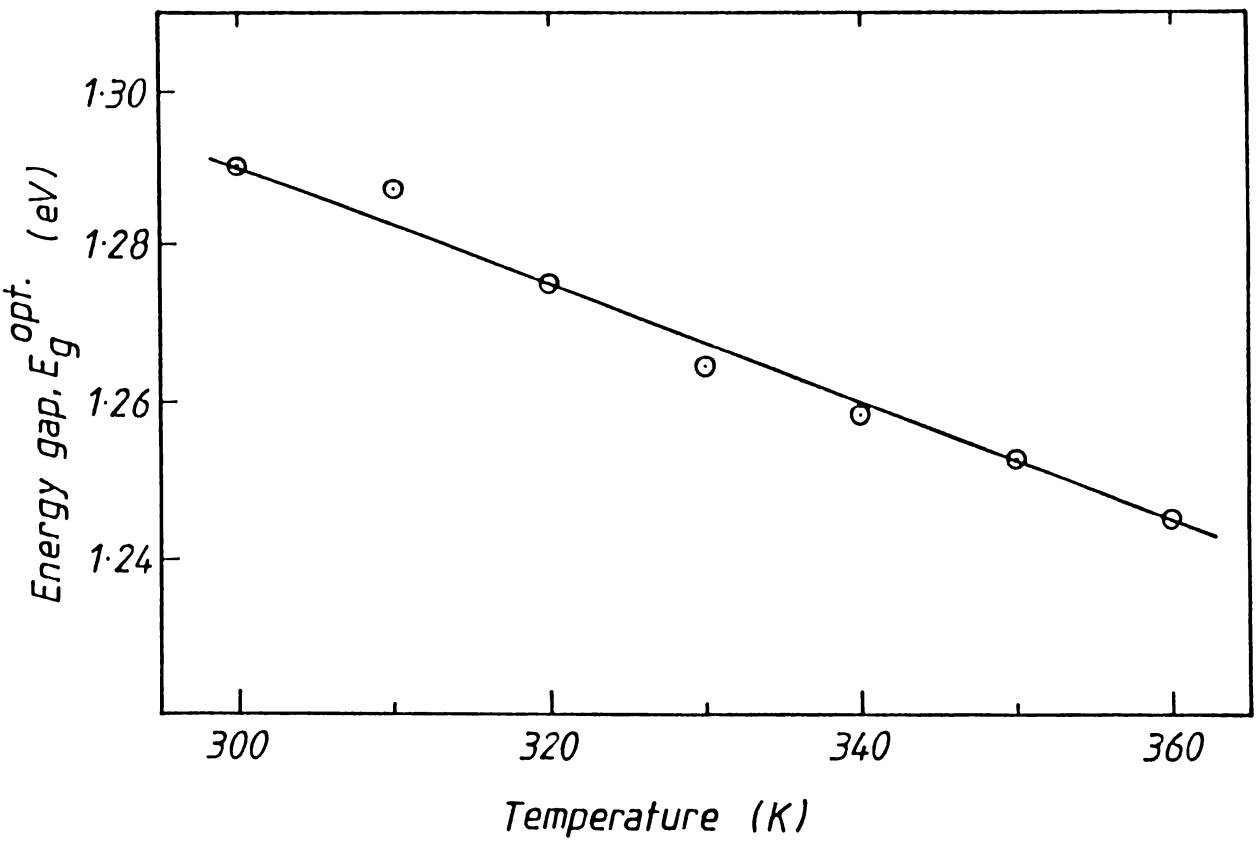

Fig.4.20 Temperature dependence of optical energy gap (film thickness 5200 Å.

$$(\alpha - \alpha_o)h\nu = A(h\nu - E_g^{opt})^{1/2} \quad \ldots (4.3)$$

where α_o is the background radiation and A is an empirical constant. The values of $E_g^{opt.}$ have been obtained from the intercept of the extrapolation of the linear portion of the curves onto the energy axis. This shows about ~1.29 eV for the monophasic films. The absorption in the sub band-gap region decreases with post depositional annealing of the film which brings in definable linear region in Fig.4.19. The higher absorption for the as-deposited films in the sub band gap region may arise from the inherent defects. These are modified during the annealing process.

In the films when the selenium gets a narrow precedence, the $E_g^{opt.}$ is found to cause a decrease in its magnitude (Fig.4.19: inset). The decrease of $E_g^{opt.}$ as result of slight increase of selenium in the compound may be due to an excessive number of mid-bandgap states near to the band edges. But, as the selenium content marginally increases, $E_g^{opt.}$ values show a tendency of increment.

The variation of the bandgap with temperature is shown in Fig.4.20. The temperature coefficient of bandgap calculated is 8.75×10^{-4} eV.K^{-1}. The variation can be explained by considering Schmidt's model (please see Chapter 2) of electron-lattice interaction in layered materials. According to eqn. 2.39 the self-energy for the free electron band is mainly determined by the properties of the electron band near the extremum. Increased temperature affects the self-energy of the electron band and thus accounts for a variation in energy gap.

4.III.D.2 Determination of refractive index

Fig.4.21 shows a typical reflectance interference recording of polycrystalline InSe film of thickness ~6000 Å on quartz substrate. The corresponding spectral dependence of the transmittance T for the same film is also shown in fig.4.21. In the figure the envelopes of R and R` are plotted with dotted lines[43,44]. The envelope touches the curves of spectral reflectance and thus give $R_{ex}$ and $R`_{ex}$. Equation (3.39) is then utilised for determining the value of n. The values of R_{ex} and $R`_{ex}$ for different wavelengths are listed in Table 4.8 and are used for obtaining the values of refractive indices plotted in Fig.4.22.

4.III.E Photoconductivity measurements.

4.III.E.1 Spectral response of photocurrent.

Figure 4.23 shows the dependence of photocurrent on wavelength in the range 650 to 1200 nm, for different bias voltages and for a fixed incident photon flux.

The photocurrent rises as the energy of the incident beam of photons increases from 1.12 eV till the band-gap absorption region. At the band-gap absorption region a broadening of the photocurrent peak occurs and thereafter it shows a decrease in the values. This may be due to the high recombination velocity of the carriers at shorter wavelengths[45].

When the ambient temperature is higher the onset of rise of

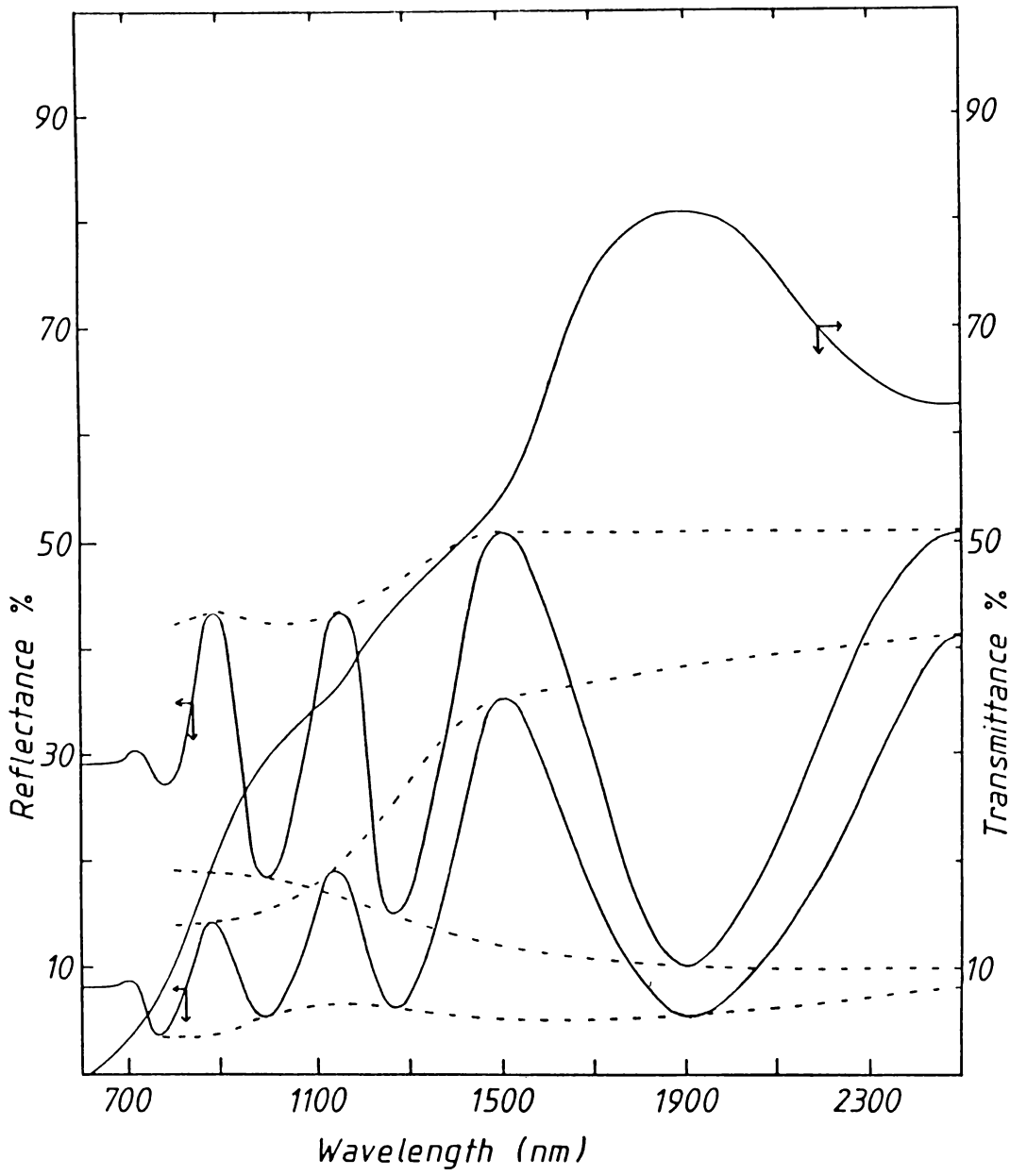

Fig.4.21 Reflectance spectra of a typical InSe film of thickness 6000 Å.

Table 4.8

Refractive index,n calculated from the values of R_{ex} and R'_{ex}.

Wavelength (nm)	R_{ex}	R'_{ex}	n
2500	41	33	3.1136
2300	41	33	3.1136
2100	41	33	3.1136
1900	41	33	3.1136
1700	40	32.3	3.116
1500	39	30	3.119
1300	33	21	3.2175
1100	26	12	3.3371
1000	25	10.8	3.3371
900	23	11	3.3042
800	24	10	3.278

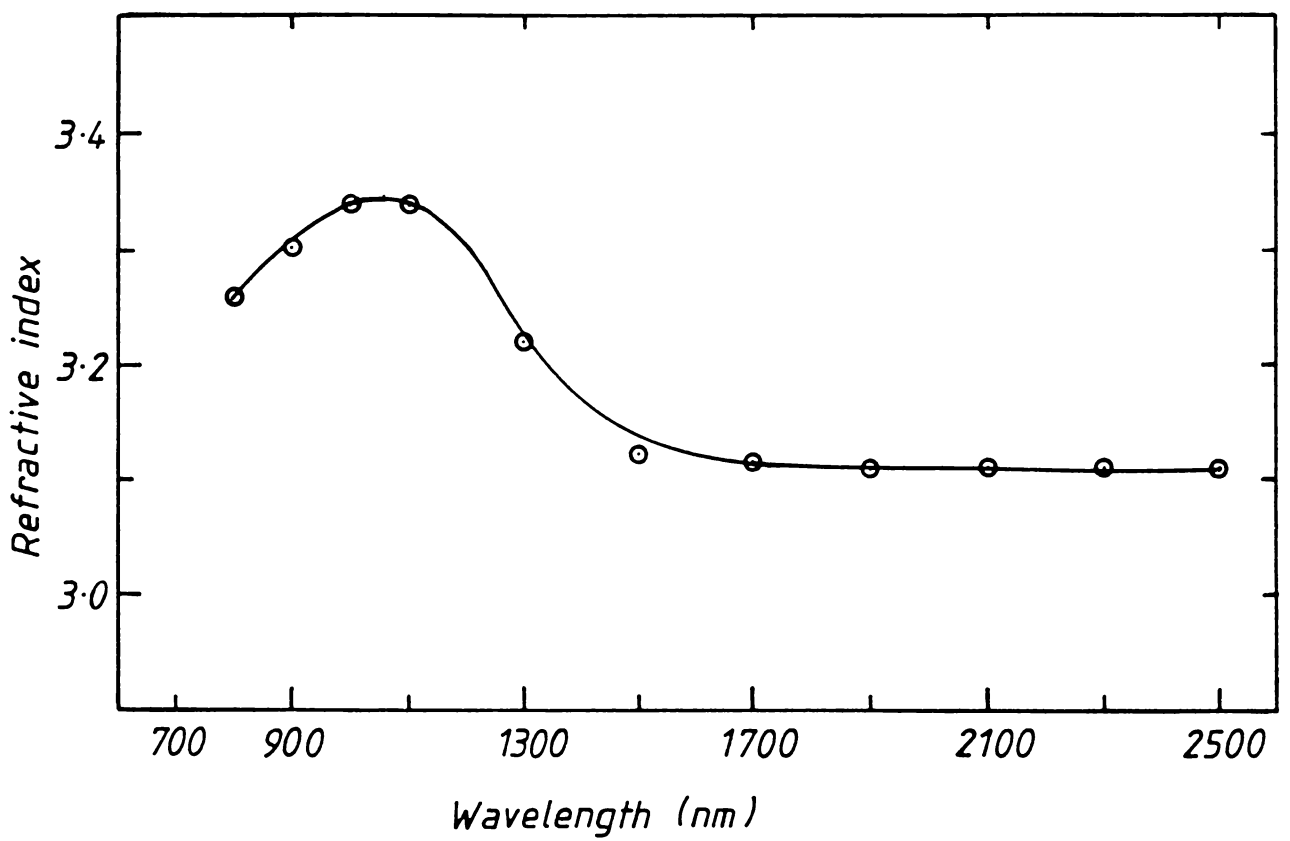

Fig.4.22 Variation of refractive index with wavelength (film thickness 6000 Å).

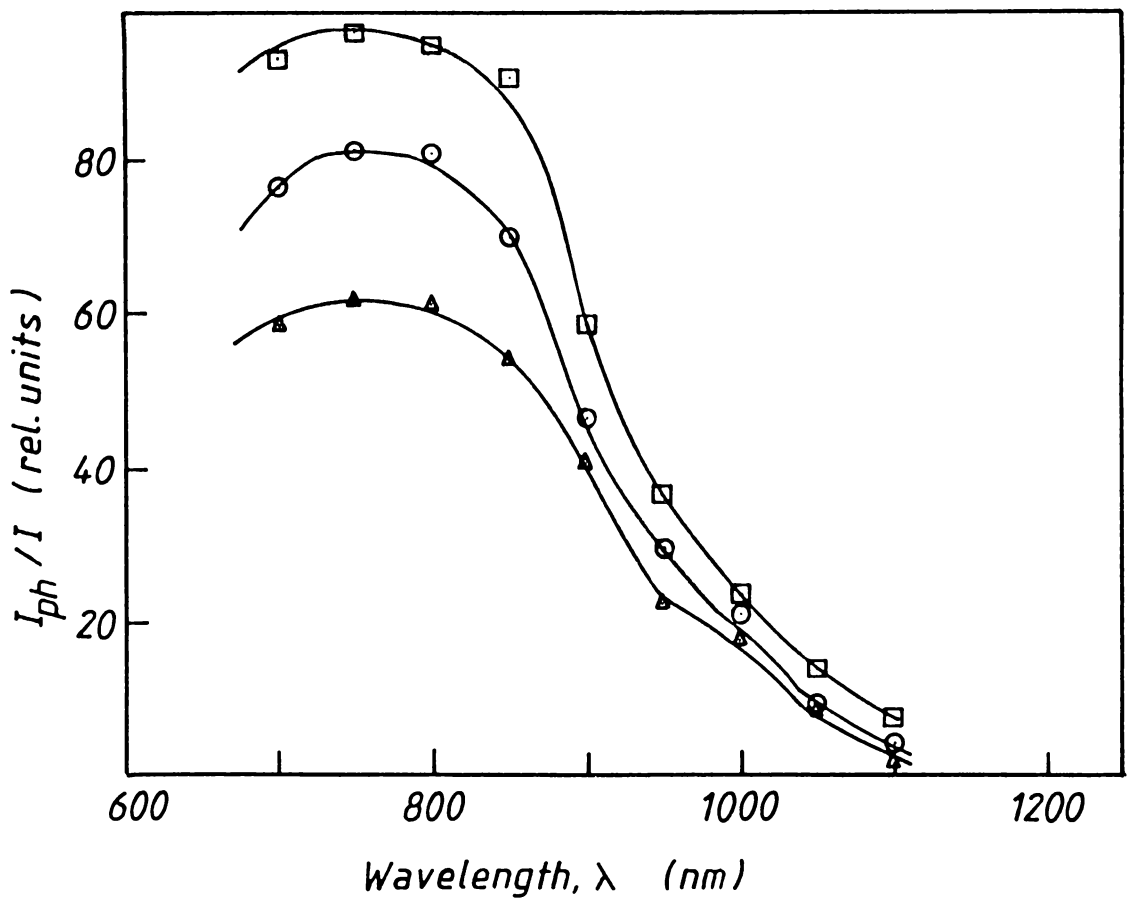

Fig.4.23 Spectral dependence of photocurrent for different bias voltages at room temperature.

(△) • 0.02 V ; (⊙) • 0.05 V ; (⊡) • 0.1 V

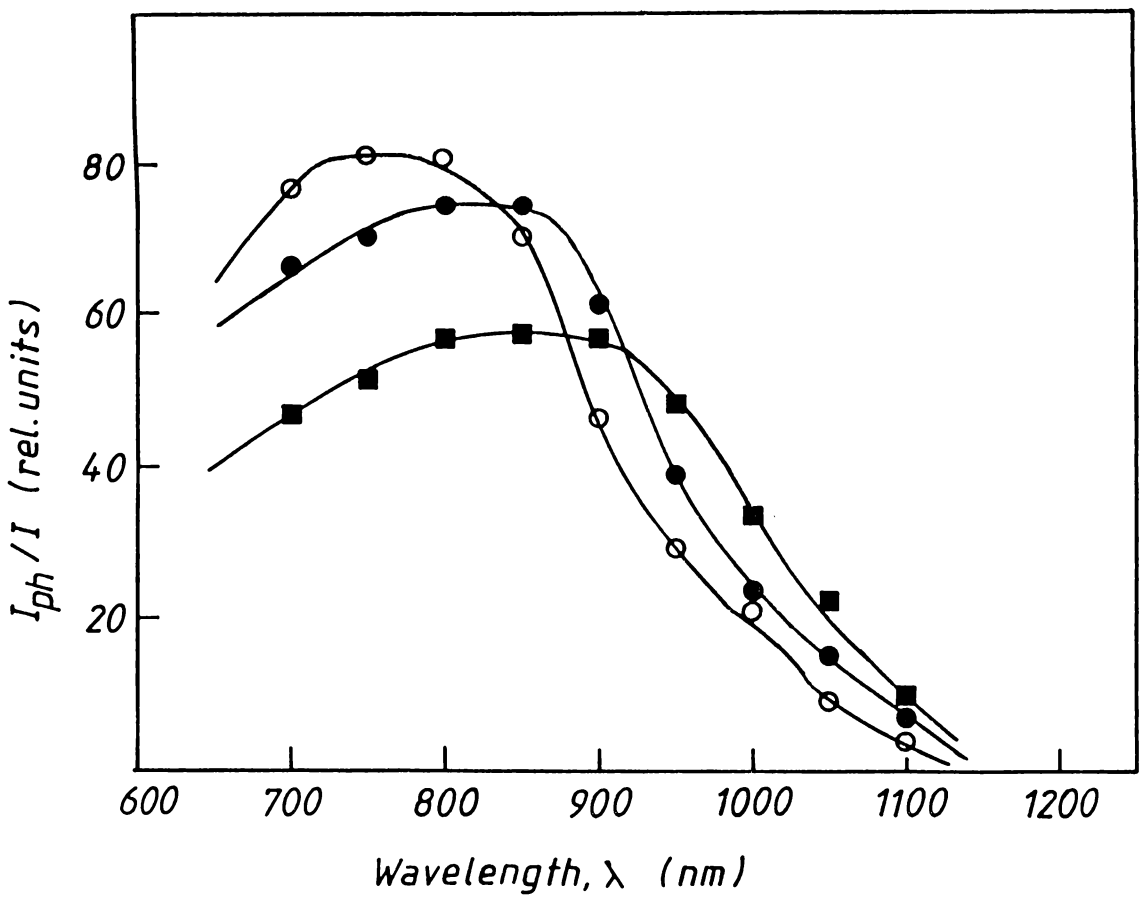

Fig.4.24 Spectral dependence of photocurrent at different temperatures for a fixed bias voltage (0.05 V). (O) • R.T ; (●) • 323 K ; (■) • 353 K

the photocurrent at lower energy side, and the broad maximum of photocurrent peak, shifts to the lower energy side further (Fig.4.24). This may be due to the increased electron-lattice interaction at higher temperatures and can be explained on the basis of the theory given in Chapter 2.

4.III.E.2 Temperature dependence of photocurrent :

Fig.4.25 shows a plot of the temperature variation of photocurrent at a fixed light intensity. The initial portion shows an increase of photocurrent as the temperature is increased. This is symptomatic of the shifting of Fermi level within the exponential trap distribution[46]. As the temperature is increased further there is a marked decrease in the photocurrent values. This happens in between 300 and 340 K. This can be attributed to desensitisation effect of the class II centers[47]. With increasing temperature, when the demarcation level associated with the class II centers moves from below to above the corresponding energy levels, such an outcome is normal.

In a more elaborate manner, this can be explained as follows. At low temperatures the probability of the hole capture at class II centers is higher than the probability of the thermal excitation of holes in the valence band. Therefore, these centers will be mainly occupied by holes, even if they belong to the category of recombination centers ; in these conditions both the lifetime and density of electrons in the conduction band are high (the material is sensitised). At higher temperatures, the probability of thermal excitation of holes from class II centers

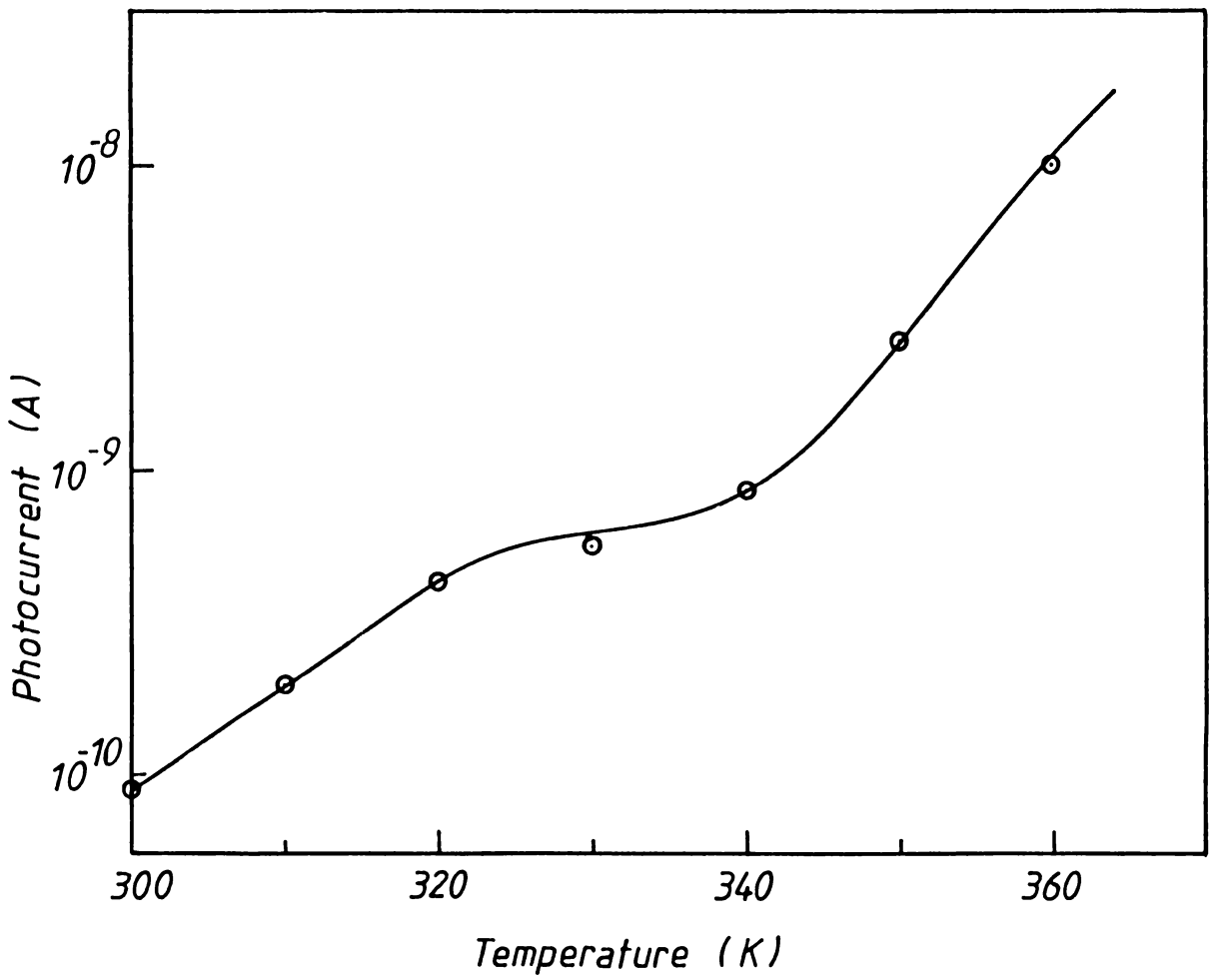

Fig.4.25 Temperature dependence of photocurrent of a typical InSe thin film (λ = 1000 nm.)

to the valence band increases, which means that holes are eventually captured by the class I centers. Therefore the recombination rate at class I centers increases, with a subsequent decrease of both the lifetime and the density of conduction electrons.

Again as the temperature is increased the photocurrent values increase with a less expeditious rate. The hole demarcation level will move upwards due to the shift of the Fermi level with increase in temperature. This will lead to the conversion of some of the recombination centers to hole traps and consequent desensitisation.

Beyond this region, a fairly steep increase in photocurrent values with temperature is observed. This may be due to the increase in defect centers with the rise of temperature. At this stage again the photocurrent can be thought of as the combined effect of the class I and class II traps.

4.III.E.3 Variation of I_{ph} with light intensity :

Fig.4.26 shows a typical plot of the variation of photocurrent with different excitation intensity at room temperature (i.e. 300 K). This lux-ampere characteristic plot consists of two regions of almost steady profile. At moderate intensities it exhibits a superlinear photocurrent behaviour and at higher intensities a quasi-saturation region corresponding to quenching of photoconductivity. In the first region $I_{ph} \sim L^{1.29}$ and in the second region $I_{ph} \sim L^{0.72}$. These variation can be explained in terms of charge-trapping and recombination

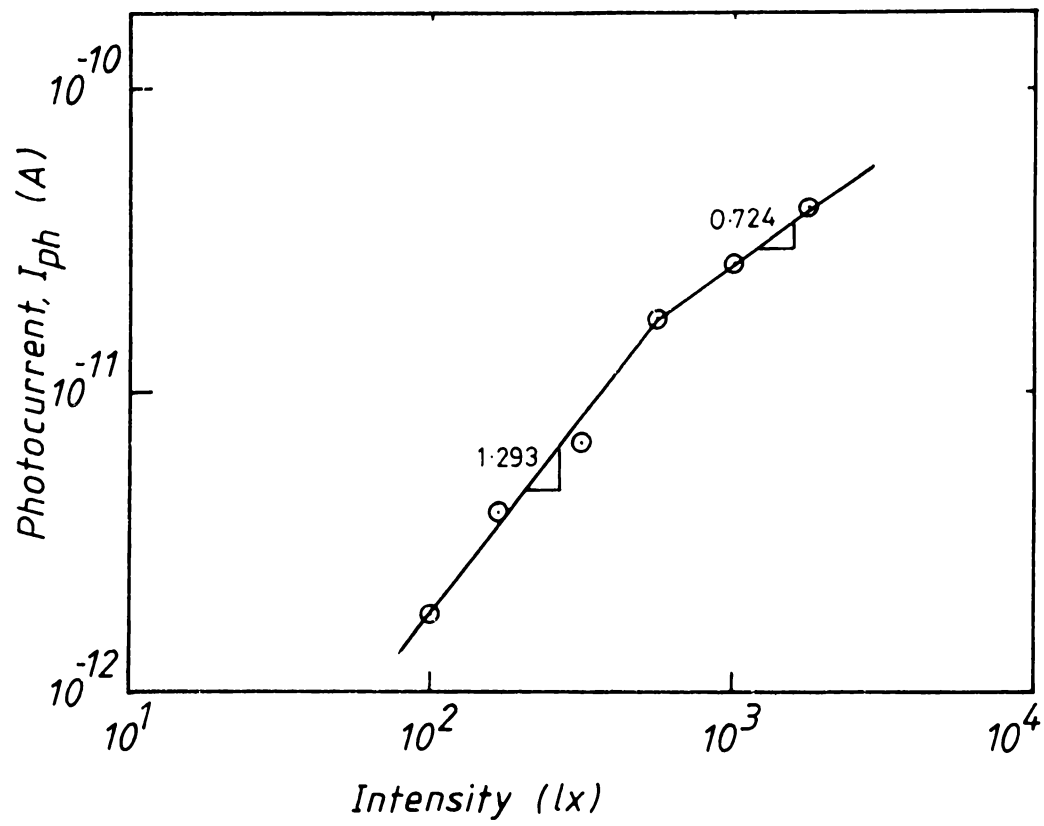

Fig.4.26 Variation of photocurrent of InSe film with incident light intensity.

processes. In the process of film deposition various imperfections may be formed and this is very strong in the case of a layered material, as seen earlier in microstructural studies. Accordingly there are two kinds of dominant states (class I and class II) possible in the forbidden gap. Class I consists of states which have roughly similar cross section for both electrons and holes. Class II states are close to the valence band and have a higher capture cross section for holes than for electrons.

With increasing illumination, when the demarcation level associated with the class II centers moves from above to below to the corresponding energy levels, an increase in photosensitivity occurs. Thus at low excitation levels the class II centers will not act as recombination centers. But when the excitation level is increased further a sublinear region results. This indicates that the occupance of class-I centers consist of a continuous distribution of electron-trapping levels lying between the conduction level and the electron Fermi level. The effect of shifting of demarcation level would be to convert more of the class - I centers to recombination levels and giving rise to a decrease in photocurrent. This type of dependence has been earlier reported in CdS_{1-x} Se_x sintered layers[48].

4.III.F Photovoltaic effect in Indium selenide schottky barriers :

4.III.F.1 Spectral response.

Fig.4.27 shows a typical spectral response plot of the

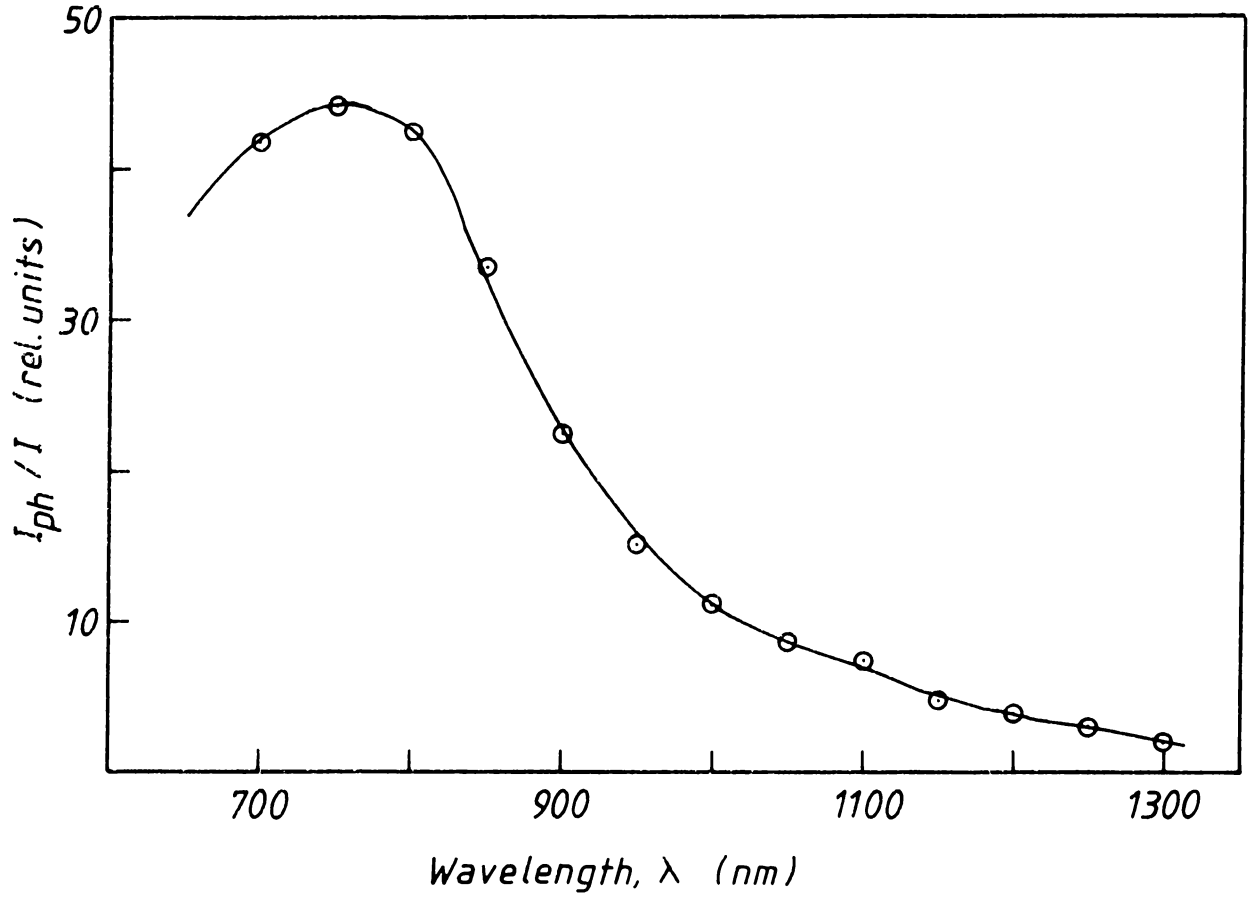

Fig.4.27 Spectral response of Schottky barrier formed with Au. (film thickness- 4800 Å).

InSe-Au system with an ohmic indium contact, in the wavelengt range 600-1300 nm.

When a beam of light enters a Schottky barrier device, thre distinct types of photo effects can take place.

1) Light can be absorbed in the metal and excite electron over the barrier into the semiconductor (say, Process I) and i commonly used to measure the barrier height $\emptyset_B$.

2) Long wavelength light can be absorbed deep in th semiconductor thus creating hole-electron pairs just as in a p-n junction (say, Process II). The holes thus created must the diffuse to the junction edge to be collected.

3) Shorter wavelength light entering the device is absorbe partly in the bulk semiconductor and partly in the depletio region, and very short wavelength light is absorbed absolutely i the depletion region (say, Process III).

Of these processes, although the excitation of carriers f the metal into the semiconductor is having a smaller eff (nearly 2 orders or more) than the band-to-band excitat mechanisms (process II and III), they can be used for finding barrier height $\emptyset_B$. In such a case, the short-circuit current absorbed photon ($J_{ph} = I_{ph}/F_o$, where F_o is known as quantum given by $F_o = I \lambda$) as a function of the photon energy given by the Fowler theory[49]

$$J_{ph}^{1/2} = A (h\nu - \emptyset_B),$$

where A is a constant.

The Fowler plot of the formed InSe-Au schottky

InSe-Au system with an ohmic indium contact, in the wavelength range 600-1300 nm.

When a beam of light enters a Schottky barrier device, three distinct types of photo effects can take place.

1) Light can be absorbed in the metal and excite electrons over the barrier into the semiconductor (say, Process I) and is commonly used to measure the barrier height ϕ_B.

2) Long wavelength light can be absorbed deep in the semiconductor thus creating hole-electron pairs just as in a p-n junction (say, Process II). The holes thus created must then diffuse to the junction edge to be collected.

3) Shorter wavelength light entering the device is absorbed partly in the bulk semiconductor and partly in the depletion region, and very short wavelength light is absorbed absolutely in the depletion region (say, Process III).

Of these processes, although the excitation of carriers from the metal into the semiconductor is having a smaller effect (nearly 2 orders or more) than the band-to-band excitation mechanisms (process II and III), they can be used for finding the barrier height ϕ_B. In such a case, the short-circuit current per absorbed photon ($J_{ph} = I_{ph}/F_o$, where F_o is known as quantum yield given by $F_o = I \lambda$) as a function of the photon energy $h\nu$ is given by the Fowler theory[49]

$$J_{ph}^{1/2} = A (h\nu - \phi_B), \qquad \ldots (4.4)$$

where A is a constant.

The Fowler plot of the formed InSe-Au schottky barrier

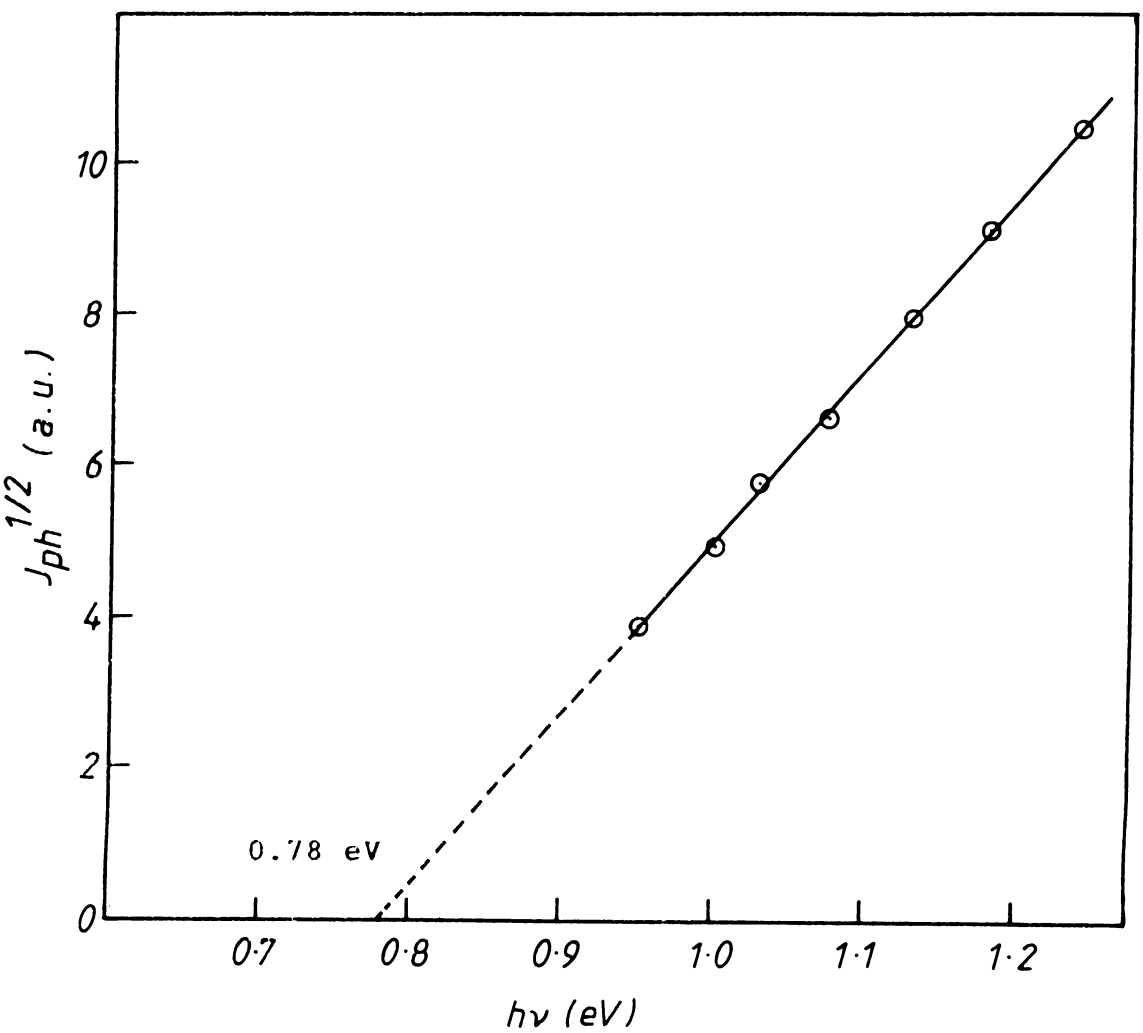

Fig.4.28 Fowler plot (for a diode formed with Au) of an Au- InSe-In structure. Meeting point of the straight line gives the barrier height, Φ_B = 0.78 eV

Table 4.9

Au- InSe Schottky barrier height determined by different methods

Cell no.	Barrier height (eV)		
	I-V	C-V	$I_{ph}^{1/2}$-V
A	0.822	0.79	0.78
B	0.78	0.78	0.79
C	0.85	0.81	0.80

device is shown in Fig.4.28. The barrier height $\emptyset_B$ is obtained from the extrapolation of the line joining the experimental points to the energy axis.

The data of the barrier heights determined by different methods is compared in Table 4.9.

4.III.F.2 I-V characteristics.

Figure 4.29 shows typical I-V characteristics measured on a cell of thickness 4000 Å.

The behaviour of the current-voltage characteristic of a Schottky barrier can be explained in terms of either the 'diode' or the 'diffusion' theory[50]. The choice of either one depends upon the width of the depletion region with respect to the mean free path of electrons scattered by acoustical phonons. When usual approximations are made, both deviations result in essentially the same current-voltage dependence. Then the forward current I_f is related to the applied voltage V, by[51]

$$I_f = I_s [\exp (qV/nkT) - 1] \quad \ldots (4.5)$$

where q is the electronic charge, k, the Boltzmann constant, T, the ambient temperature, and n, a dimensionless factor indicating the deviation from the ideal schottky cell characteristics. I_s is accounted for the saturation current given by the relation,

$$I_s = A^* S T^2 \exp (-q\emptyset_B/kT) \quad \ldots (4.6)$$

where S is the area of the cell and $\emptyset_B$ is the barrier height. In this the effective Richardson constant is given by

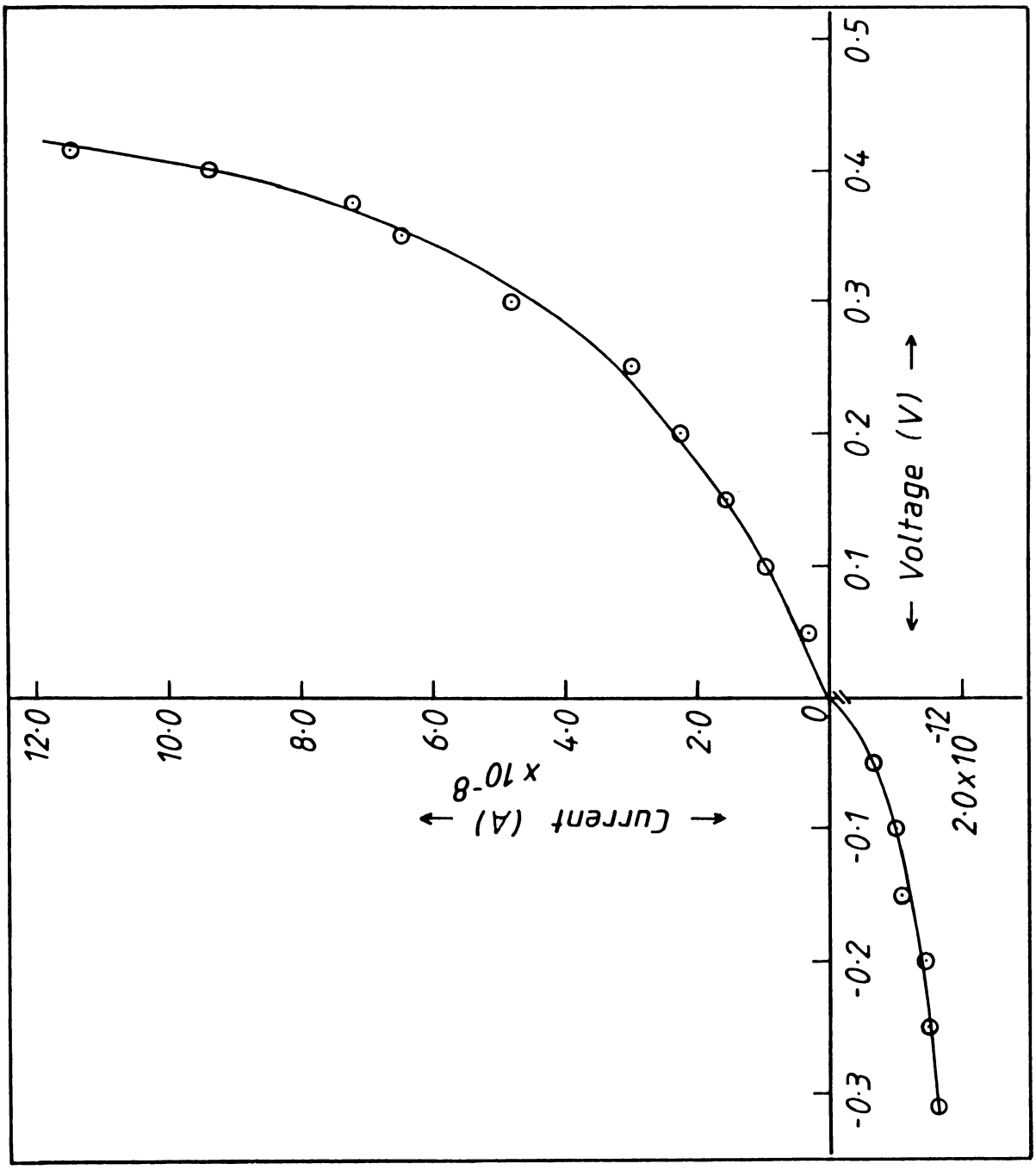

Fig.4.29 Dark I-V characteristic of an Au/InSe schottky diode.
(film thickness - 4000 Å).

$A^* = A\ (m^*/m_o)$, where A is the Richardson constant,and m^* the effective mass of the electron.

In the voltage range V > 3 kT, eqn. (4.5) can be rewritten as

$$I_f = I_s \exp\ (V/V_o) \qquad \ldots\ (4.7)$$

where I_s is the temperature-dependent saturation current. Accordingly V_o can be calculated from the slope of the V-I characteristics (Fig. 4.30).

If the diode barrier is a perfect schottky barrier, V_o would be given by

$$V_o = kT/q \qquad \ldots\ (4.8)$$

From Fig. 4.31, it is evident that it does not hold. Alternatively, a relationship of the form

$$V_o = (k/q)\ (T+T_o) \qquad \ldots\ (4.9)$$

would fit the data nicely with $T_o = 73 \pm 4$ K (Fig.4.31).

So the classical relation would read[52],

$$I_s = A^*\ ST^2 \exp\ [-q\emptyset B/k\ (T + T_o)] \qquad \ldots\ (4.10)$$

The logarithmic plot of I_s/T^2 as a function of $1/(T+T_o)$ will give the barrier height $\emptyset_B$. Fig. 4.32 shows the above plot, from which the barrier height obtained is found to be 0.822 ± 0.05eV.

4.III.F.3 C-V measurements.

Fig.4.33 shows typical C-V characteristics for low reverse bias voltages at 3 different frequencies.

When a small time - dependent voltage is superimposed upon a d.c. reverse bias, charges of one sign are induced in the metal

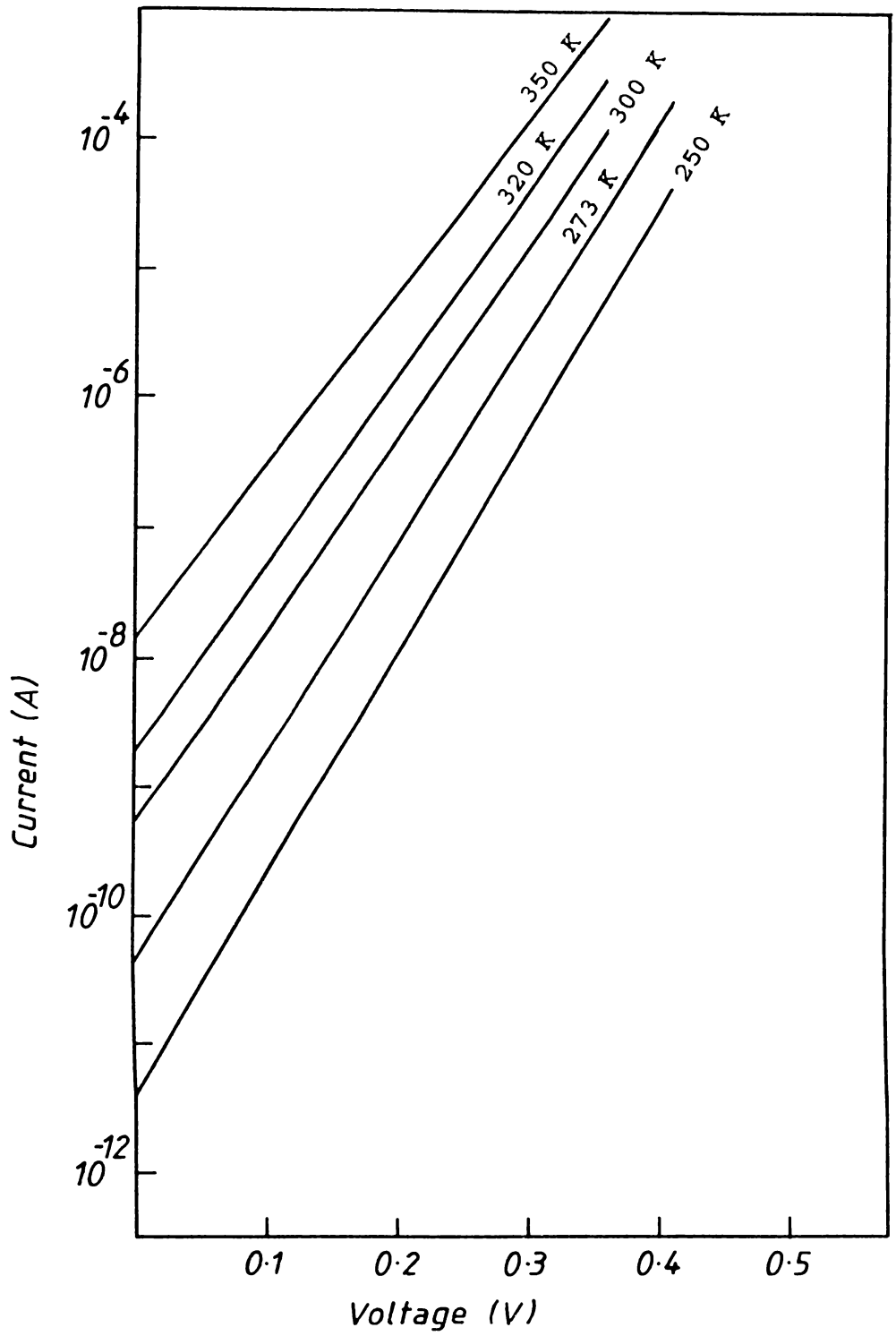

Fig.4.30 I-V characteristic of an Au/InSe schottky diode for different temperatures from 250 K to 350 K.

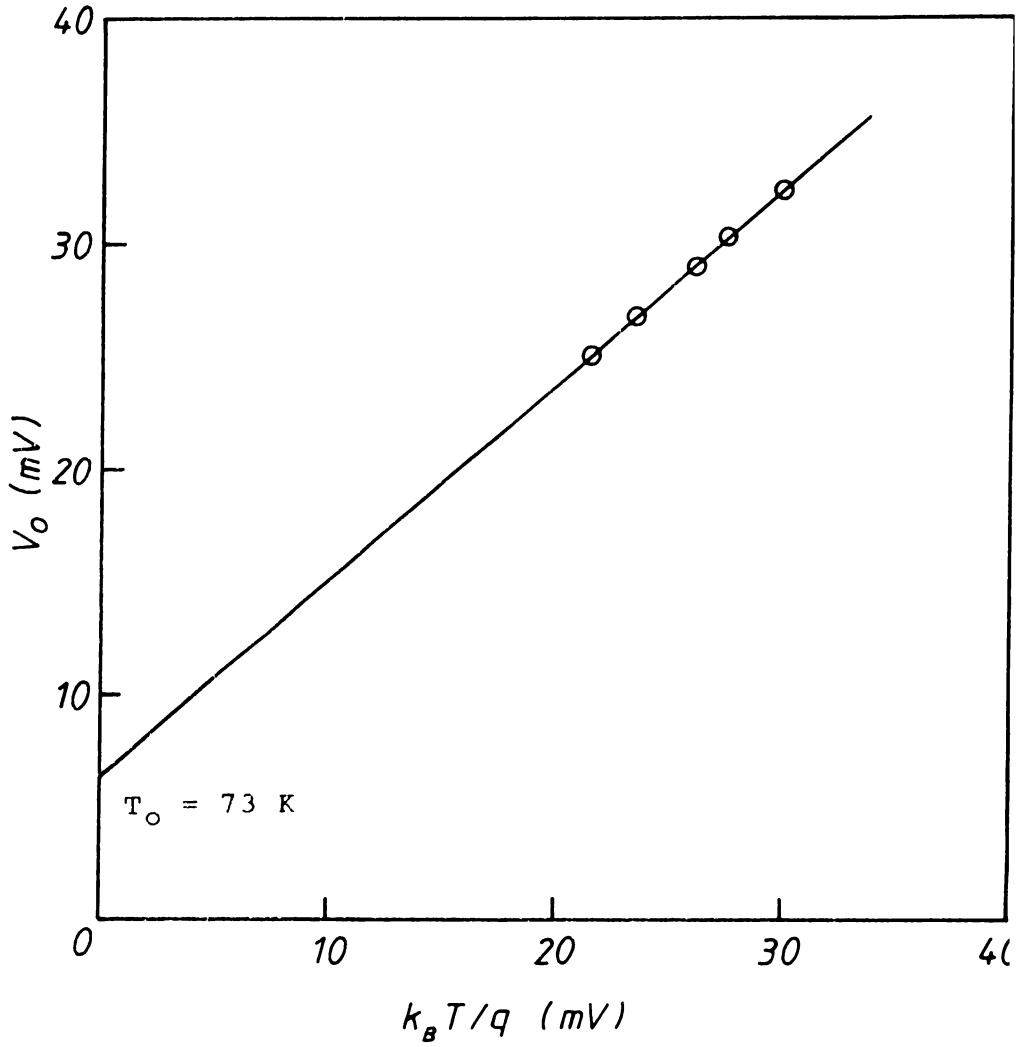

Fig.4.31 Dependence of V_o on temperature.

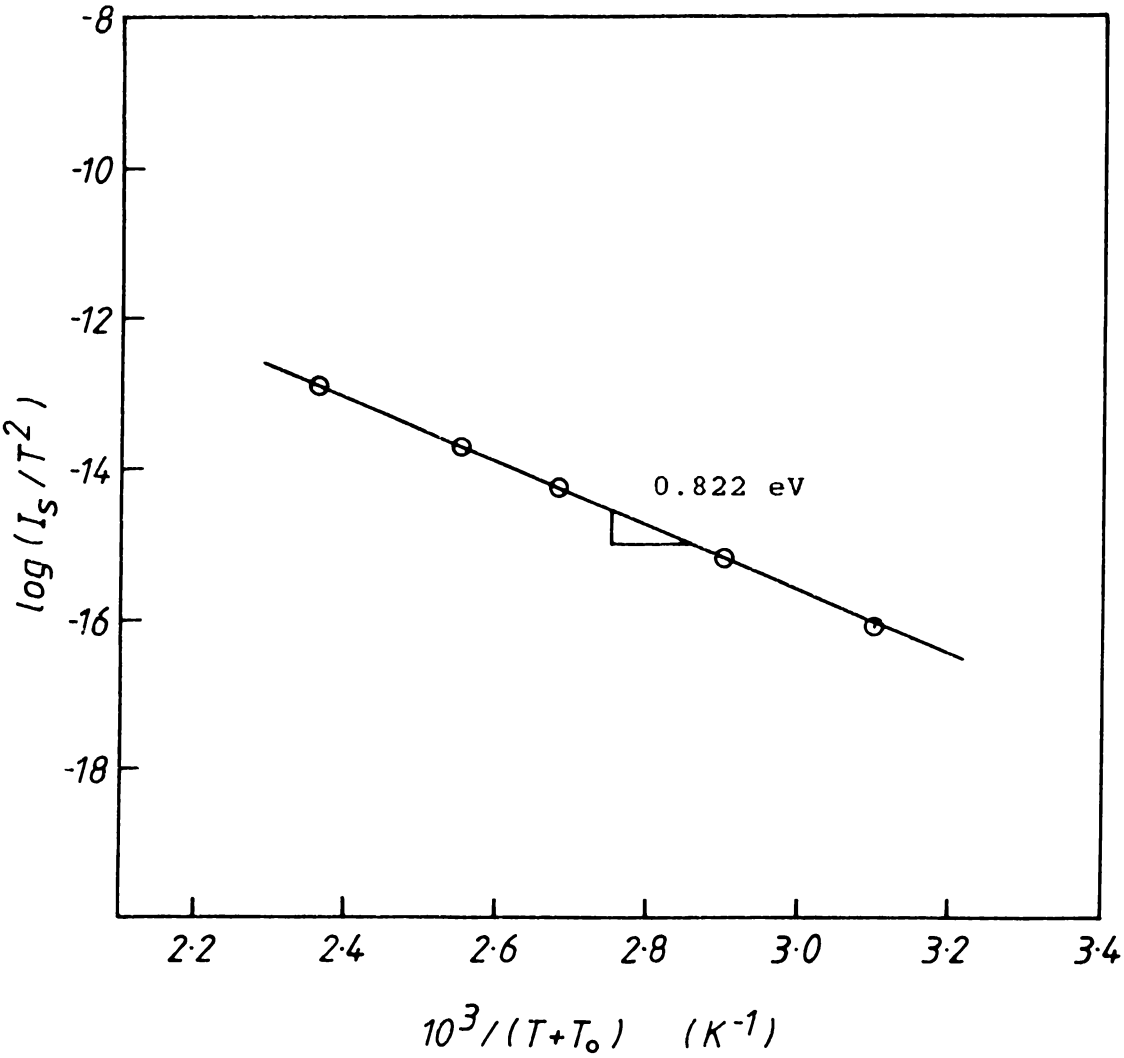

Fig.4.32 Plot of I_s/T^2 vs. $1/(T+T_o)$.

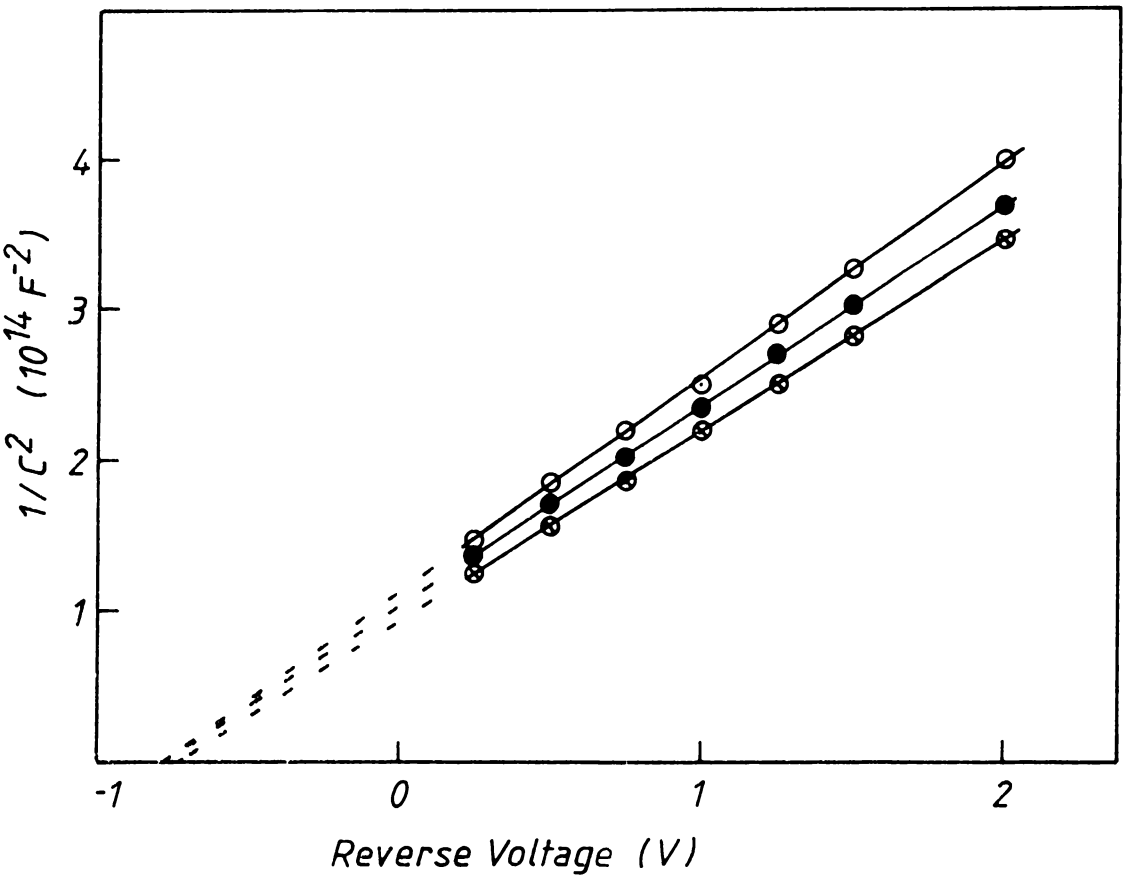

Fig.4.33 Dependence of $1/C^2$ on reverse-biased voltage for three different frequencies.

(O) - 500 Hz ; (●) - 1 KHz ; (⊠) - 5 KHz

surface and of the opposite sign in the semiconductor by a slight widening of the depletion layer width. Thus the space charge layer gives an effective capacitance $C = A\,\varepsilon\varepsilon_o/d$,where ε is the permittivity of the semiconductor (for InSe this is 9 [53]) and d, the depletion layer width. At a larger applied reverse bias voltage, the depletion layer expands according to[51]

$$d = 2\,\varepsilon\,(V_D - V)^{1/2} / q\,Neff \qquad \ldots (4.11)$$

where V_D is the diffusion voltage, Neff the concentration of noncompensated ionised donors and $\varepsilon_o = 8.85 \times 10^{-14}$ F/cm and therefore the capacitance decreases

$$C = A \frac{qN_{eff}\,\varepsilon^{1/2}}{2\,(V_D - V)} \qquad \ldots (4.12)$$

where A is the area of the cell.
It can be seen from eqn.(4.12) that if $1/C^2$ is plotted against the reverse bias voltage - V, a straight line is obtained in which the intercept is V_D.

It should be noted that this procedure does not give the barrier energy directly but only the diffusion potential V_D, which differs by the Fermi energy. In more exact terms, this is

$$\phi_B = V_D + \phi_F + kT/q \qquad \ldots (4.13)$$

where ϕ_F is the energy difference between the Fermi level and the bottom of the conduction band. The Fermi energy can be computed if the net doping density N_{eff} and the effective mass are known. The carrier density itself can also be conveniently determined from the slope of the $1/C^2$ vs. reverse bias voltage plot

$$N_{eff} = - \frac{2}{q \varepsilon \varepsilon_o A^2} \frac{dV}{d(1/C^2)} \quad \ldots (4.14)$$

The diffusion potential dervied from the intercept of the above straight line (V vs. $1/C^2$ line) on horizontal axis is equal to 0.79 ± 0.03V which is in good agreement with the value of the barrier height determined from I-V characteristics. The mean value of the noncompensated ionized donor concentration obtained for different cells is equal to ~4.9×10^{17} cm^{-3}, which is slightly less than the value determined from Hall measurements.

4.III.F.4 Determination of Diffusion length.

The diffusion length can be obtained from the plot of the incident photon fluxes F yielding the same photocurrent vs. inverse absorption coefficient α. Fig.4.34 shows such a plot of F vs. α^{-1} for two different samples of nearly 2 m thickness.

When a Schottky barrier is formed on a semiconductor material, a readjustment of charge takes place for establishing the thermal equilibrium. When an incident light falls on this junction, it is absorbed and hole-electron pairs will be created just as in a p-n junction. The field in the depletion region 'sweeps' the photogenerated carriers and results in the formation of photocurrent. The photocurrent collection from the 'base' of the Schottky barrier cell[45] is qualitatively the same as from the 'base'of a p-n junction cell. The photocurrent collected from the base region with an ohmic back contact is then

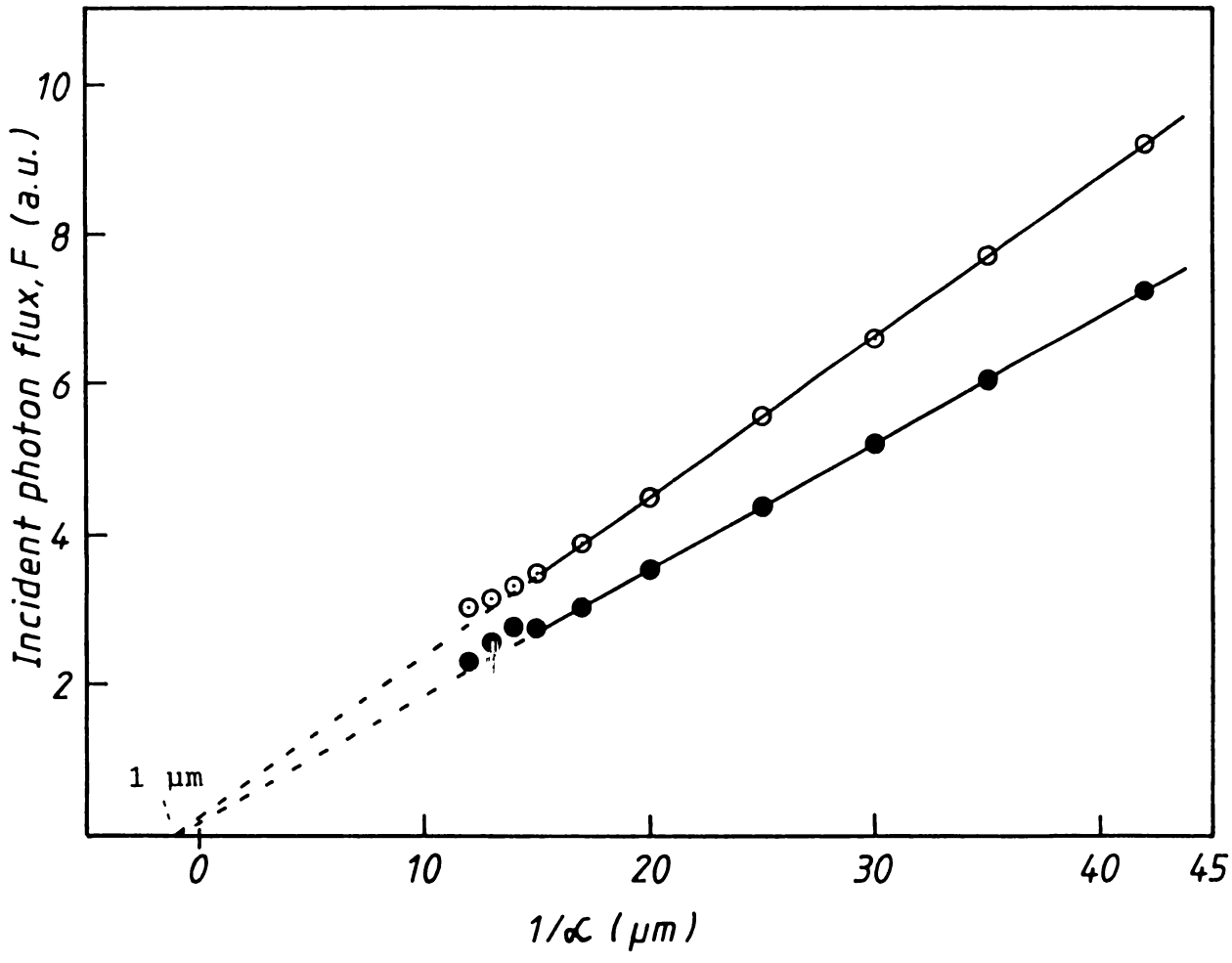

Fig.4.34 Diffusion length of minority carriers for different Au-InSe schottky diodes.

[film thickness : (O) - 1.8 µm ; (●) - 2.4 µm]

Table 4.10

Determination of minority carrier Diffusion length

Diffusion length (μm)	Cell			
	B237	B123	P37	011
L_p	1.2	1.0	0.6	0.9

$$I_{ph} = \frac{q F_o \alpha L_p}{(\alpha^2 L_p^2 - 1)} r \exp(-\alpha W)$$

$$x\left[\alpha L_p - \frac{\cosh(H'/L_p) - \exp(-\alpha H')}{\sinh(H'/L_p)}\right] \quad ...(4.15)$$

where H' is the thickness of the device minus the width of the depletion region: $H' = d-W$, F_o the incident photon flux at that particular wave length λ, α the absorption coefficient of the material, L_p the hole diffusion length, and r the function representing the reflection of light from the surface for the wavelength λ, which is equal to (1-R) where R is the reflection coefficient.

If the device thickness d is much greater than the diffusion length, $H' >> L_p$, eqn.(4.15) simplifies to[45]

$$I_{ph} = (qF_oL_p/(\alpha L_p + 1))\ r \exp(-\alpha W) \quad ... (4.16)$$

From this equation it is possible to compute the diffusion length using the value of W obtained from the capacitance measurements. If the light intensity incident on the 'base' region, $F = F_o\ r \exp(-\alpha W)$ is adjusted to maintain a constant I_{ph} at various wavelengths then eqn.(4.13) reduces to

$$F = K(\alpha^{-1} + L_p), \quad ... (4.17)$$

where K is a constant. Thus, the diffusion length can be determined from the intercept at F = 0 of the plot of F vs. α^{-1}. Fig.4.34 shows such a plot, and straight lines were obtained by joining the experimental points and both the lines intersect the abscissa at nearly the same point yielding a value of diffusion length L_p = 1.0 μm. Table 4.10 gives the diffusion length determined for different cells. These values of L are smaller

than that reported in single crystals. This may be due to the presence of grain boundaries in these films which may affect negatively the carrier movement.

4.IV Conclusions

Single-phased InSe films have been prepared by the elemental evaporation of indium and selenium. The optimum substrate temperature for this is found to be 488K with a short post-depositional annealing at 533K. The structure of the InSe films corresponds to the rhombohedral phase as determined from the XRD measurements. The compound formation is confirmed by the XPS analysis and composition of the films is ascertained by fluorimetric method. Electron diffraction patterns identify the crystallites as single crystals with preferred orientations.

The prepared monophasic films, usually are of n-type with conductivities in the range 7.0×10^{-2} - 5.0×10^{-1} ohm^{-1} cm^{-1}. The optical band-gap is determined to be ~1.29 eV. The optical-gap and the absorption coefficient are in the range of maximum of the solar spectrum and close to the optimal values required for photovoltaic applications. Photoconductivity measurements reveal that the photocurrent arises mainly from the band-gap absorption. The photovoltaic effect exibited by the gold-InSe schottky barriers demonstrates a barrier height of 0.80 eV. The barrier heights determined from various methods display an excellent coincidence. The diffusion lengths determined are clearly larger than those of from the classical semiconductors; thus favouring the choice of this compound semiconductor for device applications.

References:

1. T.Matsushita, T.T.Nang, M.Okuda, A.Suzuki and S.Yokota, Jap.J.Appl.Phys., 15, 901 (1976).
2. T.T.Nang, T.Matsushita, M.Okuda and A.Suzuki, Jap.J.Appl. Phys., 16, 253 (1977).
3. A.Segura, J.M.Besson, A.Chevy and M.S.Martin, Nuovo Cimento, 38B, 345 (1977).
4. C.Cleman, X.I.Saldana, P.Munz and E.Bucher, Phys.Stat.Solidi (a) 49, 437 (1978).
5. V.L.Bakumenko, Z.D.Kovalyuk, L.N.Kurbatov and V.F.Chishko, Sov.Phys.Semicond., 12, 1307 (1978).
6. A.Segura, J.P.Guesdon, J.M.Besson and A.Chevy, Rev.Phys.Appl, 14, 253 (1979).
7. K.Ando and A.Katsui, Thin Solid Films, 76, 141 (1981).
8. Y.Hasegawa and Y.Abe, Phys.Stat.Solidi(a), 70, 615 (1982).
9. T.Matsushita, A.Suzuki, M.Okuda, H.Naitoh and T.Nakau, Jap.J.Appl.Phys., 22, 762 (1983).
10. A.Segura, J.P.Guesdon, J.M.Besson and A.Chevy, J.Appl.Phys., 54, 876 (1983).
11. A.Segura, J.L.Valdes, F.Pomer, A.Cantarero and A.Chevy, in : Proc.5th E.C.Photovolt.Sol.Energy Conf., Kavouri,1983 (Reidel,Dordrecht,1984), p.927.
12. A.Sugura, J.L.Valdes, A.Cantarero, F.Pomer, J.P.Martinez, B.Mari and A.Chevy, in: Proc. 6th Euro.Communities Photovolt. Sol.Energy Conf., Londres,1985 (Reidel,Dordrecht,1985),p.774.
13. J.Martinez-Pastor, A.Segura, J.L.Valdes and A.Chevy, J.Appl. Phys., 62, 1477 (1987).

14. S.Shigetomi, T.Ikari, Y.Koga and S.Shigetomi, Jap.J.Appl. Phys., **27**, 1271 (1988).

15. J.P.Guesdon, C.Julien, M.Balkanski and A.Chevy, Phys.Stat. Solidi (a) **101**, 495 (1987).

16. M.Yudasaka, T.Matsuoka and K.Nakanishi, Thin Solid Films,**146**, 65 (1987).

17. M.Persin, A.Persin and B.Celustka, Thin Solid Films, **12**, 117 (1972).

18. B.S.Naidu, A.K.Sharma, D.V.K.Sastry, Y.Syamalamba and P.Jayarama Reddy, J.Non-Cryst.Solids, **42**, 637 (1980).

19. H.Hashimoto, H.Nishimura and H.Suzuki, Jap.J.Appl.Phys., **20**, 1163 (1981).

20. D.V.Krishna Sastry and P.Jayarama Reddy, Thin Solid Films, **105**, 139 (1983).

21. I.Watanabe and T.Yamamoto, Jpn.J.Appl.Phys., **24**, 1282 (1985).

22. J.P.Guesdon, C.Julien, M.Balkanski and A.Chevy, Phys.Stat. Solidi(a), **101**, 495 (1987).

23. Boben Thomas and M.G.Krishna Pillai, International Conference on Semiconductor materials, Delhi University, Delhi, Dec.13-16, 1988.

24. K.-G. Gunther, in The use of thin films in physical investigations, (Ed.)J.C.Anderson, Academic Press, New York, (1966).

25. R.Glang in L.I.Maissel and R.Glang (Eds.), Handbook of Thin Film Technology, McGraw Hill, New York,(1970) p.1-81.

26. Boben Thomas and T.R.N.Kutty, (to appear in Physica Status Solidi (a)).

27. D.R.Penn, J.Elect.Spect.Rel.Phenom., **9**, 29, (1976).

28. A.W.C.Lin, N.R.Armstrong and T.Kuwana, Anal.Chem., **49**, 1228, (1977).

29. J.H.Scofield, J.Elect.Spect.Rel.Phenom., 8, 129 (1976).

30. R.J.Thorn, J.Elect.Spect.Rel.Phenom., 31, 207 (1983).

31. J.Rigoult, A.Rimsky and A.Kuhn, Acta Cryst.,**B 36**, 916 (1980).

32. J.H.C Hogg, H.H Sutherland and D.J.Williams, Acta Cryst., **B 29**, 1590 (1973).

33. H.P.Klug and L.E.Alexander, X-ray Diffraction Procedures, Wiley, London, (1954), p.491.

34. E.F.Kaeble, Handbook of X-rays, McGraw-Hill, New York, (1967)

35. R.W.Vook and F.Witt, J.Vac.Sci.Technol., **2**, 49 (1965).

36. A.J.McEvoy, A.Parkes, K.Solt and R.Bichsel, Thin Solid Films, **69**, L 5 (1980).

37. J.A.Bearden and A.F.Burr, Rev.Mod.Phys., 39, 125 (1967).

38. C.D.Wagner, W.M.Riggs, L.E.Davis, J.F.Moulder and G.E.Muilenberg, Handbook of X-ray Photoelectron Spectroscopy, Perkin- Elmer Corporation, Physical Electronics Division, Eden Prairie, Minnesota (1979),p.92 & 173.

39. M.K.Bahl, R.L.Watson and K.J.Irgolic, J.Chem.Phys., **72**, 4069 (1980).

40. C.A.Parker and L.G.Harvey, Analyst(London), 87, 558 (1962).

41. J.Bardeen, F.J.Blatt and L.H.Hall, in: R.Breckenridge, B.Russel and T.Hahn (Eds.), Photoconductivity Conf., Wiley, New York,(1956), p.146.

42. S.W.Kurnick and J.M.Powell, Phys.Rev., 116, 597, (1959).

43. I.Ohlidal, K.Navratil and E.Schmidt, Appl.Phys., **A 29**, 157 (1982).

44. D.T.Larson, L.A.Lott and D.L.Cash, Appl.Optics, 12, 1271 (1973).

45. H.J.Hovel, in Semiconductors and Semimetals, (Eds.) R.K.Willardson and A.C.Beer, Academic Press, New York (1975).

46. R.H.Bube, Photoconductivity of Solids, Wiley, New York (1967)

47. A.Rose, Concepts in Photoconductivity and Allied Problems, Wiley, New York (1963).

48. P.K.C.Pillai, N.Shroff and A.K.Tripathi, J.Phys.D 16, 393 (1983).

49. R.H.Fowler, Phys.Rev., 38, 45 (1931).

50. H.K.Henish, Rectifying Semiconductor Contacts, Clarendon Press, Oxford (1957).

51. S.M.Sze, Physics of Semiconductor Devices, Wiley, New York (1969)

52. F.A.Padovani and G.G.Sumner, J.Appl.Phys., 36, 3744 (1965).

53. C.DeBlasi, G.Micocci, A.Rizzo and A.Tepore, Phys.Stat.Solidi (a), 74, 291 (1982).

PREPARATION AND CHARACTERISATION OF α -In_2Se_3 THIN FILMS

Abstract:

This chapter gives a clear account of the preparation and characterisation of In_2Se_3 thin films. The contraversy in the structural details of these thin films have been clarified. Optimisation of the preparative conditions employed for elemental evaporation, helped in the suppression of other phases to a very minor limit, and hence these films give extremely reliable results on In_2Se_3 thin films and shows better physical properties compared to earlier reports.

5.I. Introduction:

The semiconducting compound In_2Se_3 belongs to the family of chalcogenides with the general formula $A_2^{III} B_3^{VI}$. The structure of In_2Se_3 is polymorphic and of the different existing forms there remains some controversy in the literature[1-11]. These compounds crystallise in a layered structure in which the molecular units are bonded by first-order covalent or ionic forces extending in layers, while the layers are held together by weak Van der Waals forces[12,13]. Owing to the distinct structural features, in addition to the already established remarkable optoelectronic properties, these compounds find applications in different fields[14-19].

Recently, thin films of In_2Se_3 have been grown and investigated[20-22] in the light of their electrochemical applications. The structure of these compounds make it possible for guest atoms or molecules to diffuse into the lattice between the consecutive layers without altering the host-structure[23-25]. The insertion reaction permits to enhance a required property by introducing new materials and helps in preparing microdevices. Typical utilisation of these include their use in micro-batteries as positive electrodes with a fast ionic conductivity and in microcapacitors as solid solution electrodes with a higher charge storage capacity[26].

5.I.A Statement of problem

Elemental evaporation has now been accepted as superior from among the methods for the preparation of crystalline stoichiometric compound thin films. This is because of the adequate control over the deposition process and viability of the variation of substrate temperature to any level without affecting the stoichiometry for obtaining the requisite physical behaviour.

In this chapter, the possibility of realising stoichiometric polycrystalline In_2Se_3 thin films by multi-source evaporation on hot substrates is analysed. In addition, structure, chemical composition, morphology, electrical behaviour and optical properties of the resulting thin films are also presented.

5.II. Experimental Details:

Experimental setup and source materials are the same as that described in Chapter 4. The co-evaporation of In and Se was carried out in a vacuum enclosure under a base pressure less than 1.5×10^{-6} Torr, from two different sources as described previously. The temperatures of the two sources and the substrates are electronically controlled to within ± 1 K, by a home-built system. With fine control of the source temperatures it was possible to regulate the fluxes of the two elements _ indium and selenium _ to obtain films with required compositions. The temperature of the sources were in the range of 800-1500^{o}C for In and 160-260^{o}C for Se.

The films were deposited on glass or quartz substrates, with

temperature varied in the range of 373-500 K. Prior to evaporation the substrates were properly cleaned as described in the previous chapter. The substrates were 15 cm. away and normal to the sources. Film thickness was measured using the optical interference method.

5.II.A **Film Formation:**

In the growth of the In_2Se_3 film, the changes in the composition were essentially controlled by two parameters: (1) Indium and selenium deposition rate ratio, and (2) the substrate temperature. Since the selenium vapour pressure is high, it is more practical to keep the selenium evaporation rate at a constant value and adjust the evaporation rate of indium in proportion to the required stoichiometry, taking into account the substrate temperature. In this chapter as a rule, stoichiometric compositions refer to films with In/Se ratios approximately equal to 2/3.

In the depositions, for higher pumping rates and substrate temperatures, a large excess of selenium compared to indium was found to be necessary to get the required stoichiometry. In addition, at higher substrate temperature selenium gets reevaporated because of high vapour pressure, and layers with selenium deficiency are obtained. Careful selection of the substrate temperature and annealing conditions give samples with correct stoichiometry and stable physical properties.

Typical elemental rates for the In and Se fluxes were 2.8-6.0 and 13-14 Å/sec, respectively, as determined by cold

substrate caliberation. Resulting film growth rates varied from 4.5 to 11.0 Å/sec.

5.II.B **Characterisation procedures:**

Most of the characterisation procedures used are the same as that described in Chapter 4. Therefore to avoid repetition, unless otherwise described they should be assumed to be the same.

5.III. **Results and Discussions**

5.III.A. Structure and morphology

5.III.A.1 X-ray diffraction analysis

5.III.A.1.a Effect of deposition temperature

The X-ray diffraction technique was used to determine the phases present and the orientation of crystallites in In_2Se_3 films. The films were grown under different substrate temperatures in the range 423-473K. The results are shown in Fig. 5.1. In order to facilitate a comparison among the XRD peaks, they are shown in the same figure, allowing a translation in the intensity axis. Peaks denoted by the dark circles correspond to hexagonal α-In_2Se_3[27]. Cross marks denote the monoclinic In_6Se_7 minor phase detected in the samples.

In the case of In_2Se_3 peaks the observed diffraction pattern agree with the theoretically calculated values with regard to 'd' values and more or less with intensities. This shows that the α-In_2Se_3 is in the hexagonal structure with a space group P $6_3/mmc$.

The enhancement of the (001) peak corresponding to the In_2Se_3 in the films is indicative of a preferential orientation.

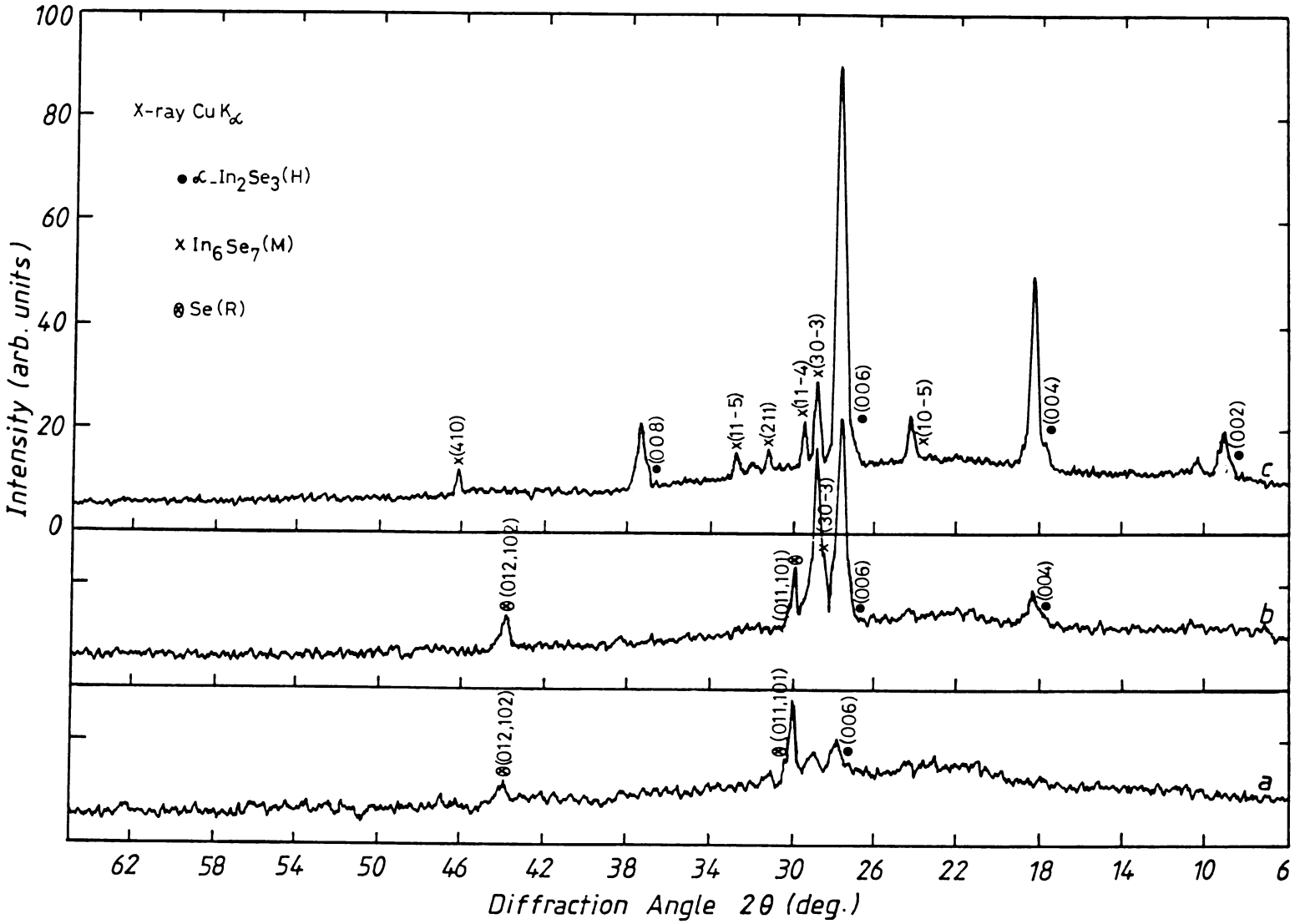

Fig.5.1 X-ray diffraction (CuK_α radiation) patterns of films deposited at different substrate temperatures, (a) 423K ; (b) 473K ; (c) 460K (H - hexagonal ; M - monoclinic ; R - rhombohedral.)

Variation of the peak intensities of the major phase as a function of substrate temperature reveals that the phase formation is very sensitive to the substrate temperature (Fig.5.1). Fig.5.1(a) shows the diffraction pattern, for films deposited at 423 K. The preferential orientation in the (001) reflections of the films deposited on glass substrates may be due to the larger stability of the corresponding planes. The change in preferential orientation is enhanced by higher substrate temperature (Fig.5.1(b)). It can be seen from the pattern (Fig.5.1(c)) that for the formation of In_2Se_3 films, the best deposition substrate temperature is at T_s = 460 K. The pattern shows that in addition to the major phase In_2Se_3, the existence of a relatively minor phase in the films corresponding to In_6Se_7. Eventhough the peaks are enhanced by the preferential orientation, the major contribution is from α-In_2Se_3 phase as confirmed by the XPS analysis.

5.III.A.1.b Effect of heat treatment

X-ray diffraction profiles are obtained also for films subjected to post-depositional annealing for different intervals of time at a temperature of 468 K. Figure 5.2(a) displays a typical pattern of the In_2Se_3 film deposited at the best observed conditions of evaporation rate and substrate temeprature, and Figs.5.2(b) and 5.2(c) show the effect of annealing of the film at a temperature of 468K for 10 and 20 minutes respectively.

From Fig.5.2(b) and 5.2(c) it can be seen that the results are modified by annealing under vacuum. Before annealing, the

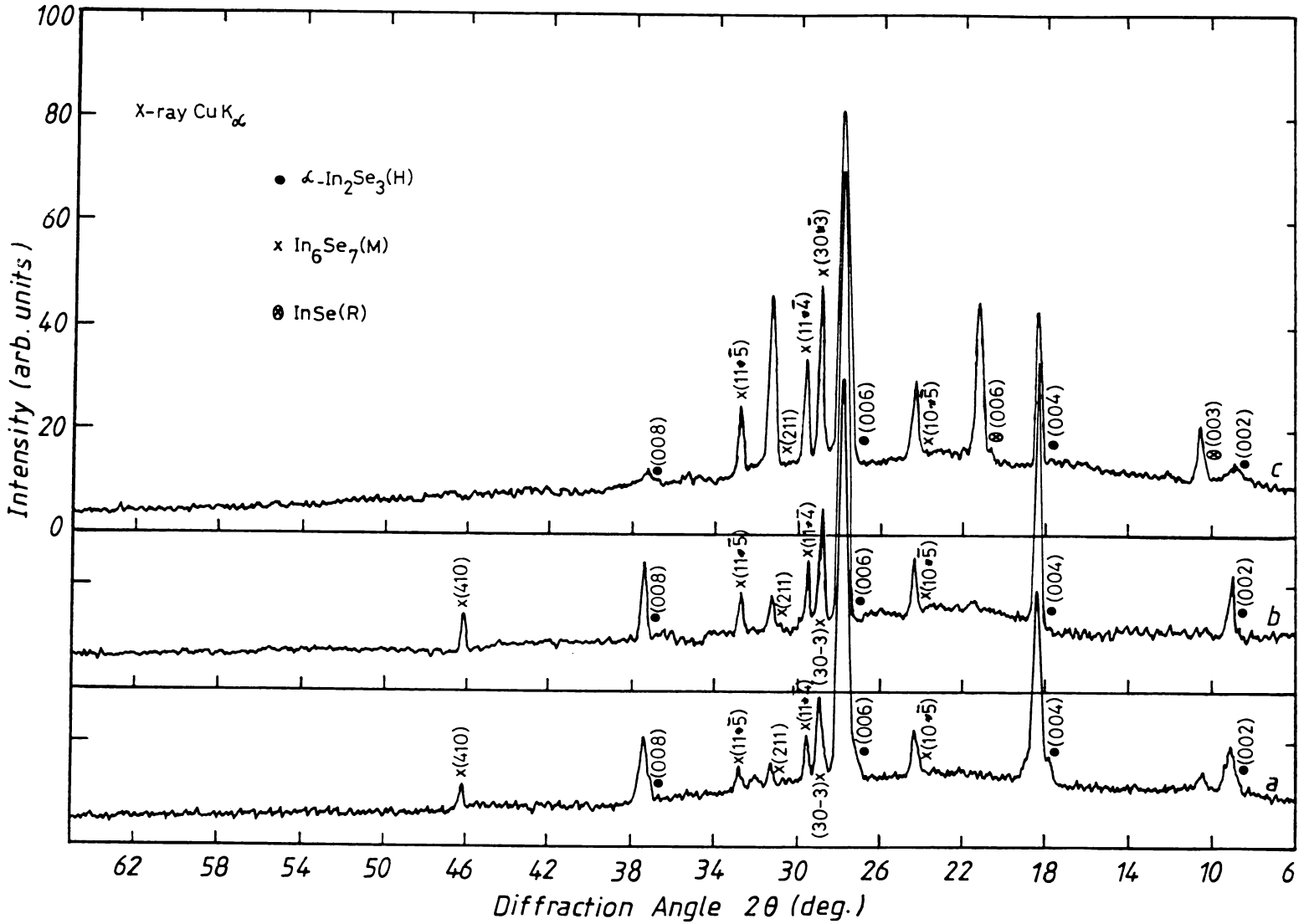

Fig.5.2 Effect of post-depositional annealing at 468 K on X-ray diffraction patterns of films for different intervals, (a) as-deposited ; (b) 10min. ; (c) 20min. (H - hexagonal ; M - monoclinic ; R - rhombohedral.)

diffraction pattern corresponding to major phase was less intense and presented broad peak intensities. But during annealing the degree of crystallite order is getting improved compared to the films deposited at a higher substrate temeprature. This is evident from the continuous increase of the peaks corresponding to the (001) reflection, of the In_2Se_3. This continues for an optimum duration eventhough the impurity phase are also slightly getting pronounced simultaneously (Fig.5.2(b)). Correspondingly, annealing slightly increases the minor phase reflections (hk•$\bar{1}$) of In_6Se_7 phase. It can be seen that whenever the (410) reflections vanish or decrease its intensity, it is contributed to (211) reflections. This can be viewed as the reorientation of the minor phase crystallites with the substrate temperature. So at this point, the impurity phase favours to align mainly in (hk•$\bar{1}$) and (211) planes.

But as the duration of annealing is increased, the In_2Se_3 phase is loosing its intensity. The formation of InSe rhombohedral phase was observable in the diffraction profile after annealing for 20 minutes (Fig.5.2(c)). At this stage, some of the In_2Se_3 is believed to have converted to In_6Se_7 due to the escape of selenium. Compositional analysis also shows a deficiency of selenium from the corresponding composition.

The distribution of the XPS intensities for two different stages are observed and will be discussed later.

The variation in the diffraction peak intensities corresponding to the main reflections, of the major as well as minor phase are plotted in Fig. 5.3 as a function of annealing

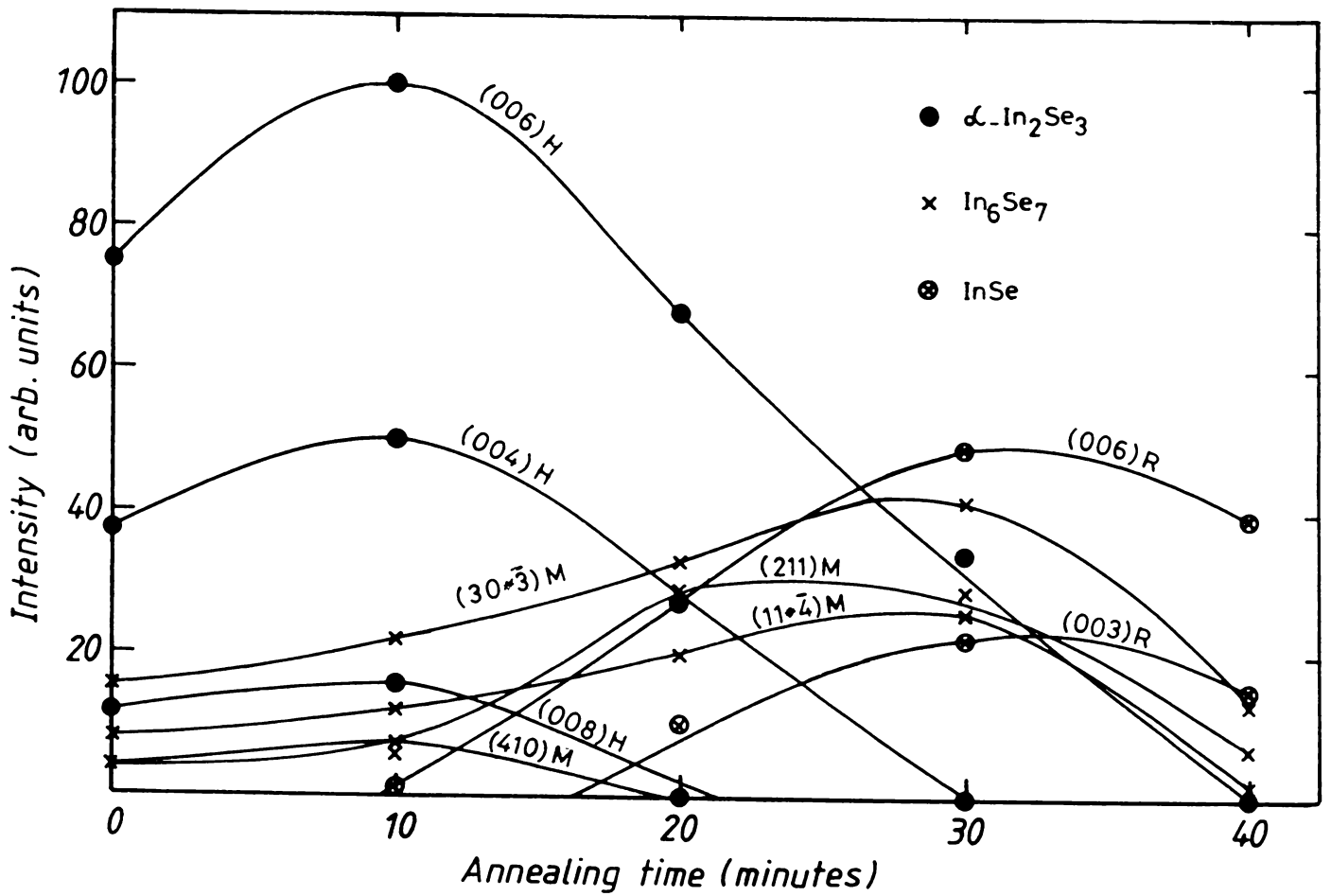

Fig.5.3 Variation in the relative intensity of different X-ray reflections as a function of annealing time.

(H - hexagonal ; M - monoclinic ; R - rhombohedral.)

time in order to have a better comparison. This plot clearly displays the formation of In_2Se_3 phase and shows a gradual conversion of this to mixed phases along with the duration of annealing. As the annealing time is increased, InSe phase dominates and then looses its intensity, along with other phases.

5.III.A.1.c Grain Size

From X-ray diffraction, the grain size of the crystallites in the film is estimated from the full-width at half-maximum (FWHM) of the diffraction peak. For specimens deposited on quartz substrates and subjected to 10 min. post depositional annealing, the mean grain size is found to be about 200 nm.

5.III.A.2 Microstructural Studies

The microstructure of the In_2Se_3 films were investigated by transmission electron microscopy (TEM). The samples were of thickness less than 1000 Å. Analysis were made with a Philips EM 301 microscope with the same settings as described in the earlier chapter.

In order to study the effect of depositional substrate temperature on crystallisation, micrographs were taken for samples deposited at different substrate temperatures. Fig.5.4 and Fig.5.5 show typical transmission electron micrographs and the corresponding electron diffraction patterns of the microstructural variation. At a lower temperature (423 K) the microstructure shows the formation of fine crystallites (Fig.5.4(a). The corresponding electron diffraction pattern reveal that the individual crystallites are polycrystalline

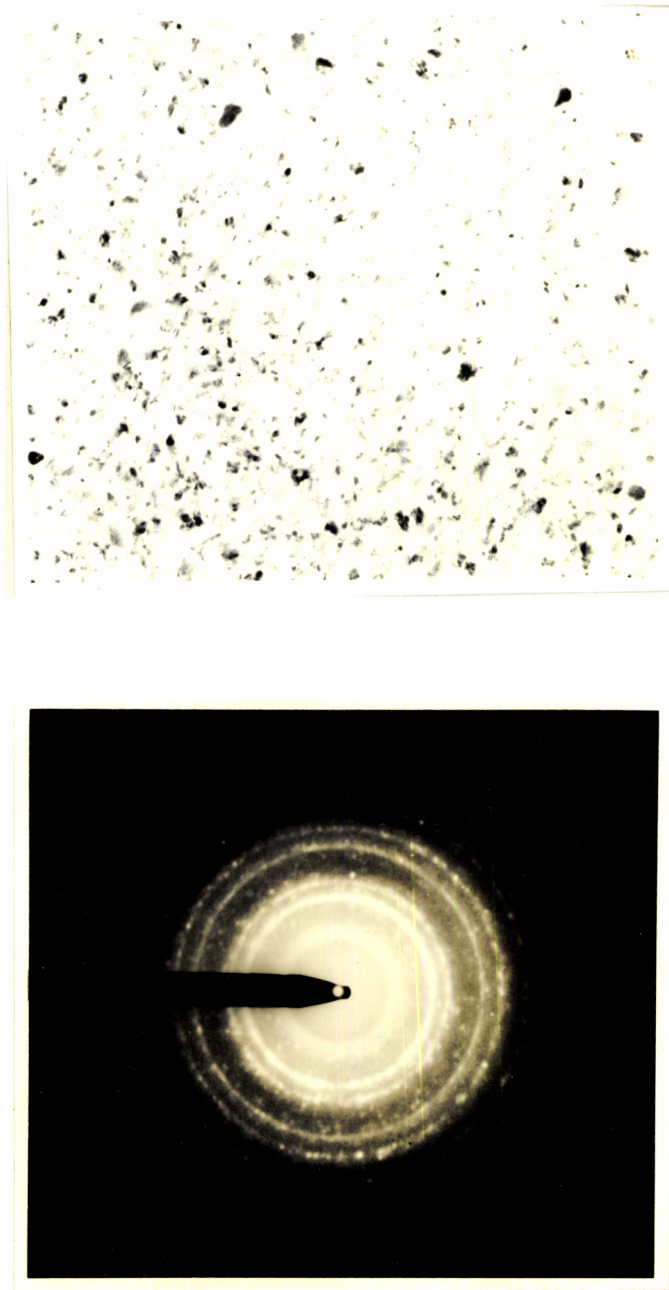

Fig.5.4 Morphology of the film from TEM and its SAD pattern (deposition substrate temperature 423K).

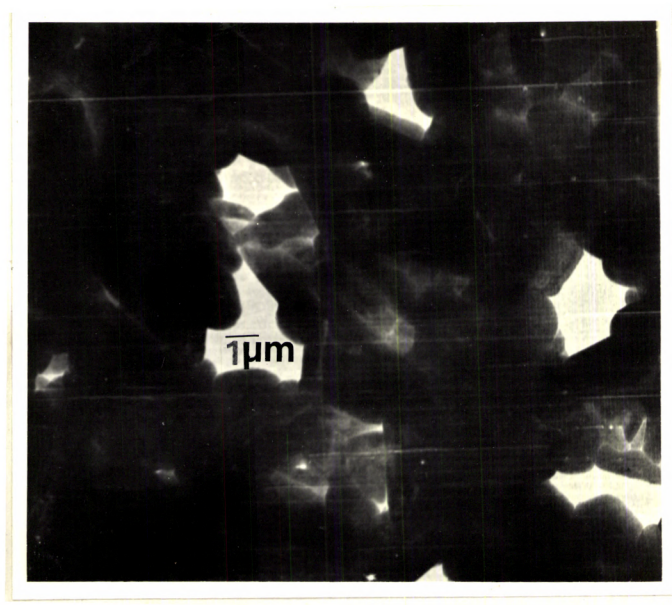

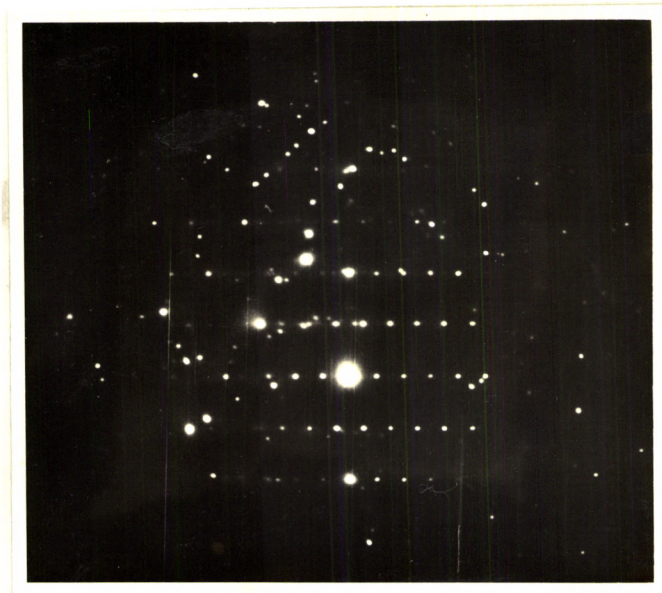

Fig.5.5 TEM micrograph showing the grains of In_2Se_3 film and its selected area electron diffraction pattern (Deposition substrate temperature 460 K with short annealing).

(Fig.5.4(b)). But when the deposition substrate temperature is increased to above 460 K, the small crystallites are seen to be merged into a continuous polycrystalline In_2Se_3 islands (size:in the range of 0.2- 0.4 μm) as shown in Fig.5.5(a). The corresponding diffraction pattern exhibits only the spots indicating single crystal grains (Fig.5.5(b)).

5.III.B Compositional Studies

5.III.B.1 XPS and DAN fluorimetry:

Electron spectroscopy for chemical analysis (ESCA) measurements were obtained with a magnesium X-ray source (1253.6 eV) operated at 10 kV and 20 mA. Instrument control and data acquisition were performed by a computer. The overall energy resolution was 0.8 eV at a pass energy of 20 eV. The quantitative studies were based on the determination of the In $3d_{5/2}$ and Se $3d_{5/2,3/2}$ peak areas and the formula,

$$\frac{N_{Se}}{N_{In}} = \frac{I_{Se}}{I_{In}} \cdot \frac{\sigma_{In}}{\sigma_{Se}} \cdot \frac{\sqrt{KE_{In}}}{\sqrt{KE_{Se}}} \cdot \frac{\lambda_{In}}{\lambda_{Se}} \qquad \ldots (5.1)$$

where N_{Se}/N_{In} is the surface composition ratio, I_{Se}/I_{In}, is the relative signal strength of the constituents' peaks, σ 's are the corresponding theoretical photo-inonisation cross-sections[28] and KE's are the kinetic energies of eletrons of the strongest core-level XPS peak and λ's are mean free path of electrons[29] for the above kinetic energies. A summary of the results of 5 typical samples subjected to estimation is given in Table 5.1. The results are within reasonable limits when compared to the DAN fluorimetry chemical analysis results.

Table 5.1

Comparision of estimation of Selenium/Indium ratio.

Sample No.	ESCA				DAN Chemical Analysis
	Observed peak area Se $3d_{5/2,3/2}$	:	In $3d_{5/2}$	Atomic ratio Se/In	Atomic ratio Se/In
G1	1123	:	1584	1.43	1.48
G12	1227	:	1715	1.444	1.51
G27	657	:	982	1.35	1.42
132	472	:	1027	0.928	0.99
160	773	:	1611	0.969	0.996

5.III.B.2 XPS peak shifts.

The correlation between thin film composition and the energy shift in the In 3d and Se 3d levels from that of elemental state has been helpful in determining the chemical state of the constituents. For In_2Se_3 samples (annealed 10 min.) the indium $3d_{5/2}$ and $3d_{3/2}$ levels are recorded at 444.3 eV and 452.1 eV respectively and Se $3d_{5/2,3/2}$ is at 53.6 eV (Fig. 5.6). In elemental states these are at 443.6, 451.4 and 55.5 eV respectively. So the shift in binding energies (Table 5.2, see also Fig.4.14 in Chapter 4) are + 0.7, + 0.7 and -1.9 eV respectively due to the compound formation. The chemical shifts of these levels and that reported for In_2Se_3 single crystals[30] are comparable eventhough all the values show a slight uniform shift in the binding energies. Nevertheless some of the results published recently for similar compounds are very close to the present observations[31,32].

When the above described In_2Se_3 samples are annealed for 30 min. the indium $3d_{5/2}$ and $3d_{3/2}$ energy levels show an increase and selenium $3d_{5/2,3/2}$ shows a decrease in their positions and the energy levels appear respectively at 444.8, 452.7 and 53.25 eV (Fig.5.7). The composition of the compound is estimated to be in the ratio Se/In $\approx$ 0.75. This indicates that 30 min. annealing reduces the selenium content in the films due to its escape. This result is consistent with the observations made during the structural studies.

In order to check the effect of excess selenium content of

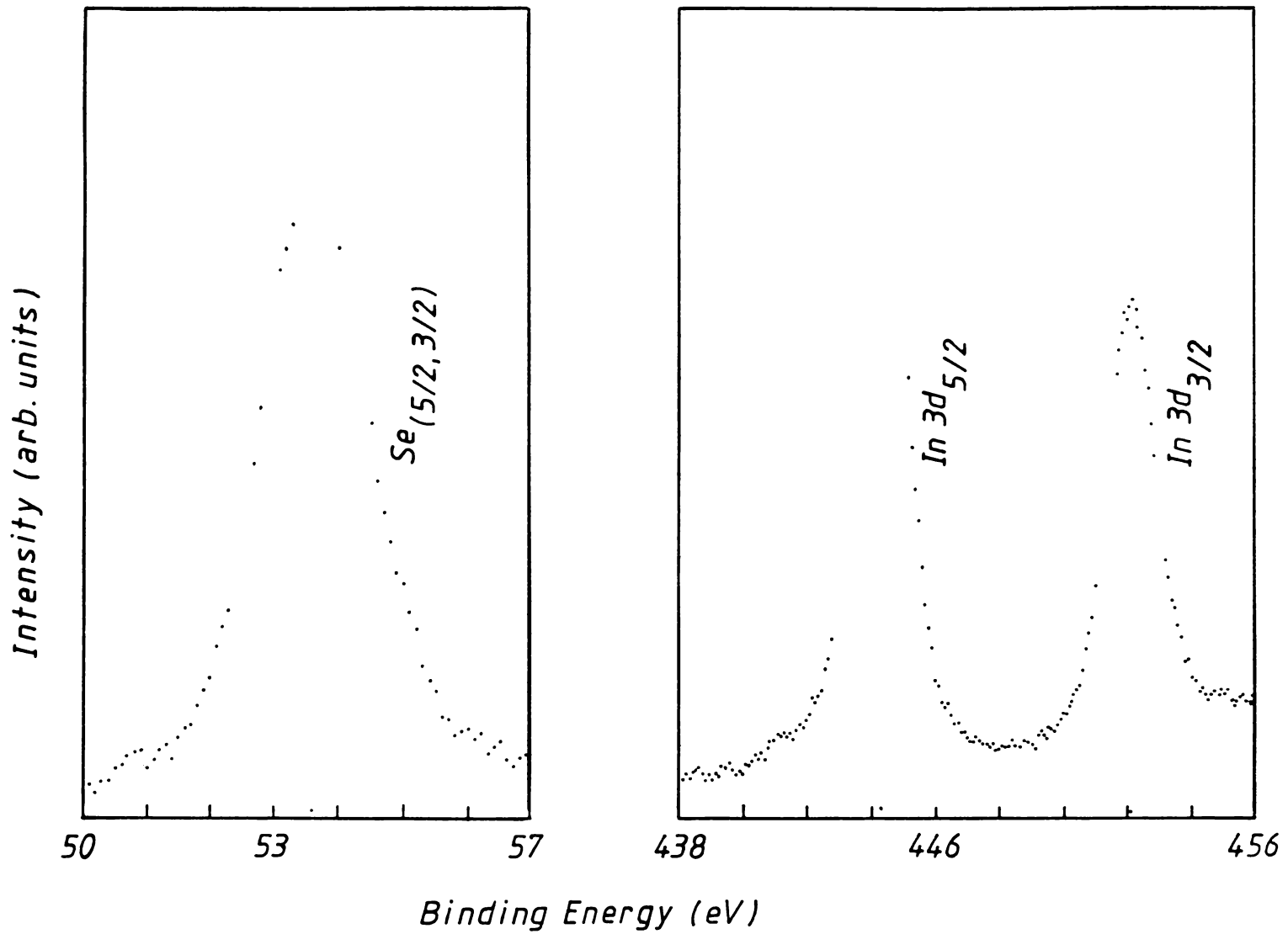

Fig.5.6 XPS spectra for the In $3d_{(5/2)}$ and Se $3d_{(5/2,3/2)}$ in In_2Se_3 thin films (10 mins. annealed).

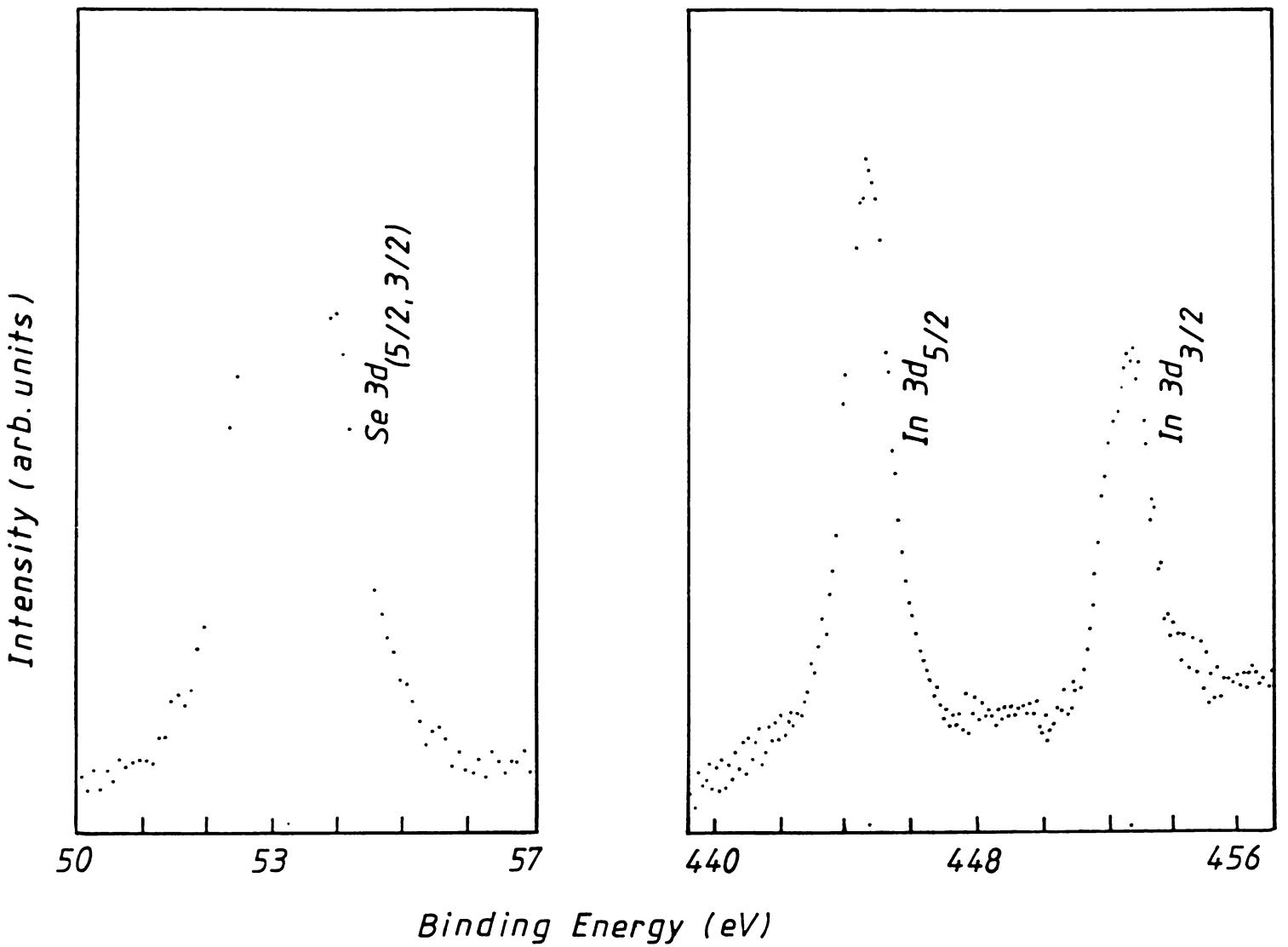

Fig.5.7 XPS spectra for the annealed In_2Se_3 thin films (30 minutes) showing a shift in the In $3d_{(5/2)}$ and Se $3d_{(5/2,3/2)}$ levels.

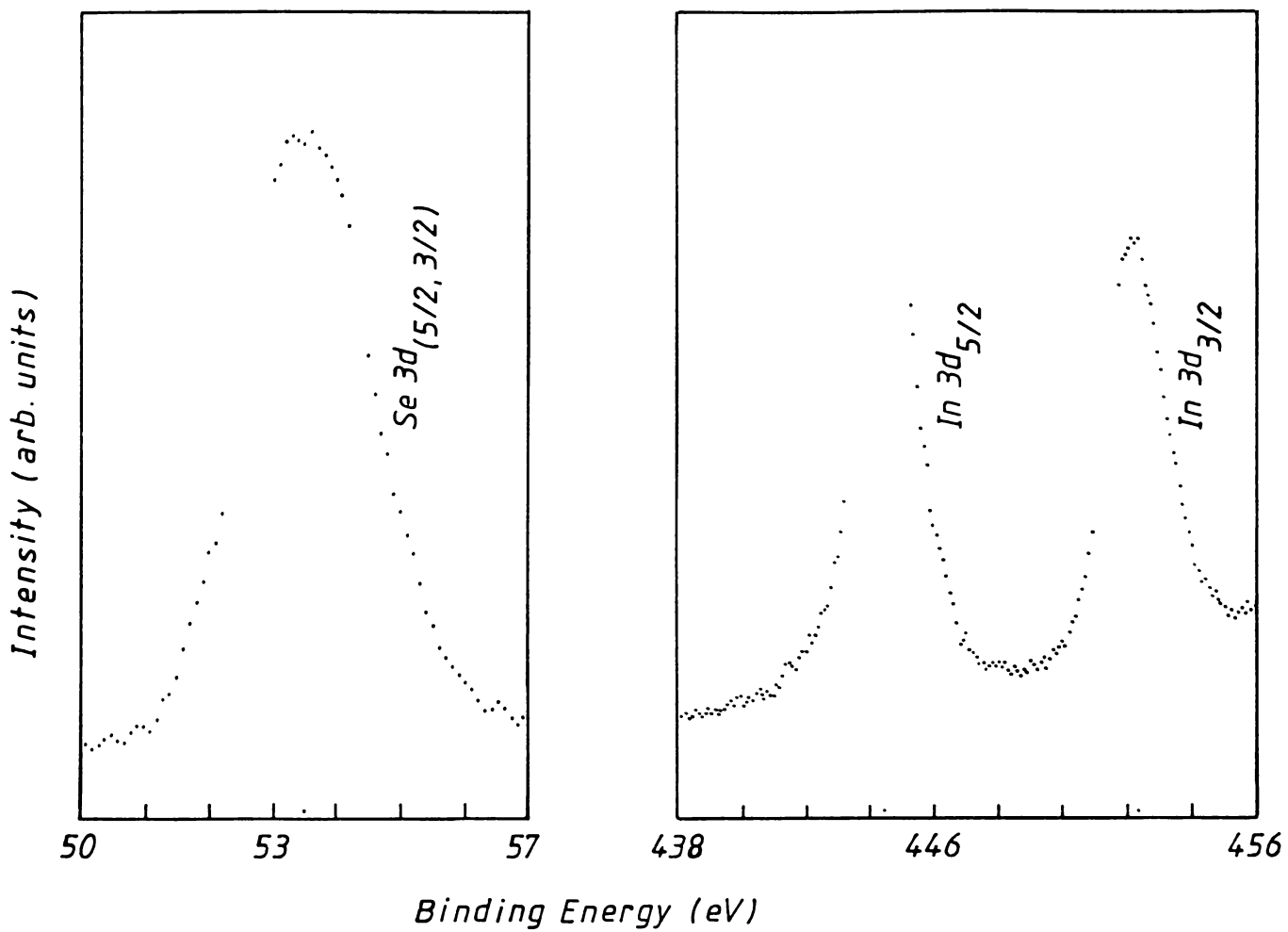

Fig.5.8 XPS spectra for the films containing a slightly excess selenium than required for In_2Se_3 film formation, (Se/ In = 1.13, corresponds to a composition In_6Se_7).

Table 5.2

Summary of the XPS peak shift results

Fig. No.	Se $3d_{5/2,3/2}$ (eV)	In $3d_{5/2}$ (eV)	In $3d_{3/2}$ (eV)	Atomic compositional ratio Se/In	Nearest formula representation
(5.2)	53.6 (-1.9)	444.3 (+0.7)	452.1 (+0.7)	1.51	In_2Se_3
(5.3)	53.25(-2.25)	444.8 (+1.2)	452.7 (+1.3)	0.77	In_4Se_3
(5.4)	53.5 (-2.0)	444.4 (+0.8)	452.2 (+0.8)	1.172	In_6Se_7

(shift from the elemental state energy* is shown in brackets)

* In $3d_{5/2}$ = 443.6 eV, In $3d_{3/2}$ = 451.4 eV, Se $3d_{5/2,3/2}$ =55.5 eV

the films on the binding energy shifts, the XPS spectra were recorded. When the Se/In ratio is 1.13 (corresponds approximately to In_6Se_7 compound) there was a modification in the selenium and indium levels as In $3d_{5/2}$ = 444.4, In $3d_{3/2}$ = 452.2 and Se $3d_{5/2,3/2}$ = 53.5 (Fig. 5.8). This means the indium 3d levels are slightly raised in their binding energy levels while the selenium 3d level shows a decline in energy. For a better comparison of the above results, they are summarised in Table 5.2.

In Fig. 5.7 and 5.8, peak asymmetry is evident in the In 3d and Se 3d peaks. This type of behaviour has been observed before, in different materials and commented on as due to multiplet splitting[33,34], "shake up" satellites[35] or mixed valencies[36]. But in the present case it is possibly due to the coexistance of compounds in different chemical states.

In all these measurements an In 3d peak splitting was recorded with an average binding energy separation of 7.8 eV but no Se 3d peak splitting was observed. It is to be mentioned that all the above measurements show no indication of any type of contamination in the formed films.

5.III.C. Electrical Measurements

5.III.C.1 Electrical Conductivity

Electrical measurements were carried out on the films under vacuum (10^{-3} Torr) in a home-made system as described previously. The standard van der Pauw technique was used for this. Ohmic contacts were made by evaporating indium through masks onto the film. The ohmic nature of the contacts were confirmed from the

linear current-voltage characteristics in the low voltage range.

The room temperature conductivity of the as-deposited films varied from 1.0×10^{-2} to $6 \times 10^{-1} ohm^{-1} cm^{-1}$. These conductivity values are two to three decades lower than that of single crystal values. This can be visualised in presence of grain boundaries[37,38] present in polycrystalline thin films. Additionally, the rate of cooling also influences the conductivity values [39,40].

The temperature dependence of the electrical conductivity is studied between 300 and 463 K for samples deposited at 453 K and typical results are shown in Fig.5.9. After the deposition of the film, the samples which were quenched showed less resistivity. When these samples are subjected to a temperature variation, conductivity varies with different slopes, indicating some phase transformation, and between the temperature range of 453-463 K it shows an abrupt variation. But, while cooling the resistivity is almost linear. Subsequent temperature variation (upto 393 K) of the sample gives a linear plot. The result is analysed by a thermally activated process,

$$\sigma = \sigma_o \exp(- \Delta E/kT) \qquad \ldots (5.2)$$

where σ_o is a pre-exponential factor and ΔE is the activation energy. The activation energy ΔE, determined was around 0.65 ± 0.03 eV, and corresponds to a band-gap of 1.3 ± 0.03 eV. This observed difference in the band-gap from that determined by optical means, may be due to the defects or gap states present in large number, in the films[41-44].

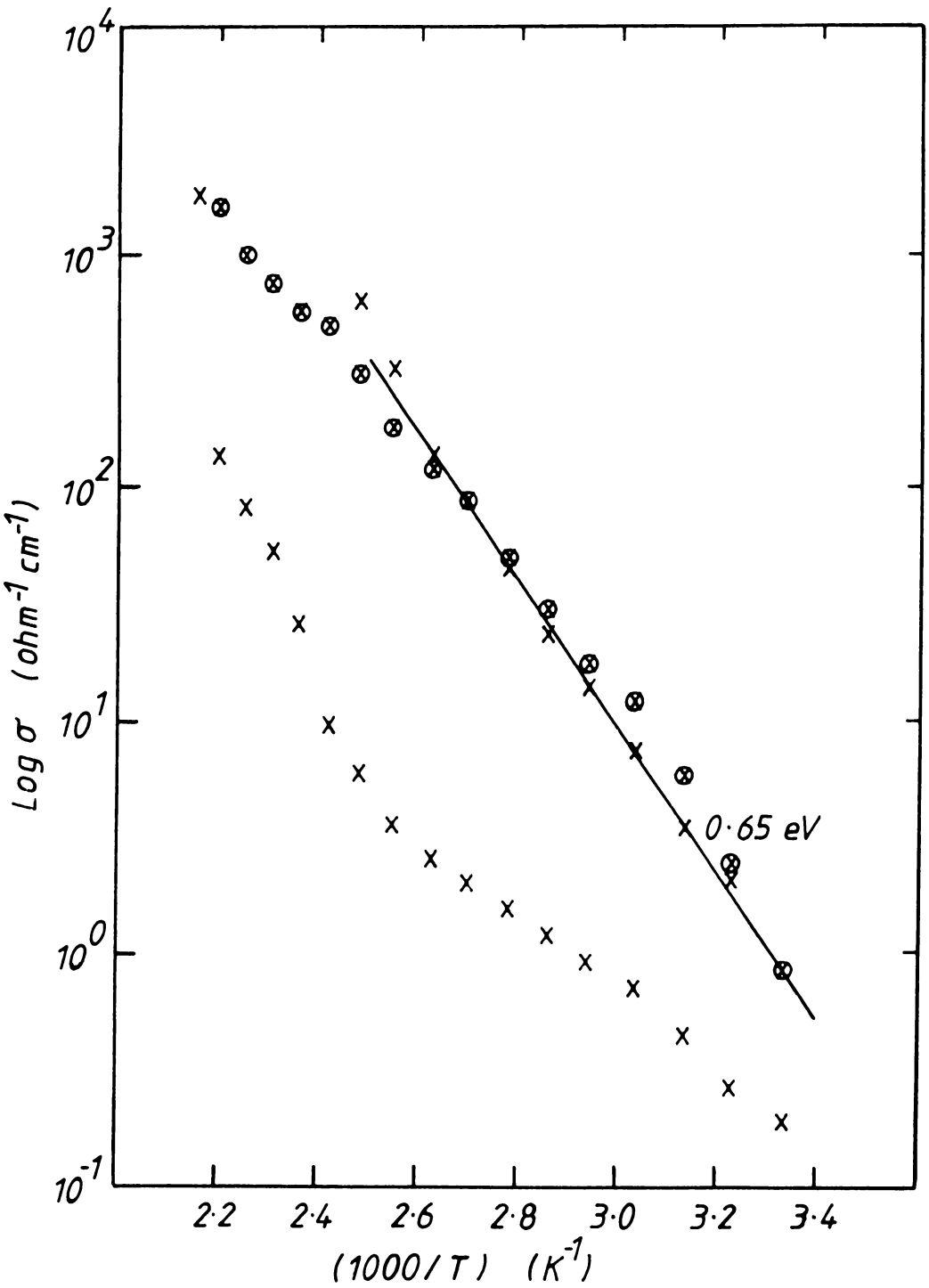

Fig.5.9 The temperature dependence of dark electrical conductivity of stoichiometric In_2Se_3 films(× annealing at 468 K ; ⊗ after annealing)

5.III.C.2 **Hall measurements:**

To understand the carrier transport mechanism, electrical measurements in combination with Hall measurements were made used of.

Measurements of Hall-effect voltage were performed using standard dc technique. Hall coefficients were then calculated using the expressions given in chapter 3,

$$R_H = V_H t/IB \quad \ldots (5.3)$$

$$R_H = 1/Ne \quad \ldots (5.4)$$

where R_H is the Hall coefficient, V_H the Hall voltage, t the film thickness, I the current forced through the sample, and B the applied magnetic field. Carrier concentration N were calculated from eqn.(5.4) which is an approximation with restricted validity. The variation of carrier concentration is governed by the conductivity and Hall mobility, μ_H by $\sigma = eN\mu_H$, where e is the electronic charge.

Table 5.3 represents the values of electrical conductivity (σ), carrier type, activation energy (E_g), Hall coefficient, Hall mobility (μ_H) and carrier concentration (N) of the In_2Se_3 films for different depositional substrate temperatures. Table 5.4 manifests these parameters for different annealing intervals.

The increase in Hall mobility with substrate temperature is due to enhanced crystallinity as implied by X-ray diffraction data in which it was observed that the peaks corresponding to In_2Se_3 phase became sharper for films deposited at higher

Table 5.3

Electrical properties of as-deposited In_2Se_3 thin films at room temperature.

Film thickness=3625 Å.

Substrate temperature (K)	Conductivity ($ohm^{-1}cm^{-1}$)	Carrier type	Activation energy (eV)	Hall coefft. (cm^3C^{-1})	Hall mobility ($cm^2V^{-1}s^{-1}$)	Carrier concen. (cm^{-3})
423	2.1×10^{-3}	n	0.46	416	0.87	1.5×10^{16}
433	3.5×10^{-2}	n	0.51	74.3	2.6	8.4×10^{16}
443	2.2×10^{-1}	n	0.63	36.71	8.08	1.7×10^{17}
453	6.9×10^{-1}	n	0.65	19.50	13.46	3.2×10^{17}

Table 5.4

Variation in electrical properties of In_2Se_3 thin films deposited at 453 K with subsequent annealing at 463 K.

Film thickness=3400 Å

Annealing time (min.)	Conductivity ($ohm^{-1}cm^{-1}$)	Activation energy (eV)	Hall coefft. (cm^3C^{-1})	Hall mobility ($cm^2V^{-1}s^{-1}$)	Carrier concen. (cm^{-3})
0	6.0×10^{-1}	0.49	22.5	13.5	2.77×10^{17}
10	8.5×10^{-1}	0.65	20.1	17.09	3.1×10^{17}
20	6.4×10^{-1}	0.70	20.7	13.25	3.0×10^{17}
30	9.7×10^{-3}	0.74	159	1.54	3.93×10^{16}
40	7.5×10^{-5}	0.66	--	--	--

substrate temperature. The increase in carrier concentration with substrate temperature for these films can be due to reduction in disorder which helps to reduce the loss of carriers at the grain boundaries[45].

It may be noted that the increase in carrier density and mobility with annealing is moderate in the case of films annealed for short durations. This indicates that, annealing for shorter duration at higher temperatures tend to remove the disorder from the films, and facilitates easy carrier movement. The same mechanism may be dominating over the reduction in carrier density for longer period annealed samples, due to the introduction of impurity phase[46,47] and reduction in grain size[48-51].

5.III.D Optical Analysis.

5.III.D.1 Transmission

Typical transmission spectra recorded at room temperature for two of the samples, deposited on quartz are shown in fig. 5.10. The transmittance is as high as 80% at λ = 1500 nm for thinner films and for thicker films it is nearly 60% at the same wavelength. The transmission edge shifts towards shorter wavelength region with increasing selenium concentration following an expected increase in the energy gap E_g.

The average transmittance values (λ= 1500 nm) for the films deposited at various substrate temperatures T_s are cited in Table 5.5. It is evident that the transmission of the films increases slightly with substrate temperature. A possible explanation for this can be like this. At lower deposition temperatures, the

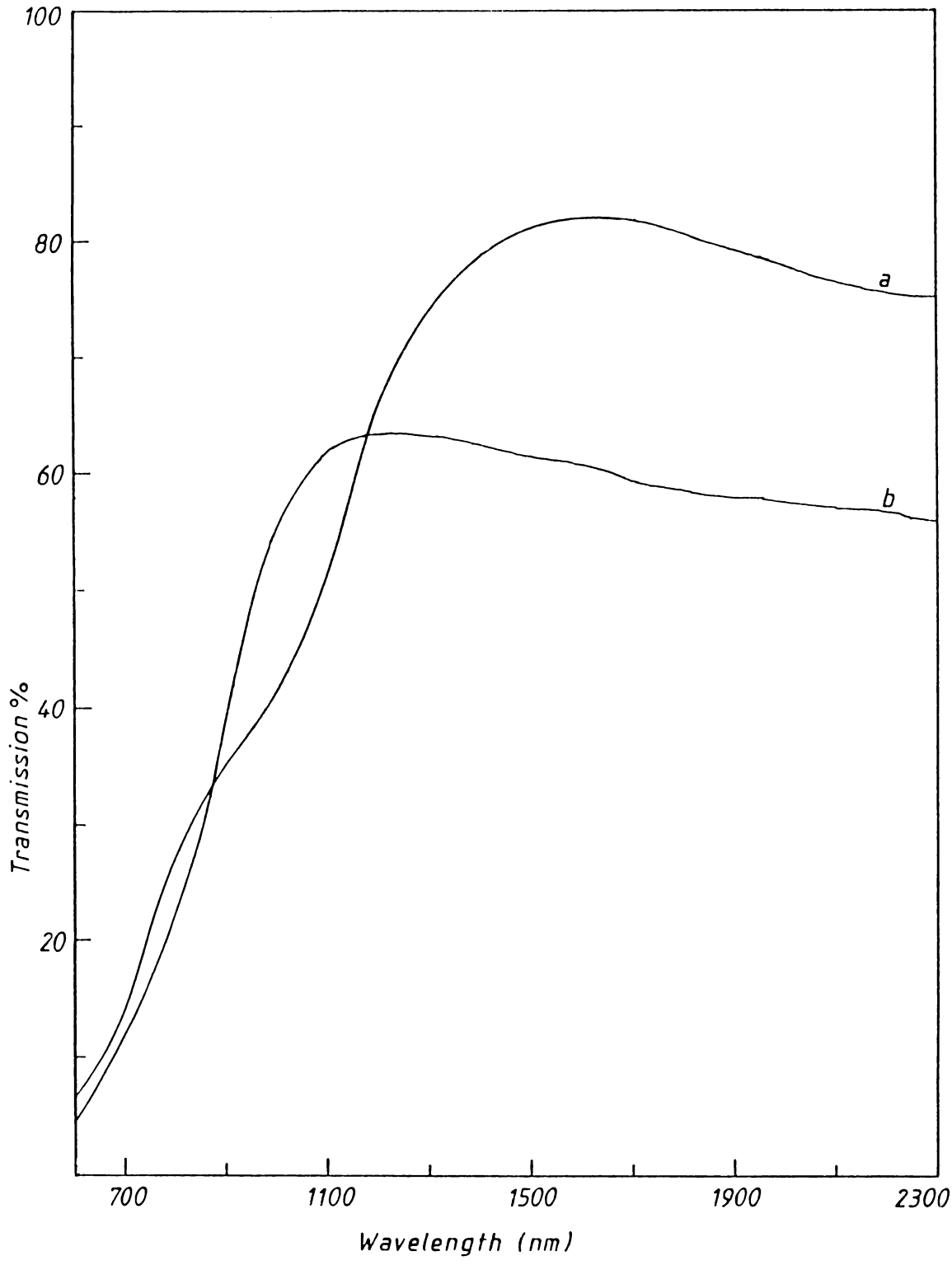

Fig.5.10 Typical transmission spectra recorded for In_2Se_3 films of different thicknesses, at room temperature.

a- 1850 Å; b-5300 Å

Table 5.5

Transmission of In_2Se_3 films deposited at different substrate temperatures.

film thickness ≃ 3000 Å

Substrate temperature (K)	Optical band-gap (eV)	Transmission at λ=1800 nm %	Transmission at λ=1200 nm %
423	--	70	60
433	1.20	70	64
443	1.31	79	72
453	1.38	81	74

formation of donor levels below the conduction band can be expected. These levels can cause sub-band gap absorption with a consequent decrease in transmittance. Annealing of the films for a limited period (10-20 min.) also increases the transmission. But, it was found that the transmission decreases if it exceeds 20 minutes. This can be viewed as an effect of change in crystallinity as evidenced by X-ray diffraction data, for the films subjected to annealing.

5.III.D.2 Optical Absorption

The optical band-gap $E_g^{opt.}$ of the In_2Se_3 films were determined by their wavelength dependence of absorption in the band-edge region. The intrinsic absorption edge of the film at room temperature (295 K) was evaluated in terms of the direct transition[52] using the equation of Bardeen et al[53] which states that the absorption coefficient α is related by

$$(\alpha - \alpha_o)h\nu = B(h\nu - E_g^{opt.})^{1/2} \qquad \ldots (5.5)$$

where α_o is the background absorption. Thus, a plot of $[(\alpha - \alpha_o)h\nu]^2$ as a function of $h\nu$ yielded a linear behaviour in the region of strong absorption near the absorption edge, indicating that absorption takes place through allowed direct interband transitions. This is shown in Fig.5.11 for the as-deposited and annealed films. The extrapolation of the straight portion of the plot to zero absorption, leads to gap values of 1.38 and 1.40 eV, respectively.

The lower energy gap values for the as-deposited films can

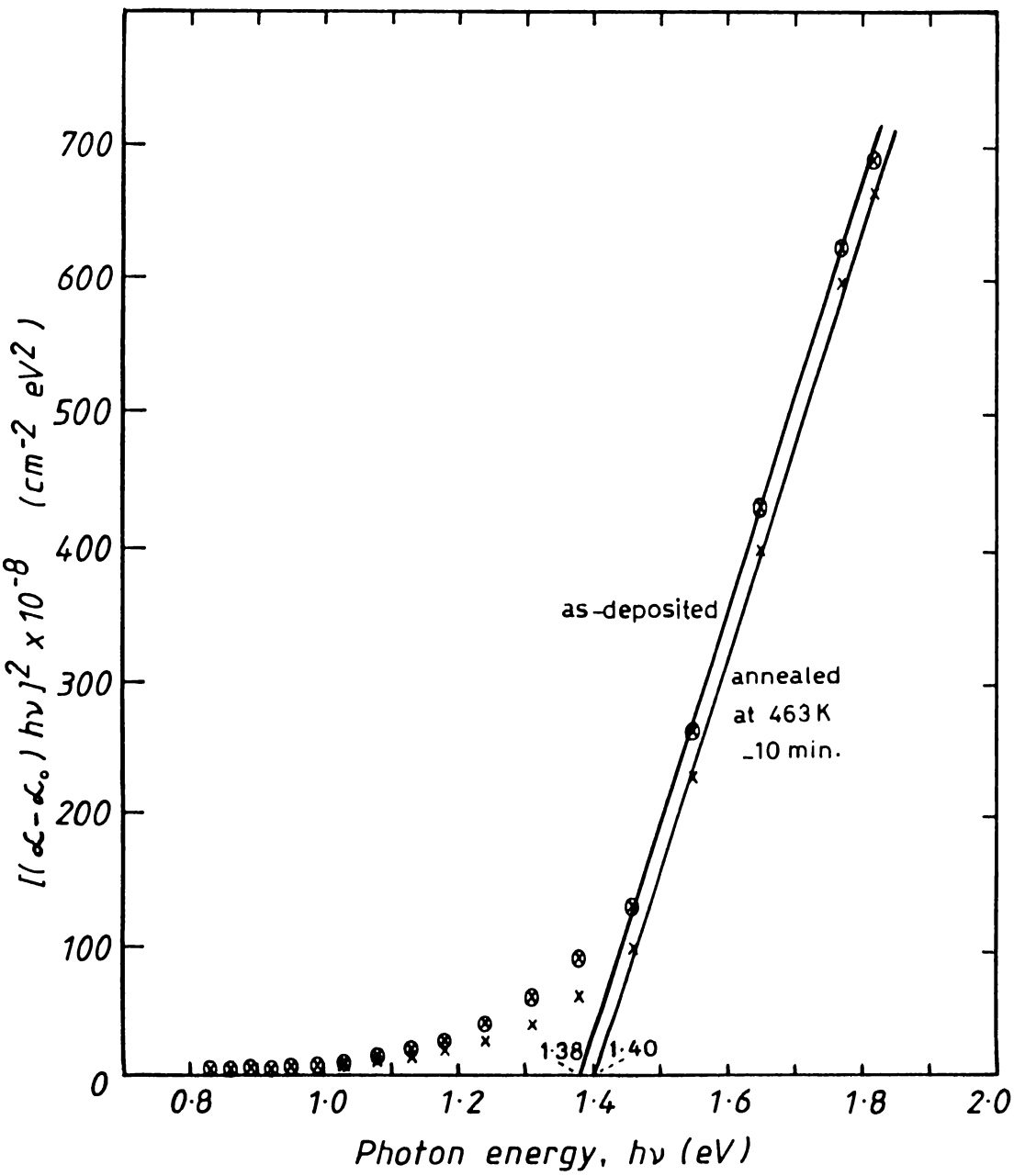

Fig.5.11 Dependence of absorbance (corrected for background) on photon energy, for as-deposited and annealed samples.

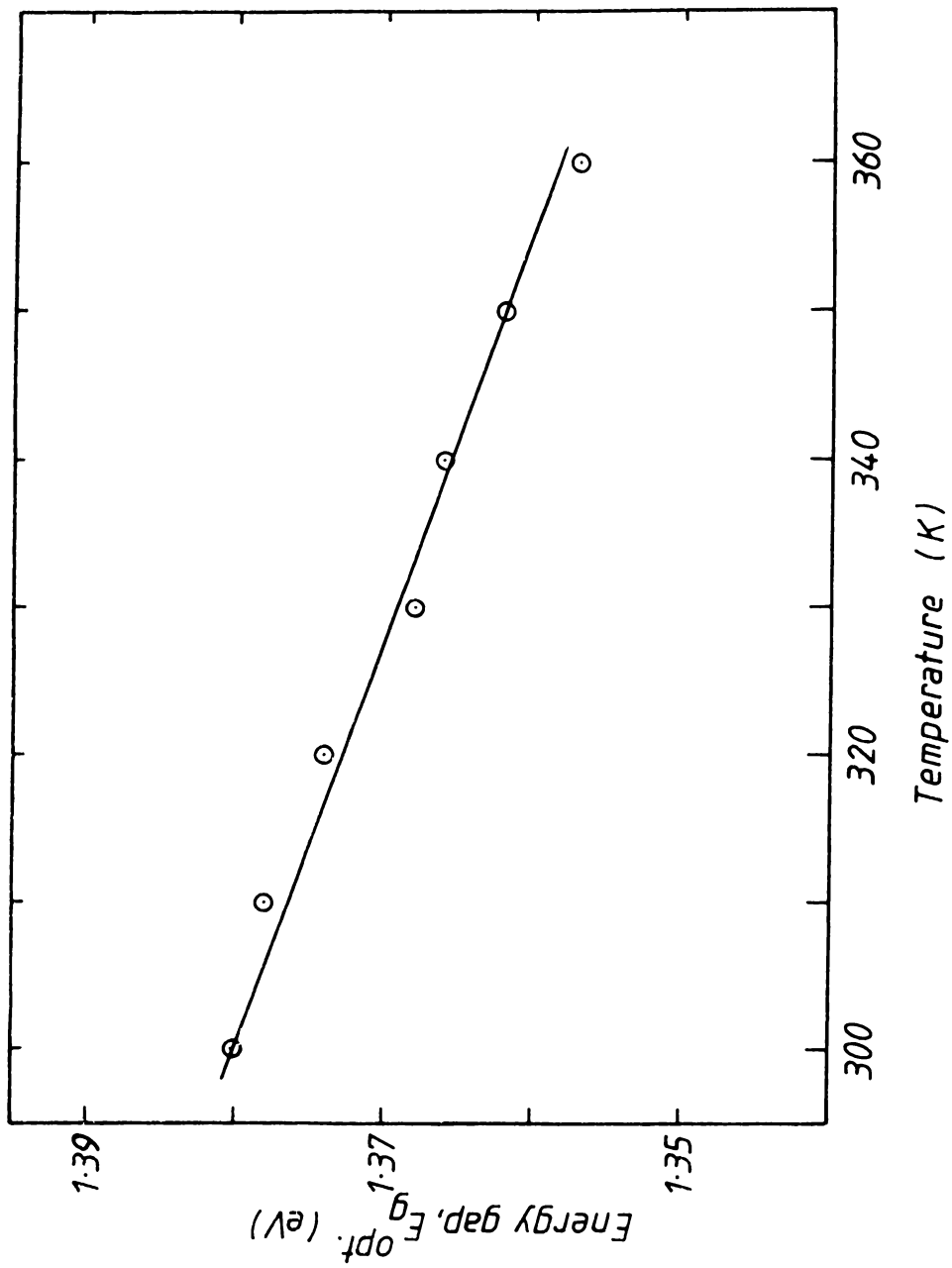

Fig.5.12 Variation of optical energy gap with film temperature.

be explained in terms of gap states near the band edges caused by structural imperfections or defects in grains and by grain boundaries. These gap states are responsible for transitions that measure lower optical band-gap values for as-deposited films. According to Hamberg et al[54] the defects in the materials make the quantum mechanical transitions between the conduction and valence band states to be collision broadened because of scattering and this broadening smears the threshold. A similiar effect has been reported by other authors for other polycrystalline compound semiconductors[55,56].

The value of E_g^{opt} = 1.39 ± 0.03 eV obtained for the films investigated in the present study was slightly lower than the band-gap value of 1.43 eV reported for In_2Se_3[20,57]. This was different from the value (E_g = 1.22 eV) stated by Mushinskii et al[58], in a primary report for In_2Se_3 single crystals obtained by modified Bridgeman method.

The decrease of band gap with temperature is also observed (Fig.5.12). The temperature coefficient of band gap is calculated to be 3.6 x 10^{-4} eV K^{-1}. Comparing this with InSe value, it can be seen that the variation is less pronounced in In_2Se_3. The effect can be understood by taking into account of eqn.2.39.

5.III.D.3 Determination of Refractive Index

The film thickness and the optical constant n of the films were determined by the wavelength dependence of reflectivity in the 800 to 2500 nm wavelength region. The interference pattern

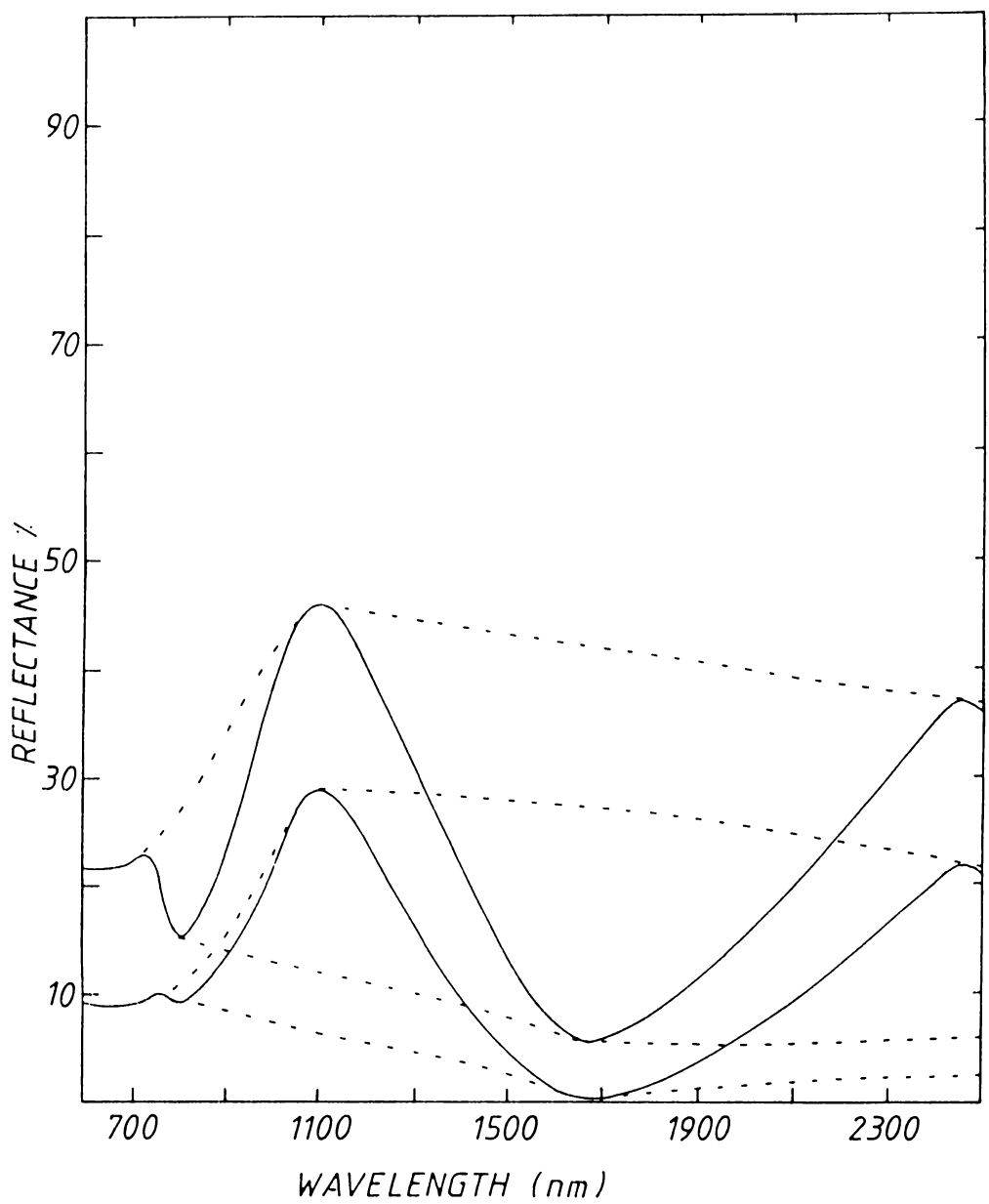

Fig.5.13 Reflectance spectra of a typical In_2Se_3 film of thickness 3010 Å.

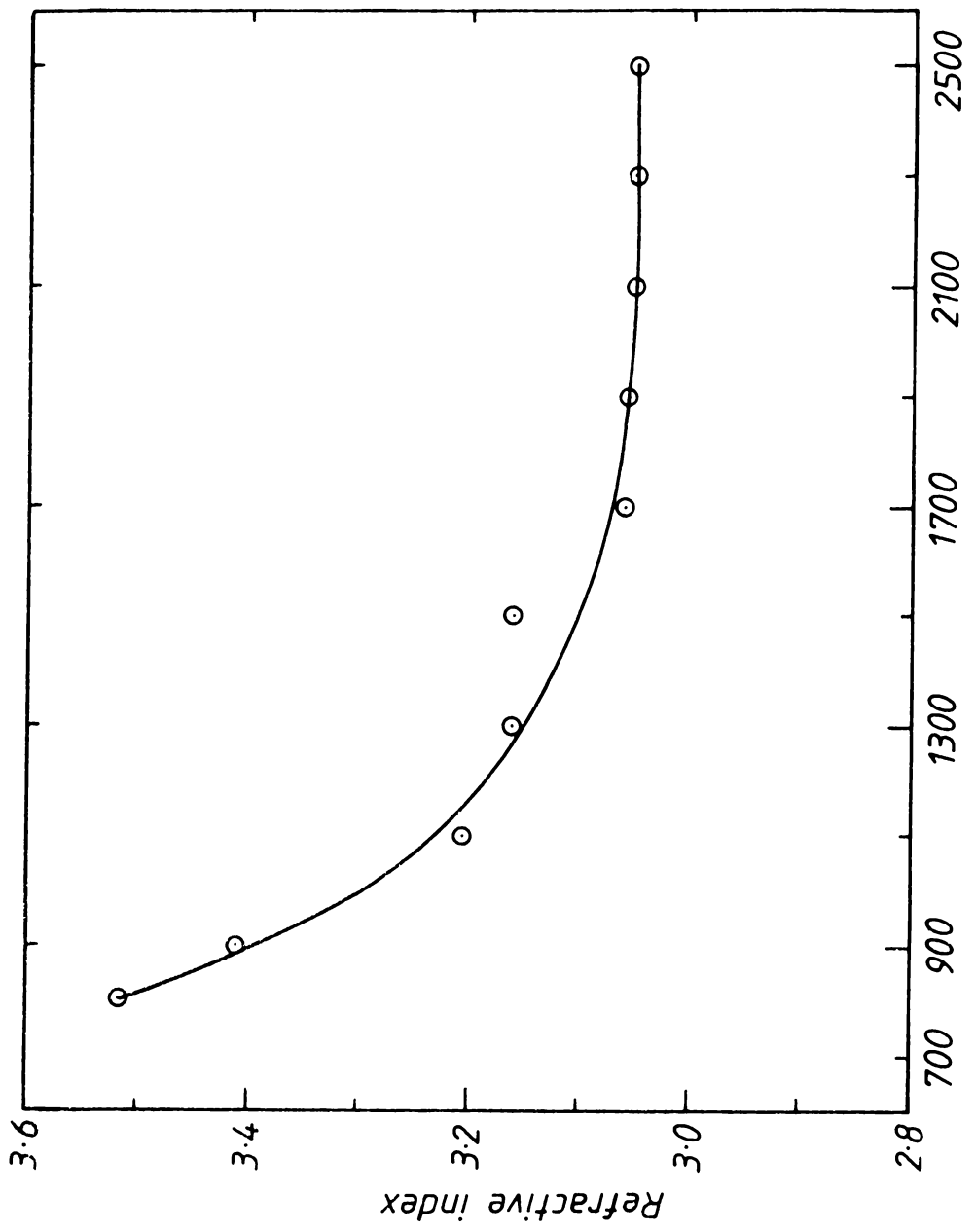

Fig.5.14 Variation of refractive index with wavelength.

due to multiple reflections facilitated these. Fig.5.13 shows a typical spectra for a film thickness of 3010 Å. The index of refraction (n) was determined from the envelope of the curves R_{ex} an R'_{ex} generated from the peaks and valleys of the interference maxima and minima employing the method given in Chapter 3. The calculated value of refractive index was 3.05 at λ = 2500 nm, and was in close agreement with the value reported by Julien, Eddrief, Kambas and Balkanski for flash evaporated In_2Se_3 thin films[20]. A slight difference in the values at lower wavelength side may be accounted for by the difference in the defect nature of these films[59,60]. However the present values match closely to that reported for single crystals. These values of refractive index are plotted in fig.5.14 for different wavelengths. The thickness of the films were calculated from the observed positions of the consecutive maxima or minima. The estimated values of thickness match closely to those measured by the multiple beam interferometry technique.

5.III.E Photoconductivity Measurements:

5.III.E.1 Spectral Response:

The spectral response of photocurrent measured at room temperature for In_2Se_3 sample, for a constant incident photon flux is shown in Fig.5.15. The corresponding absorption sepectrum is also shown for comparison. The photoconductivity signal in the low-absorption region (below 1.24 eV) is proportional to the absorption coefficient. In the relatively higher energy region the photoconductivity spectrum shows a broad maximum (1.65-1.98 eV), with a subsequent lowering.

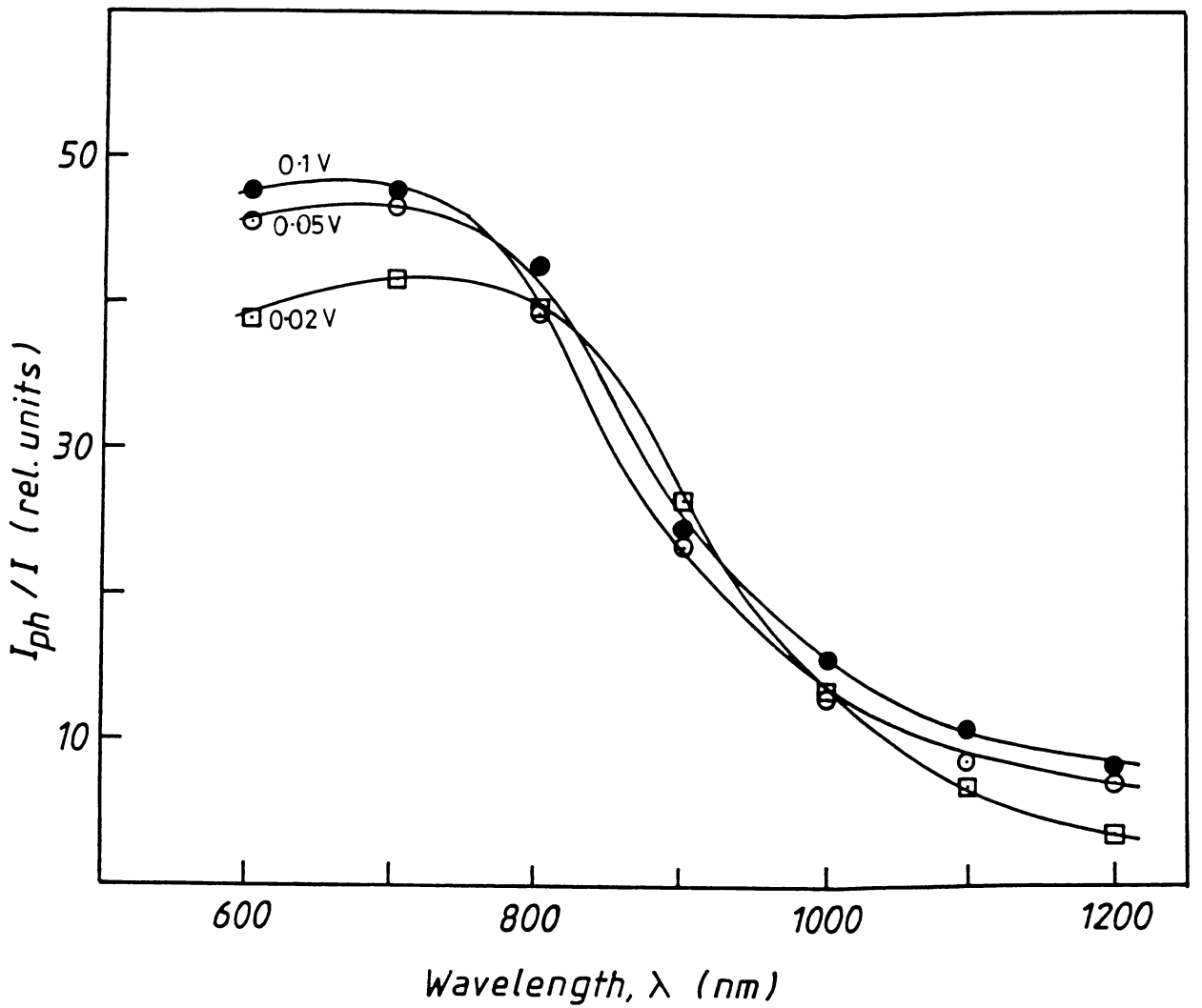

Fig.5.15 Dependence of photocurrent on wavelength for In_2Se_3 films at different bias (room temperature).

At energies lower than 1.4 eV the photoconductivity spectrum represents only the density of states within the gap introduced by defects or imperfections. As the band gap energy region is reached the photogenerated carriers account entirely for the process with a broad maximum between 1.65 eV and 1.98 eV. Again at the higher energy side (i.e., above 1.98 eV) the response decreases with respect to the broad maximum value, as expected. This observed weakening in the photoresponse is generally attributed to the change in the recombination level of the photogenerated carriers[61,62]. At higher temperatures, the photoresponse spectrum shows a slight shift (Fig.5.15) in the broad maximum, but this is less pronounced than the same observed in InSe. This is also in consistent with the temperature effect in gap energy obtained from optical measurements.

5.III.E.2 Variation of I_{ph} with light intensity:

The variation of photocurrent of the In_2Se_3 films with different excitation intensity at a fixed wavelength (λ=1000 nm) was measured at room temperature. The light intensity was varied by about three decades and a quenching of photoconductivity was observed at higher illumination levels. A typical plot is shown in Fig.5.16. The resulting lux-ampere characteristics consist of two regions: (1) a superlinear ($Iph \sim L^{1.4}$) region at low illumination levles, (2) a sublinear ($Iph \sim L^{0.57}$) region corresponds to a quasi-saturation which occurs at higher intensities.

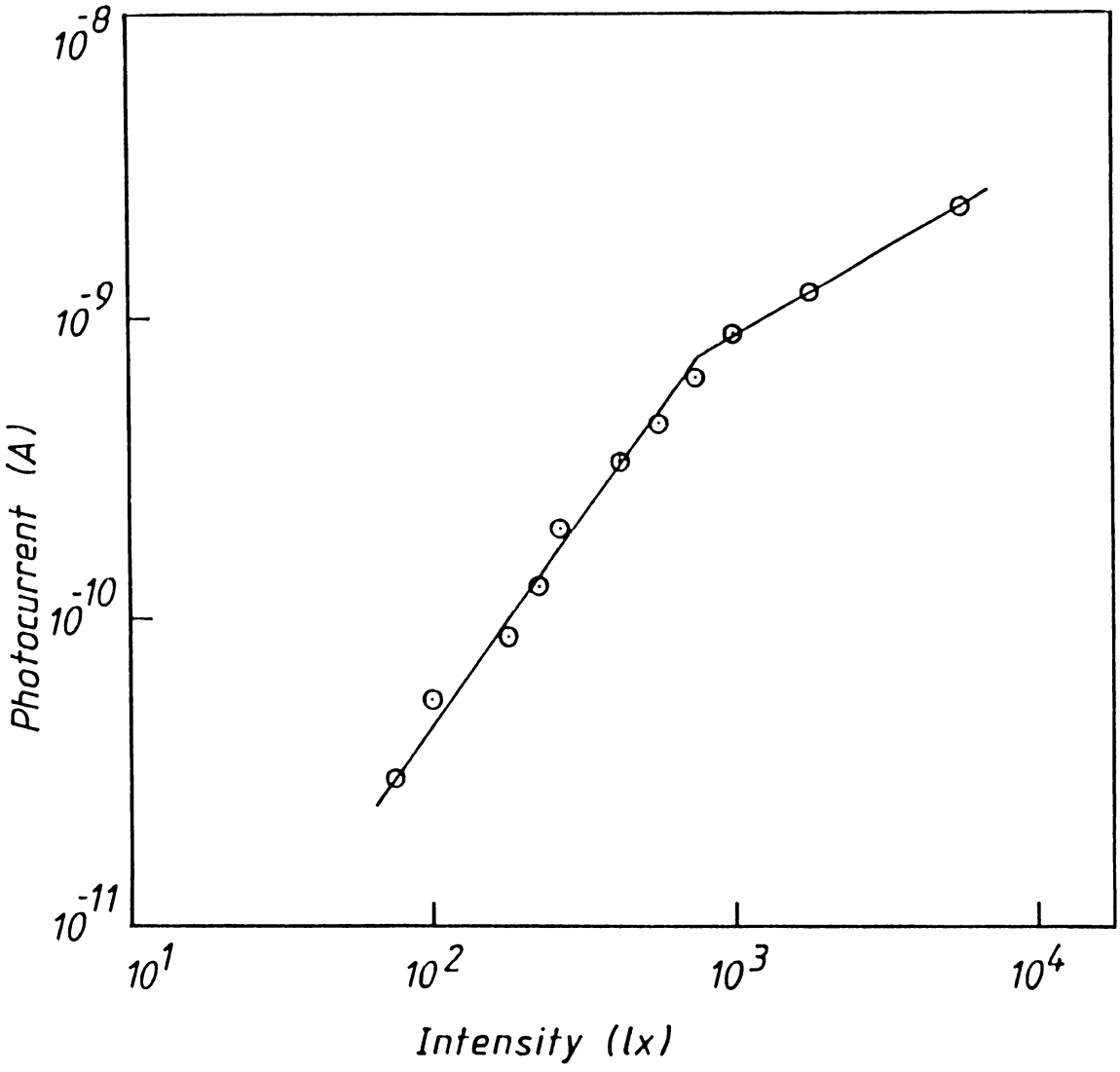

Fig.5.16 Variation of photocurrent with incident light intensity for a fixed bias at room temperature, for films annealed at 460K

The above results can be explained by a recombination model suggested by Rose and discussed for InSe in Chapter 4. According to this a thermal quenching of photoconductivity coincided with a superlinear lux-ampere characteristic, and indicates the presence of two sets of centers in the photoconductivity process. Class I centers lie above the dark Fermi level and have a much larger electron capture cross section than Class II centers, which lie below the dark Fermi level. If the number of Class II centers is greater than the number of Class I centers, superlinear intensity dependence of the photoconductivity can be expected[63,64]. The super linearity occurs as the light intensity is increased and electrons are shifted from Class II centers to Class I centers. This change in occupation level blocks recombination through Class I centers.

5.III.E.3 Dependence of I_{ph} on temperature:

Fig.5.17 shows a typical plot of temperature dependence of photocurrent at λ = 1000 nm. As the temperature is increased the photocurrent shows a steady increase in the values. Increase in temperature first excite electrons from states below the Fermi level into centers I. Under these conditions both lifetime and density of electrons in the conduction band will increase, resulting in a higher photocurrent. As the temperature is increased, the probability of thermal excitation of holes from Class II centers to the valence band increases, which means that holes are captured by the Class I centers. This shortens the electron lifetime because of recombination and consequently photocurrent values saturate.

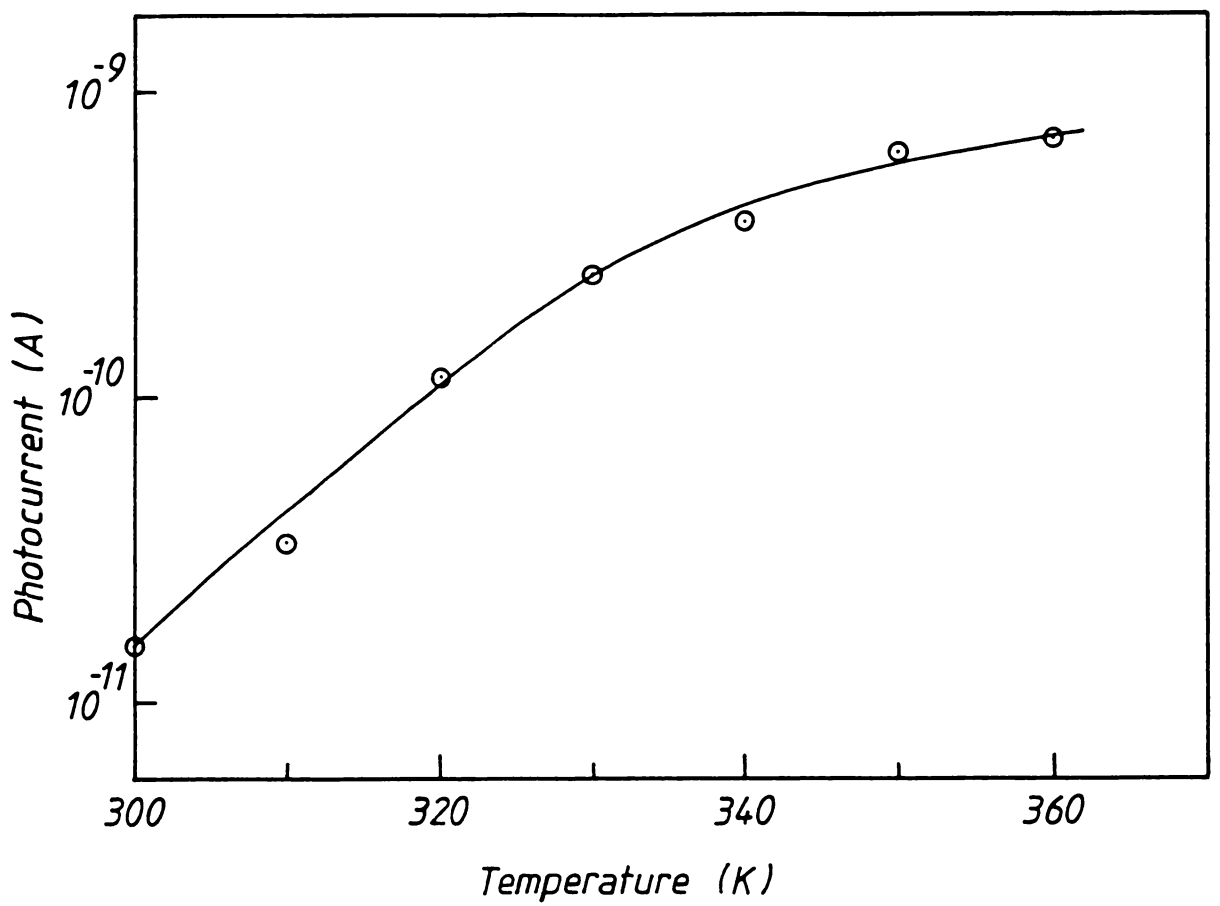

Fig.5.17 Thermal variation of photocurrent for a typical In_2Se_3 film at a fixed bias, for films annealed at 468 K.

5.IV Conclusions.

In this chapter, a systematic study, that has been undertaken to deposit and characterise In_2Se_3 thin films, has been described. The effect of deposition temperature and post-depositional annealing on the formed films have been studied in detail using different characterisation techniques. The data suggest that the increase in post-depositional annealing time from an optimum duration, changes the composition. X-ray diffraction analysis shows that the preferred orientation of the crystallites are in the (001) direction. XPS studies confirm the composition of the prepared In_2Se_3 films, and obtain the energy shifts in In 3d and Se 3d levels for this compound. The optical and electrical studies show a change in band gap from that of indium monoselenide. From the optical measurements the band gap obtained is around 1.39 ± 0.03 eV. Photoconductivity studies reveal that In_2Se_3 is less photosensitive than InSe thin films.

References:

1. H.Hahn and G.Frank, Z.Anorgan.Allg.Chem., **278**, 333 (1955).
2. H.Hahn and G.Frank, Naturawissen., **44**, 533 (1957).
3. H.Miazawa and S.Sugaike, J.Phys.Soc.Japan, **12**, 312 (1957).
4. S.A.Semiletov, Sov.Phys.Crystallogr., **5**, 673 (1961).
5. S.A.Semiletov, Sov.Phys.Solid State, **3**, 544 (1961).
6. K.Osamura, Y.Murakami and Y.Tomilie, J.Phys.Soc.Japan, **21**, 1848 (1966).
7. S.Popovic, B.Celustka, Z.Ruzic-Toros and D.Broz, Phys.Stat. Sol.(a) **41**, 255 (1977).
8. A.Likforman, D.Carre and R.Hillel, Acta Cryst.,B **34**, 1 (1978)
9. A.Likforman, P.-H Fourcroy, M.Guittard, J.Flahaut, R.Poirier and N.Szydlo, J.Solid State Chem., **33**, 91 (1980).
10. K.Kambas and C.Julien, Mat.Res.Bull., **17**, 1573 (1982).
11. J.Van Landuyt, G.Van Tendeloo, S.Amelinckx, Phys.Stat.Sol., (a) **30**, 299, (1975).
12. F.Hulliger, Structural Chemistry of Layer-type phases (Ed.) F.Levy, D.Reidel, Dordrecht (1976).
13. A.Likforman and M.Guittard, C.R.Acad.Sci. (Paris) **279C**, 33 (1974).
14. J.C.W.Folmer, J.A.Turner, R.Noufi and D.Cahen, J.Electrochem, **132**, 1319 (1985).
15. V.M.Koshkin, L.P.Gal'chinetskii, V.N.Kulik, G.K.Gusev and U.A.Ulmanis, Sov.At.Energy, **42**, 321 (1977).
16. G.Guizzetti and F.Meloni, Nuovo Cimento, D 1, 503 (1982).
17. M.Balkanski, K.Kambas, C.Julien, J.Hammerberg and D.Schleich, Solid State Ionics, **5**, 384 (1981).

18. C.Julien, E.Hatzikraniotis, A.Chevy and K.Kambas, Mat.Res. Bull., **20**, 387 (1985).

19. G.K.Slavnova, Izv.Akad.Nauk Mold.SSR, 7, 43 (1963).

20. C.Julien, M.Eddrief, K.Kambas and M.Balkanski, Thin Solid Films, **137**, 27 (1986).

21. I.Watanabe and T.Yamamoto, Jap.J.Appl.Phys., **24**, 1282 (1985).

22. M.Yudasaka and K.Nakanishi, Thin Solid Films, **156**, 145 (1988)

23. I.Samara, M.Tsahiri and C.Julien, in: Chemical Physics of Intercalation, Eds.,P.A.Legrand and S.Flandrois, NATO, ASI Ser. (Plenum, New York, 1987).

24. F.Levy (Ed.), Intercalated Layered materials, D.Reidel, Dordrecht (1979).

25. M.S.Whittingan, Prog.Solid State Chem., **12**, 41 (1978).

26. M.Balkanski, Appl.Surf.Science, **33/34**, 1260 (1988).

27. S.Popovic, A.Tonejc, B.G.-Plenkovic, B.Celustka and R.Trojko J.Appl.Cryst., 12, 416 (1979).

28. J.H.Scofield, J.Elect.Spect.Rel.Phenom., 8, 129 (1976).

29. R.J.Thorn, J.Elect.Spect.Rel.Phenom., 31, 207 (1983).

30. D.Briggs and M.P.Seah (Eds.), Practical Surface Analysis by Auger and X-ray Photoelectron Spectroscopy, John Wiley, Chichester (1983).

31. M.K.Bahl, R.L.Watson and K.J.Irgolic, J.Chem.Phys., 72, 4069 (1980).

32. A.W.C.Lin, N.R.Armstrong and T.Kuwana, Anal.Chem., **49**, 1228, (1977).

33. I.Ikemoto, K.Ishii, S.Kinoshita, H.Kuroda, M.A.Alario Franco and J.M.Thomas, J.Solid State Chem., 17, 425 (1976).

34. G.C.Allen and P.M.Tucker, Inorg.Chim.Acta, 16, 41 (1976).

35. B.W.Veal and A.P.Paulikas, Phys.Rev., B 31, 5399 (1985).

36. C.N.R.Rao, D.D.Sarma, S.Vasudevan and M.S.Hegde, Proc.R.Soc. London, Ser A 367, 239 (1979).

37. L.L.Kazmerskii, W.B.Berry and C.W.Allen, J.Appl.Phys., 43, 3515 (1972).

38. J.W.Orton and M.J.Powell, Rep.Prog.Phys., 43, 1263 (1980).

39. C.Julien, M.Eddrief, M.Balkanski, E.Hatzikraniotis and K.Kambas, Phys.Stat.Sol.,(a) 88, 687 (1985).

40. J.Fotsing, C.Julien, M.Balkanski and K.Kambas, Mat.Sci.&Eng., B 1, 139 (1988).

41. D.Das and R.Banerjee, Thin Solid Films, 147, 321 (1987).

42. L.L.Kazmerski, W.B.Berry and C.W.Allen, J.Appl.Phys., 43, 3521 (1972).

43. M.Persin, A.Persin, B.Celustka and B.Etlinger, Thin Solid Films, 11, 153 (1972).

44. I.Martil, J.Santamaria, E.Iborra, G.Gonzalez-Diaz and F.Sanchez-Quesada, J.Appl.Phys., 62, 4163 (1987).

45. S.Noguchi and H.Sakata, J.Phys.D:Appl.Phys., 13, 1129 (1980).

46. M.Yudasaka, T.Matsuoka and K.Nakanishi, Thin Solid Films, 146, 65 (1987).

47. J.Herrero and J.Ortega, Solar Energy Mat., 16, 477 (1987).

48. H.Berger, Phys.Stat.Sol., 1, 739 (1961).

49. R.G.Mankarious, Solid State Electron., 7, 702 (1964).

50. L.L.Kazmerski and Y.J.Juang, J.Vac.Sci.Technol., 14, 769 (1977).

51. L.L.Kazmerski, F.R.White, M.S.Ayyagary, Y.J.Juang and R.P.Patterson, J.Vac.Sci.Technol., 14, 65 (1977).

52. S.W.Kurnick and J.M.Powell, Phys.Rev., 116, 597 (1959).

53. E.G.Johnson, in Semiconductors and Semimetals, Vol.3, R.K.Willardson and A.C.Beer (Eds.), (Academic Press, New York 1967).

54. I.Hamberg, C.G.Granqvist, K.F.Berggren, B.E.Sernelius, L.Engstrom, Phys.Rev., B 30, 3240 (1984).

55. L.Y.Sum, L.L.Kazmerski, A.H.Clark, P.J.Ireland and D.W.Norton J.Vac.Sci.Technol., 15, 265 (1978).

56. I.Martil, G.Gonzalez-Diaz, F.Sanchez-Quesada and M.Rodriguez-Vidal, Thin Solid Films, 120, 31 (1984).

57. M.Eddrief, C.Julien, M.Balkanski and K.Kambas, Mater.Letters, 2, 432 (1984).

58. V.P.Mushinskii, V.I.Kobolev and I.Ya.Andronik, Sov.Phys. Semicond., 5, 1104 (1971).

59. K.Kambas and J.Spyridelis, Mat.Res.Bull., 13, 653 (1978).

60. M.Balkanski, C.Julien, A.Chevy and K.Kambas, Solid State Commun., 59, 423 (1986).

61. H.-J.Hoffmann and F.Stockmann, in: Advances in Solid State Physics, XIX, (Vieweg, Wiesbaden, 1979).

62. J.Jimenez, M.A.Gonzalez, B.Carbayo and J.Bonnaffe, Phys.Stat. Sol.,(a) 77, K69 (1983).

63. A.Rose, Proc.Inst.Radio Engrs., 43, 1850 (1955).

64. R.H.Bube, Proc.Inst.Radio Engrs., 43, 1836 (1955).

CHAPTER 6

CONCLUSIONS AND FURTHER SCOPE

6.I Summary, Conclusions and Further scope

Layered semiconductors are of recent interest in the field of semiconductors. Since its revelation, efforts to prepare stoichiometric crystalline thin films progressed rather slowly due to the ensued deposition or growth related problems. These include the co-existence of different phases, difficulty in the control of stoichiometry etc.

Increasing interest on the layered materials, over the last few years eventhough helped to reveal many of the structural as well as physical properties, there remain much uncertain, especially about the physical properties. The theoretical electronic energy levels, for example, of InSe have not satisfactorily been established with all its details. This is mostly because, these one way or other depends on the input of experimental information which are not clear.

In indium selenides, for different structural variations, the stacking energies required are nearly the same. So the layers in these materials can be stacked in a variety of ways, depending upon preparation conditions. This often reflects in the measured properties. As a result study of all the properties relating to the structure has become inevitable. In thin films, besides this, the co-existence of many phases and complication in maintaining the stoichiometry posed additional problems. In the present study the primary attention has been paid to prepare stoichiometric crystalline thin films of InSe and In_2Se_3 by elemental

evaporation and to investigate their properties.

Three Temperature (or Elemental evaporation) method is a powerful technique for the deposition of crystalline thin films of a large range of compositional and structural variations. The capability of depositing compounds at high temperature which is needed for the growth of crystalline and especially epitaxial films make this method a more attractive one. However, despite its apparent simplicity this elemental deposition technique, at high substrate temperature is a complex process, which involves much strenuousness and precise control over deposition process, to grow films of the desired stoichiometry.

The deposition mechanism in a three temperature method can be described precisely as follows. Condensation of solids on heated surfaces occur when the critical supersaturation of the vapour phase exceeds a certain limit. The critical values of the incident flux are related to substrate temperature and the interfacial energies of the involved vapours. At a favourable presence of component atoms in the vapour phase, these can react and condense onto a substrate even at an elevated temperature.

For preparing films with desired stoichiometry, geometries of sources as well as control of flux ratios are important. For accomplishing the later, the necessary control instrumentation was done. With separate control over the flux of the reactive ions and the amount of component atoms delivered, the composition of the film can be varied.

In the present study, thin films were deposited on glass, quartz or NaCl substrates. Films deposited on glassy substrates were all polycrystalline while, those deposited on crystalline substrates were much more crystalline. Both in InSe and In_2Se_3, the thinner films were reddish brown and thicker films were silvery black. But for thinner In_2Se_3 films which were much more reddish in their appearance.

Deposition rate appears to be an important parameter that affects the orientation of crystallites in the deposited films. Slower deposition rates resulted in more highly oriented crystallites in the films. Also it affects the grain size and the rise of optical absorption. An increase in the deposition temperature, resulted in an increase in the indium content in the films, which may be because of the decrease of sticking coefficient of the selenium atoms. Post depositional annealing at temperatures above 480 K for longer duration resulted in selenium-deficient films.

The deposited InSe films were of single composition and single phase of γ-polytype with practically no admixture. But the In_2Se_3 films formed were in the low temperature modification called α -phase. Detailed X-ray diffraction (XRD) analysis showed that the films deposited above 423 K were polycrystalline with highly oriented crystallites. In InSe this was in the (0 0 3n) direction and in In_2Se_3, in the (0 0 1) direction. The FWHM of the XRD peaks showed that the individual grains are fairly large in size. The TEM measurements also confirmed the grain size.

Composition of the films were checked by XPS analysis as well as by DAN flurimetry. The XPS spectra for different compositions were recorded and the energy shifts were interpreted in terms of composition. In addition, the XPS spectra were analysed for its energy levels.

In InSe the dark electrical conductivity at room temperature was in the range of 7.0×10^{-2}- 5.0×10^{-1} ohm^{-1} cm^{-1}. At the same time these values for In_2Se_3 films were still higher of about $2.0 - 7.0 \times 10^{-1}$ ohm^{-1} cm^{-1}. Annealing for longer time was found to decrease the conductivity. Activation energies were also evaluated and seen to be 0.63 ± 0.005 eV and 0.64 ± 0.01 eV respectively for InSe and In_2Se_3. These estimated activation energies vary a little from the values obtained in optical measurements due to reasons discussed earlier.

All the stoichiometric InSe films were of n-type with carrier concentration ranging from 9.2×10^{17} to 6.0×10^{18} cm^{-3}. The Hall coefficient measured was between 1.0 - 20.0 cm^2 C^{-1}. In In_2Se_3 films, these were $1.5 - 3.5 \times 10^{17}$ cm^{-3} and 18.0 -29.0 cm^2 C^{-1} respectively.

Optical properties were a good guide to the characterisation and for the establishment of microstructural details. Absorption tail of polycrystalline films was of quite significance and it assisted to get some idea about the degree of crystallinity and compared it with TEM results. The forbidden energy gap of these compounds, InSe and In_2Se_3, were found to be 1.29 eV and 1.39 eV respectively prepared at the optimum substrate temperatures. This

value of InSe is in close agreement with single crystal value while for In_2Se_3, no reliable data exists. Absorption coefficient of these compound thin films of InSe and In_2Se_3 are in the order of 4.8×10^4 and 6.4×10^4 respectively.

Optical gap increases with annealing indicating the decrease of localised states upto an optimum time and temperature of heat treatment. This is also evident from the increasing sharpness of absorption or transmission spectrum.

The spectral dependence of the refractive index of the films were measured by spectrophotometric method. The oscillations in the reflectivity spectra were used to calculate this. The refractive index obtained for InSe and In_2Se_3 were 3.11 ± 0.005 and 3.05 ± 0.02 respectively at 2000 nm.

Wavelength and light intensity dependence of steady state photoconductivity showed a broadened peak of photocurrent response maximum occurring near the bandgap absorption region. In light intensity dependence, there are two regions and the results were analysed using a simple recombination model proposed by Rose. The temperature dependence suggests the presence of recombination centers and trap centers in the band gap region.

Schottky barriers are effective in analysing the interface behaviour and for the study of barrier heights. On the schottky barrier diodes formed with Au, the spectral dependence, and the I-V and C-V characteristics were recorded. The barrier heights determined by these methods for InSe with Au, matches well with

each other and is in the range of 0.805 ± 0.02 eV. The diffusion length was also measured from the C-V characteristics and about 1.0 μm.

From these measurements, it is evident that, these thin films are of high-quality and matches well in its properties to that of single crystals.

From the present studies of attempts to grow indium selenide thin films, the most significant result is the formation of single-compositional film namely indium monoselenide in the In -Se system of compounds. Further, this work shows the feasibility of thin film photovoltaic junctions of the Schottky barrier type.

In the preparation of single phase films, the evaporation flux in relation to the substrate temperature is a key parameter. With a good regulation of the amount of component atoms delivered to the growing film, both the stoichiometry and the physical properties of the film can be tailored to meet the practical requirements. However much remains to be done on the different aspects of compositional variations and the addition of impurities. Electrical properties of the films may get modified by doping and has to be studied in detail to map out the changes in parameters. A detailed study of photoconductive properties in relation to other properties can also shed more light on the details of the electronic processes occurring in the material. More information is required about the nature of barriers with different junction materials to tap the full potential of the material and to gain an understanding of the variability with slight changes in surface parameters.

We also remain poorly informed about the nature of the gap states in this semiconductor thin films. Surface morphology, internal voids and grain boundaries are of great technological importance and are responsible in a large number of cases in increasing the solar absorption. Investigations to determine the critical structural parameters and proper degree of textural effects that may increase the solar absorption, remains to be done. Such measurements in InSe, In_2Se_3 and other compositions in the In -Se system will demonstrate the comparative feasibility of these materials in thin film solar cells. Studies of the stability of the films under intense radiations may be useful from the practical point of view.

It is anticipated that indium selenides in the intercalated form, will emerge as a major material in the application of solid state batteries, apart from its use in solar cells and high-resolution optical recording. In conclusion, the present work provides an enlightenment of properties and potential in the application of indium selenide and it suggests additional research to elucidate more fully the pertinent process variables so that this material and techniques may be used more easily and effectively to evidence exciting new happenings in the microelectronics field in the years ahead.
